Advances in generating high repetition rate EUV frequency combs

Andreas Vernaleken

München 2013

Advances in generating high repetition rate EUV frequency combs

Andreas Vernaleken

Dissertation
an der Fakultät der Physik
der Ludwig–Maximilians–Universität
München

vorgelegt von
Andreas Vernaleken
aus Fulda

München, den 18. 11. 2013

Erstgutachter: Prof. Dr. Theodor W. Hänsch
Zweitgutachter: Prof. Dr. Ferenc Krausz
Tag der mündlichen Prüfung: 16. Dezember 2013

Zusammenfassung

Die vorliegende Arbeit berichtet über experimentelle Fortschritte in der Entwicklung von vielseitig einsetzbaren Frequenzkämmen mit hoher Repetitionsrate im extremen Ultraviolett (EUV).

Dauerstrichlaser, die in diesem Spektralbereich emittieren, scheinen gegenwärtig nicht realisierbar. Daher wird auf nichtlineare Konversionsprozesse wie zum Beispiel die Erzeugung hoher Harmonischer (HHG, von engl. "high harmonic generation") in Gasen zurückgegriffen, um kohärentes, extrem ultraviolettes Licht mit verfügbaren Lasern zu generieren. Die zur Zeit am häufigsten dafür genutzen Lasersysteme erzeugen die hohen Harmonischen im Einzeldurchgang, jedoch bei vergleichsweise niedrigen Repetitionsraten im kHz-Bereich. Es war bislang dem Ansatz der HHG in resonanten Femtosekunden-Überhöhungsresonatoren vorbehalten, EUV-Licht mit den für einige Anwendungen, beispielsweise die Präzisions-Frequenzkamm-Spektroskopie, benötigten oder vorteilhaften Repetitionsraten im MHz-Bereich zur Verfügung zu stellen. Ein schwieriges Unterfangen dabei blieb jedoch, das erzeugte Licht aus dem Resonator auszukoppeln, ohne dabei dessen Überhöhung zu verschlechtern.

Für die vorliegende Arbeit wurde der Prozess der nicht-kollinearen Harmonischen-Erzeugung sowohl experimentell als auch mit Hilfe numerischer Simulationen untersucht. Diese nicht-kollineare Geometrie scheint sich hervorragend als breitbandige, vermeintlich verlustfreie Auskoppelmethode für Überhöhungsresonatoren zu eignen, weil die generierte EUV-Strahlung entlang der Winkelhalbierenden der beiden sich im Gas kreuzenden erzeugenden Laserstrahlen emittiert wird, was eine räumliche Trennung ermöglicht. In ersten spektral aufgelösten Experimenten mit verstärkten Laserpulsen konnte diese prinzipielle Eignung bestätigt werden. Weitere Experimente und Simulationen zur Abhängigkeit der Emissionsrichtung und des Fernfeld-Strahlprofils der EUV-Strahlung von experimentellen Parametern wurden durchgeführt. Die genaue Analyse der Abhängigkeit des NCHHG-Prozesses von der Verzögerung zwischen den treibenden Pulsen führte zu der Überlegung, die nicht-kollineare Geometrie möglicherweise zur Erzeugung von isolierten Attosekundenpulsen verwenden zu können.

Ein weiterer Schwerpunkt der Arbeit war die Erzeugung von EUV-Frequenzkämmen durch HHG im Einzeldurchgang bei bislang mit solchen Systemen unerreichten Repetitionsraten von 10 MHz und 20 MHz. Dies wurde durch den Einsatz eines Hochleistungslaserverstärkers der neuesten Generation ermöglicht. Obwohl sich mit Überhöhungsresonator-basierten Systemen gegenwärtig noch höhere Ausgangsleistungen im EUV erzielen lassen als hier ($\sim 1\,\mathrm{nW}$ bei $\sim 70\,\mathrm{nm}$) gezeigt, verspricht die Harmonischen-Erzeugung im Einzeldurchgang ein deutlich höheres Maß an experimenteller Kontrolle und Flexibilität, da Parameter wie die Repetitionsrate, die Polarisation oder die Fokussierung der Fundamentalen vergleichsweise einfach variiert werden können. Es wird erwartet, dass auf HHG im Einzeldurchgang basierende Systeme aufgrund ihrer Vielseitigkeit weite Verbreitung finden werden.

Summary

This dissertation reports on experimental advances in the development of versatile high repetition rate extreme ultraviolet (EUV) frequency combs.

Since continuous wave laser sources are not conceivable in the EUV, nonlinear conversion processes such as high harmonic generation (HHG) are employed to produce coherent light in this spectral region. The currently most widespread systems generate high harmonic radiation in a single pass geometry, but operate at low repetition rates of several kHz. However, several applications, for example precision EUV frequency comb spectroscopy, demand or profit from higher repetition rates in the MHz regime. In the past, the latter could only be realized via cavity-assisted HHG. In this approach, the available seed radiation is resonantly enhanced in an external broadband resonator and high harmonics are generated in an intracavity target. Therefore, a suitable method to extract the generated EUV light from the resonator without disturbing its performance is required.

In the first part of the work presented here, non-collinear high harmonic generation (NCHHG) was investigated in detailed experimental and numerical studies. In NCHHG, the EUV radiation is emitted along the bisector of two driving beams intersecting in the target at an angle. This intrinsic spatial separation of fundamental and EUV promises the applicability of NCHHG as a wavelength-independent and highly efficient outcoupling method for cavity-assisted HHG. In spectrally resolved experiments with amplified laser pulses, non-collinear high harmonic emission was observed and hence the potential of NCHHG as an outcoupling method confirmed. Independent control of the driving beams allowed the investigation of the spatio-temporal coupling produced by the NCHHG process. It was found experimentally and reproduced in numerical simulations that the far field profiles of the non-collinearly generated EUV light show strong spatial modulations that depend on the delay between the driving pulses and on the intensity-dependent dipole phase. The generation of angularly separated, isolated attosecond pulses was identified as a potential application of NCHHG.

The main result described in the second part of this thesis is the first demonstration of single pass HHG at unprecedented repetition rates of 10 MHz and 20 MHz in a scalable, versatile setup. These proof-of-principle experiments were rendered possible by the emergence of laser amplifiers with suitably high output powers. The generated EUV powers of up to ~ 1 nW around 70 nm are not comparable yet to those currently produced by cavity-assisted HHG. However, single pass HHG shows favorable scaling properties because it is less sensitive to nonlinear phase shifts that were identified as detrimental in cavities. Single pass HHG also enables the generation of high repetition rate EUV frequency combs at an unprecedented level of experimental control because parameters such as repetition rate, polarization, driving geometry, and focusing conditions can be varied rather easily. An increasing number of applications for such versatile table-top sources is expected.

Contents

1 Introduction

In the now more than fifty years since the first observation of light amplification by stimulated emission of radiation ("laser") [1], lasers have become indispensable tools in science, industry, and every-day life. Their fields of application are as diverse as laser cooling, precision spectroscopy, photolithography, data transmission, and otorhinolaryngology. New applications have inextricably been linked to advances in laser development and technology so that extending the spectral band in which laser radiation is available has been one of the paramount goals of laser research. Currently, the spectral coverage of commercial lasers is limited to the wavelength range between $\sim 200\,\mathrm{nm}$ and hundreds of μm.

Making the vacuum ultraviolet (VUV) and particularly the extreme ultraviolet (EUV) spectral regions[1] directly accessible to laser radiation is highly desirable for a number of applications in industry and science. Coherent EUV sources could, for example, be used both for metrology and material inspection in the next generation of EUV lithography at 13.5 nm. On the other hand, the simplest atoms and ions of the periodic table such as hydrogen, helium, and both hydrogen- and helium-like ions all have ground state transitions in the EUV. Therefore, precision laser spectroscopy of the latter could enable stringent tests of the underlying fundamental theory of light matter interactions, bound state quantum electrodynamics (QED).

This thesis reports on advancements of versatile, coherent table-top laser sources of high spectral purity in the EUV. Building such a source is challenging for a number of reasons. Since all solid materials become rather opaque below $\sim 105\,\mathrm{nm}$ and since EUV photon energies exceed the ionization potentials of most gases as well, a vacuum environment is essential and only few (noble) gases or plasmas can be used as laser media at all. Moreover, enormous pump power densities are required to create inversion, and in the absence of suitable highly reflecting mirrors, single pass laser configurations have to be used. The past decade has witnessed remarkable progress in the development of coherent table-top EUV sources that are based on discharge- or laser-produced plasmas and operate at repetition rates of several Hz. However, a coherent narrow-band continuous-wave (cw) EUV source is currently not conceivable.

Given the constraints outlined above, nonlinear frequency conversion processes in a gaseous media appear to be the most promising path to this spectral region. Among those, high harmonic generation (HHG) is particularly attractive since it allows to coherently upconvert the radiation from an appropriate visible or infrared (IR) laser to very high photon energies beyond the ionization potential of the target gas. However, HHG only occurs when atoms interact with fields comparable to atomic field strengths which

[1] See Table 1.1 for the definitions of spectral regions used in this work

	Abbreviation	Wavelength range [nm]
soft x-rays	SXR/XUV	$0.1 - 10$
extreme ultraviolet	EUV	$10 - 121$
vacuum ultraviolet	VUV	$10 - 200$

Table 1.1: *Excerpt of definition of solar irradiance spectral categories according to ISO 21348*

can be translated to threshold intensities above $\sim 10^{13}\,\mathrm{W/cm^2}$. The latter make the use of ultrashort pulses imperative, which at first glance appears to preclude applications requiring spectrally pure, coherent sources. However, optical frequency comb synthesizers [2, 3] favorably unite the large peak intensities of the infinite pulse trains that they emit with the high spectral purity of the discrete comb components that constitute their broadband spectra. Thus, HHG can enable the realization of an ensemble of extreme ultraviolet quasi-cw lasers by coherently transferring the frequency comb structure to the EUV.

In view of both the efficiency of the nonlinear HHG process and the intended application, a crucial parameter to be considered is the pulse repetition rate of the frequency comb synthesizer. Intuitively, the best approximation of a cw laser is obtained for the highest possible repetition rate. The latter results in a frequency comb spectrum with well-separated modes and narrow linewidths which is benfeficial for spectroscopy of both single- and two-photon transitions: On the one hand, the average power per comb mode is higher assuming a constant attainable EUV power while on the other hand, a larger mode spacing allows to unequivocally resolve a transition with a large natural linewidth or multiple simultaneously excited transitions. Apart from spectroscopy, there are several other applications that can leverage such a high repetition rate EUV source as well. Prominent examples comprise techniques for the investigation of solid state surface dynamics such as time- and angle-resolved photoelectron spectroscopy (PES) and time-resolved photoelectron emission microscopy (PEEM) [4]. If the available EUV average power is distributed over more pulses, the resulting peak intensity is lower so that detrimental space charge accumulation, sample heating, and damage can be avoided. At the same time, high repetition rates enable investigations with both high spatial and high temporal resolution at high signal-to-noise ratios [5]. In low event rate coincidence techniques such as the reaction microscope [6], high repetition rates result in significantly reduced acquisition times to obtain good statistics.

The main technical challenge in the realization of an EUV frequency comb at multi-MHz repetition rate is to reach the enormous peak intensities necessary for high harmonic generation. Since the achievable average and peak powers of typical femtosecond laser systems are limited by the damage threshold of the employed gain media and optical components, the so far most commonly used approach has been to increase their peak powers at the expense of repetition rate using techniques such as chirped pulse amplification (CPA) [7]. EUV radiation can then be generated in a single pass geometry, but at repetition rates in the kHz regime. An elegant way to circumvent this limitation in repetition rate is provided by the concept of cavity-assisted HHG [8, 9]. Here, the output

of a femtosecond oscillator is coupled into an external passive femtosecond enhancement resonator to boost the available average power at the full oscillator repetition rate. High harmonic radiation is generated collinearly with the fundamental in an intracavity gas target so that a viable mechanism to outcouple the EUV from the resonator becomes necessary.

Since the first proof-of-principle demonstrations [8,9], cavity-assisted HHG has emerged quite successfully. Several orders of magnitude higher EUV output powers reaching $\sim 100\,\mu$W in a single harmonic order [10] are now available and have enabled the first spectroscopic experiments employing cavity-based EUV sources recently [11, 12]. Major advances were enabled by more elaborate dispersion management and ingenious outcoupling methods. The latter include precisely etched cavity mirrors that simultanously serve as gratings for the EUV [13] and outcoupling of a fraction of the generated EUV through a hole in the first cavity mirror behind the target [14, 15]. Nevertheless, further scaling of the available EUV power is becoming increasingly challenging because damage and nonlinear responses of the cavity mirrors as well as ionization dynamics in the gas target currently limit the fundamental intracavity power to below 10 kW [10, 16–18].

In the course of this thesis, two approaches were studied that promise improved scalability and pave the way towards higher available EUV powers: single pass high harmonic generation and non-collinear high harmonic generation (NCHHG). The latter can still be used in combination with an enhancement cavity, but as the name suggests, the high harmonics are emitted along the bisectrix of two crossing fundamental beams and can thus pass between cavity mirrors. In contrast to other outcoupling methods, NCHHG works for all high harmonic wavelengths with the same (theoretically unity) outcoupling efficiency. At the same time, omitting the enhancement cavity with its associated difficulties has become feasible due to impressive developments in the field of amplified high power femtosecond lasers. The single pass HHG configuration grants significantly more freedom in designing experiments that would be very hard if not impossible using an enhancement cavity: The conversion efficiency could be improved using techniques such as quasi phase matching in a hollow core fiber and the beam profile, the wavelength, and the polarization of the driving pulses could be varied or the repetition rate tuned.

The results of our efforts are presented in the following way: Chapter 2 provides a basic mathematical description of ultrashort pulses and their properties along with a summary of related quantities and phenomena for further reference. Chapter 3 gives a detailed review of the theory of high harmonic generation whose understanding both on a microscopic and a macroscopic level has proven to be crucial for the optimization of EUV frequency comb sources. In Chapter 4, the results of our experimental and numerical investigations of non-collinear high harmonic generation are summarized. After confirming its potential application as a combined generation and outcoupling technique for cavity-assisted HHG in an experiment with amplified pulses, the focus of our studies was diverted towards the analysis of the strongly modulated high harmonic far field profiles and their dependence on experimental parameters. Chapter 5 presents the experimental results of the first proof-of-principle demonstrations of single-pass high harmonic generation at multi-MHz repetition rates using a robust, versatile, and scalable approach based on a recently developed high power solid state amplifier system.

2 Basics

2.1 Ultrashort optical pulses

This section is meant to give a brief (mathematical) description of ultrashort optical pulses and their characteristics as a reference for this thesis. More detailed and elaborate summaries can be found in the pertinent literature, e.g. in [19–21].

2.1.1 General description

As the naming suggests, ultra*short* pulses can be described as a time domain phenomenon. Likewise, however, there is a fully equivalent frequency domain description. Time and frequency domain are linked via a Fourier transform, and it is thus also common to talk about ultrabroadband pulses. The most general representation of an optical pulse has to take into account the polarization and the dependence of the electric field on space and time. Here, we will first focus on the time-dependence of linearly polarized light thus neglecting the vector character of the electric field and its spatial dependence. We also take advantage of the common and convenient practice of using the complex representation of the electric field as a short-hand notation. In the following, we thus omit the complex conjugates that are required to obtain real physical quantities. The time dependent field of an optical pulse then reads

$$E(t) = A(t)e^{i\phi(t)} \tag{2.1}$$

with (real) pulse envelope $A(t)$ and temporal phase $\phi(t)$. The equivalent spectral representation

$$E(\omega) = \mathcal{E}(\omega)e^{-i\Phi(\omega)} \tag{2.2}$$

with (real) spectral amplitude $\mathcal{E}(\omega)$ and spectral phase $\Phi(\omega)$ can be obtained via Fourier transformation

$$E(t) = \frac{1}{\sqrt{2\pi}} \int_{-\infty}^{\infty} E(\omega)e^{i\omega t}d\omega \tag{2.3a}$$

$$E(\omega) = \frac{1}{\sqrt{2\pi}} \int_{-\infty}^{\infty} E(t)e^{-i\omega t}dt. \tag{2.3b}$$

As long as the spectral bandwidth $\Delta\omega$ of the pulse is much smaller than the carrier frequency ω_1 at the pulse peak[1], it is convenient to expand the temporal phase $\phi(t)$

[1] The denotation ω_1 for the carrier frequency instead of the more common ω_0 allows a more intuitive description of frequency relations in the context of high harmonic generation.

about $t = 0$, so that

$$\phi(t) = \phi_0 + \omega_1 t + \phi_{\mathrm{NL}}(t). \tag{2.4}$$

Here, ϕ_0 denotes the so-called carrier-envelope phase, which quantifies the phase advance of the electric field with respect to the pulse envelope, and the phase function $\phi_{\mathrm{NL}}(t)$ absorbs all but the linear phase variations. Taking the time derivative of (2.4),

$$\omega(t) = \frac{d\phi(t)}{dt} = \omega_1 + \frac{d\phi_{\mathrm{NL}}(t)}{dt}, \tag{2.5}$$

we can introduce the instantaneous frequency $\omega(t)$. A non-vanishing, nonlinearly time-dependent $\phi_{\mathrm{NL}}(t)$ means that the instantaneous carrier frequency varies with time. In that case, the pulse is called "chirped". For

$$\frac{d\omega(t)}{dt} > 0, \tag{2.6}$$

the pulse is up-chirped (sometimes also called positively chirped) while in the opposite case

$$\frac{d\omega(t)}{dt} < 0 \tag{2.7}$$

the pulse is down-chirped (or negatively chirped). A purely quadratic modulation of the phase function $\phi_{\mathrm{NL}}(t)$ corresponds to the special case of linear chirp, i.e. $\omega(t) = \omega_1 + a_2 t$ where a_2 is the linear chirp parameter.

All of the above is valid if the pulse envelope just exhibits slow variations with respect to the carrier frequency. Thus, this condition is called slowly-varying envelope approximation (SVEA). For few-cycle pulses, the SVEA obviously breaks down. In all the cases relevant for this thesis, however, it can be assumed to be valid.

The relation between the optical intensity $I(t)$ and the corresponding electric field $E(t)$ is given by

$$I(t) = \frac{c\varepsilon_0 n}{2} |E(t)|^2 = \frac{c\varepsilon_0 n}{2} A(t)^2 \tag{2.8}$$

where c, n, and ε_0 are the vacuum speed of light, the refractive index of the material in which the pulse propagates, and the permittivity of free space, respectively.

The pulse duration (or pulse width) τ is defined as the full-width at half-maximum (FWHM) of the temporal pulse intensity given in (2.8), i.e. as the FWHM of the squared pulse envelope function $A(t)$. In an analogous manner, the spectral width $\Delta\omega$ can be defined. Since the spectral and the time domain are linked via the Fourier transforms in (2.3), τ and $\Delta\omega$ are linked by the time-bandwidth product

$$\Delta\omega\, \tau = 2\pi \Delta\nu\, \tau \geq 2\pi\, C_{\mathrm{tbp}} \tag{2.9}$$

where the exact numerical value of the constant C_{tbp} depends on the specific pulse shape and the definition of the pulse width[2]. The equality in (2.9) holds for unchirped pulses which are also called bandwidth- or Fourier-limited.

[2] A generalized definition of the time-bandwidth product based on Wigner distributions and their mean square deviations defined as pulse and spectral widths yields a similar relation as in (2.9) where equality is given for bandwidth-limited Gaussian pulses [19].

2.1.2 Spatial properties

In this section, the spatial properties of laser beams are discussed for further reference. All statements are restricted to cases in which the paraxial approximation is valid. In that case, the fundamental solution of the wave equation is the transverse elecromagnetic mode TEM_{00} that is also called fundamental or Gaussian mode.

2.1.2.1 Gaussian beams

The field of a laser beam propagating along the z-axis with an axially symmetric Gaussian profile is described by

$$E(r,z) = E_0 \frac{w_0}{w(z)} \exp\left(-\frac{r^2}{w^2(z)}\right) \exp\left[-i\left(kz - \varphi_g(z) + \frac{kr^2}{2R(z)}\right)\right]. \tag{2.10}$$

The beam radius w, which is defined as the distance from the beam axis at which the field amplitude drops to $1/e$ of its on-axis value, varies along the direction of propagation according to

$$w(z) = w_0 \sqrt{1 + \left(\frac{z}{z_R}\right)^2} \tag{2.11}$$

and reduces to a minimal value w_0 at the waist or focus (here taken to coincide with the origin at $z = 0$ for the sake of simplicity). The parameter z_R defines the so-called Rayleigh range according to

$$2z_R = 2\frac{\pi w_0^2}{\lambda} = k w_0^2 = b \tag{2.12}$$

and describes the distance from the focus after which the beam radius has increased by a factor of $\sqrt{2}$. The confocal parameter b represents a measure of the collimation of the beam since the on-axis intensity changes by no more than a factor of 2 within one confocal parameter. In Chapter 3, it will thus be used to approximate the interaction volume of a focused Gaussian laser beam with a gas target. In the far field ($|z| \gg z_R$), (2.11) yields a roughly linear increase of the beam radius with distance. The proportionality factor

$$\theta = \frac{\lambda}{\pi w_0} \tag{2.13}$$

specifies the divergence of the beam. In contrast to a plane wave, a Gaussian beam accumulates an additional phase, the Gouy phase

$$\varphi_g(z) = \arctan\left(\frac{z}{z_R}\right), \tag{2.14}$$

along the propagation axis. This additional geometric phase $\varphi_g(z)$ is negative for $z < 0$ and positive for $z > 0$ and leads to an overall phase shift of π across the focus. The curvature of the wavefronts $R(z)$ of the beam which can be defined by

$$\frac{1}{R(z)} = \frac{z}{z^2 + z_R^2}, \tag{2.15}$$

also changes sign across the focus where the curvature is infinite.

2.1.2.2 Beam quality factor M^2 and brightness

Although there is almost no reasonable chance to find an adequate and universally applicable measure to assess the spatial quality of a laser beam, the concept of the beam quality factor M^2, within certain limits, is a meaningful method to do so [22] that has been standardized in ISO 11146. According to the standard, M^2 is determined from a set of measurements of the beam radius at different positions along the propagation axis. The beam radius has to be specified according to the second moments method (also called D4σ method) in which twice the variance of the intensity profile defines the beam radius. The evolution of the beam radius along the propagation axis can then be obtained from generalized versions of (2.11), (2.12), and (2.13) with the substitution $\lambda \to M^2\lambda$, for example

$$\theta = M^2 \frac{\lambda}{\pi w_0} \tag{2.16}$$

Generally, $M^2 \geq 1$ applies for arbitrary beam profiles. The limit of purely Gaussian spatial characteristics, by definition, corresponds to $M^2 = 1$, in which case the beam is called "diffraction-limited". For beams that lack full axial symmetry, it is quite common to specify the beam quality factor along two orthogonal axes. In this thesis, the sloppy notation $M^2 = M_i^2 \times M_j^2$ will be used for that case. Experimentally, all measurements of beam quality were conducted with a CCD-based beam propagation analyzer (Spiricon M2-200FW) which, unlike several competing commercial products that rely on simple knife-edge scans, evaluates the full spatial beam profile. To enable meaningful background subtraction, the device records the beam profiles with the same exposure time at all positions after automatically attenuating the beam accordingly.

Equation (2.16) illustrates that the minimal beam radius to which a not diffraction-limited beam can be focused is a factor M^2 larger than that of a purely Gaussian beam for a given divergence angle. Since the outcome of highly nonlinear processes such as high harmonic generation critically depends on the focused optical intensity (see Chapter 3), this becomes especially important if these processes are to be driven by high power lasers and amplifiers whose beam quality is usually deteriorated to $M^2 > 1$ by nonlinear effects that emerge in both gain media and other optical components as a consequence of the high powers. Hence, it is a mandatory requirement to deliberate whether a potential scaling of the output power of a laser system at the expense of beam quality will lead to an overall benefit.

The quantity to be maximized is the brightness of the laser source which is defined as the total radiated power divided by the product of the mode area and the solid angle, which becomes

$$\Xi = \frac{\Delta P}{\Delta A \Delta \Omega} = \frac{P}{\lambda^2 (M^2)^2} \tag{2.17}$$

when Equation (2.16) is used. Since the total emitted power P, the beam propagation factor M^2, and the wavelength[3] λ of the emitted light are constant for a given source, the brightness cannot be improved by use of optical elements.

[3]The dependence on the wavelength is omitted in some definitions.

2.1.3 Phase modulation in linear media: dispersion

In the most general sense, the term "dispersion" describes the phenomenon that waves with different frequencies travel through a medium at different phase velocities which depend on the properties of the medium via the frequency dependent index of refraction $n(\omega)$ [23]. Hence, if a pulse propagates through a linear dispersive medium with negligible absorption, its envelope will disperse in time. The phenomenon is best treated in the frequency domain where the linear response after propagation through a medium over a distance z consists of an accumulation of spectral phase

$$\Phi(\omega, z) = k(\omega)z = n(\omega)\frac{\omega_1}{c}z \tag{2.18}$$

while the spectral amplitude of the pulse remains unaffected. After expanding the dispersive propagation phase about the carrier frequency

$$\Phi(\omega) = \sum_m \frac{\Phi_{\omega_1}^{(m)}}{m!}(\omega - \omega_1)^m \tag{2.19}$$

where the notation $\Phi_{\omega_1}^{(m)} = \frac{\partial^m}{\partial\omega^m}\Phi(\omega)\big|_{\omega_1}$ is used, one can identify the effects of the different orders. The zeroth order term $\Phi_{\omega_1}^{(0)}$ simply causes a constant carrier envelope offset and leaves the pulse envelope unchanged. The first order term $\Phi_{\omega_1}^{(1)}(\omega-\omega_1)$ results in a group delay, i.e. a shift of the pulse envelope (or the time axis), but does not affect the shape of the envelope, either. Therefore, both terms usually just become relevant for applications that are sensitive to the carrier envelope phase. The quadratic phase term $\frac{1}{2}\Phi_{\omega_1}^{(2)}(\omega-\omega_1)^2$, however, describes the group delay dispersion (GDD) that quantifies the rate at which the pulse duration of an initially unchirped pulse changes during propagation. In the ultrafast community, GDD is commonly specified in units of fs^2 which also allows to avoid confusion that may originate as the term "dispersion" is often colloquially used as a synonym for GDD. Higher order terms in the expansion (2.19) can be neglected in many cases. However, the third and fourth order dispersion terms, abbreviated TOD and FOD, respectively, are found to matter in certain applications, e.g., in nonlinear pulse compression. Since the GDD as defined above depends on the respective propagation distance in the medium, it is convenient to expand (2.18) in terms of $k(\omega)$, that is,

$$k(\omega) = \sum_m \frac{k_{\omega_1}^{(m)}}{m!}(\omega - \omega_1)^m \tag{2.20}$$

with $k_{\omega_1}^{(m)} = \frac{\partial^m k(\omega)}{\partial\omega^m}\Big|_{\omega_1}$. In analogy to (2.19), different physical quantities can be identified in (2.20): The zeroth order term $k_{\omega_1}^{(0)}$ is proportional to the inverse of the phase velocity $v_p(\omega_1) = c/n(\omega_1)$, whereas the inverse of $k_{\omega_1}^{(1)}$ yields the group velocity $v_g = \left(\frac{\partial k(\omega)}{\partial\omega}\big|_{\omega_1}\right)^{-1}$. The second order coefficient $k_{\omega_1}^{(2)}$ characterizes the group velocity dispersion (GVD) which is a material property typically specified as GDD per unit length.

2.1.4 Nonlinear effects

In the previous section, the frequency-dependent effects of pulse propagation through a linear transparent medium have been discussed. For the peak intensities reached by ultrashort pulses, any nonlinear response of the medium, parameterized by an intensity dependence of the index of refraction, will additionally affect the pulses both spatially and temporally. Among the different contributions to this intensity-dependent index, only the nonlinearities due to the optical Kerr and due to thermal effects will be considered here so that the refractive index becomes [24]

$$n(I) = n + n_2 I(r, z, t) + \frac{\partial n}{\partial \vartheta} \Delta\vartheta(r, z, t) \tag{2.21}$$

where the Kerr parameter n_2 and the temperature dependence of the index $\frac{\partial n}{\partial \vartheta}$ are material properties. The Kerr effect can be considered instantaneous for fs-pulses whereas the formation of temperature gradients is comparably slow. The temperature difference $\Delta\vartheta$ can either result from the propagating pulses themselves or from a different heat source. While the first case typically just needs to be considered for very high average powers, the second case is particularly important for the design of laser oscillators and amplifiers since a fraction of the strongly absorbed pump beams is always dissipated into heat.

In combination with the spatial index variation, e.g., of a Gaussian beam, the Kerr nonlinearity leads to self-focusing. For a temporal index variation, the Kerr effect results in self-phase modulation (SPM) or cross-phase modulation (XPM) depending on whether the pulse itself or a second pulse causes the variation. Both phenomena normally occur simultaneously so that transient effects such as reshaping of the temporal pulse envelope within the medium (self-steepening) have to be accounted for to accurately model propagation. Nevertheless, they can be treated independently within certain limits to obtain approximate expressions as will be presented in the following.

2.1.4.1 Self-focusing

The spatial index variation that is caused by the radial intensity profile of a Gaussian laser beam gives rise to a modulation of the spatial phase. Since this approximately parabolic phase dependence equals the action of a focusing lens and consequently causes the beam to converge, the effect is called self-focusing or self-lensing[4].

While the often undesirable ocurrence of self-focusing can rarely be avoided when working with ultrashort pulses and high powers, it can also be exploited successfully. In so-called Kerr-lens mode-locked lasers, for example, self-lensing in either the laser crystal itself or a designated nonlinear element leads to reduced losses at a hard aperture placed in the laser resonator or to a higher gain due to better overlap with the pump beam so that pulsed operation is favored over cw operation.

[4]Here, $n_2 > 0$ has been assumed as is the case for most transparent bulk media. A more general term including self-defocusing as well would be self-amplitude modulation (SAM).

If the length L of the medium that causes self-focusing is short enough, the effective focal length of the Kerr lens within a purely parabolic (i.e. aberrationless) thin lens approximation becomes [19, 20]

$$f_{n_2}(t) = \frac{w_0^2}{4n_2 L\, I_0(t)} \tag{2.22}$$

with on-axis intensity $I_0(t)$. For extended media, the effect of self-focusing can cancel or even exceed the usual diffraction of the beam during propagation. The former case has been named self-guiding or self-trapping since the laser beam propagates with constant beam diameter in a self-induced waveguide. In the latter case, called catastrophic self-focusing, the laser beam eventually converges to a small filament whereby the medium is damaged through dielectric breakdown. Since both the diffractive spread of the beam and the self-focusing effect depend on the beam cross-section, the characteristic quantity for the effect is the critical power

$$P_c = a\frac{\lambda^2}{n_2 n} \tag{2.23}$$

rather than a critical intensity. Here, a is a numerical factor that differs depending on the exact definition of the condition described by the critical power. Numerical simulations of propagation including the Kerr effect suggest the existence of a regime of catastrophic self-focusing above a critical power P_c that corresponds to $a \approx 0.15$ [19, 20]. Note, however, that catastrophic self-focusing only occurs if the medium is long enough.

A thermal lens effect in transparent media was first observed for cw lasers by Gordon and co-workers [25]. For radial heat flow in the sample, a Gaussian laser beam experiences an additional lensing effect which corresponds to the action of a lens with an effective focal length [20]

$$f_\vartheta = \frac{\kappa\pi w_\vartheta^2}{P_\vartheta \frac{\partial n}{\partial \vartheta}}. \tag{2.24}$$

Here, κ and w_ϑ denote the thermal conductivity of the medium and the waist radius of the laser beam causing the temperature gradient, respectively. P_ϑ is the fraction of power absorbed by the material from that laser beam which is dissipated into heat.

2.1.4.2 Self-phase modulation (SPM)

The spatial consequences of the nonlinear refractive index have been discussed in the previous section. Similarly, the intensity variation of an ultrashort optical pulse with respect to time, i.e. the temporal pulse shape or pulse (intensity) envelope, leads to a time-dependent alteration of the refractive index at a fixed position in the nonlinear medium during the passage of the pulse. Since this results in a modulation of the temporal phase of the pulse, the effect is called self-phase modulation (SPM).

The so induced total on-axis nonlinear phase shift after propagation through a medium of length L

$$B = \frac{2\pi}{\lambda}\int_0^L n_2 I(z,t)dz \tag{2.25}$$

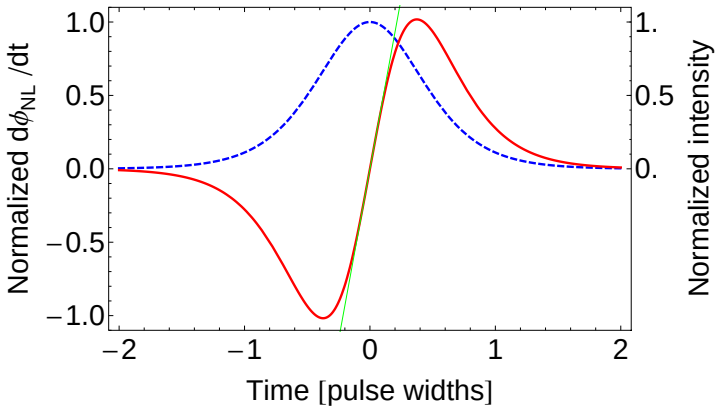

Figure 2.1: *Normalized intensity profile of a* sech^2*-pulse (dashed blue line) and corresponding normalized nonlinear instantaneous frequency shift due to self-phase modulation (solid red line). The SPM-induced frequency chirp is appproximately linear at the center of the pulse (thin green line).*

is often referred to as the B-integral, particularly in the context of laser engineering [20]. For sufficiently short media or propagation in a guided mode, attenuation and reshaping of the pulse envelope during propagation can be neglected. Including the global sign from the propagation phase, (2.25) then reduces to

$$\phi_{\mathrm{NL}}(t) = -n_2 \frac{2\pi}{\lambda} I(t) L \tag{2.26}$$

which applies to all cases discussed in detail in this thesis. As becomes obvious from (2.5), the additional phase $\phi_{\mathrm{NL}}(t)$ temporally chirps an initially bandwidth-limited pulse. In the frequency domain, this chirp corresponds to the generation of additional frequencies and hence a broadening of the spectrum of the pulse. Figure 2.1 shows the instantaneous frequency shift $\frac{d}{dt}\phi_{\mathrm{NL}}(t)$ that is caused by SPM of a sufficiently strong sech^2-pulse. It can be seen that the leading edge of the pulse generates additional frequencies at the low frequency end of the spectrum whereas the trailing edge likewise extends the spectrum on the blue side. In a reasonably large range around the peak of the pulse that is further extended when including the effects of group velocity dispersion during propagation, the impressed chirp is approximately linear. This allows for its removal by a simple dispersive delay line, i.e. an optical element with adjustable GVD. Such a rephasing of the spectral components can produce a pulse with a duration shorter than that of the original one. Therefore, the combination of nonlinear spectral broadening and subsequent (mostly linear) dispersive temporal shortening is called nonlinear pulse compression. Since such an SPM-based nonlinear pulse compression technique was employed in one of the experiments described in this thesis (cf. Section 5.3.1), the following section will provide more details and review the considerations to be made before an experimental realization.

2.1.5 Nonlinear pulse compression

High (average) power laser systems like the one employed for some experiments described in this thesis (see Chapter 5) are difficult to realize technically with gain materials supporting pulse durations shorter than 100 fs. Depending on the application, it can thus be advantageous or even mandatory to shorten the emitted pulses in a dedicated setup outside the laser system. In the case of HHG, for example, shorter driving pulses enable the generation of radiation with higher energy and may lead to a better conversion efficiency due to a reduced level of ionized target atoms (cf. Section 3.4.2).

To compress fs-pulses, only optical compression techniques, which were first proposed and demonstrated in the late 1960s with ps-pulses, can be used. Generally speaking, nonlinear pulse compression always consists of two steps: In the first step, which ideally leaves the temporal envelope of the pulse unchanged, the pulse spectrum is broadened through a temporal phase modulation that can, for example, result from self-phase modulation as described by (2.26). In the second step, which ideally does not alter the spectrum of the pulse, the (preferably linear) chirp that was impressed onto the pulse in the first step is removed by a dispersive delay line. That way, by introducing the proper amount of GDD (and higher order dispersion), the spectral phase of the pulse is transformed into that of an unchirped one with shorter duration. For broader spectra, the higher order dispersion terms of (2.19) become more important. However, even the temporal shape of the pulse obtained from an ideal compressor may contain satellite structures, since maximum compression always corresponds to highest peak power irrespective of exact pulse shape.

For a given input pulse energy,(2.26) seems to indicate that the largest spectral broadening effect can be achieved by focusing tightly into the longest possible material with the largest nonlinear index coefficient n_2. This is a fallacy in most cases since, as already mentioned at the beginning of Section 2.1.4, self-phase modulation is always accompanied by the corresponding spatial domain effect of self-lensing that, for a typical non-uniform spatial beam profile, may cause beam distortions or even lead to catastrophic self-focusing. Consequently, unless the input pulses are already short enough to allow strong spectral broadening in a bulk medium significantly shorter than the self-focusing length, some guiding mechanism that preserves the spatial pulse profile has to be employed to obtain spatially uniform spectral broadening.

Since optical fibers provide a guided spatial mode, they have successfully been used for SPM-induced spectral broadening and pulse compression since the first demonstrations in the 1970s. Depending on the initial and the desired final pulse parameters, the best results are attained with different fiber types and parameters. The applicability of regular bulk fibers is limited by their optical damage threshold (typically at the $\sim \mu\mathrm{J}/\mu\mathrm{m}^2$ level), because guiding of just the fundamental mode requires small core diameters, and by other nonlinear phenomena, e.g. Raman processes. If a thin gas-filled capillary or a hollow-core fiber is used as the guiding element instead, larger mode areas become feasible, the damage threshold of the nonlinear medium increases, and its nonlinearity is adjustable through the selection of gas and pressure so that mJ-pulses can be compressed to pulse durations in the few-cylce regime [26–28]. This scheme

can be further extended by cascading several nonlinear pulse compression stages [29–31] and related alternatives relying on either self-guiding through filamentation [32, 33] or propagation in a gas-filled multi-pass cell [34, 35] exist. For pulses with high average powers, damage at the incoupling facet of the fiber is particularly critical so that large mode area (LMA) solid or gas-filled hollow core photonic crystal fibers (PCFs) are preferably used for spectral broadening [36–41].

To remove the chirp impressed onto the pulse, compressor units that usually consist of diffraction gratings, Brewster-cut prisms, dispersion compensating mirrors, and combinations thereof are typically used. Alternatively, there are other schemes based on active modulators such as, for example, liquid crystal modulators or acousto-optic programmable delay filters. Pioneered by Szipöcs and co-workers [42], the idea behind dispersion compensating or chirped mirrors is to modulate the Bragg wavelength of the regular quarterwave coating layers which results in a frequency-dependent group delay because different frequencies are reflected at different depths in the coating. The use of chirped mirrors is especially advantageous for the compression of high energy or high average power pulses, because they have a high damage threshold and can be engineered to provide large amounts of dispersion and almost arbitrarily high reflectivity over an extremely broad bandwidth.

For the experiments described in Section 5.3.1, the 680 fs pulses from a high power laser system were to be compressed in order to drive the highly nonlinear HHG process at higher peak power and to reduce the detrimental effects of ionization. The pressures and propagation distances to achieve significant broadening of the maximally $\sim 10\,\mu$J pulses in a gas-filled fiber are very large and were considered too cumbersome to realize experimentally. Systematic experiments carried out by our collaborators identified a short piece of fused silica LMA-PCF as the most suitable option [43]. It achieves strong spectral broadening within a short distance while preserving the fundamental mode reasonably well, however, at the expense of a rather low damage threshold of about $2\,\mu$J. The effects of SPM and GVD on the pulses from propagation through the PCF can be compared using the related characteristic length scales, i.e. the dispersion length

$$L_{\mathrm{D}} = \frac{\tau^2}{\left|k^{(2)}_{\omega_1}\right|}, \tag{2.27}$$

where $k^{(2)}_{\omega_1}$ represents the GVD parameter from (2.20), and the nonlinear length

$$L_{\mathrm{NL}} = \frac{cA_{\mathrm{eff}}}{n_2\,\omega_1 P_p} \tag{2.28}$$

with effective mode area A_{eff} and peak power P_p. Since in our case $L_{\mathrm{D}} \gg L_{\mathrm{NL}}$ applies, the spectral broadening can be assumed to originate purely from SPM. In that case, the broadened power spectral density is simply given by the Fourier transform

$$S(\omega) = \left| \frac{1}{\sqrt{2\pi}} \int_{-\infty}^{\infty} A(t) e^{i(\omega_1 t + \phi_{\mathrm{NL}}(t))} e^{-i\omega t} dt \right|^2 \tag{2.29}$$

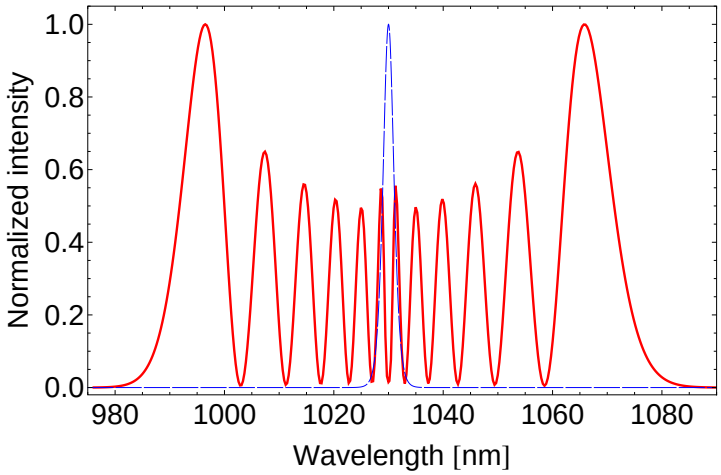

Figure 2.2: *Nonlinearly broadened spectrum. The parameters of the experiment described in Section 5.3.1 have been used and the broadening mechanism was considered to be pure SPM. The initial pulse spectrum is shown as a reference by a dashed blue line.*

where the pulse amplitude has been assumed to remain unaffected during propagation.

The characteristically modulated spectrum resulting from a numerical simulation of (2.29) is depicted in Figure 2.2. Matching the experimental conditions of the single pass HHG experiment that will be described in Section 5.3.1, the simulation was carried out for a sech^2-pulse with an impressed maximum nonlinear phase of $\sim 10\pi$ which yields a FWHM spectral bandwidth of about 80 nm. For comparison, the initial pulse spectrum is also shown.

Figure 2.3 illustrates the pulse shape calculated from the broadened spectrum of Figure 2.2 under the assumption of flat spectral phase, corresponding to a full rephasing of the spectral components by an ideal compressor. The retrieved FWHM width of the compressed pulse amounts to ~ 31 fs. As mentioned earlier, the pulse shows weak satellite structures as a result of the strongly modulated spectrum. The power content of the central part of the pulse is about $\sim 80\%$.

2.1.6 Relation to experimentally accessible parameters

For a meaningful comparison between experiment and simulation(s), it is necessary to convert the experimentally accessible parameters such as average power P_0, repetition rate f_r, FWHM pulse duration τ, and waist radius w_0 into the corresponding electric field E which is a typical quantity required for the simulation. Therefore, in the following, the relations between these parameters will be summarized.

The energy content of an optical pulse is a good parameter for comparisons between different experiments because it is independent of the exact pulse shape. Although the pulse energy can also be measured directly using specially designed meters, it is typically computed from the average power P_0 and the repetition rate f_r,

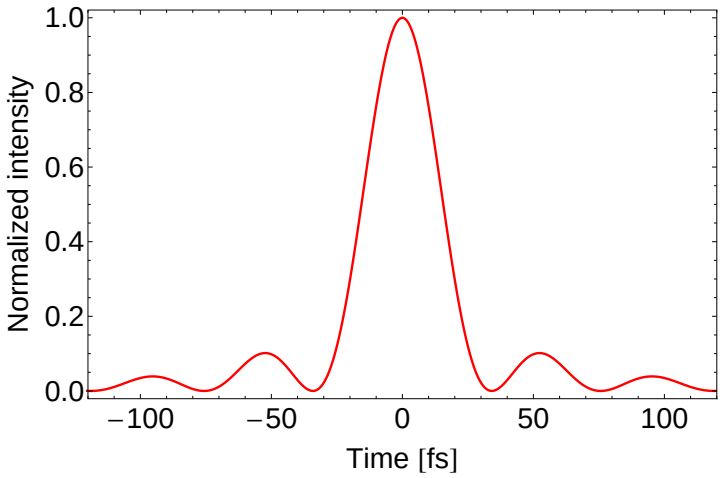

Figure 2.3: *Ideally compressed pulse corresponding to the broadened spectrum shown in Figure 2.2. Broadening was assumed to originate purely from self-phase modulation. The compressed pulse has a FWHM duration of about* 31 fs *and concentrates* $\sim 80\%$ *of the power in its central lobe.*

$$W_P = \frac{P_0}{f_r}. \tag{2.30}$$

Contrary to the pulse energy, the peak power depends on the temporal shape of the pulse, which is taken into account in

$$P_p = \eta \frac{W_P}{\tau} \tag{2.31}$$

by the temporal pulse shape factor η. In the case of a temporally flat-top pulse, $\eta = 1$. The values for Gaussian or sech^2-pulses, η_g and η_s, can be calculated from the respective temporal pulse shapes $g(t)$ and $s(t)$ in the following way: Consider a regular train of temporally flat-top pulses that do not overlap in time and have a constant amplitude A and FWHM pulse duration τ, i.e. a constant pulse area $A\tau$. Gaussian or sech^2-pulses with the same pulse length τ and the same pulse area $A\tau$ have temporal pulse intensity envelopes

$$g(t) = 2\sqrt{\frac{\ln 2}{\pi}} A e^{-4 \ln 2 \frac{t^2}{\tau^2}} \tag{2.32}$$

and

$$s(t) = \operatorname{arsech}\left(\frac{1}{\sqrt{2}}\right) A \operatorname{sech}^2\left(2 \operatorname{arsech}\left(\frac{1}{\sqrt{2}}\right) \frac{t}{\tau}\right) \tag{2.33}$$

and thus $\eta_g = 2\sqrt{\frac{\ln 2}{\pi}} \approx 0.94$ and $\eta_s = \operatorname{arsech}\left(\frac{1}{\sqrt{2}}\right) \approx 0.88$. These factors are often neglected in estimations of peak powers or intensities because other experimental quantities, e.g. the waist radius w_0, are not known well enough anyway.

From the peak power, the peak intensity can be calculated via

$$I_0 = \frac{P_p}{\zeta} = \frac{\eta P_0}{\zeta f_r \tau} \tag{2.34}$$

if the spatial characteristics and thus the area ζ over which the energy is distributed are known. For a spatially uniform beam with radius w_0, this area is $\zeta = \pi w_0^2$. For a spatially Gaussian beam, the on-axis peak intensity at the focus is twice as high as for a spatially uniform beam of the same radius, i.e. $\zeta_g = \frac{1}{2}\pi w_0^2$. In that case, substituting (2.8) into (2.34), the relation between maximum field strength and experimental parameters becomes

$$|E| = \frac{2}{w_0}\sqrt{\frac{\eta P_0}{f_r \tau c \varepsilon_0 \pi}} \approx \frac{2}{w_0}\sqrt{\frac{P_0}{f_r \tau c \varepsilon_0 \pi}}. \tag{2.35}$$

2.2 The optical frequency comb

This section provides a brief summary of properties and applications of optical frequency combs. More detailed reviews can, for example, be found in [2, 3, 44, 45].

The output of a mode-locked laser consists of an infinite number of replicas of the pulse circulating in the laser cavity. Since these pulses are evenly spaced in time, with a temporal separation determined by the length of the laser cavity, the Fourier transform of this infinite pulse train consists of a series of equidistant, narrow spectral lines. The latter resemble the teeth of a comb which is why a spectrum with a broadband spectral envelope and a highly discrete, highly regular spectral substructure has been denoted "frequency comb". The bandwidth of the whole spectrum, i.e. the width of the spectral envelope, is determined by the oscillator characteristics and hence by the bandwidth of the gain material eventually. For typical oscillator repetition rates on the order of 100 MHz, the coherence between successive pulses is maintained very well so that each comb mode exhibits an extremely narrow bandwidth. Therefore, a frequency comb can also be considered as an array of narrow-band continuous wave lasers.

The optical frequency ν_s of a single comb tooth is described by the equation

$$\nu_s = \nu_c + s f_r \tag{2.36}$$

where s is a positive or negative integer and f_r is the pulse repetition frequency given by $f_r = c/L_r$ with (optical) resonator length L_r, which is in the radio frequency domain for typical oscillators. The optical frequency ν_c denotes the frequency of some arbitrary comb tooth, typically chosen to be the carrier frequency and thus near the center of the power spectrum.

The significance of the frequency comb becomes obvious in a different parametrization of the spectrum. Since the spectral separation between different comb modes is equidistant, one can theoretically extend the succession of comb teeth from the optical domain to the origin of the frequency axis. The comb equation (2.36) then becomes

$$\nu_m = m f_\mathrm{r} + f_0 \tag{2.37}$$

where f_0 is the spectral offset of the whole frequency comb from zero frequency, i.e. $f_0 < f_r$, and the so-called mode number m is a large positive integer. The physical manifestation of f_0 is best described by a glimpse into the time domain. The carrier-envelope phase (CEP) ϕ_0 introduced in (2.4) quantifies the phase advance of the electric carrier field with respect to the pulse envelope. The time derivative of ϕ_0 determines the carrier-envelope frequency according to

$$f_0 = \frac{1}{2\pi}\frac{d\phi_0}{dt} = \frac{\Delta\phi_0}{2\pi} f_\mathrm{r}, \tag{2.38}$$

where $\Delta\phi_0$ denotes the pulse-to-pulse slippage of the CEP. The parametrization of (2.37) shows that the optical frequency comb provides a direct link between the optical and the radio frequency domain.

Strictly speaking, it is not until both f_r and f_0 are measured and controlled that the spectrum of a mode-locked laser forms a frequency comb [3]. This can be routinely achieved for f_r using a fast photodiode and feedback to a piezo-eletric actuator changing the length L_r of the laser resonator. In contrast, the development and implementation of a scheme to measure f_0, where no spectral power is available, was crucial for the realization of the first frequency combs [46, 47].

The most commonly used method to access f_0 is the so-called f-to-$2f$ self-referencing technique[5]. As can easily be verified using (2.37), frequency-doubling of light at frequency ν from the low frequency part of the laser spectrum and subsequently heterodyning it with light at frequency 2ν from the high frequency part of the spectrum provides access to f_0. The obvious requirement for this technique to work, an octave-spanning laser spectrum, is challenging to be met directly even for broadband Ti:sapphire oscillators. However, nonlinear spectral broadening outside the laser, e.g. by self-phase modulation in a photonic crystal fiber (PCF) [48], can be used to suitably extend the spectral bandwidth. Once measured, stabilization of f_0 is possible by phase-locking f_0 to a stable rf reference and applying the generated feedback signal to the femtosecond oscillator or by recently demonstrated feed-forward schemes [49, 50].

Since its first successful realization, the optical frequency comb has enabled breathtaking developments in a still growing number of diverse fields. Frequency combs can be used as frequency "rulers" in optical frequency metrology [51]. In that role, they are used to accurately determine the frequency of atomic resonances in precision spectroscopy experiments or to enable the precise calibration of astronomical spectrographs for the search of extrasolar planets [52]. Likewise, frequency combs provide the clockwork for current all-optical atomic clocks [53, 54] and could do so for the next generation "nuclear" clocks [55, 56]. Apart from their use as a reference, frequency combs can also be used directly for spectroscopic investigations of single- or two-photon transitions in atoms and molecules [57], Fourier transform spectroscopy [58], and dual comb spectroscopy [59].

Frequency combs are also ideally suited to realize fully coherent laser-like sources in spectral regions that are currently or may not be at all directly accessible by laser technology. A prominent example is the spectral region ranging from the vacuum ultraviolet (VUV) via the extreme ultraviolet (EUV) to the soft x-ray region (SXR) that can be accessed by driving the extremely nonlinear process of high harmonic generation with a frequency comb. The topic of this thesis is the advancement of existing EUV sources based on that concept. In the following chapter, the theory of high harmonic generation is discussed.

[5] In the notation used here to distinguish between radio and optical frequencies, it should rather be called ν-to-2ν technique.

3 Theory of high harmonic generation

3.1 Introduction

The first observation of high[1] harmonic generation (HHG) dates back to the late 1980's when the rapid progress in the development of intense pulsed lasers rendered experimental investigations with focused intensities exceeding $10^{13}\,\mathrm{W/cm^2}$ possible for the first time. In a pioneering experiment, McPherson and co-workers observed that the spectrum of the radiation generated by focusing $\sim 350\,\mathrm{fs}$ pulses of up to 20 mJ into neon vapor contained up to the 17th harmonic of their KrF laser emitting at 248 nm [60]. Almost at the same time, Ferray and colleagues reported the generation of harmonics up to the 33rd, 29th, and 21st order in argon, krypton, and xenon, respectively, with an Nd:YAG laser producing 30 ps pulses at 1064 nm [61]. Remarkably, in contrast to the expected pertubative behavior where the intensity I_q of the qth harmonic order scales with the laser intensity as $I_q \propto I^q$, the spectra observed by both groups showed a plateau of almost equal harmonic intensities spreading over several orders and ranging up to a sharp cutoff while only the lowest harmonic orders followed the expected fall-off.

These baffling observations, which had been partially foreseen by Shore and Knight [62], along with the high directionality (collinear with the driving laser beam) and low divergence of the high harmonic radiation that offered the prospect of EUV spectroscopy with laboratory-scale sources sparked an immediate strong interest in the theoretical aspects of high harmonic generation. Historically, these were first studied by numerical simulations of the time-dependent Schrödinger equation (TDSE) since the field strengths achieved in the focused laser beam are on the order of the atomic Coulomb potential and thus too high to be treated analytically by a perturbative approach. However, due to the immense computational task, physically meaningful approximations of the problem had to be found, which is why these numerical simulations [63–65] eventually led to the formulation of an intuitive semi-classical description of HHG by Corkum [66] that is today widely known and accepted as the so-called "three-step model" or "simple man's model". Despite the considerable predictive power of the three-step model, which, for example, allows to link the expectable highest harmonic order to the laser parameters, it falls short of explaining the origin of certain crucial properties of high harmonic radiation such as its coherence or its intensity-dependent phase.

However, it was shown by Lewenstein and co-workers [67] that the semi-classical model is completely absorbed by a relatively simple analytic and quantum mechanical description of HHG within the so-called strong field approximation (SFA). Despite several

[1] It is neither immediately obvious nor precisely specified what "high" means in this context. Here, as a rule of thumb, harmonic orders q are considered high when $q \geq 9$.

shortcomings, this model, which is now commonly referred to as "Lewenstein model", provides deeper insight into the physics and, for example, explains both the coherence and the intensity-dependent phase of the high harmonic radiation. At the same time, it enables fast numerical calculations of the experimentally observable macroscopic high harmonic response, that is, the far-field analysis of the coherent superposition of the harmonic dipole emission from all individual atoms in the target.

While intricate theoretical details of HHG are still an extremely active field of research, the basic theory has been exhaustively treated in numerous excellent review articles and several books [68–74]. Despite their existence and although a full theoretical account of high harmonic generation is clearly beyond the scope of this thesis, a summary with a rather high level of detail is still presented here. Apart from explicitly being meant to serve as an introduction into the field for successive students, the reason is that HHG and its extension to hitherto unexplored parameter space is the common major topic of the experimental work discussed in the later chapters of this thesis and that the optimization of an HHG-based EUV source for applications is a complex task that requires a thorough understanding of the underlying mechanism. Consequently, this chapter first summarizes the microscopic picture of HHG, i.e. the interaction of a single atom with an intense light field in the framework of both the intuitive three-step model and the more accurate Lewenstein model, and then provides a detailed review of the macroscopic response and potential ways to optimize it through tuning of experimentally accessible parameters.

3.2 Microscopic description: single atom response

3.2.1 Simple man's model

The physically intuitive semi-classical three-step or simple man's model [66] is ideally suited for a first insightful discussion of the interaction of an atom with an intense laser field. For the sake of simplicity, it is assumed here that only one of the electrons of the atom interacts with the laser field whereas the remaining electrons just form an effective static potential together with the nucleus. This so-called single active electron (SAE) approximation is a rather strong approximation, but yields results that agree well with experimental data in most cases. According to the three-step model, the crucial steps of the laser-atom interaction are:

Ionization The active electron tunnel-ionizes out of the quasi-static potential formed by the Coulomb potential and the laser field and appears in the continuum with zero velocity at the origin of the coordinate system. This process happens twice during one period of the laser field.

Acceleration After ionization, the Coulomb potential is entirely neglected. The electron propagates under the influence of the laser field. As a free charged particle, it obeys the classical equations of motion with the initial conditions given in the first step.

Recombination Only for a linearly polarized laser field, there are electron trajectories which return to the ionic core. Upon impact, the electron recombines with its

parent ion and radiates off the entire kinetic energy acquired in the laser field in the form of a single energetic photon.

The description given above is semi-classical because just the second step follows fully classical arguments whereas the first and the last step are treated quantum-mechanically. This will now be further elucidated.

3.2.1.1 Ionization

In low intensity laser fields, an atom may undergo the process of multi-photon ionization (MPI) where it needs to absorb n photons from the laser field to be ionized. This form of ionization can be treated perturbatively and the corresponding ionization rate reads $w_{\mathrm{MPI}} = \sigma_n I^n$ with the n-photon ionization cross-section σ_n. With increasing field strength, non-perturbative effects such as above-threshold ionization (ATI) begin to arise. In ATI, the atom absorbs more photons from the field than are minimally required to be ionized which manifests iteself in the observation of peaks separated by the photon energy in the kinetic energy spectra of the freed electrons. Once the laser field strength becomes comparable to the field strength associated with the atomic binding potential, there is a non-zero probability for the electron to tunnel through the resulting instantaneous potential barrier.

These different regimes of ionization can be roughly distinguished with the help of the so-called Keldysh-parameter [75]

$$\gamma_K = \sqrt{\frac{U_I}{2U_P}} \tag{3.1}$$

which relates the ionization potential U_I of the atom to the intensity I and the wavelength λ of the laser field by means of the ponderomotive potential

$$U_P = \frac{e^2 E_0^2}{4 m_e \omega_1^2} = \frac{e^2 \lambda^2 I}{8\pi^2 m_e \varepsilon_0 c^3} \tag{3.2}$$

that corresponds to the average kinetic energy of an electron with mass m_e subject to a harmonic field $E(t) = E_0 \cos(\omega_1 t)$. Typically, the quasi-static tunneling regime and the multi-photon ionization regime are associated with Keldysh parameters $\gamma_K \ll 1$ and $\gamma_K \gg 1$, respectively, which is based on Keldysh's original idea of comparing the tunneling time to the period of the optical field. In particular in the case of very high repetition rates, however, HHG experiments are often also conducted at Keldysh parameters of $\gamma_K \approx 1$. It has been shown [76] that tunneling is both possible and significant in this intermediate regime. Consequently, a strict distinction of cases based on the value of the Keldysh parameter is neither recommendable nor possible.

The calculation of the ionization rate for particular atoms and initial electronic configurations under certain conditions has been the subject of several investigations, including the already mentioned seminal work of Keldysh [75], the more general so-called PPT theory[2] [77], the commonly used ADK rate[3] [78], and the Yudin-Ivanov model [76]

[2] Named after the authors of [77], Perelomov, Popov, and Terentev.
[3] Named after the authors of [78], Ammosov, Delone, and Krainov.

that yields more accurate results also for $\gamma_K \approx 1$. All rates basically share a common exponential dependence given by [75]

$$w_{\mathrm{QS}} \propto \frac{U_I^{5/2}}{E_0} \exp\left(-\frac{4\sqrt{2m_e}U_I^{3/2}}{3e\hbar E_0}\right) \tag{3.3}$$

when ground state depletion is neglected. It is of vital importance for efficient HHG to gain some insight about the degree of ionization that is caused by the driving pulses because an ionized atom cannot contribute to HHG within the SAE approximation. The fraction of ionization at time t can be calculated from the time-dependent instantaneous ionization rate $w(t)$ according to

$$\Lambda(t) = 1 - e^{-\int_{-\infty}^{t} w(\tau)d\tau} \tag{3.4}$$

where $\Lambda = 0$ and $\Lambda = 1$ correspond to no and full ionization, respectively. It is then possible to determine a saturation intensity, for which a certain fraction of the atoms is ionized at the peak or after the pulse. We will see later that the saturation intensity depends on the pulse length. For a comparison with real experiments, the spatial variation of the intensity in the focused laser beam has to be taken into account as well.

In an extremely intense laser field, the atomic potential can be suppressed completely so that the electron is not bound at all momentarily. Such "barrier suppression ionization" of an atom occurs at intensities above [68] $I_{\mathrm{BSI}} \simeq 4 \times 10^9 (U_I[\mathrm{eV}])^4\,\mathrm{W/cm^2}$ where the ionization potential has to be inserted in units of eV. For xenon atoms, $I_{\mathrm{BSI}} \simeq 8.66 \times 10^{13}\,\mathrm{W/cm^2}$.

3.2.1.2 Acceleration

Once the electron is ionized, the influence of the atomic potential is neglected in the simple man's model. Consequently, the dynamics of a free electron subject to a monochromatic[4] laser field $\boldsymbol{E}(t) = \boldsymbol{E}_0 \cos(\omega_1 t + \varphi)$ can be directly determined starting from the classical equation of motion in three dimensions of space[5]

$$m_e \frac{d^2\boldsymbol{r}}{dt^2} = -e\boldsymbol{E}(t) = -e\boldsymbol{E}_0 \cos(\omega_1 t + \varphi) \tag{3.5}$$

with the inital conditions $\boldsymbol{r}(t_i) = \boldsymbol{0}$ and $\dot{\boldsymbol{r}}(t_i) = \boldsymbol{0}$. The resulting electron trajectories consist of a superposition of a constant linear drift and a driven oscillatory motion, respectively. Since HHG originates from recombination of the electron with the parent ion, the relevant trajectories are those that return to the parent ion at some later time t_r. However, $\boldsymbol{r}(t_r) = \boldsymbol{r}(t_i)$ only holds in general for a linearly polarized laser field so that

[4] The results of the following discussion remain valid for pulsed lasers, as long as their pulse envelope varies slowly with respect to the carrier.

[5] As usual, bold symbols denote vector quantities.

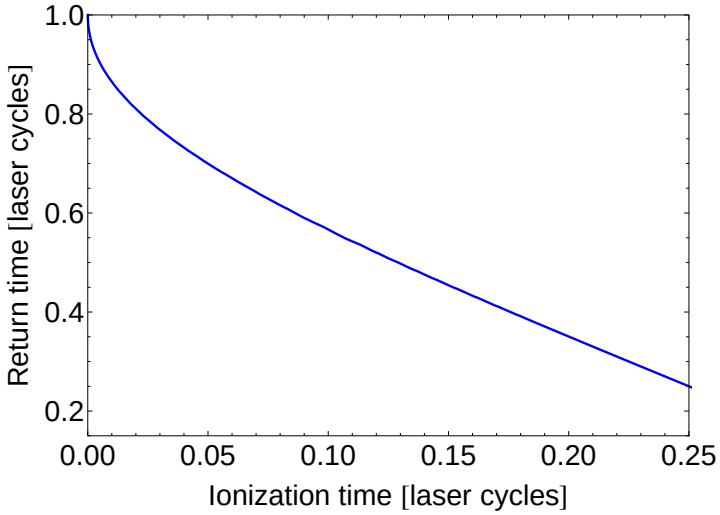

Figure 3.1: *Return time t_r as a function of ionization time t_i. Both times are normalized to the laser period T_0. For the specified cosine field with $\varphi = 0$, only electrons ionized in the first quarter of a laser cycle follow trajectories that return to the parent ion. Electrons that get ionized early during a cycle return later than those which are ionized later.*

we can restrict the solution of (3.5) to one dimension, namely

$$\dot{x}(t) = -\frac{eE_0}{m_e\omega_1}\left(\sin(\omega_1 t + \varphi) - \sin(\omega_1 t_i + \varphi)\right) \tag{3.6a}$$

$$x(t) = \frac{eE_0}{m_e\omega_1^2}\left[\left(\cos(\omega_1 t + \varphi) - \cos(\omega_1 t_i + \varphi)\right) + \omega_1(t - t_i)\sin(\omega_1 t_i + \varphi)\right] \tag{3.6b}$$

3.2.1.3 Recombination

The condition $x(t_r) = x(t_i) = 0$ for recombination does not have analytical solutions. However, the time of recombination t_r can be found numerically as a function of the time of ionization t_i. The resulting plot is depicted in Figure 3.1 for the specified cosine field with $\varphi = 0$. The trajectories that return to the ionic core correspond to ionization times within the first quarter of the laser cycle[6]. The travel time, i.e. the time between ionization and recombination $t_t = t_r - t_i$, is longest for those electrons that get ionized early during a cycle. In principle, recurring returns without recombination are possible, however, the cross section for recombination is highest for the first return.

Once the electron returns to the parent ion, there are three possible scenarios that may occur: elastic scattering with the ion and further acceleration of the electron, inelastic scattering leading to further ionization of the core (non-sequential double-ionization), and recombination with emission of a high energy photon, i.e. high harmonic generation, which is discussed here. Every recombining electron radiates off its entire kinetic energy

[6]Here, the discussion is restricted to the first half-cycle. Of course, ionization times in the third quarter of the laser period similarly lead to returning trajectories.

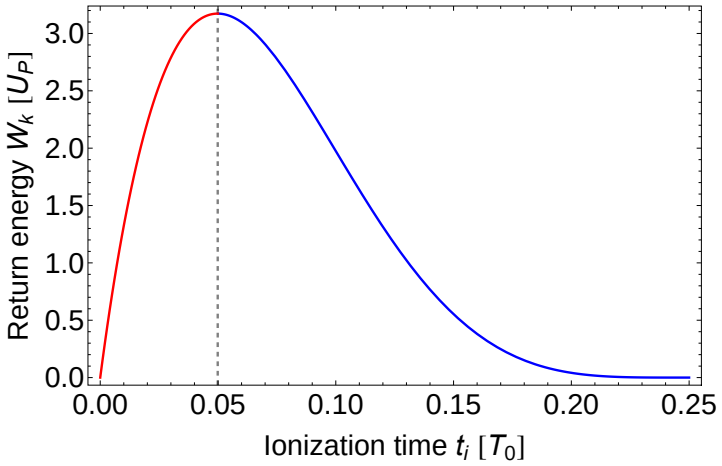

Figure 3.2: *Kinetic energy W_k of returning electrons in units of U_P as a function of ionization time t_i (given in laser cycles). The maximum kinetic energy $W_k^{\max}$ amounts to $3.17U_P$ and corresponds to a trajectory with an ionization time $t_i \simeq 0.05T_0$ and a return time $t_r \simeq 0.7T_0$. For every $W_k < W_k^{\max}$, there are two returning trajectories per cycle that only differ in travel time. Hence, they have been termed "short" and "long" trajectory. In the figure, energies corresponding to short and long trajectories are indicated by blue and red color, respectively.*

acquired in the laser field in a single photon. Hence, the total energy of the emitted photon

$$W_\nu = h\nu = \hbar\omega = W_k(t_r) + U_I \tag{3.7}$$

is given by the sum of this kinetic energy $W_k(t_r)$ at the time of recombination and the released binding energy, which is identical to the ionization potential U_I. In Figure 3.2, the kinetic energy upon return is illustrated as a function of ionization time. The maximum kinetic energy $W_k^{\max} \simeq 3.17U_P$ is acquired by the electrons that are ionized at $t_i \simeq 0.05T_0$ so that the maximum photon energy, the so-called harmonic cutoff energy, is given by

$$\hbar\omega_c = U_I + 3.17U_P \tag{3.8}$$

For every W_k except the cutoff energy, there are two trajectories per cycle that return to the parent ion after different travel times. Therefore, these trajectories have been named "short" and "long" trajectory. In the Figure 3.2, the return energies corresponding to short and long trajectories are indicated in blue and red, respectively. Note that although the atoms are most likely ionized at the peaks of the laser field, the return energy of the corresponding electrons is zero.

The emission of a single photon during the recombination process of an electron with its parent ion occurs into a random direction and with a statistically distributed photon energy. However, since the emission process happens twice per laser period, the spectrum of the light originating from an atom subject to multiple cycles of the laser field is given by the Fourier transform of a train of radiation bursts and thus becomes discrete with a frequency spacing of twice the driving laser frequency ω_1. Due to this inherent symmetry and the anisotropy of the free target atoms, only odd harmonics at frequencies $\omega_q = q\omega_1$,

where q is a positive odd integer, can be observed. However, even harmonics can be generated if the symmetry of the HHG process is disturbed or broken, e.g. by adding a weak second harmonic laser field, using few cycle driving pulses, or working with a target consisting of oriented asymmetric molecules. In addition, real experimental spectra are the superposition of the emissions of all target atoms and thus include macroscopic effects as well. These do not only lead to directional emission, but can also significantly alter the shape of the observed spectra which will be discussed in more detail in Section 3.3.

3.2.1.4 Real cutoff law

According to Equation (3.8), there are several ways to shift the harmonic cutoff towards higher energies: Since $U_P \propto \lambda^2 I$ (cf. (3.2)), one can either resort to a laser with a longer wavelength or try to increase the peak intensity by, for example, focusing more tightly. Alternatively, one can choose an atomic target with a larger ionization potential. While, amongst others, all these measures have been taken to generate extremely short wavelengths reaching into the water window [79] and beyond [80], scaling the intensity can generally not be exploited to an arbitrary extent because ground state depletion due to ionization leads to saturation of harmonic generation at a certain intensity $I_s(\tau)$ which depends on the pulse duration and the atomic parameters. Assuming linear polarization, sech^2-pulses, and ionization to dominantly occur in the leading edge of the pulse, one can find an approximate closed form expression for the saturation intensity from the ADK rates [72, 81] which, when substituted into (3.8), leads to the modified cutoff law

$$W_\nu^{\max} = \hbar\omega_c(I_s) = U_I + \frac{0.5\, U_I^{3.5}\lambda^2}{\left[\ln\left(\frac{0.86\,|C_{n^*l^*}|^2 G_{lm} 3^{2n^*-1} U_I \tau}{-\ln(1-\Lambda_s)}\right)\right]^2} \tag{3.9}$$

where both $W_\nu^{\max}$ and U_I are in units of eV while τ and λ are in fs and μm, respectively. Note that the definition of the saturation intensity I_s depends on the assumed fraction of ionization Λ_s at the pulse peak. The coefficients $|C_{n^*l^*}|^2$, G_{lm}, n^* and l^* can be found in [72][7]. Equation (3.9) reveals that ω_c depends nonlinearly on U_I via the saturation intensity which reflects the fact that a laser pulse with the same parameters is less likely to deplete the ground state of an atom with a larger ionization potential. Note that macroscopic effects such as, for instance, phase matching or plasma defocusing have not been considered in the derivation of (3.8) so that the experimentally observed cutoff may be at lower energies, particularly for tight focusing geometries. Nevertheless, a comparison of experimental results with the expectations based on (3.9) assuming $\Lambda_s = 0.98$ shows very good agreement [81].

[7] For Xe, $|C_{n^*l^*}|^2 = 3.88241$, $G_{lm} = 3$, $n^* = 1.05906$ and $l^* = 0.05906$.

3.2.1.5 Achievements and limitations of the simple man's model

The simple man's model provides an intuitive picture of HHG and allows to correctly predict several fundamental properties of the generated radiation despite the strong approximations involved. Most importantly, it explains the extension of the high harmonic spectrum up to the cutoff, whose frequency is given by (3.8) and whose spectral intensity, unlike the lowest harmonic orders, cannot be described by a perturbative intensity scaling $I_q \propto I^q$. The three-step model also predicts an intrinsic chirp of the harmonic radiation originating from the fact that different harmonic frequencies are associated with different return times of the active electron. The existence of this harmonic chirp has been confirmed both in experiments and by more advanced theories.

As can be seen from (3.7), the validity of the simple man's model is restricted to harmonic orders with photon energies larger than the ionization potential of the atom because the so-called below-threshold harmonics, for which $\hbar\omega_q < U_I$, would require unphysical negative kinetic energies of the returning electrons. More importantly, the three-step model falls short of explaining crucial properties like the coherence of the high harmonic radiation. While the existence of contributions originating from different trajectories directly emanates from the model, it does not make accurate predictions about the phases of the trajectories. As will be shown below, this problem is solved by the quantum mechanical Lewenstein model in which different quantum orbits exhibit a characteristic intensity-dependent phase.

3.2.2 Exact quantum mechanical model

An exact quantum mechanical description of a process like high harmonic generation requires solving the time-dependent Schrödinger equation

$$i\hbar\frac{\partial}{\partial t}\left|\Psi(t)\right\rangle = \hat{\mathrm{H}}(t)\left|\Psi(t)\right\rangle \tag{3.10}$$

in which $\hat{\mathrm{H}}(\mathrm{t})$ denotes the Hamiltonian of the respective quantum system and $|\Psi(t)\rangle$ is its time-dependent state vector in Dirac's bra-ket representation. The formal solution

$$\left|\Psi(t)\right\rangle = e^{-\frac{i}{\hbar}\int_{t_i}^{t} d\tau \hat{\mathrm{H}}(\tau)}\left|\psi_i\right\rangle \tag{3.11}$$

fully describes the time evolution of the quantum system from some initial state $|\psi_i\rangle = |\Psi(t = t_i)\rangle$ at an initial time t_i up to a time t under the influence of the specific Hamilton operator $\hat{\mathrm{H}}(t)$. However, analytical solutions exist just for a very limited number of specific problems so that, in the most general case, finding a practically useful solution to (3.10) requires numerical calculations.

Depending on the problem to be solved, different partitions of the Hamilton operator can be useful to reduce the computational efforts. If, for instance, a stationary solution is known, $\hat{\mathrm{H}}$ can be partitioned into $\hat{\mathrm{H}}(t) = \hat{\mathrm{H}}_0 + \hat{\mathrm{H}}_{\mathrm{int}}(t)$ where $\hat{\mathrm{H}}_0$ denotes the stationary Hamiltonian and $\hat{\mathrm{H}}_{\mathrm{int}}(t)$ absorbs the time-dependent interaction so that the (still exact)

formal solution becomes

$$|\Psi(t)\rangle = e^{-\frac{i}{\hbar}\hat{\mathrm{H}}_0(t-t_i)}\,|\psi_i\rangle - \frac{i}{\hbar}\int_{t_i}^{t} dt' e^{-\frac{i}{\hbar}\int_{t'}^{t} d\tau \hat{\mathrm{H}}(\tau)}\hat{\mathrm{H}}_{\mathrm{int}}(t') e^{-\frac{i}{\hbar}\hat{\mathrm{H}}_0(t'-t_i)}\,|\psi_i\rangle \tag{3.12}$$

where the first summand guarantees the initial condition $|\Psi(t=t_i)\rangle = |\psi_i\rangle$. Reading (3.12) from the right to the left, it is possible to identify the following steps: The system starts in some initial state $|\psi_i\rangle$ at time t_i and evolves freely until time t' when the interaction absorbed in $\hat{\mathrm{H}}_{\mathrm{int}}$ sets in instantaneously. From this instant until time t, the system then evolves under the influence of the full Hamiltonian $\hat{\mathrm{H}}(t)$. Therefore, despite still being useless in the sense that (3.12) is not any easier to compute than (3.11), the exact formal solution to the partitioned Hamiltonian yields an intuitive general physical picture and hence represents a good starting point for reasonable approximations.

In the case of high harmonic generation, the source of the high harmonic emission from a single atom is its time-dependent laser-induced dipole moment $\boldsymbol{\mu}(t) = q\boldsymbol{r}(t)$ that can be obtained from

$$\boldsymbol{\mu}(t) = \langle\Psi(t)|\,\hat{\boldsymbol{\mu}}\,|\Psi(t)\rangle \tag{3.13}$$

where $\hat{\boldsymbol{\mu}}$ is the dipole operator. The spectral response $\boldsymbol{\mu}(\omega)$ is just the Fourier transform of (3.13). To calculate $|\Psi(t)\rangle$ from (3.12), the Hamiltonian for HHG is required. Applying the single-active electron approximation, disregarding effective mass effects and spin, and assuming sufficiently non-relativistic field strengths so that the magnetic field component can be entirely neglected, the Hamiltonian of a single active electron[8] of mass m_e bound by an atomic potential $V(\boldsymbol{r})$ and subject to an external electromagnetic field reads

$$\hat{\mathrm{H}} = \frac{1}{2m_e}\left(\hat{\boldsymbol{p}} + e\boldsymbol{A}(\hat{\boldsymbol{r}}, t)\right)^2 + V(\hat{\boldsymbol{r}}) + e\Phi(\hat{\boldsymbol{r}}, t) \tag{3.14}$$

where $\boldsymbol{A}$ and Φ are the vector and the scalar potential describing the electric field according to $\boldsymbol{E}(\boldsymbol{r}, t) = -\nabla\Phi - \frac{\partial \boldsymbol{A}}{\partial t}$ and $\hat{\boldsymbol{p}}$ denotes the operator of the canonical momentum which is defined as $\boldsymbol{p} = m_e\boldsymbol{v} - e\boldsymbol{A}$. As mentioned before, different partitions of the Hamiltonian in (3.14) can be chosen, for example

$$\hat{\mathrm{H}}(t) = \hat{\mathrm{H}}_0 + \hat{\mathrm{H}}_{\mathrm{int}}(t) \tag{3.15a}$$

$$= \hat{\mathrm{H}}_{\mathrm{GV}}(t) + \hat{\mathrm{H}}_V \tag{3.15b}$$

where (3.15a) represents the choice from above where the field-free stationary and the laser-interaction Hamiltonian have been separated. In (3.15b), the full Hamiltonian has been partitioned into the ionic potential $\hat{\mathrm{H}}_{\mathrm{V}}$ and the Hamiltonian of a free electron in an electromagnetic field $\hat{\mathrm{H}}_{\mathrm{GV}}$, for which Gordon [82] and Volkov [83] derived relativistic analytical solutions that are commonly referred to as (Gordon-)Volkov states also in the non-relativistic case considered here.

[8] Throughout this thesis, the electron charge is $q_e = -e$ where e is the (positive) elementary charge.

3.2.3 Strong field approximation and stationary phase evaluation: Lewenstein model

The crucial step of the strong field approximation (SFA) is to entirely ignore the effect of the atomic potential when the laser field is present. This corresponds to replacing the full Hamiltonian $\hat{\mathrm{H}}(t)$ in the formal solution (3.12) by the Gordon-Volkov-Hamiltonian

$$\begin{aligned}
\hat{\mathrm{H}}_{\mathrm{GV}}(t) &= \frac{\hat{\boldsymbol{p}}^2}{2m_e} + \hat{\mathrm{H}}_{int}(t) \\
&= \frac{\hat{\boldsymbol{p}}^2}{2m_e} + \frac{e}{m_e}\boldsymbol{A}(\hat{\boldsymbol{r}},t)\cdot\hat{\boldsymbol{p}} + \frac{e^2}{2m_e}\boldsymbol{A}^2(\hat{\boldsymbol{r}},t) && = \hat{\mathrm{H}}_{\mathrm{GV}}^{\mathrm{CG}} && (3.16a)\\
&\simeq \frac{\hat{\boldsymbol{p}}^2}{2m_e} - \hat{\boldsymbol{\mu}}\cdot\boldsymbol{E}(t) && = \hat{\mathrm{H}}_{\mathrm{GV}}^{\mathrm{LG}} && (3.16b)
\end{aligned}$$

for which the solutions to the TDSE, the Gordon-Volkov states $|\chi_{\boldsymbol{p}}(t)\rangle$, are known. Equations (3.16a) and (3.16b) explicitly show the Gordon-Volkov-Hamiltonian in the so-called Coulomb and length gauge, respectively. To obtain (3.16b), the electric dipole approximation has been made, that is, the dependence of the vector potential (and thus the electric field) on the spatial coordinates has been neglected. This approximation is justified if the field strength is small enough so that non-dipole effects do not matter and if the typical length scales of the atom are small compared to the wavelength of the laser so that the atom just sees a spatially homogeneous electric field that varies in time. Although the choice of gauge has been the topic of ongoing debates [84, 85], the length gauge is usually employed within the SFA. The important constraint to be aware of is that the usage of the length gauge is restricted to cases when the dipole approximation applies while the more general Coulomb gauge also remains valid beyond [85, 86][9]. In the following, the length gauge will be used in accordance with most literature on the topic.

The eigenstates $|\chi_{\boldsymbol{p}}(t)\rangle$ of the Gordon-Volkov-Hamiltonian are eigenstates of the canonical momentum operator $\hat{\boldsymbol{p}}$ and form a complete basis of continuum states at every

[9] Remember that Maxwell's equations and thus all physical observables are invariant under the gauge transformation $\boldsymbol{A} \to \boldsymbol{A}' = \boldsymbol{A} + \nabla\chi$ and $\Phi \to \Phi' = \Phi - \frac{\partial\chi}{\partial t}$ with an arbitrary real differentiable function $\chi(\boldsymbol{r},t)$. Since the potentials are not uniquely defined, they can be chosen accordingly to simplify the TDSE and reduce the computational load. A particular choice is the Coulomb gauge which is defined by the conditions $\nabla\cdot\boldsymbol{A} = 0$ and $\Phi = 0$ in empty space. Note that the resulting compact form $\hat{\mathrm{H}}_{\mathrm{GV}}^{\mathrm{CG}}$ of the Gordon-Volkov-Hamiltonian given in (3.16a) can be further simplified if the dipole approximation is imposed as well and the spatial dependence of the vector potential is dropped so that $\nabla\cdot\boldsymbol{A} = 0$ holds automatically. This common combination of Coulomb gauge and dipole approximation is then referred to as the "velocity gauge" [73, 85]. Within the dipole approximation, a gauge transformation with $\chi = -\boldsymbol{r}\boldsymbol{A}(t)$ yields the length gauge representation $\hat{\mathrm{H}}_{\mathrm{GV}}^{\mathrm{LG}}$ of (3.16b).

instant of time. Their length gauge representation is

$$|\chi_{\boldsymbol{p}}(t)\rangle = |\boldsymbol{p} + e\boldsymbol{A}(t)\rangle\, e^{-\frac{i}{\hbar}S_\chi(\boldsymbol{p},t,t_0)} \tag{3.17a}$$

$$S_\chi(\boldsymbol{p},t,t_0) = \frac{1}{2m_e}\int_{t_0}^{t}\big(\boldsymbol{p} + e\boldsymbol{A}(\tau)\big)^2 d\tau \tag{3.17b}$$

$$\mathbb{1} = \int_{\boldsymbol{p}} d\boldsymbol{p}\, |\chi_{\boldsymbol{p}}(t)\rangle\langle\chi_{\boldsymbol{p}}(t)| \tag{3.17c}$$

In coordinate space, these states correspond to plane electron waves with kinetic momentum $\boldsymbol{p}_v(t) = \boldsymbol{p} + e\boldsymbol{A}(t)$. Since the canonical momentum $\boldsymbol{p}$ is a conserved quantity, the kinetic momenta at different times t and t' are strictly related. Using (3.17), the Gordon-Volkov propagator $\hat{\mathrm{U}}_{\mathrm{GV}}(t,t')$, which describes the time evolution of a system from t' to t under the influence of $\hat{\mathrm{H}}^{\mathrm{LG}}_{\mathrm{GV}}$, can be written down formally as

$$\begin{aligned}\hat{\mathrm{U}}_{\mathrm{GV}}(t,t') &= e^{-\frac{i}{\hbar}\int_{t'}^{t} d\tau \hat{\mathrm{H}}_{\mathrm{GV}}(\tau)} \\ &= \int_{\boldsymbol{p}} d\boldsymbol{p}\, |\chi_{\boldsymbol{p}}(t)\rangle\, \langle\chi_{\boldsymbol{p}}(t')| \\ &= \int_{\boldsymbol{p}} d\boldsymbol{p}\;\; e^{-\frac{i}{\hbar}S_\chi(\boldsymbol{p},t,t')}\, |\boldsymbol{p} + e\boldsymbol{A}(t)\rangle\, \langle\boldsymbol{p} + e\boldsymbol{A}(t')|\end{aligned} \tag{3.18}$$

It can be seen from (3.18) that the action of $\hat{\mathrm{U}}_{\mathrm{GV}}(t,t')$ on a system described by an initial kinetic momentum state $|\boldsymbol{p}_v(t')\rangle = |\boldsymbol{p} + e\boldsymbol{A}(t')\rangle$ corresponds to the evolution of the system to a different kinetic momentum state $|\boldsymbol{p}_v(t)\rangle = |\boldsymbol{p} + e\boldsymbol{A}(t)\rangle$ at a later time t. During this evolution, the system acquires an additional phase factor which is determined by the time integral over the instantaneous kinetic energy $W_v(t) = \frac{1}{2m_e}\left[\boldsymbol{p}_v(t') - e\boldsymbol{A}(t') + e\boldsymbol{A}(t)\right]^2$ (cf.(3.17b)).

After inserting (3.18) into (3.12), the dipole moment (3.13) can be calculated within the SFA. The so obtained expression for the dipole moment can be further simplified if the initial state $|\psi_i\rangle$ is expanded in the basis of bound states, $|\psi_i\rangle = \sum_m a_m(t_i)\,|m\rangle$ and additional assumptions are involved. For low-frequency ($\hbar\omega_1 \ll U_I$), low-intensity ($I < I_s$) driving laser fields, it is justified to assume that the system starts purely in the ground state, i.e. $|\psi_i\rangle = a_0(t_i)\,|0\rangle$, and that depletion of the ground state and possible intermediate contributions of other bound states can be neglected at all times, i.e. $a_m(t) \simeq \delta_{m0}$ for all t.[10] The dipole moment (3.13) then becomes

$$\boldsymbol{\mu}(t) = \frac{i}{\hbar}\int_{t_i}^{t} dt' \int_{\boldsymbol{p}} d\boldsymbol{p}\, \langle 0|\, \hat{\boldsymbol{\mu}}\, |\boldsymbol{p} + e\boldsymbol{A}(t)\rangle\, e^{-\frac{i}{\hbar}S(\boldsymbol{p},t,t')}\, \langle\boldsymbol{p} + e\boldsymbol{A}(t')|\, \hat{\boldsymbol{\mu}}\cdot\boldsymbol{E}(t)\, |0\rangle + c.c. \tag{3.19}$$

where potential continuum-continuum contributions were neglected and the ground state was assumed to have no dipole moment. The phase factor in (3.19) is determined by

[10] Here, δ_{mn} is the Kronecker delta which takes a value of 1 for $m = n$ and 0 otherwise

the quasi-classical action

$$S(\boldsymbol{p}, t, t') = \frac{1}{2m_e} \int_{t'}^{t} \big(\boldsymbol{p} + e\boldsymbol{A}(\tau)\big)^2 d\tau + U_I(t - t') \tag{3.20}$$

where the term "quasi-classical" refers to the fact that, contrary to what is often stated in the literature, (3.20) is not identical to but only resembles the classical action because it just contains its energy part and is additionally shifted by the ionization potential of the atom U_I.

Reading (3.19) from the right to the left, the three steps of HHG according to the simple man's model can immediately be identified: $\langle \boldsymbol{p} + e\boldsymbol{A}(t')| \, \hat{\boldsymbol{\mu}} \cdot \boldsymbol{E}(t) \, |0\rangle$ is the probability amplitude for ionization at time t', linking the ground state with the continuum under the influence of the laser field. The propagation in the continuum leads to the acquistion of a phase factor $e^{-\frac{i}{\hbar}S(\boldsymbol{p},t,t')}$ that has no classical counterpart and strongly affects the macroscopic properties of the generated high harmonic radiation. Finally, $\langle 0| \, \hat{\boldsymbol{\mu}} \, |\boldsymbol{p} + e\boldsymbol{A}(t)\rangle$ represents the probability amplitude for recombination in the form of a dipole transition from a continuum state to the ground state.

To obtain the spectral components of the dipole response of a single atom $\boldsymbol{\mu}(\omega)$, the Fourier transform of (3.19), has to be calculated. The evaluation of the multiple integrals required for that purpose can be significantly simplified because the modified action $S(\boldsymbol{p}, t, t')$ is a highly oscillatory function compared to the other factors (as long as $U_P \gg \hbar\omega_1$ and for short enough excursion times $t - t'$) so that the well-known saddle point method can be applied. The latter approximates the integration by the sum over all dominant contributions which are found at the stationary points of the oscillating function. Applied to the quasi-classical action with the restriction of positive harmonic frequencies ω_q, this yields the following conditions

$$\nabla_{\boldsymbol{p}} \Big(S(\boldsymbol{p}, t, t') + \hbar\omega_q t \Big) = \frac{1}{m_e} \int_{t'}^{t} \big(\boldsymbol{p} + e\boldsymbol{A}(\tau)\big)^2 d\tau = \boldsymbol{r}(t) - \boldsymbol{r}(t') = \boldsymbol{0} \tag{3.21a}$$

$$-\frac{\partial}{\partial t'} \Big(S(\boldsymbol{p}, t, t') + \hbar\omega_q t \Big) = \frac{1}{2m_e} \big(\boldsymbol{p} + e\boldsymbol{A}(t')\big)^2 + U_I = 0 \tag{3.21b}$$

$$\frac{\partial}{\partial t} \Big(S(\boldsymbol{p}, t, t') + \hbar\omega_q t \Big) = \frac{1}{2m_e} \big(\boldsymbol{p} + e\boldsymbol{A}(t)\big)^2 + U_I - \hbar\omega_q = 0 \tag{3.21c}$$

which retrieve the complex quantum analogon of the assumptions of the three-step model: Equation (3.21a) requires the relevant trajectories in the continuum to return to the parent ion while (3.21c) indicates energy conservation in the recombination process. The condition given by (3.21b) cannot be met classically because it implies an imaginary kinetic momentum (which is approximately zero for strong fields $U_P \gg U_I$) at the beginning of the interaction, hence indicating a quantum mechanical tunnel process.

The analytic quantum mechanical description of HHG highlighted above was first presented in the seminal paper of Lewenstein et al. [67] and has thus been termed "Lewenstein model" by the community. While the Lewenstein model fully absorbs the

semi-classical three-step model, it also possesses several unique distinctive features. In contrast to the classical trajectories, the quantum paths and all their characteristic parameters are complex so that trajectories with complex recombination times and thus harmonic photon energies above the classical single atom cutoff predicted by (3.8) are allowed. However, their contributions decay exponentially so that the increase in cutoff energy only amounts to up to $0.32U_I$ [67] and can easily be masked by macroscopic effects in experiments.

A crucial prognosis of the Lewenstein model is the existence of an additional dipole phase factor (cf. (3.19)) that is determined by the quasi-classical action (3.20) and causes strong amplitude-to-phase coupling. The latter becomes obvious from a comparison of (3.20) and (3.6a) which reveals that the quasi-classical action is proportional to $U_P(t-t')$ with $U_P \propto I$. Although the excursion time in the continuum $(t-t')$ weakly depends on the harmonic order and thus on the intensity, the dipole phase can be linearized as $\varphi_I^{(j)} = \alpha_j I$ in good approximation. The phase coefficients α_j differ significantly for different trajectories due to their dependence on the excursion time (cf. Figs. 3.1 and 3.2).

The Lewenstein model includes the possibility of interference between different quantum paths that can be explained in the intuitive framework of Feynman's path integral formalism. As shown by Salières and co-workers both theoretically and experimentally [87], the probability amplitude for high harmonic emission at a certain frequency is obtained by coherently adding the contributions of all possible quantum paths leading to the same final state. Here, the quasi-classical action determines the weights of the individual paths of which in general just the two with the shortest travel times are found to have relevant contributions. The macroscopic manifestations of the distinguishable phase of the trajectories will be discussed in Section 3.3.

3.2.3.1 Extensions of the Lewenstein model

Despite providing a successful quantum mechanical description of HHG, the Lewenstein model in its simplest form contains several oversimplifications such as the neglection of the Coulomb potential in the strong field approximation that, however, can be included as corrections in extended versions of the theory [86, 88]. In this way, inaccuracies of the prefactors of the SFA transistion rates resulting from the lack of gauge invariance of the SFA if the Volkov propagator is used in the length gauge can be eliminated [89]. Likewise, while not included in the SFA, scattering of the returning electron wavepacket off the ionic core is considered in an extended version known as SFA2 [90] and problems caused by the overcomplete basis set used in the SFA are resolved in the so-called quantitative rescattering theory(QRS) [91–93].

3.3 Macroscopic description

In the previous section, the physical mechanism of HHG was discussed for a single atom. This microscopic description provides intuitive insight into the physics and is capable of explaining several typical features that are observed experimentally, for example, the discrete spectrum and both the existence and, in good approximation, the position of the cutoff. However, it cannot accurately predict the exact shape of the spectrum and the relative harmonic intensities because the experimentally observable harmonic yield depends on the coherent superposition of the contributions from a macroscopic ensemble of target atoms [94].

Maximizing this yield necessitates carefully balancing several intertwined factors: While a certain threshold intensity has to be exceeded for the generation of a certain harmonic order q and the single atom dipole response scales nonlinearly with intensity, the benefit of increasing the driving intensity to maximize the dipole response is counterbalanced at a certain level by the simultaneously growing fraction of ionized atoms which impairs phase-matching of the contributions from as many atoms within the target as possible. To further scale up the harmonic yield, one can therefore raise the intensity level at which the optimum balance occurs, for example, by choosing a target medium with higher ionization potential[11]. Alternatively, in the case of free focusing geometries, one can resort to looser focusing conditions for which the number of contributing atoms is enlarged in the transverse dimension and for which phase-matching is also possible at a higher level of ionization due to the reduced geometric phase shift.

While guided geometries, i.e. gas-filled waveguides or capillaries, have very successfully been employed as targets for HHG, phase-matching of high harmonic radiation will be reviewed for free focusing geometries in the following section. In these experimental configurations, the driving laser beam is focused into gas targets consisting of a pressurized gas cell or a freely expanding gas jet produced by a pressurized nozzle. The latter target design is a particularly suitable choice for the special case of tight focusing geometries, which are mandatory for driving lasers with low peak powers and thus typical of HHG at multi-MHz repetition rates. Subsequently, after a brief review of existing quasi-phase matching techniques for HHG, some general properties of the macroscopically observed high harmonic radiation will be summarized and manifestations of the microscopic response in the macroscopic signal will be highlighted.

3.3.1 Phase-matching

3.3.1.1 General

The effects of phase-matching in standard HHG experiments, in which a noble gas is usually employed as the nonlinear medium, can be fully accounted for by solving Maxwell's equations non-relativistically for an isotropic, non-magnetic medium. For

[11] Unfortunately, the recombination cross section and thus the conversion efficiency is lower for the lighter noble gases with higher ionization energies so that the best choice of medium also depends on the desired photon energy.

axially symmetric and not too divergent beams, for which the paraxial approximation applies, propagation in the generating medium and to a far-field detector can be calculated by solving the coupled wave equations of the fundamental and the high harmonic fields in dependence of the radial and longitudinal spatial coordinates r and z, respectively, and time t. The harmonic field originates from the laser-induced polarization $P_q(r,z,t) = \sum \mu_q(r,z,t)$ which is given by the sum over all contributing dipole moments. To numerically obtain the latter, the Lewenstein model or other simplified models are usually employed because the combination of a 3d propagation code and solving the TDSE increases the required computational time to an unfavorably high and thus impractial level.

Phase-matching is achieved when the driving field at fundamental frequency ω_1 propagates with the same phase velocity as the produced qth harmonic field at frequency $\omega_q = q\omega_1$ so that the contributions at ω_q are in phase at all positions within the target at all times. For an unguided focusing geometry, the degree of phase-matching in the direction collinear to the driving beam can be quantified by

$$\begin{aligned} \xi_q(r,z,t) = \frac{\partial}{\partial z}\Big[\Delta\Phi_q(r,z,t)\Big] &= \frac{\partial}{\partial z}\Big[q\ \Phi_1(r,z,t) - \Phi_q(r,z,t)\Big] \\ &= \frac{\partial}{\partial z}\Big[\Delta\varphi_n + \Delta\varphi_p - \Delta\varphi_g - \varphi_I\Big] \end{aligned} \tag{3.22}$$

where $\Delta\varphi_n$ and $\Delta\varphi_p$ describe the dispersive phase mismatch in the target due to the neutral atoms and the electron plasma produced by ionization, respectively, while $\Delta\varphi_g$ results from the difference in Gouy phase of the fundamental and the harmonic fields and φ_I represents the intensity-dependent dipole phase of the harmonic radiation. Since ξ_q indicates the slope of the longitudinal dephasing, it is common to define the so-called coherence length

$$L_{\mathrm{coh}}(q) = \frac{\pi}{|\xi_q|} \tag{3.23}$$

which quantifies the length scale on which the contributions of atoms at different positions within the target to the harmonic field at frequency $\omega_q = q\omega_1$ add up constructively.

3.3.1.2 Time-dependence

For a given experimental geometry and realistic (i.e. not temporally square) laser pulses, all factors in (3.22) are (at least weakly) time-dependent so that phase-matching becomes a dynamic process and can therefore just be achieved transiently during a finite time window within the pulse [95,96]. Since the time-dependence originates from the effects of ionization and from the intensity-dependence of the dipole phase, it is largely mitigated for short low intensity driving lasers pulses that lead to negligible ionization during the pulse. In that case, the maximum harmonic emission consequently happens at the peak of the fundamental pulse and the coherence length remains roughly constant in time. For a given focusing geometry, phase-matching can then be achieved by adjusting the target pressure such that the coherence length is maximized [97]. However, as can be derived

by inserting (3.2) into the cutoff law (3.8), the generation of a certain high harmonic order q requires the driving intensity to exceed a certain threshold value

$$I_{th}(q) = \frac{2m_e c\varepsilon_0\omega_1^2}{e^2}\frac{(q\hbar\omega_1 - U_I)}{3.17} \tag{3.24}$$

that inevitably corresponds to a certain level of (time-dependent) ionization. The latter is determined by the pulse duration, the fundamental wavelength, and the target atom. Therefore, as soon as ionization becomes non-negligible, a time-dependent treatment of phase-matching is required. The time dependence is additionally complicated for repetition rates at the MHz level and above because the gas atoms in the target are not fully replaced between subsequent pulses. Hence, transient effects of the generated plasma, whose lifetime exceeds the temporal pulse spacing, have to be taken into account. While this requires a simultaneous time-resolution on both the fs-scale within the duration of the pulse and on the ns-scale to include the effects of subsequent pulses in a simulation, it also means that it is extremely challenging to devise an exhaustive analytic description of phase-matching. Hence, the following discussions will remain on a qualitative level for the most part.

3.3.1.3 Phase matching without absorption

It is instructive to discuss phase-matching for three different situations that can be distinguished by the functional dependence of $\xi_q(r,t,z)$ and its derivative $\partial_z\xi_q(r,t,z)$ on the longitudinal coordinate z. In order of increasing complexity, these three cases are: i) perfect phase-matching, i.e. $\xi_q = 0$, ii) linear phase evolution, i.e. $\xi_q \neq 0$ and $\partial_z\xi_q = 0$, and iii) nonlinear dephasing, i.e. $\xi_q \neq 0$ and $\partial_z\xi_q(z) \neq 0$.

The special case i) of perfect phase-matching ($\xi_q = 0$) corresponds to a longitudinally constant or identically vanishing phase mismatch $\Delta\Phi_q$ and thus an infinite coherence length so that the harmonic field grows linearly with propagation distance in the medium. Therefore, the harmonic intensity increases quadratically with the target length, or more specifically, since the number density N of the medium is adjustable, with the density-length product. This means that the harmonic yield scales with the square of the number of (coherently) contributing atoms.

In the second case ii), when ξ_q is constant with respect to z, the fundamental and the harmonic field dephase completely within a finite distance given by $L_{\mathrm{coh}}(q)$. Due to the constant increase of the phase mismatch $\Delta\Phi_q$ with the density-length product, the achievable harmonic yield is strongly reduced compared to the case of perfect phase-matching. In approximately lossless media, the functional dependence of the harmonic yield on the density-length product NL becomes $\propto (NL)^2\,\mathrm{sinc}^2\,(\Delta\Phi_q(NL)/2)$. The resulting oscillatory maxima in the yield are known as Maker fringes [98] from second harmonic generation in nonlinear crystals and have also been observed in HHG as a modulation of the harmonic intensity with target pressure at fixed experimental target length [95, 99, 100].

In the most general case iii) of nonlinear dephasing, ξ_q still depends on z so that it becomes extremely challenging, if not impossible, to obtain an analytical expression to

predict the harmonic yield. However, the different individual contributions to the phase mismatch as described in the second line of (3.22) can be discussed qualitatively. Here, for the sake of simplicity, the discussion is restricted to the symmetry axis, i.e. $r = 0$, and potential reshaping of the pulse envelope and few-cylce effects are neglected. The first two contributions, $\Delta\varphi_n$ and $\Delta\varphi_p$, are of dispersive nature and simply originate from the different refractive indices of the target medium for fundamental and harmonic frequencies. The dispersive effects have been split into the directly related contributions of neutral atoms and free electrons because either of the two can be dominant at the expense of the other depending on the experimental conditions. As discussed in Section 2.1.3, dispersion leads to a frequency-dependent index of refraction which for a partially ionized gas becomes [72]

$$\begin{aligned} n_q(\omega_q, z, t) &= 1 + \delta n_n + \delta n_p \\ &\approx 1 + \frac{e^2}{2\varepsilon_0 m_e} \frac{N\big(1 - \Lambda(z,t)\big)}{\omega_r^2 - \omega_q^2} - \frac{\omega_p^2(z,t)}{2\omega_q^2} \end{aligned} \tag{3.25}$$

where the plasma frequency

$$\omega_p^2(z,t) = \frac{N\Lambda(z,t)e^2}{\varepsilon_0 m_e} \tag{3.26}$$

is much smaller than ω_q for all q so that the effect of the plasma is largest for the fundamental beam. Here, the density of free electrons is given by the product of the atomic number density N and the fraction of ionization $\Lambda(z,t)$. The resonance frequency ω_r of the target atom is determined by the energy separation between its ground and first excited state. For atomic xenon, which was used for all HHG experiments described in this thesis, $\hbar\omega_r = 8.32\,\mathrm{eV}$ [101]. Using (3.25), the phase mismatch due to the neutral atom dispersion becomes

$$\begin{aligned} \Delta\varphi_n(\omega_q, z, t) &= q\frac{\omega_1}{c}\delta n_n(\omega_1)z - \frac{\omega_q}{c}\delta n_n(\omega_q)z \\ &= q\frac{\omega_1}{c}\frac{e^2 N\big(1 - \Lambda(z,t)\big)}{2\varepsilon_0 m_e}\left(\frac{1}{\omega_r^2 - \omega_1^2} - \frac{1}{\omega_r^2 - \omega_q^2}\right) z \end{aligned} \tag{3.27}$$

whereas the phase mismatch due to the plasma is given by

$$\begin{aligned} \Delta\varphi_p(\omega_q, z, t) &= q\frac{\omega_1}{c}\delta n_p(\omega_1)z - \frac{\omega_q}{c}\delta n_p(\omega_q)z \\ &= \frac{\omega_p^2}{2c\,\omega_1}\left(\frac{1 - q^2}{q}\right) z \end{aligned} \tag{3.28}$$

which is the dominant dispersive effect in the case of strong ionization. Note that the effective degree of ionization and thus the resulting phase mismatch can be higher than suggested by (3.28) when the temporal pulse separation is smaller than the plasma lifetime so that there is residual plasma left when a subsequent pulse arrives at the target. This can be incorporated into (3.28) if $\Lambda(z,t)$ in (3.26) is modified to account for the effective ionization fraction.

Contribution to ξ_q	Sign	
	$z<0$	$z>0$
$\partial_z \Delta\varphi_n$	$+$	$+$
$\partial_z \Delta\varphi_p$	$-$	$-$
$-\partial_z \Delta\varphi_g$	$-$	$-$
$-\partial_z \varphi_I$	$-$	$+$

Table 3.1: *Signs of the longitudinal evolution of the different contributions to the phase mismatch (see (3.22)).*

The focusing that is usually required to reach the threshold intensities for HHG gives rise to a geometric phase difference on axis

$$\begin{aligned}\Delta\varphi_g(\omega_q, z, t) &= \left(q \arctan\left(\frac{2z}{n_1 b}\right) - \arctan\left(\frac{2z}{n_q b}\right)\right) \\ &\approx (q-1)\arctan\left(\frac{2z}{b}\right)\end{aligned} \tag{3.29}$$

that can be very large and the dominating contribution in (3.22) for low gas densities or tight focusing geometries.

The intensity-dependent dipole phase φ_I can be linearized in good approximation so that

$$\varphi_I(z,t) = \sum \alpha_q^{(j)} I(r=0,z,t) = \sum \alpha_q^{(j)} \frac{I_0(t)}{1+\left(\frac{2z}{b}\right)^2} \tag{3.30}$$

where all quantum orbits involved in the generation of the harmonic order q under consideration contribute with their individual linear phase parameters $\alpha_q^{(j)}$. For the short trajectories, $\alpha_q^{(1)}$ is on the order of 1 in units of $10^{-14}\,\mathrm{cm^2/W}$ whereas the phase parameter of the long trajectory $\alpha_q^{(2)}$ is on the order of 10 in the same units.

Looking at (3.27), (3.28), (3.29), and (3.30), some general considerations concerning the interplay of the different contributions to phase-matching on axis within one confocal parameter according to (3.22) can be made[12]. The intensity-dependent phase $\varphi_I(z,t)$ evolves with z as the on-axis intensity so that the contribution $-\partial_z\varphi_I(z,t)$ is always negative for $z<0$ and positive for $z>0$. Since the geometric phase mismatch $\Delta\varphi_g$ increases monotonically with z, $-\partial_z\Delta\varphi_g$ is always negative. For the plasma dispersion, $\Delta\varphi_p \propto -\Lambda(z)z$ applies for all high harmonic orders q and since $\Lambda(z)$ is a symmetric function due to its intensity dependence, $\partial_z\Delta\varphi_p$ is negative for all $|z|<b$. Similarly, for q such that $\omega_q > \omega_r$, the neutral dispersion $\Delta\varphi_n$ is proportional to $\big(1-\Lambda(z)\big)z$ so that $\partial_z\Delta\varphi_n > 0$ holds for $|z|<b$ because the values of $\Lambda(z)$ range from 0 (no ionization) to 1 (full ionization).

[12]Note that while the overall sign may be different in some literature due a different definition of the phase mismatch $\Delta\Phi_q$, the signs of the individual contributions to (3.22) are consistent within this thesis.

From these general considerations, whose results are also summarized in Table 3.1, it can be seen that $\partial_z \Delta\varphi_n$ is the only positive contribution around the focus (where $\partial_z \varphi_I \approx 0$) and has to compensate for both $\partial_z \Delta\varphi_p$ and $-\partial_z \Delta\varphi_g$. This is possible for certain experimental conditions by adjusting the gas pressure [97]. However, if the gas target is placed at the focus, the short and the long trajectory are phase-matched simultaneously which can be unfavorable in an experiment because of their different divergence resulting from the radial intensity variation (see Section 3.3.1.5 and Section 3.3.3.3). Positioning the gas target behind the focus ($z > 0$), where $-\partial_z \varphi_I$ contributes as an additional positive term, allows to preferably phase-match the short trajectory whose intensity-dependent phase varies less strongly than that of the long trajectory. For tight focusing geometries or strong ionization, a high gas pressure is required for phase-matching. In order to reduce the demands on the necessary density of atoms in the interaction region, it is thus at least beneficial to keep ionization at a low level, if not mandatory to experimentally achieve phase-matching at all [97, 102].

This is especially important because high gas pressures inevitably lead to reabsorption of the generated harmonic radiation within the target.

3.3.1.4 Phase matching including absorption

To analyze the effect of absorption in more detail, it is again instructive to differentiate between the three cases from above. When absorption is considered for perfect phase-matching conditions ($\xi_q = 0$), the harmonic yield does not infinitely grow quadratically with the density-length product anymore, but saturates for propagation distances in the target medium that are much larger than the absorption length L_{abs}. The latter is defined as the distance over which $1/e$ of the harmonic power is transmitted according to

$$L_{\mathrm{abs}}(q) = \frac{1}{N\sigma_q} \tag{3.31}$$

with absorption cross section σ_q. The asymptotically achievable harmonic intensity I_{abs} is independent of the gas pressure and just depends on the driving laser intensity, the harmonic frequency, and the gas species. For $NL \ll NL_{\mathrm{abs}}$, the harmonic yield scales quadratically with the density-length product as in the absorption-free case. About 99% of I_{abs} are reached for a density-length product of $10NL_{\mathrm{abs}}$ [72].

In the case of linear phase evolution ($\partial_z \xi_q = 0$), the effect of the finite coherence length $L_{\mathrm{coh}}(q)$ has to be taken into account in addition to that of the absorption length. Since the length of the target does typically not vary at least within a single experimental run, the harmonic yield for a fixed medium length L_{med} becomes [103, 104]

$$I_q(N) = \frac{I_{\mathrm{abs}}}{1 + 4\pi^2 \left(\frac{L_{\mathrm{abs}}}{L_{\mathrm{coh}}}\right)^2} \left(1 + e^{-\frac{L_{\mathrm{med}}}{L_{\mathrm{abs}}}} - 2\cos\left(\frac{\pi L_{\mathrm{med}}}{L_{\mathrm{coh}}}\right) e^{-\frac{L_{\mathrm{med}}}{2L_{\mathrm{abs}}}}\right). \tag{3.32}$$

Note that (3.32) depends on the (adjustable) gas density N via L_{abs} and L_{coh}. Therefore, similar to the lossless case, the harmonic yield can show oscillations (Maker fringes) as a function of pressure due to the cosine term in (3.32). To obtain more than 50% of

the maximum harmonic yield, the conditions $L_{\mathrm{med}} > 3L_{\mathrm{abs}}$ and $L_{\mathrm{coh}} > 5L_{\mathrm{abs}}$ have to be met as a rule of thumb [103]. Harmonic generation is then said to be absorption-limited. It is important to note again that (3.32) strictly only applies for $\partial_z \xi_q = 0$, which can be realized in a loose focusing geometry ($b \gg L_{\mathrm{med}}$) [105], and for $\partial_t \xi_q \approx 0$. However, as long as the coherence length fulfills the absorption-limited conditions within a finite time window during the pulse and the nonlinear contributions to ξ_q are small enough not to cause destructive interference, (3.32) can also be used to approximate the harmonic yield for a larger range of experimental conditions [96, 97].

In the most general case that the phase mismatch $\Delta\Phi_q$ nonlinearly depends on z, which is the case for tight focusing geometries ($b \ll L_{\mathrm{med}}$), numerical methods are usually employed to predict the harmonic yield for certain experimental conditions. An important step in such a typical numerical procedure is to determine the level of ionization at each position in the target as a function of time from adequate ionization models (e.g. [76, 78]) which then allows to evaluate the different contributions to the (nonlinear) dephasing parameter $\xi_q(r, z, t)$.

3.3.1.5 Effects of the radial intensity dependence

So far, it has been assumed that the spatial properties of the focused driving laser beam are those of a Gaussian beam that remains Gaussian at all times. However, due to the radial variation of the driving beam intensity, ionization leads to a radially decreasing density of free electrons that acts as a diverging lens. When ionization is strong, the main consequence of this so-called plasma defocusing is that the fundamental beam just reaches an effective intensity in the medium that can be significantly lower than its focused intensity in vacuum [106, 107]. In that case, the single atom dipole response is lower and both the geometric phase mismatch and the intensity-dependent phase are strongly altered compared to the situation of low ionization and purely Gaussian spatial propagation of the fundamental, thereby leading to largely different phase-matching conditions.

Independent of the level of ionization, the dipole phase as given in (3.30) becomes approximately parabolic in the radial coordinate r when considering the effect of the radial intensity profile of the fundamental beam. This parabolic phase variation, which corresponds to the transfer function of a lens, differs for the contributions from the short and the long trajectories. As will be detailed in a later section (Section 3.3.3), the resulting difference in divergence can be observed in the far-field and exploited to macroscopically separate the contributions from both trajectories.

3.3.2 Quasi phase-matching

As has been discussed in the previous section, efficient phase-matching of high harmonic radiation is a complex task. For non-vanisihing phase mismatch $\Delta\Phi_q$, linear or nonlinear dephasing restricts the distance over which the harmonic field can build up constructively to one coherence length $L_{\mathrm{coh}}(q)$. In addition, the high level of ionization that unavoidably accompanies the high threshold intensities required for the generation of the highest

energy photons limits phase-matching to high harmonic energies below 130 eV [108]. Motivated by the quest to overcome this limit and to extend phase-matched HHG into the soft x-ray region, the concept of quasi-phase matching (QPM) has been adopted from frequency conversion in nonlinear crystals and schemes applicable to HHG have been devised and studied. Since QPM techniques may also be suitable to selectively enhance the conversion efficiency of a particular harmonic order under the tight focusing conditions that are currently required for single-pass HHG experiments at repetition rates on the MHz level, existing concepts shall be briefly mentioned in this section.

The basic idea behind QPM of nonlinear frequency conversion processes is to either periodically adjust the phase mismatch such that a constructive build-up is possible over a larger distance in the nonlinear medium or to actively disrupt the nonlinear process in spatial regions whose contributions would otherwise destructively interfere with the harmonic wave. Since the target media typically employed for HHG are isotropic, several QPM schemes that rely on a spatially periodic modulation of either the medium density [109] or of the driving laser intensity have been proposed and demonstrated for HHG. Note that although all of them yield or promise significantly increased conversion efficiencies, the exact definition of the achievable enhancement varies and therefore makes a direct comparison of the techniques described in the following difficult.

The group of Kapteyn and Murnane in Boulder proposed [110] and later realized [111] quasi-phase matched HHG in a hollow waveguide with a perdiodically varying inner diameter leading to alternating driving laser intensity along the waveguide. Following earlier proposals by Birulin and co-workers [112] and Peatross et al. [113], this scheme was then turned into an all-optical one based on the interaction of the strong driving laser beam with a weaker counterpropagating pulse train in the waveguide that leads to suppression of HHG in regions where the pulses overlap [114–116]. Depending on whether the counterpropagating pulses are parallely or orthogonally polarized with respect to the main driving laser beam, the disruption of the HHG process is caused by the induced strongly varying phase or by the resulting nonlinear polarization in the regions of overlap, respectively, where the former has been shown to be more efficient [117]. A similar approach where mode beating in a capillary partially suppresses HHG has been demonstrated [118].

In unguided HHG geometries, a variation of the target medium density can be realized by using several successive gas targets or an array of targets with appropriate spacing [119, 120]. If the targets are alternatingly supplied with an efficient medium for HHG and a second, more quickly ionizing gas, the full ionization of the latter during the rising edge of the fundamental pulse can prevent high harmonic generation completely in this spatial region [120]. Recent theoretical studies come to the conclusion that the passive character of the second medium, which was hydrogen in the experimental demonstration reported in [120], may not purely originate from its lower ionization threshold compared to the HHG medium (Ar in [120]), but also from a significantly lower recombination cross section [121].

Yet another theoretically proposed spectrally tunable QPM scheme suitable for free focusing geometries is based on HHG in the presence of a static electric field with periodically modulated amplitude along the propagation direction of the driving laser beam

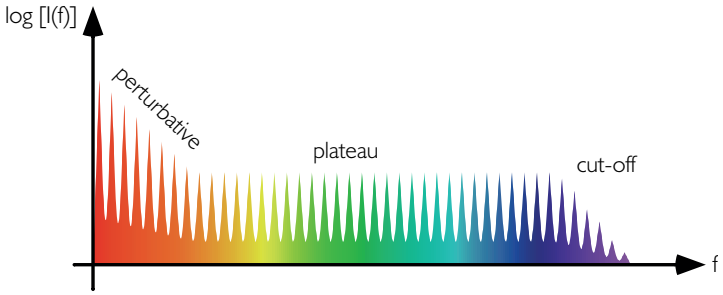

Figure 3.3: *Generic high harmonic spectrum.*

in the interaction volume [122, 123]. The suggested experimental method to produce an approximately static electric field is to illuminate a suitable amplitude mask with a pulsed long-wavelength laser propagating orthogonally to the driving laser beam. The QPM effect observed in numerical simulations was attributed to phase variations of the laser-induced dipole moments that are caused by the static field. The peak field strength of the latter in the simulations was about three orders of magnitude lower than that of the driving laser.

Interestingly, one of the earliest proposals for QPM already mentioned HHG in a non-collinear geometry with two driving beams crossing at angles close to 0 or 180° as a potential means to increase the conversion efficiency by a partial compensation of the medium dispersion and to generate angularly resolved high harmonics [112]. Non-collinear HHG has been the subject of investigations carried out by the author of this thesis that will be presented in Chapter 4.

3.3.3 Macroscopic properties of high harmonic radiation

Aside from providing the opportunity to access the spectral regions from the VUV to the XUV and beyond with comparably simple, inexpensive, and versatile table-top experimental systems, the attractiveness of high harmonic generation originates from the superior properties of the generated radiation. To name a few, the light produced by HHG is highly directional, shows a high degree of both spatial and temporal coherence, and grants access to ultrafast timescales. While an exhaustive review of all aspects is beyond the scope of this thesis, this section intends to briefly recapitulate the key properties of high harmonic radiation. Many of these characteristics are interlinked so that the classification presented below is merely meant to provide some guidance for the reader.

3.3.3.1 Spectrum

A generic high harmonic spectrum, as it is typically produced by a many-cycle driving laser, is shown in Figure 3.3. Only odd harmonics of the driving frequency ω_1 can be observed. While this feature of the high harmonic spectrum was explained in Section 3.2.1 by the time periodicity of the emission process (twice per fundamental cycle) that leads

to a $2\omega_1$ spacing of the harmonics in the frequency domain, a different explanation shall be presented here: For HHG to be a coherent process, the final state has to be identical to the initial state so that the parity of the wavefunction must not change, i.e. the number of involved photons has to be even. At the same time, HHG corresponds to the conversion of q driving laser photons into a single qth harmonic photon so that parity conservation requires $(-1)^{q+1} = 1$. Consequently, q needs to be odd.

The second characteristic of the spectrum is the plateau of equally intense harmonics that extends up to the cutoff frequency ω_c predicted in (3.8) by single atom considerations. The wavelength range covered by high harmonic radiation reaches down into the biomedically interesting so-called water window [79] between 4.4 nm and 2.34 nm, where water is transparent so that the radiation can be used for in vivo microscopy, and up to harmonic orders of ~ 5000 and keV energies [80]. Unlike the lowest harmonic orders, which obey the perturbative intensity scaling $I_q \propto I^q$, the plateau harmonics approximately follow an effective power law $I_q \propto I^p$ with $p < q$. Different values for the exponent p have been used in the literature to approximate the harmonic dipole scaling depending on the harmonic order under consideration (for example, $p \approx 5$ was used for plateau harmonics in [124]) and the values derived from experiments vary as well. Note that the shape of experimental spectra can significantly differ from the generic spectrum shown in Figure 3.3 both due to the effects of phase-matching and when generated by multi-color driving fields or few-cycle driving lasers (see below).

Under the assumption that the time-bandwidth product remains constant in the HHG process, the spectral width of individual high harmonic orders centered about frequencies $\omega_q = q\omega_1$ is predicted to be $\Delta\omega_q = \sqrt{q}\Delta\omega_1$ from lowest order perturbation theory and reduces to $\Delta\omega_q = \sqrt{p}\Delta\omega_1$ in the case of an effective power law. In reality, a combination of factors can cause deviations of both the spectral width and the center frequency. For example, the harmonics generated later during the fundamental pulse are blueshifted because the density of free electrons increases during the pulse and the resulting refractive index change blueshifts the fundamental frequency. At the same time, the spectral width of the plateau harmonics is found to increase while that of the cutoff harmonics remains unaffected. This can be attributed to the spatial variation of ionization: The same plateau harmonic can be generated both in regions with high and low ionization and thus with both shifted and unshifted fundamental frequency whereas the cutoff harmonics can only be generated in the spatially narrow regions of highest intensity [125–129]. In addition, the intensity-dependent dipole phase leads to spectral broadening of the generated harmonics via self-phase modulation but does not affect the center frequency as long as ionization is negligible. For increasing degrees of ionization, the shape of the harmonic pulse and its corresponding spectrum is successively altered due to the depletion of the medium, the index variation due to the free electrons, and eventually also plasma defocusing. Since all of these effects mostly affect the trailing edge of the harmonic pulse, the harmonic center frequency is blue-shifted. This shift can be larger than the one caused by the blueshift of the fundamental [95, 130].

3.3.3.2 Pulse duration

The pulse duration of a single harmonic order q has been the subject of detailed theoretical and experimental investigations. From lowest order perturbation theory, a harmonic pulse duration $\tau_q = \tau_1/\sqrt{q}$ can be expected whereas longer pulse widths $\tau_q = \tau_1/\sqrt{p}$ are predicted by models based on an effective process nonlinearity p [68]. More elaborate theoretical analyses show that the harmonic pulse duration strongly depends on parameters such as the driving intensity and the position of the gas target with respect to the focus due to the effects of the intensity-dependent dipole phase and ionization [130]. However, all these predictions agree that the harmonic pulses can be much shorter than the generating pulses of the driving lasers.

Therefore, advanced experimental schemes are usually necessary to measure the harmonic pulse duration. Common techniques rely on the detection of photoelecton spectra obtained from cross-correlating the harmonic and the generating pulses in a gas target [131, 132] while others are based on polarization gating or streaking [133]. Similarly, adapting and extending established IR pulse characterization methods has enabled frequency-resolved optical gating (FROG) [134] or spectral phase interferometry for direct electric-field reconstruction (SPIDER) [135] in the EUV. As expected from theoretical investigations, the measured pulse durations vary significantly depending on experimental parameters and harmonic orders [132, 136–138]. For instance, a pulse width of 10 fs was obtained at the 15th harmonic (at ~ 53 nm) for a 40 fs fundamental pulse by means of a ponderomotive streaking method [139], which is in excellent agreement with the pure perturbative expectation. In contrast, an energy-resolved cross-correlation method yielded rather long 60 fs 5th harmonic pulses in comparison to the 80 fs driving pulses at 400 nm [140]. Likewise, pulse durations clearly shorter than perturbatively expected were measured using EUV FROG (10 fs 9th harmonic pulses from 44 fs pulses) [134] and EUV SPIDER (13 fs 11th harmonic pulses from 40 fs pulses) [135]. In the latter experiment, the initially chirped 22 fs harmonic pulses were further compressed using a polarization gating method. Such a (negative) chirp of the generated harmonic pulse intrinsically results from HHG as a consequence of the intensity-dependent dipole phase [130]. It has thus been studied in detail along with potential ways to (pre-)compensate for it [141, 142] which is particularly important for spectroscopic applications.

3.3.3.3 Divergence and beam quality

Among other properties, the usability of high harmonic radiation crucially depends on the divergence and the beam quality because they determine the brightness of the harmonic source according to (2.17). In the typical HHG geometry, the harmonics are emitted collinearly with the driving beam (see Chapter 4 for an alternative geometry). While the divergence that can be obtained from a measurement of the far field angular distribution of the generated light has been found to approach the prediction of lowest order perturbation theory, i.e. $\theta_q = \theta_1/\sqrt{q}$, for harmonic orders near the cutoff [143, 144], the plateau harmonics show a nearly constant divergence [143, 144] that reasonably agrees

with the smaller divergence $\theta_q = \sqrt{p}\,\theta_1/q$ [68] suggested by an effective power law for the harmonic intensity. Most favorably for experimental applications, the generated high harmonic radiation can exhibit near diffraction-limited beam quality ($M^2 \approx 2$ was measured at 55 nm, for example [145]). Additionally, it has been shown that the experimental parameters resulting from an optimization of the conversion efficiency also lead to the best harmonic beam quality so that the highest harmonic flux is obtained at the highest brightness [146].

As mentioned earlier, the radial intensity variation of a Gaussian driving beam causes self-defocusing of the harmonic radiation on account of the intensity-dependent dipole phase. The effect is larger for the long trajectory and manifests itself in a far-field beam profile consisting of a collimated central part from the short trajectory on top of a more divergent pedestal from the long trajectory [147, 148]. This macroscopically observable difference enables the geometrical post-selection of the contribution from a certain quantum orbit for applications. Moreover, it also allows the direct experimental determination of the atomic dipole phase from spatial interferometry [149–151] in contrast to approaches where the phase is inferred from the chirp rate of the harmonics [141, 152].

3.3.3.4 Coherence

The high degree of spatial and temporal coherence of high harmonic radiation is one of its most important properties because it permits its use for optical frequency metrology [51, 153], for diagnostic purposes in the field of EUV lithography, and for time-resolved microscopy with high spatial resolution. While high harmonic radiation would naively be expected to be coherent from purely classical considerations due to the coherence of the driving source and the nonlinear conversion process itself, the semi-classical description of HHG according to the three-step model does not explain the coherence at all. Although a quantum mechanical description remedies this shortcoming, several intrinsic details of the HHG process can potentially limit the coherence: Since contributions to a certain harmonic order can originate from different quantum orbits with different associated intensity-dependent phases and from different half-cycles within a driving laser pulse, minor amplitude noise of the fundamental laser can cause large amplitude and phase noise of the harmonic radiation. At the same time, both spatial and temporal variations of the experimental conditions such as, for example, a refractive index change due to the electron plasma caused by ionization or density fluctuations in the gas target can also be deleterious to the coherence of the harmonic radiation. Several research groups have thus conducted experiments to study the coherence properties of high harmonics (see [95] for a review of results).

The spatial coherence has been investigated by analyzing the fringe visibility of the interference pattern produced by either moving a double slit across the illuminating harmonic beam [154–156] or by a Fresnel-mirror interferometer [157]. Early experiments using a free focusing geometry measured high spatial coherence for a large number of harmonic orders with the general trend of decreasing coherence with increasing order and intensity [154, 155]. The latter was attributed to ionization and possibly intensity-dependent phase effects. Later experiments corroborated this hypothesis and addition-

ally investigated the influence of the target pressure and the focus position with respect to the target [157], thereby confirming earlier theoretical predictions [130]. An extremely high degree of spatial coherence surpassing that achieved in free focusing geometries was found for high harmonic radiation generated under the improved phase-matching conditions provided by a hollow fiber [156].

The temporal coherence of high harmonics has been studied in similar experiments by measuring the fringe visibility of the intereference pattern produced by two spatially separated EUV sources whose driving pulse trains originated from the same laser and had a variable time delay [158–160]. While long coherence times could be deduced from the centers of the interference patterns in good agreement with the expected harmonic pulse durations, spatially separable interference structures were observed in the far field for certain orders. These were attributed to the different contributions from the short and the long trajectory, of which the former showed a high degree of temporal coherence, whereas the latter exhibited a very short coherence time. The observed variations of coherence times as a function of harmonic order and experimental parameters such as laser intensity and longitudinal target position are in good agreement with theoretical predictions of the semi-classical model [161–163].

In terms of spectroscopy, HHG provides a method to transfer frequency comb technology into the extreme ultraviolet because each harmonic order will contain a frequency comb centered about the respective harmonic frequency if the driving laser is a frequency comb and the mutual phase coherence of consecutive pulses is maintained during the generation process. Since the phase noise power spectral density scales as q^2 with harmonic order, which can eventually lead to the so-called carrier collapse beyond some order q, proving the comb structure of the generated EUV radiation has been one of the main challenges since the first realization of table-top high repetition rate EUV sources [8, 9]. The comb coherence was confirmed experimentally for the 3rd harmonic [8] and the 7th harmonic [164] and for the 7th, 13th, and 17th harmonic via direct frequency comb spectroscopy of single photon transitions in atomic Xe, Ar, and Ne, respectively [11, 12]. More recently, the first heterodyning of two EUV frequency combs was reported [165, 166].

3.3.3.5 Conversion efficiency and wavelength scaling

As was detailed above in the section on phase-matching, the achievable overall conversion efficiency of HHG is extremely sensitive to the experimental conditions. In numerous theoretical and experimental studies (e.g. [96, 97, 102, 103, 105, 107, 167–186]), special attention has therefore been paid to the optimization of the high harmonic yield and its dependence on parameters such as the focusing geometry, the shape and the pressure of the target medium, and the beam profile, the pulse duration and the wavelength of the driving laser. The attainable conversion efficiencies also depend on the spectral region of interest: The generation of the shortest wavelengths is only possible with light noble gases due to their higher ionization potential while the recombination cross section and thus the yield is larger for heavier noble gases. Consequently, the highest conversion efficiencies into a single harmonic order, reaching 4.3×10^{-4} [187] for the 11th harmonic ($\sim 73\,\mathrm{nm}$) and about 5×10^{-5} [103, 187, 188] for the 15th harmonic ($\sim 53\,\mathrm{nm}$)

of Ti:sapphire-based sources, have been reported for Xe as a target medium. Higher energy radiation has been generated with decreasing efficiencies ranging from 3×10^{-5} for the 23rd harmonic (35 nm) [96] and 1.5×10^{-5} for the 27th harmonic (29.6 nm) [189] generated in Ar to 5×10^{-7} for the 59th harmonic (13.5 nm) [190, 191] generated in Ne. At multi-MHz repetition rates, the largest conversion efficiencies on the order of 10^{-7} [192,193] have been achieved for the 11th harmonic ($\sim$ 72 nm) using cavity-assisted HHG.

While both experimental and theoretical studies agree that the harmonic yield varies strongly with the wavelength λ_1 of the driving laser, the extracted scaling law for the conversion efficiency, $\propto \lambda_1^{-(5...6)}$, differs depending on which parameters are fixed in the comparisons and whether the considered harmonic orders belong to the plateau or to the cutoff region of the high harmonic spectrum [168, 171, 178, 179, 186, 194–208]. In an attempt to exploit this favorable scaling with wavelength, a femtosecond enhancement cavity for intracavity-HHG using a driving laser in the visible was set up in our group. However, problems arising from a degradation of the cavity mirrors when subjected to high intracavity power levels in a vacuum environment were found to limit the overall performance of the system [209]. Efforts to overcome these limitations are currently under way.

In addition to the general dependences sketched above, the macroscopic harmonic yield is found to show unexpected modulations as a function of laser intensity under certain experimental conditions. These can be attributed to so-called quantum path interferences, which result from a coherent superposition of the contributions of different quantum paths to the overall harmonic signal [164, 210, 211].

3.3.3.6 Polarization

When isotropic media like noble gases are employed as the nonlinear medium for HHG, according to the simple man's model, the driving laser needs to have linear polarization for the active electron to return to the nucleus in the recombination step. In that case, the generated high harmonic radiation is also linearly polarized in the same direction as the driving field, thereby excluding the possibility to separate fundamental and harmonic radiation using a polarization-based scheme. Studies of the influence of varying degrees of ellipticity of the driving laser indeed reveal that the high harmonic yield decreases substantially for ellipticities on the level of a few percent [194,212–214]. However, several different schemes based on elliptic driving pulses and proper combinations thereof have been proposed and realized to generate high harmonic radiation with an adjustable elliptic polarization (see, for instance, [215] and references therein). In that context, it was also realized by Corkum and co-workers that the polarization dependence of HHG can be used as a so-called gating mechanism. Such a polarization gate, implemented by overlapping two fundamental pulses with elliptic or circular polarization in a suitable way, limits efficient high harmonic generation to the narrow temporal window in which the resulting driving polarization is linear. If this temporal window is adjusted to be shorter than one cycle of the fundamental field, only a single burst of high harmonic radiation, commonly denoted an isolated attosecond pulse, will be emitted [213]. The

following section attempts to provide an ultra-brief synopsis of the vast field of attosecond pulses.

3.3.3.7 Attosecond pulses

Extending an earlier idea of Hänsch [216] who had suggested the Fourier synthesis of sub-femtosecond pulse trains via nonlinear phase sychronisation of several cw lasers operating at equidistant frequencies, the intrinsic potential of high harmonic generation and its periodic spectrum as a means to provide attosecond pulse trains was first realized by Farkas and Tóth [217] and Harris, Macklin, and Hänsch [218]. Similar to mode-locking theory, the fundamental requirement is that different harmonic orders have comparable amplitudes and are locked in phase. While the plateau in the high harmonic spectrum assures the former in most instances, the latter requirement cannot easily be fulfilled on a single atom level without trajectory selection [219]. However, it was shown theoretically that sufficiently robust experimental conditions for the generation of several phase-locked harmonics from the contributions of a single trajectory exist [219,220]. The first experimental observation of a train of attosecond pulses was reported by Paul et al. [221] who reconstructed 250 as pulses from measured data. The achievable pulse duration should, in principle, become shorter when the number of contributing phase-locked harmonics rises. However, there exists an optimum number of contributing harmonic orders beyond which the duration of the attosecond pulses increases because the chirp resulting from the HHG process leads to a frequency-dependent phase-difference between adjacent harmonic orders [222].

The earliest proposed schemes for the generation of isolated attosecond pulses (IAPs) either relied on polarization gating of many-cycle pulses [213], as mentioned above, or on selective filtering of the continuous part of the high harmonic spectrum that is produced near the cutoff when using few-cycle driving pulses [223–225]. It was not until 2001 that Hentschel and co-workers [226] experimentally demonstrated an isolated 650 as pulse centered at about 90 eV for the first time. There have been strong experimental efforts to push the achievable pulse durations towards the atomic unit of time (~ 24 as) which seems within reach given the current records for the shortest IAPs (~ 80 as [227] and 67 fs [228]). To generate IAPs with experimentally less challenging longer fundamental pulses, different gating mechanisms have been proposed and realized (see [229] for a review). A recent proposal [230] discussed a scheme that is based on a spatiotemporal coupling of the fundamental laser beam and should allow to resolve the individual pulses of the generated attosecond pulse train angularly. This more universal method, termed "attosecond lighthouse" because of the angular separation of the attosecond pulses, was recently demonstrated in an experiment involving HHG from a solid target [231]. As will be discussed briefly in Chapter 4, a non-collinear geometry for the generation of high harmonics, which was investigated in detail in the course of this thesis, may be well-suited to implement a similar technique .

Further and more detailed information on attosecond physics can be found in respective reviews and books [70–73, 232, 233].

3.3.3.8 Multi-color driving fields

Since the first observation of HHG, there has been a strong interest in how a multi-color fundamental field affects the generated high harmonic radiation and in how it can potentially be used to optimize the harmonic yield (see, e.g., [194,234–238] and references therein). One striking result of the investigations concerning this matter, which were mostly done with combinations of commensurate frequencies such as ω_1 and $2\omega_1$ due to experimental convenience, is the occurence of even harmonics of ω_1 in the spectrum. Compared to the case of a single-color driving field, for which the HHG process repeats itself symmetrically twice per laser period (cf. Section 3.2.1), the addition of a weak field of different color is sufficient to break this inherent symmetry so that high harmonic emission can happen only once per cycle. In the frequency domain, this periodicity leads to a spacing of the harmonic orders by ω_1. An attractive effect of a multi-color driving field is that the conversion efficiency[13] can be orders of magnitude larger than in the single-color case because of an enhanced, but not yet detrimental ionization rate and a favorable alteration of the contributing trajectories. For example, Kim et al. reported a conversion efficiency as high as 5×10^{-5} for the 38th harmonic (21.6 nm) generated in He [237] when using a bichromatic driving field.

[13] The most unambiguous definition of conversion efficiency in the multi-color case is, of course, to relate the generated high harmonic power to the total driving power incident on the gas target. However, it is advisable to check the exact definitions used when comparing numbers from the literature.

3.4 Practical considerations

Due to the limited average power of currently available laser systems providing ultrashort pulses, high harmonic generation is most commonly driven at pulse repetition frequencies in the kHz range or below. At these comparably low repetition rates, even moderate average powers result in pulse energies on the mJ-level and above, which are sufficiently high to reach the required threshold intensities for HHG (cf. (3.24)) using rather relaxed focusing conditions. That way, the geometric phase mismatch is minimized while the confocal parameter and thus the potential interaction volume and the high harmonic yield are simultaneously maximized.

If the repetiton rate is to be increased by three or more orders of magnitude to the multi-MHz regime, an according boost in average power will be required to obtain the same peak power for otherwise unchanged laser parameters so that the same focusing geometry can be used. However, current laser technology is not capable of providing these extreme average powers on the order of kW in pulses with extremely short durations due to the damage thresholds of the employed gain materials.

The emergence of cavity-assisted high harmonic generation, i.e., driving the HHG process inside a passive external enhancement resonator that can boost the average power of the driving laser by factors exceeding 1000, has enabled the successful realization of EUV sources at repetiton rates of more than 100 MHz [8, 9, 164, 209]. Nevertheless, the achievable fundamental peak powers still necessitate tighter focusing into the gas target than required at kHz repetition rates. The same is true for the latest state-of-the-art solid state and fiber laser systems whose output powers are approaching the kW-level [239,240], however, at the expense of longer pulse durations and not diffraction-limited beam quality so that tight focusing remains mandatory for HHG.

The following subsections therefore present some practical considerations for the experimentally realistic case that a certain harmonic order shall be generated efficiently at a very high repetition rate with a laser system whose peak power makes a comparably tight focus necessary. Although it is fairly impossible to estimate the harmonic yield in a simple way because the details of phase-matching cannot be fully captured without a numerical simulation, some general insight can be gained concerning the required focusing and the associated level of ionization at the resulting intensity as a function of both the wavelength and the pulse duration of the driving laser and the choice of the target gas.

3.4.1 Threshold volume

For a Gaussian laser beam with peak power P_p focused to a certain peak intensity I_0, the threshold intensity $I_{th}(q)$ limits the spatial extent of the interaction region in which $I \geq I_{th}(q)$ so that the respective (non-perturbative) qth harmonic can be generated. On axis, $I_{th}(q)$ is reached in the symmetric interval $\{-0.5L_{th}(q), 0.5L_{th}(q)\}$ around the laser focus with

$$L_{th}(q) = b\sqrt{\frac{I_0}{I_{th}(q)} - 1} \tag{3.33}$$

which becomes equal to the confocal parameter b when the peak intensity I_0 of the laser is twice as high as the threshold intensity of the harmonic order under consideration. The transversal threshold radius

$$w_{th}(z,q) = w_0\sqrt{\frac{1+(\frac{2z}{b})^2}{2}\ln\left(\frac{I_0}{\left(1+(\frac{2z}{b})^2\right)I_{th}(q)}\right)} \tag{3.34}$$

also depends on the longitudinal distance from the focus and reaches a maximal value

$$w_{max}(q) = w_{th}(z=0,q) = w_0\sqrt{\frac{1}{2}\ln\left(\frac{I_0}{I_{th}(q)}\right)} \tag{3.35}$$

at the focus. Using (3.33) and (3.34), the volume in which the laser intensity exceeds the threshold intensity $I_{th}(q)$, henceforth denoted threshold volume, can be approximated from the integration of $\pi w_{th}^2(z,q)$ over a distance $L_{th}(q)$ across the laser focus by

$$V_{th}(q) \simeq \frac{1}{18}\lambda\, b^2\left[\sqrt{\frac{I_0}{I_{th}(q)}-1}\left(5+\frac{I_0}{I_{th}(q)}\right) - 6\arctan\left(\sqrt{\frac{I_0}{I_{th}(q)}-1}\right)\right]. \tag{3.36}$$

Since the maximally available peak power P_p is determined by the usually fixed pulse energy W_P and pulse duration τ of the available laser system, (2.34) yields an upper limit

$$b_{th}(q) = \frac{4P_p}{\lambda I_{th}(q)} \tag{3.37}$$

for the experimentally adjustable confocal parameter and hence for the threshold volume. Note that for a focusing geometry corresponding to a confocal parameter $b_{th}(q)$, the threshold intensity is just reached at a single point (on-axis at the focus) so that even tighter focusing is necessary to obtain a finite threshold volume.

Since (3.36) is only valid for $b \leq b_{th}(q)$, it can be rewritten in terms of the quantity $b_q = b/b_{th}(q)$ to obtain the normalized threshold volume

$$V_q \propto b_q^2\left[\sqrt{\frac{1}{b_q}-1}\left(5+\frac{1}{b_q}\right) - 6\arctan\left(\sqrt{\frac{1}{b_q}-1}\right)\right] \tag{3.38}$$

which is plotted in Figure 3.4 and shows a clear optimum at $b_q \simeq 0.363$ corresponding to a peak intensity of $I_0 \simeq 2.75 I_{th}(q)$. It is obvious that lasers with high peak powers allow weaker focusing and accordingly larger confocal parameters to reach I_{th} than lasers with lower peak powers, i.e. the absolute size of the threshold volume depends on the laser parameters. If those are fixed, the purely geometric considerations presented above yield a condition to maximize the potential generation volume of a specific harmonic order q.

It is, however, important to realize that while the threshold intensity $I_{th}(q)$ is a physically meaningful parameter because the generation of the desired harmonic order can be expected once the focused peak intensity of the driving laser exceeds it, the physical

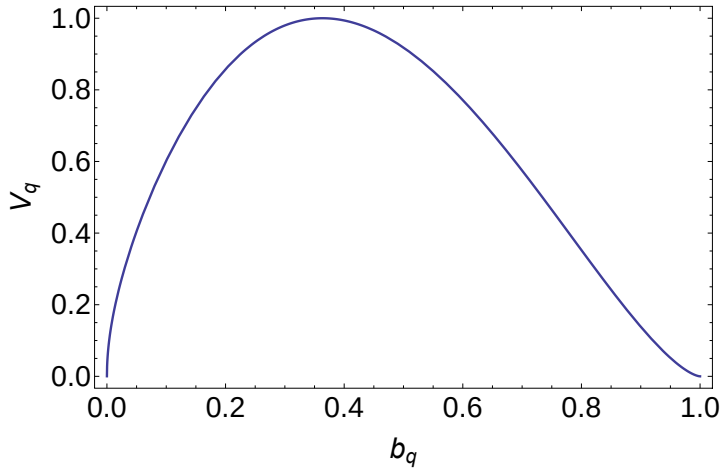

Figure 3.4: *Normalized threshold volume V_q as a function of normalized confocal parameter b_q. The maximum value is obtained at $b_q \simeq 0.363$ which corresponds to a peak intensity of $I_0 \simeq 2.75 I_{th}(q)$.*

significance of the maximum threshold volume is limited. There are two main reasons for that: Firstly, the spatial intensity distribution of a Gaussian laser beam within the threshold volume is not homogeneous (and additionally time-dependent) so that a higher yield may be obtained from a considerably smaller interaction volume than the maximum threshold volume because of the highly nonlinear intensity-dependence of the dipole response. Secondly, since phase matching eventually determines the effective interaction volume, the latter can be significantly smaller than the maximum threshold volume. Therefore, focusing to $2.75 I_{th}(q)$ should just be considered as a good starting point for further experimental investigations. In practice, modifications of the focusing conditions can be more easily realized for a single pass than for a cavity-assisted HHG experiment because a simultaneous readjustment of the resonator is required in the latter to maintain the enhancement.

Apart from the varying threshold volume, an important consequence of adjusting the confocal parameter and thus the peak intensity is the change of the level of ionization that will be discussed in the following.

3.4.2 Ionization in different gases for various laser parameters

As already mentioned before, the generation of a certain harmonic order q is always connected with an unavoidable degree of ionization which may form a significant contribution to phase matching due to the dispersion of the generated free electrons. It is therefore instructive to calculate the resulting level of ionization for a variety of laser parameters under the assumption that harmonic radiation at a certain wavelength is to be produced in different noble gases.

For obvious reasons, the particular target wavelength chosen for the following discussion is $\sim 60.8\,\mathrm{nm}$, the one required to excite the 1s-2s two-photon transition in He^+. Light at this wavelength can, for example, be generated as the 17th harmonic of an

	547 nm ($q^* = 9$)	**790 nm** ($q^* = 13$)	**1030 nm** ($q^* = 17$)	I_{BSI}
Xe	9.3	4.5	2.7	8.7
Kr	7.2	3.5	2.1	15.4
Ar	5.2	2.5	1.5	24.7

Table 3.2: *Threshold intensities $I_{th}(q^*)$ for the generation of $\sim 60.8\,\mathrm{nm}$ radiation in different noble gases from different fundamental wavelengths according to (3.24) in units of $10^{13}\,\mathrm{W/cm^2}$. The barrier suppression intensity I_{BSI} (see Section 3.2.1) is also listed for comparison.*

Yb-based laser emitting at a center wavelength of about 1030 nm, as the 13th harmonic of a Ti:Sapphire laser operating at $\sim 790\,\mathrm{nm}$, or as the 9th harmonic of an optical parametric amplifier tuned to $\sim 547\,\mathrm{nm}$. The respective threshold intensities depend both on the driving laser wavelength and the target gas and are summarized in Table 3.2 for the above laser systems and the noble gases xenon (Xe), krypton (Kr), and argon (Ar). While the barrier suppression intensity (see Section 3.2.1) is also listed for comparison, the noble gas neon (Ne) is omitted in the table because the chosen target wavelength corresponds to a below-threshold harmonic for which (3.24) and hence the threshold intensity concept is not valid.[14]

Since ionization depends on the pulse duration, an intensity range starting at the individual threshold intensities is considered for a set of four representative pulse durations, namely 10 fs, 35 fs, 100 fs, and 680 fs. Pulses of the latter duration are provided by the Yb:YAG-based Innoslab amplifier that was employed for the single pass HHG experiments presented in Chapter 5. As will be described there, the pulses have been used both uncompressed and nonlinearly compressed to about 35 fs which explains the choice of the first two pulse durations. The additional pulse widths considered in the comparison are picked as complementing examples of typical pulses used in HHG experiments.

The results presented below have been calculated employing the Yudin-Ivanov ionization model [76] because the widely used ADK rate underestimates the degree of ionization produced in the considered transient intensity regime of Keldysh parameters $\gamma_K \approx 1$ that is typical of HHG at multi-MHz repetition rates. Note that in the following discussion, certain parameters have been fixed to experimentally reasonable values in order to simplify the presentation.

3.4.2.1 Ionization at fixed intensity and driving wavelength

As a first example, Figure 3.5 depicts a comparison of the fraction of ionization caused in xenon (solid magenta), krypton (dashed blue), argon (dash-dotted red), and neon (dotted green) by a single pulse of either 680 fs or 35 fs duration. The results are obtained for pulses with a center wavelength of 1030 nm that are focused to an intensity of

[14] Ionization rates can also be calculated for the generation of the desired radiation as a below-threshold harmonic in Ne. However, this does not harm or restrict any of the discussions of general trends presented here.

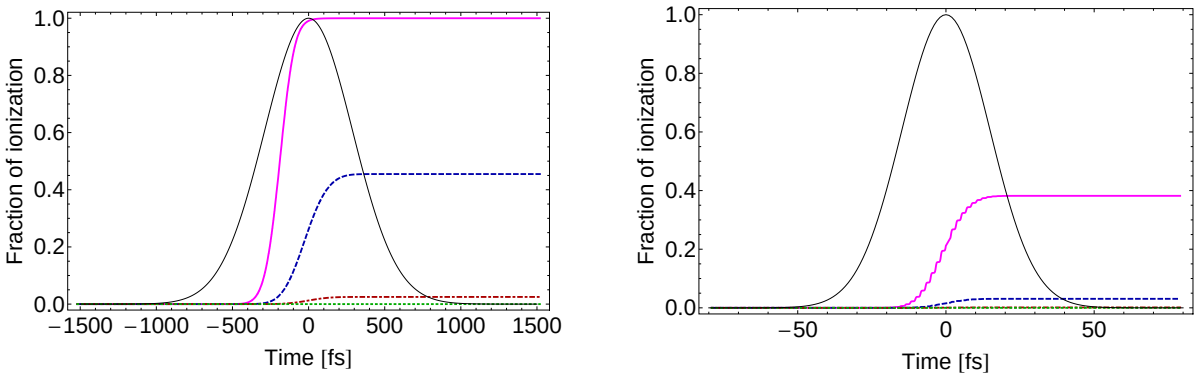

(a) *680 fs pulse* **(b)** *35 fs pulse*

Figure 3.5: *Comparison of the fraction of ionization of xenon (solid magenta), krypton (dashed blue), argon (dash-dotted red), and neon (dotted green) subject to a single (a)* 680 fs *and a single (b)* 35 fs *pulse at the same peak intensity of* $7.3 \times 10^{13}\,\mathrm{W/cm^2}$ *which corresponds to* $2.75I_{th}$ *for the generation of the 17th harmonic in Xe with a driving wavelength of* 1030 nm. *The normalized pulse envelope is shown as a thin solid black line for reference. (a) While Xe is fully ionized at the pulse peak, the degree of ionization after the passage of the pulse reaches about 45% in Kr, about 3% in Ar, and practically zero in Ne. (b) The level of ionization is reduced to less than 40% in Xe, less than 5% in Kr, and about zero for Ar and Ne.*

$7.3 \times 10^{13}\,\mathrm{W/cm^2}$, which corresponds to $2.75I_{th}(17)$ for Xe at 1030 nm. When subject to the 680 fs pulse (Figure 3.5a), Xe is already fully ionized at the pulse peak whereas the degree of ionization after the passage of the pulse reaches about 45% in Kr, about 3% in Ar, and practically zero in Ne. As illustrated in Figure 3.5b, the level of ionization is significantly reduced to less than 40% in Xe, less than 5% in Kr, and about zero for Ar and Ne for a 35 fs pulse with the same peak intensity.

Without consideration of the different recombination cross sections of the noble gases, this comparison for a given focusing geometry and peak intensity emphasizes two things: (i) It may be advantageous to use shorter pulses and lighter noble gases for HHG because the lower plasma dispersion from the free electrons can be compensated by the neutral atom dispersion more easily or at all. (ii) Depletion of the ground state is less significant for shorter pulses so that there are more neutral atoms left to contribute to HHG, particularly after the temporal peak of the pulse when the intensity still exceeds the threshold intensity (as long as plasma defocusing is neglected).

3.4.2.2 Ionization for different driving wavelengths

Figure 3.6 shows the fraction of ionization at $2.75I_{th}(q^*)$, where q^* denotes the respective harmonic order required to reach the target wavelength of ~ 60.8 nm, caused in Xe, Kr, and Ar by pulses at three different center wavelengths for the same pulse durations as in Figure 3.5.

As can bee seen in Figure 3.6a, the high threshold intensities at 547 nm result in complete ionization of all gases directly after the 680 fs pulse. At 790 nm, ionization is

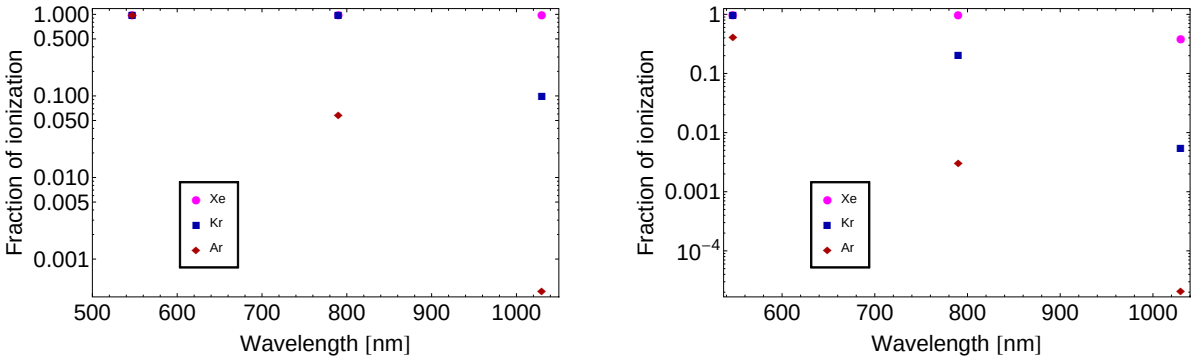

(a) *680 fs pulse* **(b)** *35 fs pulse*

Figure 3.6: *Fraction of ionization caused in Xe, Kr, and Ar by single (a)* 680 fs *and (b)* 35 fs *pulses at three different center wavelengths of* 547 nm, 790 nm, *and* 1030 nm *at 2.75 times the respective threshold intensities for the generation of* $\sim$ 60.8 nm *radiation in the different noble gases. The level of ionization caused by the long pulses (a) is only different from 100% for Kr and Ar at* 1030 nm *and for Ar at* 790 nm.

only different from 100% in Ar, which has the highest ionization potential of the three considered noble gases, and amounts to about 5%. At 1030 nm, switching from Xe to Kr and Ar drastically reduces the corresponding level of ionization from 100% to 10% and below 0.1%, respectively. The same trend, that is, a lower fraction of ionization for larger U_I and longer λ_1 also holds in an even more pronounced way for the 35 fs pulse as becomes obvious from Figure 3.6b. When a driving laser at 1030 nm is employed, the per pulse ionizations amount to below 1% except in the case of Xe, for which the ionized fraction is about 40%. At the Ti:sapphire wavelength, Xe is fully ionized whereas Kr and Ar exhibit reduced ionization levels of about 20% and 0.3%, respectively. The visible laser causes complete ionization but in the case of Ar where ionization reaches 40%.

Assuming the same relative peak intensities of $2.75 I_{th}(q^*)$, the fraction of ionization is depicted for Xe (Figure 3.7a), Kr (Figure 3.7b), and Ar (Figure 3.7b) separately for the same three driving wavelengths and two additional pulse durations. It becomes very obvious that the generation of 60.8 nm light from the short wavelength driver at this intensity will be accompanied by full ionization after the pulse if the target medium is Xe or Kr whereas using Ar leads to less than 50% ionization for the sub-50 fs pulses. A Ti:sapphire driving laser system will cause strong ionization in Xe while allowing HHG at ionization levels below 50% for all but the 680 fs pulse in Kr and below 10% in Ar, thus promising relaxed phase matching conditions for the generation of 60.8 nm light. As expected, the longest driving wavelength causes the least amount of ionization in all gases and is thus most promising in terms of phase matching.

Note that the nearly complete ionization of the more efficient noble gases Xe and Kr at the end of a single 547 nm pulse does not necessarily prevent the generation of the desired harmonic order during the pulse as long as there are neutral atoms left before the threshold intensity is reached. Consequently, since the conversion efficiency of HHG scales with $\lambda_1^{-(5...6)}$ (cf. Section 3.3.3.5), the overall yield can still be reasonably high for

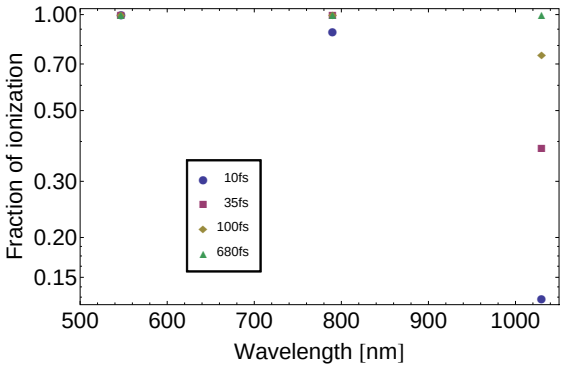

(a) *Xe*

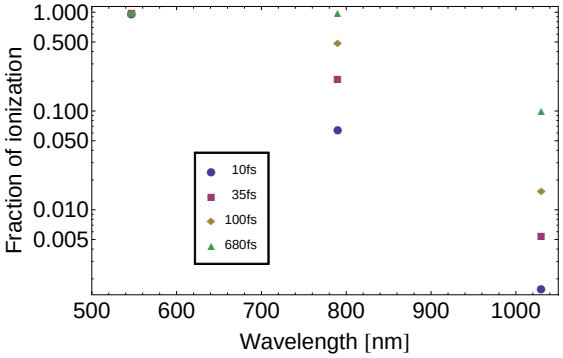

(b) *Kr*

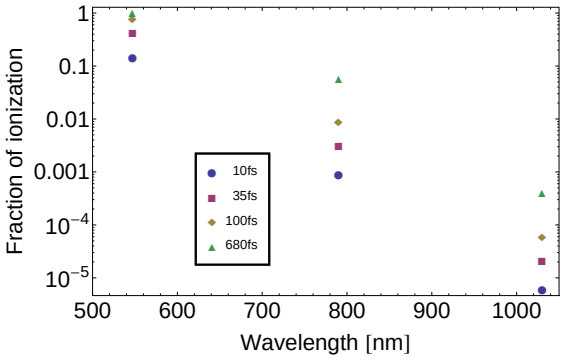

(c) *Ar*

Figure 3.7: *Fraction of ionization caused in (a) Xe, (b) Kr, and (c) Ar after single* 10 fs, 35 fs, 100 fs, *and* 680 fs *pulses at three different center wavelengths of* 547 nm, 790 nm, *and* 1030 nm *at 2.75 times the respective threshold intensities for the generation of* $\sim$ 60.8 nm *radiation in the different noble gases.*

a short wavelength driving laser even in the extreme case of full depletion of the target medium after the pulse as shown by Ditmire et al. by loosely focusing a high energy laser into neon [171]. However, once the repetition rate reaches the regime in which the target atoms cannot be replaced efficiently before the next laser pulse is incident, the yield is expected to drop significantly because there are effectively no neutral atoms left for HHG.

3.4.2.3 Ionization as a function of intensity

The intensity level that has been considered so far was $2.75 I_{th}(q^*)$ which maximizes the geometric threshold volume. To illustrate the highly nonlinear intensity-dependence, Figure 3.8 presents the level of ionization in Xe and Kr for a 1030 nm driving laser and different pulse durations as a function of intensity. Again, Xe is seen to be very likely ionized with increasing intensity whereas Kr remains almost neutral in the covered intensity range for all considered pulses but the 680 fs one which cause up to 10% ionization.

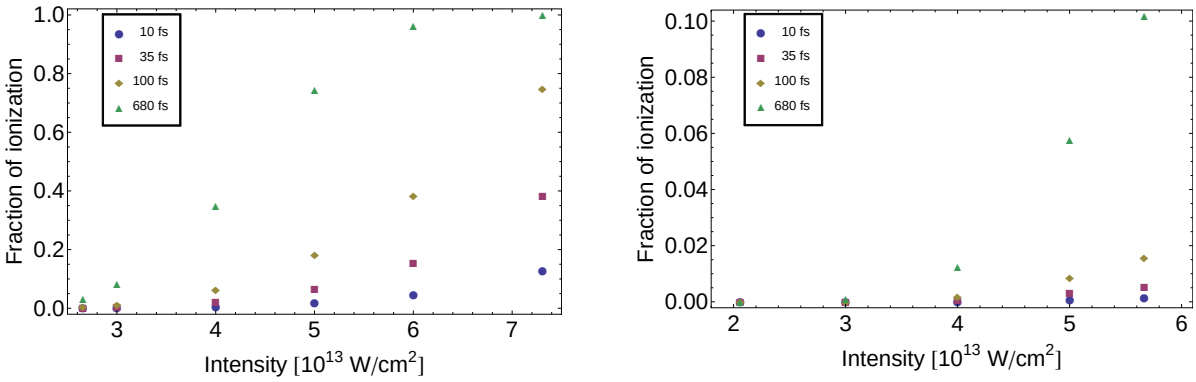

(a) *Xe* **(b)** *Kr*

Figure 3.8: *Ionization in (a) Xe and (b) Kr caused by a* 1030 nm *driving laser with* 10 fs, 35 fs, 100 fs *and* 680 fs *pulses at different intensities between (gas-specific)* $I_{th}(q = 17)$ *and* $2.75I_{th}(q = 17)$ *(compare Table 3.2). While the fraction of ionization becomes quite significant in Xe with increasing intensity even for the* 10 fs *pulse, the degree of ionization in Kr is less than 2% even at* $2.75I_{th}$ *for all pulses except the* 680 fs *one which causes 10% ionization.*

All ionization levels presented so far were calculated for the passage of a single pulse. At repetition rates in the multi-MHz regime, additional plasma effects arise because the target atoms cannot be exchanged at a sufficiently high rate (i.e. within nanoseconds) so that the same target atom experiences several successive pulses. Consequently, some residual degree of ionization exceeding the one predicted by single pulse ionization rates remains on average. This background plasma may cause deleterious phase shifts and instabilities in femtosecond enhancement cavities used for cavity-assisted HHG [17, 18, 241] and thus severely constrain the achievable enhancement (particularly due to the reduced spectral overlap of the seed laser and the spectrally blueshifted fundamental inside the resonator). For single pass HHG, the main effect of the higher plasma density is that it aggravates phase matching.

From the comparisons of ionization levels presented in this section and the discussion of phase matching in Section 3.3.1, it can be concluded that higher gas pressures are required for phase matching when heavier and more efficient noble gases are to be used as the target medium because they ionize more quickly and hence cause a higher free electron plasma density at the same laser parameters. Finding the optimum balance between a strong dipole response, which profits from higher intensity, and good phase matching, which becomes increasingly difficult at higher levels of ionization and thus at higher intensities, is a challenging and intricate task for itself. In addition, technical constraints due to the finite pumping speed of available vacuum pumps may come into play. From a technical point of view, it is therefore desirable to generate high harmonics at the lowest possible target pressure to reduce the gas load on the vacuum system.

3.4.3 Gas target

The necessity of tight focusing geometries for HHG at multi-MHz repetition rates poses an important constraint on viable gas target designs because the gas distribution has to be extemely localized to avoid reabsorption of the generated harmonic radiation within the target, particularly when high phase matching pressures are needed. There are three different generic designs that have been commonly used in experiments for unguided HHG: So-called through-nozzles typically consist of a thin, end-sealed metal tube or glass capillary from which the gas exits along the axis of propagation of the driving beam through small (often laser-drilled) holes. To minimize this collinear extension of the target, one can alternatively use metal needles or glass capillaries from which the target gas freely expands into the vacuum orthogonally to the laser beam. These nozzles, sometimes denoted "end-fire nozzles" [193, 241], produce transsonic gas jets with rather localized gas density profiles. Gas cells, which have predominantly been used in combination with large laser confocal parameters at low repetition rates, form the third generic design. Since such a cell basically merges into a through nozzle when its dimensions are adapted to small confocal parameters, this design will not be discussed here further.

The main advantage of the through-nozzle geometry is that the density distribution of the target gas inside it is rather homogeneous and allows suitably high interaction pressures, which are known in good approximation from the backing pressure in the gas supply line, at low background pressures in the vacuum chamber. While it is comparably easy to align the through-nozzle because the laser beam has to be guided through it, the gas effuses from the nozzle in the direction of propagation of the laser. This can be disadvantageous because it leads to a larger spatial extent of the target and thus higher absorption of the generated harmonics in it. Furthermore, the gas exchange rate is lower than for an end-fire nozzle which leads to plasma accumulation near the laser focus and hence limits the usage of that nozzle type in cavity-assisted HHG [241].

End-fire nozzles are much harder to align in practice but produce very localized gas jets, thereby minimizing absorption along the laser propagation axis. In addition, since the gas propagates at trans- and supersonic speed, it is exchanged faster than in a through nozzle so that the influence of plasma accumulation at repetition rates on the MHz-level is mitigated. The main disadvantage of the end-fire geometry is that the density distribution of the freely expanding gas varies strongly as a function of position which makes it very challenging to estimate actual interaction pressures in an experiment and requires a much higher gas intake into the vacuum chamber than for a through nozzle.

The single pass HHG experiments described in Chapter 5 were performed using end-fire nozzles. Since the gas density seen by the laser beam is an important parameter for phase matching, the density profiles produced by end-fire nozzles shall be briefly reviewed in the following. While the full description of a supersonic expansion of a real compressible gas from a pressurized nozzle into a vacuum chamber requires numerical methods and simulations that are, for example, available in the field of computational fluid dynamics (CFD), a lot of general insight can be gained studying the one-dimensional

adiabatic expansion of an ideal gas into vacuum which can be described analytically. The ideal gas equation

$$p = \rho R_s T \tag{3.39}$$

links pressure p, (mass) density ρ, and temperature T of the gas via the specific gas constant $R_s = \frac{R}{m_m}$, where R and m_m are the universal gas constant and the molar mass of the gas, respectively. It is thus sufficient to know two quantities, e.g. temperature and pressure, initially to fully characterize the behavior of the gas. The gas flow directly at the interface between nozzle and vacuum will always be sonic irrespective of the residual background pressure p_b in the vacuum chamber if the ratio of initial pressure p_0 to background pressure p_b is larger than $((\gamma+1)\gamma^{-1})^{\gamma(\gamma-1)^{-1}}$ where $\gamma = \frac{C_p}{C_V}$ is given by the ratio of the (specific) heat capacities at constant pressure and volume, respectively. From equating the speed of sound $c_s = \sqrt{\gamma R_s T}$ with the speed of the gas $U = \sqrt{2C_p(T_0 - T)}$ that can be derived from thermodynamics under the assumption of constant $C_p = \frac{\gamma}{\gamma-1}R_s$ one gets

$$\frac{T}{T_0} = \left(1 + \frac{\gamma-1}{2}M^2\right)^{-1} \tag{3.40a}$$

$$\frac{p}{p_0} = \left(1 + \frac{\gamma-1}{2}M^2\right)^{\frac{\gamma}{\gamma-1}} \tag{3.40b}$$

$$\frac{\rho}{\rho_0} = \left(1 + \frac{\gamma-1}{2}M^2\right)^{\frac{1}{\gamma-1}} \tag{3.40c}$$

where the Mach number $M = \frac{U}{c_s}$ has been introduced. Since the flow is underexpanded due to the pressure difference between nozzle and vacuum chamber, the velocity of the gas has to increase during the expansion to fulfill the continuity equation $\dot{m} = \rho U A$ that requires constant mass flow $\dot{m}$ through unit area A. Consequently, the Mach number M increases with increasing distance from the nozzle outlet. In good approximation, the occurrence of shocks in the flow that abruptly terminate the increase in gas velocity to meet the external pressure conditions can be neglected here because the ratio of nozzle and background pressure usually amounts to several orders of magnitude in typical HHG experiments so that the gas reaches the free molecular flow regime after a distance smaller than that for the Mach disk shock.

As mentioned above, real gas jets require a 3d numerical analysis. However, it is possible to fit analytical formulas to these results to approximate the behavior of the flow. Using the closed form approximations given in [242], the pressure drop normalized to the backing pressure along the centerline of end-fire nozzles with different orifice diameters is shown in Figure 3.9 as a function of distance from the outlet for monoatomic gases ($\gamma = \frac{5}{3}$) such as the noble gases. In agreement with full CFD simulations [193, 241], the figure reveals that at a finite distance from the nozzle orifice, higher gas densities are reached for larger diameter nozzles. However, moving the driving laser beam very close to the nozzle to exploit the high gas densities there may lead to irreversible and uncontrolled damage of the nozzle. Hence, using nozzles with bigger orifices than required to match the threshold volume is expected to be beneficial as long as the larger spatial extent of

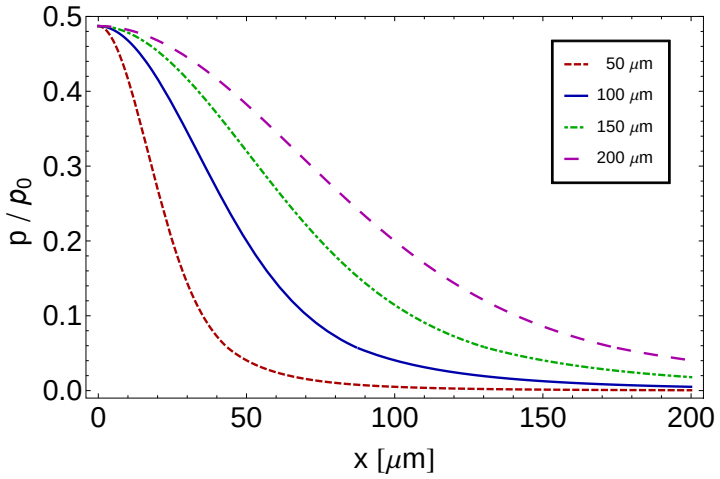

Figure 3.9: *Evolution of ratio between local pressure p and backing pressure p_0 as a function of distance from the nozzle orifice along the centerline of nozzles with different orifice diameters.*

the gas jet along the propagation axis of the laser beam remains small enough not to absorb the generated harmonics. Again, careful experimental optimization of the target parameters is required.

The high gas intake into the vacuum chamber can be mitigated by additional gas catch assemblies. If these are located in direct proximity to the target and connected to a roughing pump, they reduce the load on the (turbomolecular) pumps attached to the vacuum chamber and hence minimize absorption of the generated harmonic radiation upon propagation in the chamber. The efficient implementation of such a gas trap has been reported [243].

4 Non-collinear high harmonic generation (NCHHG)

This chapter reports on the results of a detailed experimental and numerical investigation of non-collinear high harmonic generation (NCHHG). In particular, we will show that the non-collinear geometry allows a time-resolved analysis of how a temporally varying, spatially modulated driving field affects the spatial emission pattern of the generated high harmonic radiation. That way, NCHHG provides partial access to the microscopic high harmonic response. Experimental results will be compared both to a numerical simulation based on a simple Fraunhofer diffraction dipole model and to a full numerical simulation within the strong field approximation. The potential application of NCHHG for the generation of spatially detached isolated attosecond pulses will be discussed.

4.1 Introduction

The experimental geometry that has been used in the majority of high harmonic generation experiments is the collinear one illustrated in Figure 4.1a: A strong driving laser is focused into a gas target behind which the unconverted fundamental light and the generated high harmonic radiation propagate collinearly so that their separation requires some additional optical element such as a grating or a beam splitter.

In contrast, when adopting the non-collinear geometry depicted in Figure 4.1b for HHG, collimated emission of high harmonic radiation along the bisector of the two driving beams overlapping in the generating medium can be expected[1]. Therefore, non-

[1] In fact, once the gas target in Figure 4.1b is replaced by a nonlinear crystal, the figure illustrates the background-free mode of operation of an optical autocorrelator.

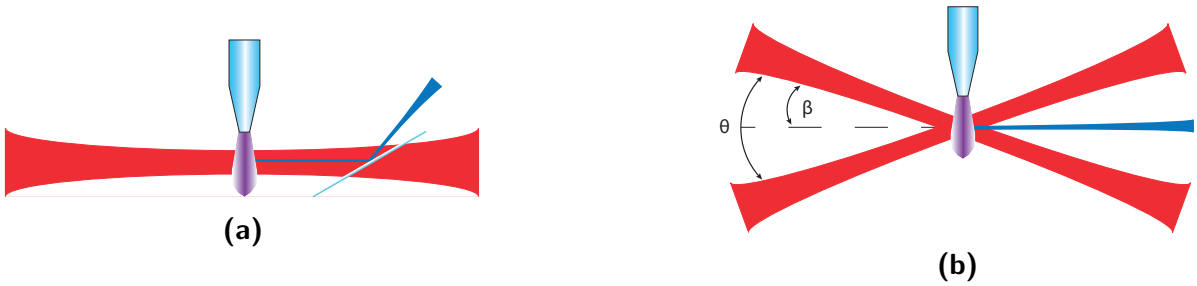

Figure 4.1: *Sketch of generic high harmonic generation geometries: (a) collinear HHG, (b) non-collinear HHG*

collinear high harmonic generation (NCHHG) holds the intrinsic potential to allow the generation of EUV radiation that is spatially separated from the strong fundamental beams. For exactly that reason, a very related non-collinear geometry was already used in HHG experiments with a single fundamental beam whose central part had been blocked before focusing into the target. Since the intensity distribution of the resulting annular driving beam has an on-axis maximum at the focus, the generated harmonics propagate on axis and can be isolated by an aperture placed at the position of the image of the annular beam block behind the focus [244].

First theoretical studies of NCHHG with two independent driving beams were done by Birulin and co-workers in 1996 for beams intersecting at angles close to zero and 180° [112,245]. Non-collinear HHG geometries, in which the driving beams were focused to very close, yet spatially separated positions in the target were used to study the temporal coherence of the generated radiation [159] and to measure the high harmonic dipole phase [149,150]. To our knowledge, interest in NCHHG with a common focus as illustrated in Figure 4.1b did not rekindle until 2002, when Fomichev and co-workers [246] reported results of both a numerical simulation of NCHHG for various non-collinear angles and an experimental investigation. For the latter, a mask with two narrow slits was placed in front of the focusing optics to create two non-collinearly interacting, yet not independently controllable driving beams. From their studies of the far field emission pattern of the generated high harmonic radiation, the authors of [246] concluded that the strength and the direction of high harmonic emission was strongly dependent on the non-collinear angle. Recent experimental work on NCHHG in a two-color experiment focused on a demonstration of the nonlinear optical wave mixing characteristics of NCHHG and their description in a pertubative theoretical framework [247].

Our interest in NCHHG was motivated by its potential application as a combined generation and outcoupling method in cavity-assisted HHG [14]. Stimulated by numerical results obtained by Wu and Zeng, who found that cavity-assisted high harmonic generation was possible in a non-collinear geometry [248], we started an experimental investigation of NCHHG with two independently adjustable driving beams produced by a chirped pulse amplification (CPA) laser system. After the initial proof-of-principle experiments, however, the focus of our work was diverted towards a more detailed analysis of the NCHHG process itself by the phenomena observed in the course of the studies.

The following section recapitulates the motivation for and the results of our initial experiments on NCHHG. After that, important aspects of the non-collinear geometry are emphasized before our experimental setup and the applied methods are introduced. Subsequently, a detailed investigation of the dependence of the high harmonic spatial far field emission profile on the delay between the driving pulses is presented and discussed in comparison with numerical results.

4.2 Application to cavity-assisted HHG

As sketched in the introduction, typical collinear HHG geometries necessitate the use of an additional optical element to separate fundamental and the generated harmonics. The efficient separation, which is required or at least beneficial for applications, can be a rather challenging task: Typical conversion efficiencies are rather low ($\sim 10^{-6}$ or below, see Section 3.3.3.5) so that the power ratio of fundamental and EUV is usually rather large. In addition, the simplest polarization-based schemes cannot be used because the directions of polarization of fundamental and harmonic radiation are the same.

In particular, in cavity-assisted high harmonic generation, some mechanism to extract the generated EUV radiation from the resonator is required because it would otherwise be absorbed completely by the cavity mirrors. To this end, in the first demonstrations of cavity-assisted HHG [8, 9, 249], a thin plate made of sapphire was placed inside the enhancement resonator at Brewster's angle for the fundamental beam (see Figure 4.1a). However, while this approach was successful in the sense that a fraction of the generated high harmonic radiation could be extracted due total external reflection at the Brewster plate, it brings about several limitations: The reflectivity of such a Brewster plate depends strongly on the material and on the wavelength of the radiation to be outcoupled. For highly energetic high harmonic radiation, there are virtually no materials that exhibit suitable reflectivities. Moreover, inserting the outcoupler into the cavity introduces unwanted additional dispersion, which has to be (pre)compensated by the cavity mirrors. The strongest limitation of the achievable enhancement and thus the overall system performance, however, results from the nonlinear response of the material, e.g. the intensity-dependent group delay dispersion, when subject to the high power intracavity beam [249, 250]. Consequently, finding alternative outcoupling methods has since been the goal of several theoretical and experimental studies [13–15, 248, 251–254].

Among the discussed potential candidates was the use of a non-collinear high harmonic generation geometry (see Figure 4.1b). Due to the intrinsic spatial separation of the generated EUV radiation from the fundamental, NCHHG shows the potential to overcome all problems associated with the Brewster plate: Since the insertion of additional material into the cavity becomes unnecessary, the achievable power enhancement is not limited and the applicability of the method is not restricted to a certain wavelength region. Additionally, the use of just partially EUV-transmissive filters to block residual reflections of the fundamental from the outcoupler is not required, resulting in higher available high harmonic powers.

Our initial experiments were intended to verify the potential of NCHHG as an output coupling method and thus focused on the favorable geometric separation of fundamental and high harmonic radiation. To this end, we employed amplified pulses to demonstrate NCHHG in a proof-of-principle experiment for two different (full) non-collinear angles, namely 30 mrad and 45 mrad. The latter angle was the largest one to be realized with our experimental apparatus. The main result is shown in Figure 4.2 for the $\theta = 30$ mrad case [255]. Collinear HHG was observed when either of the two driving beams was applied alone (top and bottom panel). In contrast, when both equally intense driving beams overlapped spatially and temporally, similarly intense high harmonic radiation

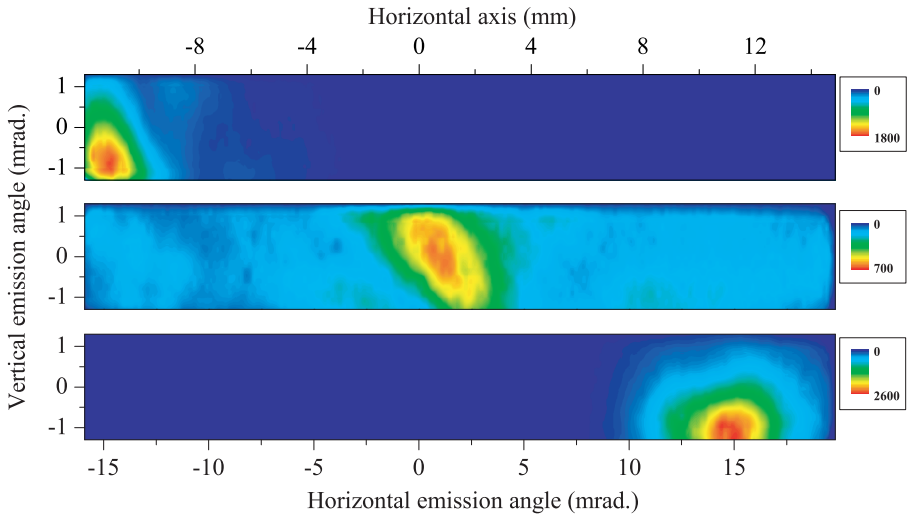

Figure 4.2: *Spectrally unresolved far-field spatial profiles of high harmonic radiation generated in a non-collinear geometry [255]. Collinear HHG is observed with each individual driving beam alone (top and bottom panel). High harmonic emission occurs non-collinearly when both driving pulses overlap spatially and temporally.*

was emitted purely along the bisector between the driving beams (central panel). Note that the generated high harmonics were not resolved spectrally in all three cases. This experimental demonstration confirmed the general potential of NCHHG as a combined generation and output coupling method for cavity-assisted high harmonic radiation.

However, in view of an experimental implementation of this geometry in a femtosecond enhancement cavity, a more detailed study of the dependence of NCHHG on experimental parameters such as the delay between the driving pulses, the intensity balance of the fundamental beams, and the non-collinear angle was required. Simultaneously, the possible spectroscopic application of the non-collinearly generated high harmonic radiation necessitated an analysis of its spectral and spatial properties.

In the course of our additional investigations, we found that it was possible to continuously alter the direction of emission of the non-collinear high harmonics by tuning the power balance between the two driving beams, where the extreme case corresponded to collinear HHG with a single fundamental beam. In addition, we observed that the spectrally resolved far field emission pattern of the generated EUV radiation can exhibit a spatial modulation depending on the phase delay between the two driving pulses [256]. The following sections summarize the efforts to scrutinize this intriguing observation in more detail.

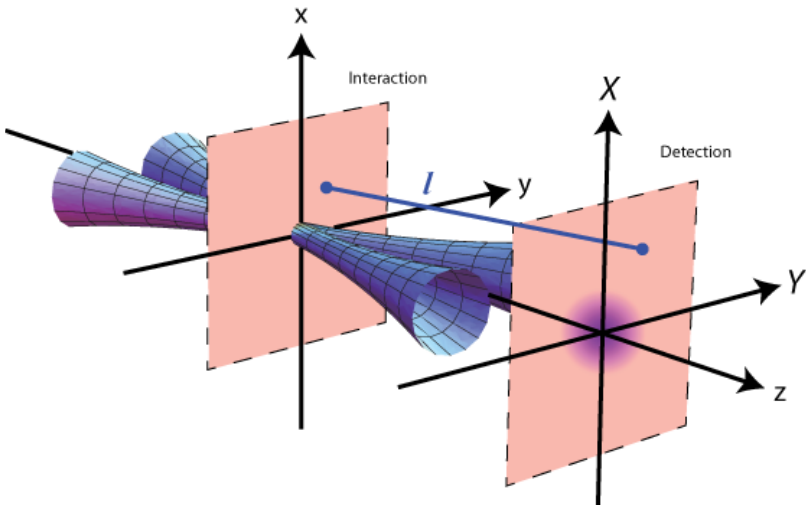

Figure 4.3: *Schematic of the non-collinear geometry and the employed coordinate system(s). Adapted from [256].*

4.3 The non-collinear geometry

In this section, important aspects and consequences of the special geometry of NCHHG are introduced and discussed.

A sketch of the non-collinear geometry and the employed coordinate system(s) is shown in Figure 4.3. The two spatially Gaussian driving beams propagate in the y-z-plane at an angle $\pm\beta$ with respect to the z-axis so that the full non-collinear angle between the two beams amounts to $\theta = 2\beta$ as indicated in Figure 4.1b. The resulting fundamental field E_f can be written as

$$\begin{aligned} E_f(x,y,z,t) = \; & E_{f1}\left(x, y\cos\beta + z\sin\beta, -y\sin\beta + z\cos\beta, t\right) \\ & + E_{f2}\left(x, y\cos\beta - z\sin\beta, y\sin\beta + z\cos\beta, t\right) e^{i\Delta\phi} \end{aligned} \tag{4.1}$$

where the phase delay $\Delta\phi = \omega_1 \Delta t$ accounts for the time delay between the driving pulses in the two beams. The fundamental (angular) frequency ω_1 is the same for E_{f1} and E_{f2} since they are generally assumed to originate from the same laser here.

When the delay between the pulses is so large that there is no temporal overlap between them, the driving field at the focus is simply that of each individual beam. As soon as the delay Δt becomes smaller than a couple of pulse widths, the fields of both driving beams interfere. The resulting temporally varying, spatially modulated intensity distribution at and around the focus depends on the non-collinear angle and the waist radii.

The non-collinear intensity distribution in the plane of the driving beams ($x = 0$) is shown in Figure 4.4 for a (full) non-collinear angle $\theta = 30\,\text{mrad}$ for two distinct temporal delays of $\Delta\phi = 0$ and $\Delta\phi = \pi$. For the plots, the same or at least the estimated experimental conditions were assumed, i.e. equal power in both beams as well as identical waist radii of $63\,\mu\text{m}$ and a common focus position. The intensity profiles at the focus along the y-axis, i.e. for $x = z = 0$, are also shown.

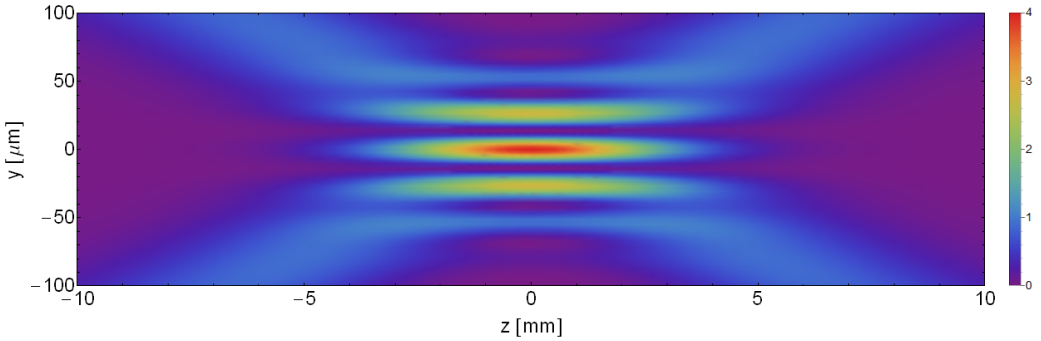

(a) *Driving intensity near the focus in the* $x = 0$ *plane for* $\Delta\phi = 0$, $\beta = 15\,\mathrm{mrad}$, *and* $w_0 = 63\,\mu\mathrm{m}$

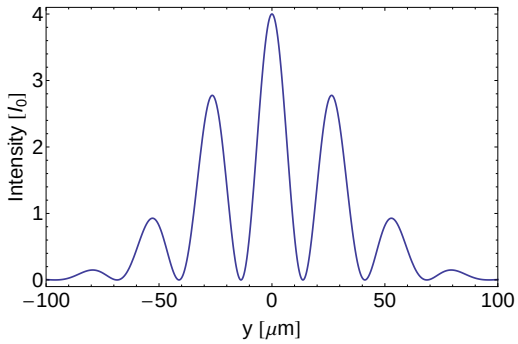

(b) *Intensity profile at* $x = z = 0$ *for the above.*

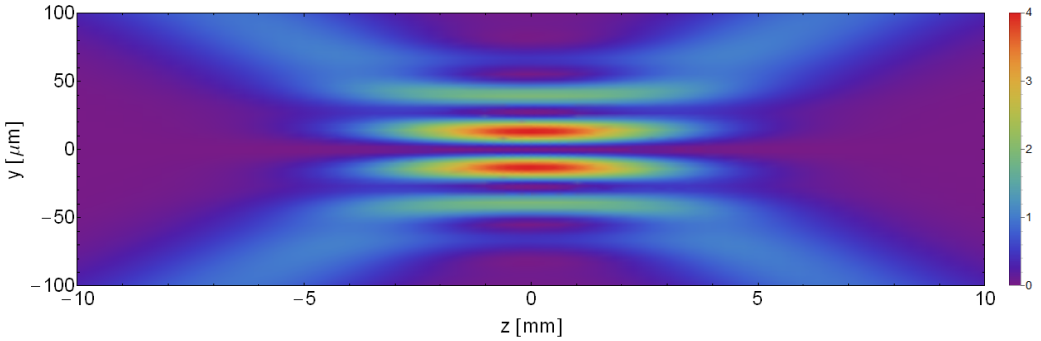

(c) *Driving intensity near the focus in the* $x = 0$ *plane for* $\Delta\phi = \pi$, $\beta = 15\,\mathrm{mrad}$, *and* $w_0 = 63\,\mu\mathrm{m}$

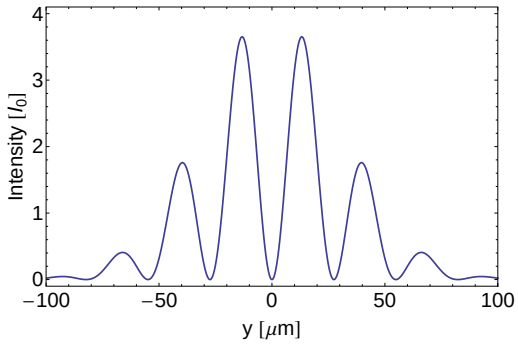

(d) *Intensity profile at* $x = z = 0$ *for the above.*

Figure 4.4: *Non-collinear driving intensity distribution near the focus.*

The interference pattern of the two infrared beams exhibits fringes whose spacing of λ/θ can be easily derived from substituting the product of (2.1) and (2.10) into (4.1). The positions of the fringes shift continuously for increasing phase delay and are inverted for $\Delta\phi = \pi$. Consequently, while the driving intensity pattern for $\Delta\phi = 0$ is characterized by a strong on-axis fringe (Figure 4.4a and Figure 4.4b), a minimum is obtained for $\Delta\phi = \pi$ (Figure 4.4c and Figure 4.4d). Note that the maximum peak intensity achieved in this non-collinear geometry is a factor of 4 higher than that of each individual driving beam alone. The intensity scales of the plots have been normalized to the single beam intensity, here denoted I_0.

High harmonics can only be generated at positions within the interaction region where the driving intensity exceeds the threshold intensity. Hence, it is obvious that the HHG process is spatially modulated in the non-collinear geometry because the interference pattern produced by the two fundamental driving pulses varies periodically during the passage of the pulses through the gas target.

Since our experimental setup grants us independent control of both driving beams, we can scan the delay between the fundamental pulses in order to study the effects of this time-dependent spatial modulation on the observed far field emission profiles of the generated high harmonic radiation.

4.4 Experimental setup and methods

The experimental setup, which is largely identical to the one used for the proof-of-principle experiments described above [255, 256], is schematically shown in Figure 4.5. Seeded by a Ti:sapphire oscillator operating at $\sim 100\,\mathrm{MHz}$, a chirped pulse amplification (CPA) system (Spectra-Physics Spitfire) provides 120 fs pulses with an average pulse energy of up to 2.3 mJ at a repetition rate of 1 kHz and a center wavelength of about 823 nm. The output beam of the CPA system is first guided through an adjustable circular aperture and then split into two equally strong beams with a 50:50-beamsplitter. Both beams propagate along paths of about equal length and are subsequently focused non-collinearly into a xenon gas jet inside a vacuum chamber by means of two identical spherical mirrors ($f = 300\,\mathrm{mm}$).

One of the two focusing mirrors is mounted onto a manual translation stage to adjust the spatial overlap and the position of the foci of the two fundamental beams. The pathlength from the beamsplitter to the focus is fixed for one of the driving beams, which is henceforth denoted “direct beam”. In contrast, the path of the other beam (referred to as “stage beam” in the following) contains a computer-controllable delay stage and a pair of piezo-actuated fused silica wedges so that the time delay Δt between the pulses propagating along the different paths can be precisely adjusted. While the tuning of the delay with the wedge pair is quasi-continuous, yet in a very limited range, the delay stage allows us to scan the delay in a large range of up to several picoseconds, which corresponds to the case where the two driving pulses are no longer overlapping temporally. We achieve a technical resolution of $\sim 0.25\,\mathrm{fs}$ which is determined by the minimum step size of the delay stage.

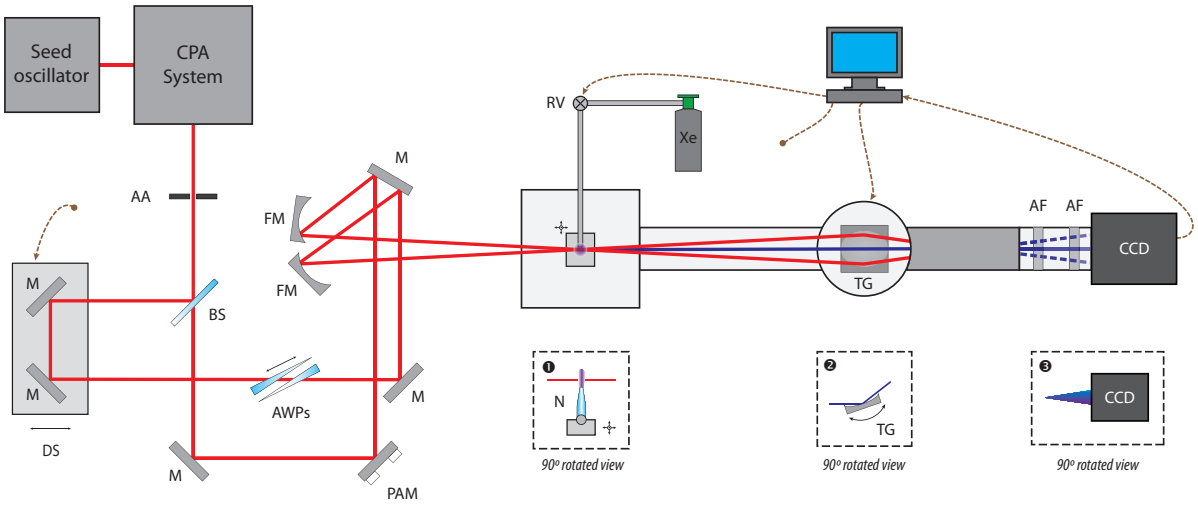

Figure 4.5: *Setup for spectrally resolved non-collinear high harmonic generation experiments. The (solid) dashed dark blue lines indicate the generated (non)-collinear high harmonic radiation. To illustrate the spatial and the spectral plane of the experimental geometry, the insets ❶-❸ depict a 90° rotated view of the respective parts. AA: adjustable aperture, BS: beam splitter, (F)M: (focusing) mirror, DS: delay stage, AWPs: adjustable wedge plates, PAM: piezo-actuated mirror, N: nozzle, RV: regulating valve, TG: toroidal grating, AF: aluminum filter, CCD: EUV-sensitive charge-coupled device.*

In contrast to the previously reported experiments [255], the gas target is produced by a self-made tapered glass nozzle with an orifice of $\sim 150\,\mu$m. Figure 4.6 shows a microscope image of the nozzle after extensive use in the NCHHG experiments. The nozzle is arranged such that the gas jet intersects the plane formed by the two laser beams orthogonally (see inset ❶ in Figure 4.5), thereby avoiding asymmetries that could potentially arise from positioning the gas jet in the same plane as the laser beams. The gas flow to the nozzle can be adjusted with a regulating valve (Pfeiffer Vacuum EVR 116) and is set to $2...5 \times 10^{-1}\,\mathrm{mbar}\cdot\mathrm{l/s}$ during all the experiments discussed here. After visual prealignment of the nozzle with respect to the non-collinearly intersecting driving beams, we use the strongly increased plasma fluorescence as an indication of optimized spatial overlap when the gas target is operated.

During the experiments, the output beam from the CPA system is apertured down using the adjustable iris to maximize the observed HHG signal [105]. In order to be able to estimate the resulting peak intensities, the beam profiles of a single driving beam at the focus were recorded for different aperture settings in a separate measurement at strongly attenuated power. Figure 4.7 depicts the measured profile for the typical aperture setting used in the experiments, i.e. an aperture radius resulting in a power transmission of $\sim 50\%$. In this case, the waist radius at the focus is extracted to be $w_0 \approx 63\,\mu$m. This corresponds to an estimated peak intensity of up to $6 \times 10^{13}\,\mathrm{W/cm^2}$ for each individual driving beam.

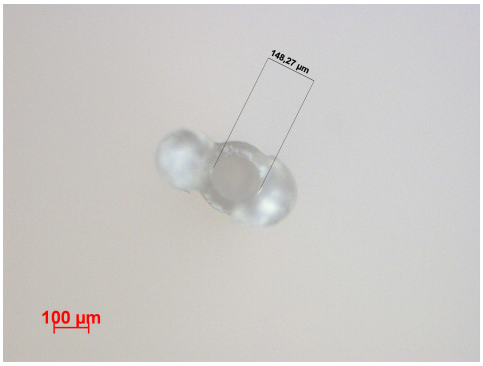

Figure 4.6: *Microscope image of home-built glass nozzle (top view) after operation in the NCHHG experiments. It can be seen that the nozzle tip was partially melted by the driving beam.*

The largest modification of the setup compared to [255] is the implementation of a scanning toroidal grating monochromator (Jobin Yvon LHT 30) into the beamline which makes a spectral characterization of the generated EUV radiation possible [256]. The monochromator is set up such that the spectral diffraction is in a plane orthogonal to the one formed by the two IR driving beams and the collinearly generated high harmonic radiation in order to decouple the spatial and the spectral features of the non-collinear HHG geometry as well as possible (see insets ❷ and ❸ in Figure 4.5). Behind the monochromator, two consecutive aluminum filters (200 nm thickness each, Lebow 0.2Al-0-L3.0) block the residual IR stray light. Due to the aluminum filters, harmonic radiation above 70 nm (orders $q < 11$) is strongly suppressed and can thus not be detected.

The spatial profiles of the generated EUV radiation are both monitored and recorded with a back-illuminated CCD (Princeton Instruments PIXIS XO-100B, 1340×100 pixels, pixel size $20 \times 20\,\mu$m) that is cooled to -10°C to reduce the background signal. The spatial field of view covered by the long edge of the CCD is limited to an angle of ~ 40 mrad by the geometry of our experimental setup. Spatial and spectral information overlap in the direction along the short edge of the CCD chip. A limited spectral range of ~ 2 nm can be monitored or recorded simultaneously for a certain grating position. In our experiments, however, the spatial information dominates over the spectral information. Spatially, the CCD covers an angle of about 3 mrad in the plane orthogonal to that of the non-collinear driving beams.

Since the CCD camera allows live-montoring of the generated EUV signal, we maximize the observed harmonic signal by adjusting several experimental parameters: The fundamental beam is apertured down with the adjustable iris (see above), the chirp of the driving pulses emitted by the CPA system is tuned by moving the compressor grating, and the nozzle position and the gas flow are adjusted. The pressure in the interaction chamber is in the 10^{-6} mbar range without operation of the gas target and rises to a steady-state pressure of about 1.4×10^{-2} mbar with gas load.

Several important experimental parameters such as the angle of the monochromator grating, the position of the delay stage, and the gas flow to the glass nozzle are con-

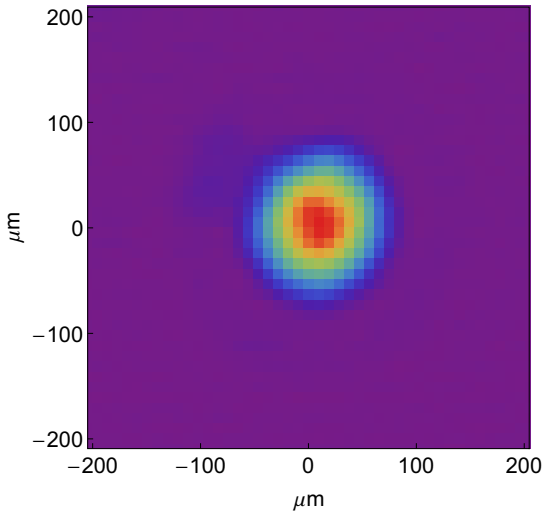

Figure 4.7: *Measured beam profile of single IR driving beam at focus for typical aperture setting of* $\sim 50\%$ *power transmission that was found to optimize the beam profile and the intensity of the non-collinearly generated high harmonics. The extracted IR beam radius is* $w_0 \approx 63\,\mu$m.

trolled from a personal computer using a commercial software environment (National Instruments LabView). Likewise, the data acquisition from the CCD camera during the experiments is fully automated. All plots of experimental data that will be discussed in the following sections are based on a series of image frames acquired from the CCD that show the far-field spatial intensity distribution of the generated EUV radiation. In each series, either the monochromator grating angle or the position of the delay stage is varied between consecutive frames so that every frame corresponds to, for example, a certain delay between the driving pulses. A characteristic image frame recorded at the wavelength of the 17th harmonic order for a phase delay of $\Delta\phi = \omega_1 \Delta t = \pi$ between the pulses is shown in Figure 4.8. In order to be able to illustrate the dependence of the observed spatial high harmonic intensity distribution on the altered experimental parameter, all image frames from a certain series are post-processed during data evaluation. After subtraction of the individual background, each frame is converted into a harmonic intensity profile by integration of the image data along the spatio-spectral axis of the image, i.e. along the short edge of the CCD field of view. Figure 4.9 shows the intensity profile resulting from the image frame shown in Figure 4.8. The so obtained intensity profiles of the high harmonic emission pattern are then stitched together to obtain a 2d plot in which the EUV intensity is color-coded (see Figure 4.10 and Figure 4.12, for example).

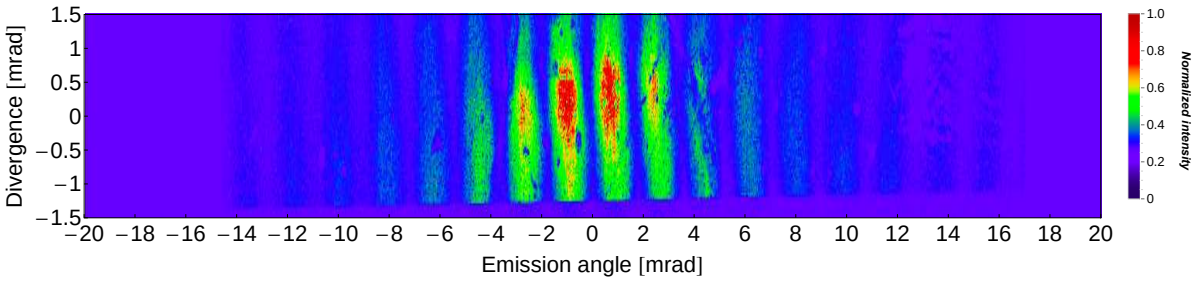

Figure 4.8: *Typical recorded full frame CCD image showing non-collinearly emitted EUV radiation at the 17th harmonic wavelength for a phase delay $\Delta\phi = \omega_1 \Delta t = \pi$ between the fundamental pulses. The emission angle lies in the plane of the two non-collinear driving beams. Spectral and spatial information overlap in the orthogonal plane, for which the spatial labeling has been chosen here.*

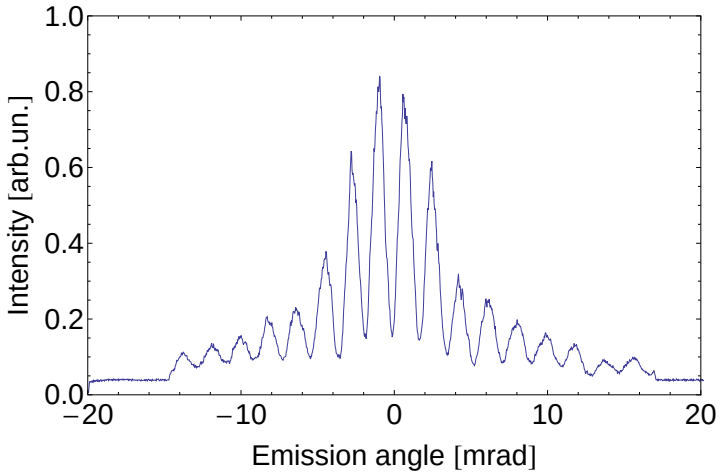

Figure 4.9: *Spatial intensity profile for a phase delay $\Delta\phi = \pi$ resulting from integration of the full CCD frame shown in Figure 4.8 along the axis labeled "divergence".*

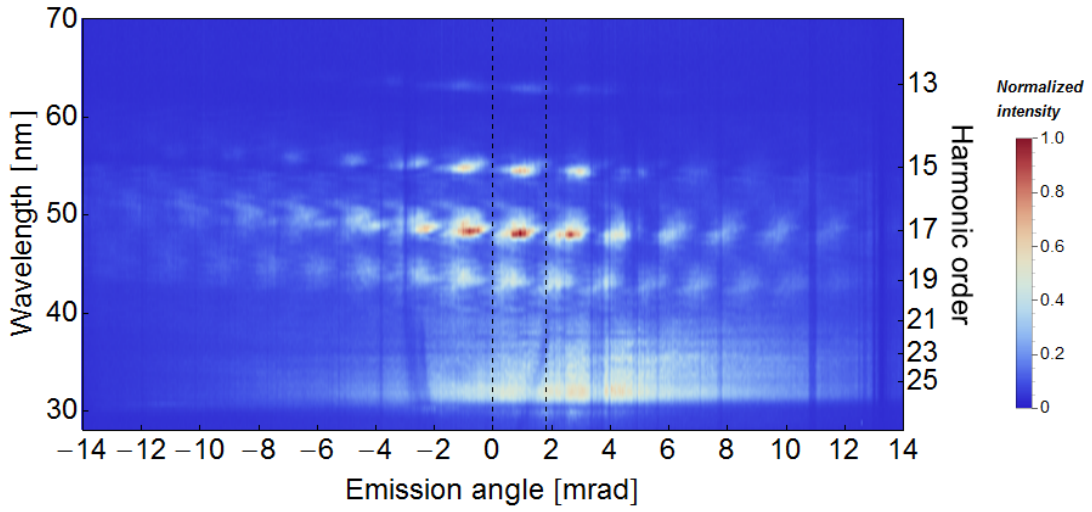

Figure 4.10: *Spectrally resolved non-collinear high harmonic far-field emission pattern. Data was recorded with a CCD camera behind two consecutive aluminum filters and then post-processed (see text for details). The dashed black lines indicate the range of directions that were considered for the spectrum shown in Figure 4.11.*

4.5 Experimental results

Since our initial proof-of-principle experiments [255] lacked spectral resolution, we employed the improved experimental setup to both confirm our earlier findings and spectrally characterize the non-collinearly generated high harmonic radiation. The majority of experimental data was then taken to investigate the dependence of the produced EUV radiation on the delay between the fundamental pulses. To this end, we investigated the dependence of the far-field spatial intensity distribution of the generated high harmonic radiation on the delay for all high harmonic orders that our setup could efficiently detect.

4.5.1 Non-collinear high harmonic spectrum

Figure 4.10 shows the spectrally resolved non-collinear high harmonic emission pattern that has been obtained from the CCD frames recorded during a wavelength scan of the monochromator in the way described in the previous section. EUV radiation ranging from the 13th (63.3 nm) up to the 19th (43.3 nm) order can be clearly identified. Lower harmonic orders with wavelengths longer than 70 nm are strongly suppressed by the two consecutive Al filters in our beamline and thus not shown. The signal between 30 nm and 40 nm is likely to originate mostly from stray light caused by the zeroth diffraction order of the monochromator grating hitting the walls of the vacuum chamber. This suspicion is corroborated by the fact that no spatial structure is observed in this wavelength range, whereas the high harmonic orders 13 to 19 exhibit a pronounced spatially modulated emission pattern. Note that the modulation period clearly varies with harmonic order so that the spectral content of the EUV radiation depends on the direction of emission. As expected from our previous investigations [255, 256] and as

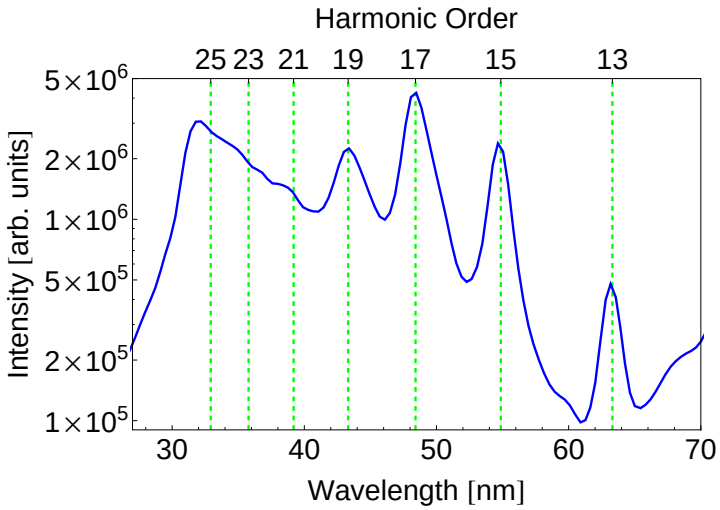

Figure 4.11: *Non-collinear high harmonic spectrum obtained by summation of data within angular range indicated by black dashed lines in Figure 4.10. Note that the data has been corrected for the spectral sensitivity of the CCD and the transmission of the Al filters. Dashed green lines show the spectral positions of the high harmonic orders calculated from the central wavelength of the driving laser. The increasing signal between* 40 nm *and* 30 nm *is most probably caused by stray light that originates from the 0th diffraction order of the monochromator grating bouncing off the walls of the vacuum chamber.*

already apparent from Figure 4.8 and Figure 4.9, the non-collinear emission pattern is centered about the bisector of the driving beams, where also most of the power is concentrated. However, the lower intensity wings of the far-field pattern extend up to emission angles of ±12 mrad. A possible explanation for this observation will be given in Section 4.6.4.

In order to analyze the spectral properties of the high harmonic radiation emitted in the narrow angular region close to the bisectrix of the fundamental beams, all contributions from the range indicated by the dashed black lines in Figure 4.10 are summed up. The resulting non-collinear high harmonic spectrum is shown in Figure 4.11. The green dashed lines indicate the expected spectral positions of the high harmonic orders calculated from the central wavelength of the driving laser ($\lambda_1 = 823$ nm). Using these expected spectral positions of the harmonic orders, the absolute wavelength of the data obtained from the monochromator can be re-calibrated with the observed spectrum. Note that the data has been corrected for the spectral sensitivity of the CCD and the transmission of the two aluminum filters, but not for the unknown, yet most likely approximately constant spectral efficiency of the monochromator grating. Among the clearly identified harmonic orders, the 17th is the strongest and the 13th is the weakest with about an order of magnitude lower measured intensity. Therefore, the exposure times of the images recorded during the delay scans that are presented in the following sections have been individually adjusted for each harmonic order to maximize the signal level.

4.5.2 Delay scans for individual harmonic orders

To investigate the effects of the delay between the fundamental pulses on the spatial emission pattern of the generated high harmonic radiation in detail, several series of measurements were performed for all clearly observable harmonic orders, i.e. for the 13th to 19th order (compare the spectrum in Figure 4.11). In each of these series, the pulse delay was scanned in various temporal ranges and with different (technical) temporal resolutions determined by the step size of the computer-controlled delay stage.

4.5.2.1 Large range delay scans

The result of a typical delay scan with a large scan range of about 2 ps and a temporal resolution of 1 fs is shown in Figure 4.12 for the 17th harmonic. The delay axis is encoded by $\Delta t = t_{\text{stage}} - t_{\text{direct}}$ where t_{stage} and t_{direct} correspond to the times[2] when the pulses from the stage beam and the pulses from the direct beam pass through the center of the gas target (cf. Figure 4.5). This means that for $\Delta t > 0$, the pulses from the direct beam arrive at the gas target before those from the stage beam and vice versa for $\Delta t < 0$. The origin of the delay axis ($\Delta t = 0$), which corresponds to maximum temporal overlap between the pulses from both paths, cannot be determined accurately neither in the experiment nor from the data. Therefore, since high harmonic emission along the bisector of the driving beams is just expected when the pulses fully overlap in time, the delay axis of the long range scan data is moderately adjusted so that $\Delta t = 0$ best coincides with the detection of EUV signal at an emission angle of 0 mrad.

Figure 4.12 reveals that our experiment corresponds to collinear high harmonic generation with each individual driving beam for very large positive or negative delays since the pulses do not overlap temporally in that case. The harmonic signal is thus detected under an emission angle of $\sim |14|$ mrad simultaneously. This observation agrees with the expectations from our analysis of the non-collinear geometry in Section 4.3.

Several interesting phenomena can be observed in the time window from $\Delta t \simeq -150$ fs to $\Delta t \simeq 150$ fs when the pulses from the two arms at least partially overlap in the gas jet temporally: The direction of EUV emission changes continuously from the direction of the stage beam (14 mrad) towards the bisector of the driving beams and further to the direction of the direct beam (−14 mrad). In this time window, collinear harmonic radiation is not detected. Interestingly, the change in the direction of emission is asymmetric, i.e. even though both individual beams create harmonic radiation for large enough delays, the directions of emission are only continuously linked for the pulses that reach the gas jet first, i.e. those from the stage beam for negative delays and those from the direct beam for positive delays. This results in an "anti-crossing"-like shape of the spatio-temporal emission profile shown in Figure 4.12. This effect most likely originates from the fact that the first pulse generates harmonics, primarily at its leading edge, but also significantly ionizes the medium while crossing through the gas jet. Since the medium cannot be exchanged quickly enough before the immediately following second pulse passes through the jet, no harmonics are generated.

[2] As long as these times are referenced to a common time axis, its origin does not matter here.

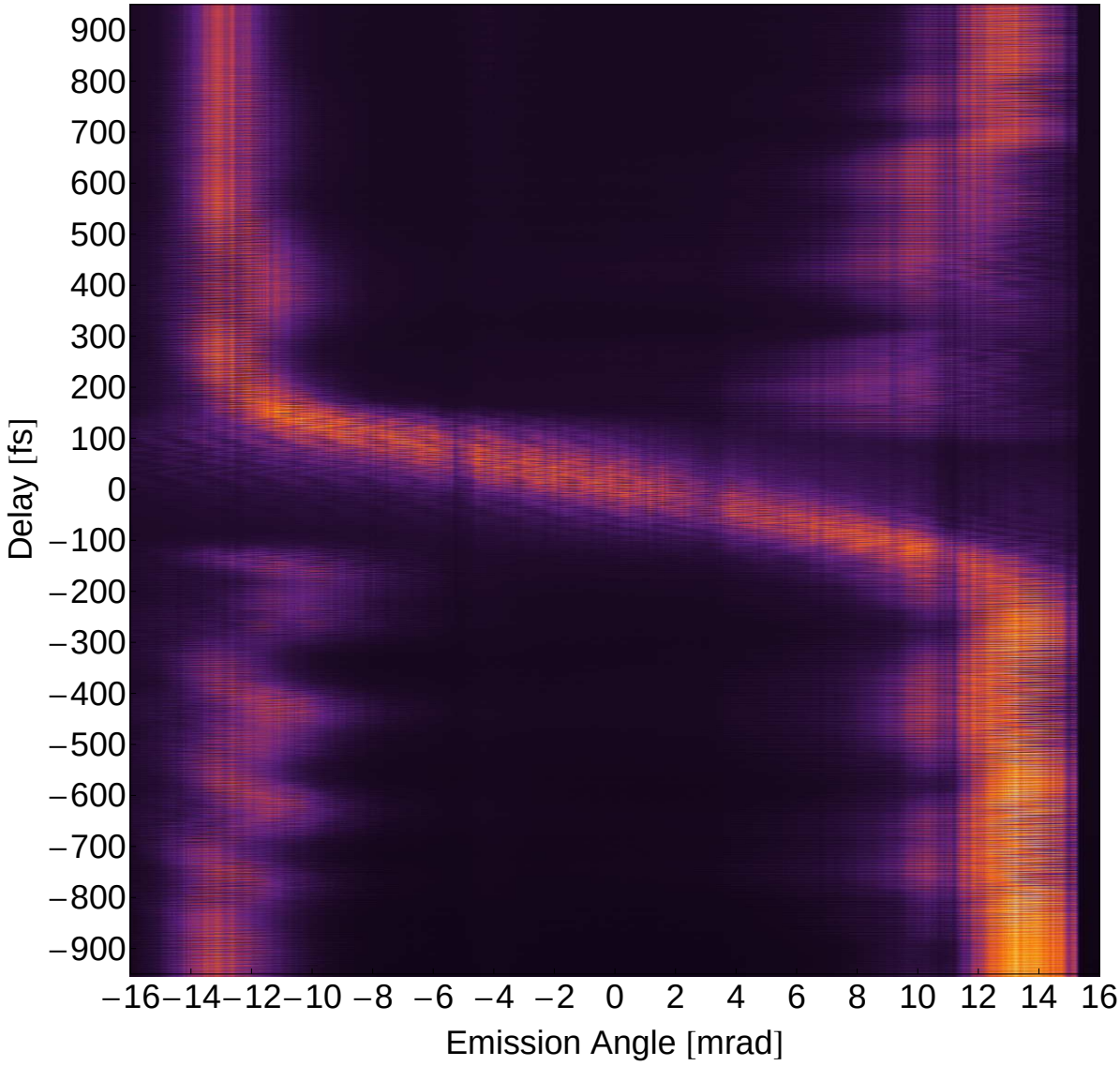

Figure 4.12: *Delay scan for the 17th harmonic with* 1 fs *temporal resolution in the range of* ±1 ps *delay between the driving pulses.*

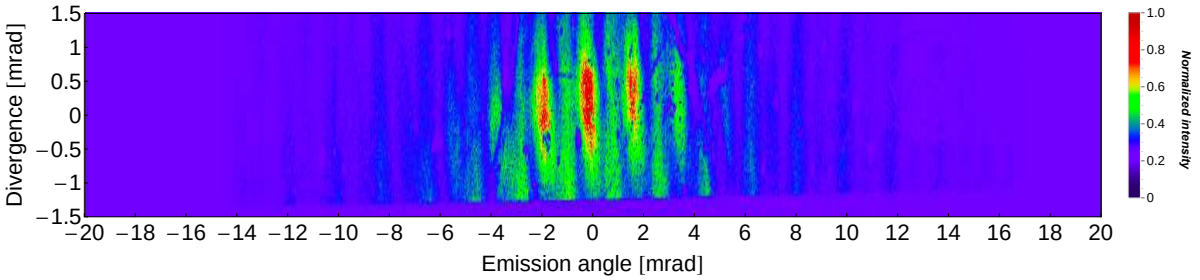

Figure 4.13: *Beam profile of non-collinear high harmonic radiation for phase delay* $\Delta\phi = 0$.

For delays outside the temporal window of non-collinear EUV emission, the angle under which the high harmonic signal is detected shows several and in part rather strong deviations from the two collinear directions. Although our experimental system is not stabilized in any way during the experiments so that fluctuations in beam pointing certainly affect the observed signal, they can be excluded as the main origin of the angular deviations because these exhibit a two-fold unequivocal point symmetry about zero pulse delay. Hence, we believe that the additional angular structure for large delays is caused by a fundamental pulse shape that contains weak satellite pulses. Satellite structures before and after both the leading and the trailing edge of the pulse, respectively, will temporally overlap with the main pulse at certain times. Likewise, the satellite pulses can also overlap at a larger delay between the peaks of the pulse envelopes. In that sense, the spatio-temporal information of Figure 4.12 encodes information about the shape and the duration of the fundamental pulse. Similar to frequency-resolved optical gating, NCHHG can thus be considered an extension of the auto-correlator technique.

4.5.2.2 High resolution delay scans

An interesting phenomenon that can be observed during the delay scans with higher temporal resolution is the recurring appearance of spatially modulated far field emission profiles. Depending on the delay, modulation patterns with two distinct periods appear. A typical image frame exemplifying the spatial modulation in the 17th harmonic emission profile for a phase delay[3] of $\Delta\phi = \pi$ was already shown in Figure 4.8. The emission pattern of the same harmonic for a phase delay of $\Delta\phi = 0$ is depicted in Figure 4.13 while the corresponding integrated spatial intensity profile is shown in Figure 4.14. The angular spacing of the observed far field fringes is half of that seen for a delay of $\Delta\phi = \pi$.

We did not observe any spatial modulation in our initial experiments [255], which is likely to be due to the lack of spectral resolution at that time. First spectrally resolved investigations [256] showed far field fringes only for certain delays around $\Delta\phi = \pi$ but none at all for $\Delta\phi = 0$. However, as the temporal resolution of the delay scans was not high enough at that time, the patterns around $\Delta\phi = 0$ with a lower fringe spacing were probably washed out by instabilities of the experimental system.

[3] All phase delays discussed here are modulo π.

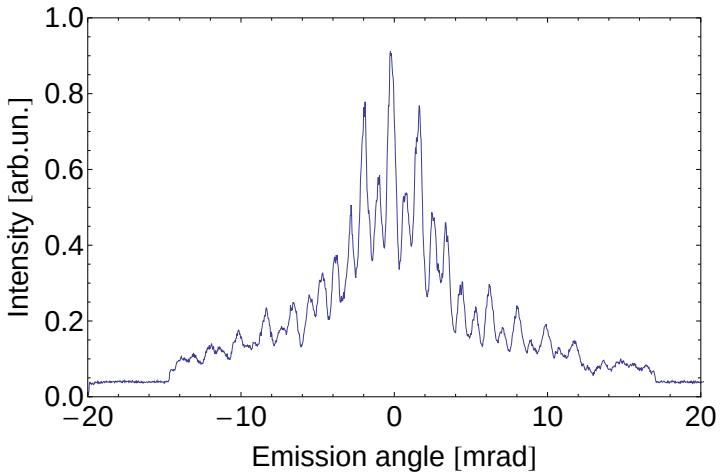

Figure 4.14: *Spatial intensity profile of non-collinear high harmonic radiation for phase delay* $\Delta\phi = 0$ *obtained from CCD frame shown in Figure 4.13.*

In order to gain more insight into the observed delay dependence, we reduced the scan range to about $\pm 25\,\mathrm{fs}$ around $\Delta t \approx 0$ and recorded delay scans with a higher temporal resolution of 0.5 fs for the 13th to 19th harmonic. The results are depicted in Figure 4.15.

Most strinkingly, the high resolution delay scans yield very regular far field patterns for all four harmonic orders under scrutiny. The two observed spatial fringe periodicities are different for each harmonic order and alternate regularly with the delay. Note that no active stabilization was employed in the experimental system which both emphasizes the robust nature of the underlying effect and provides a possible explanation for the irregularities in Figure 4.15. The latter are most obvious in the case of the 19th harmonic.

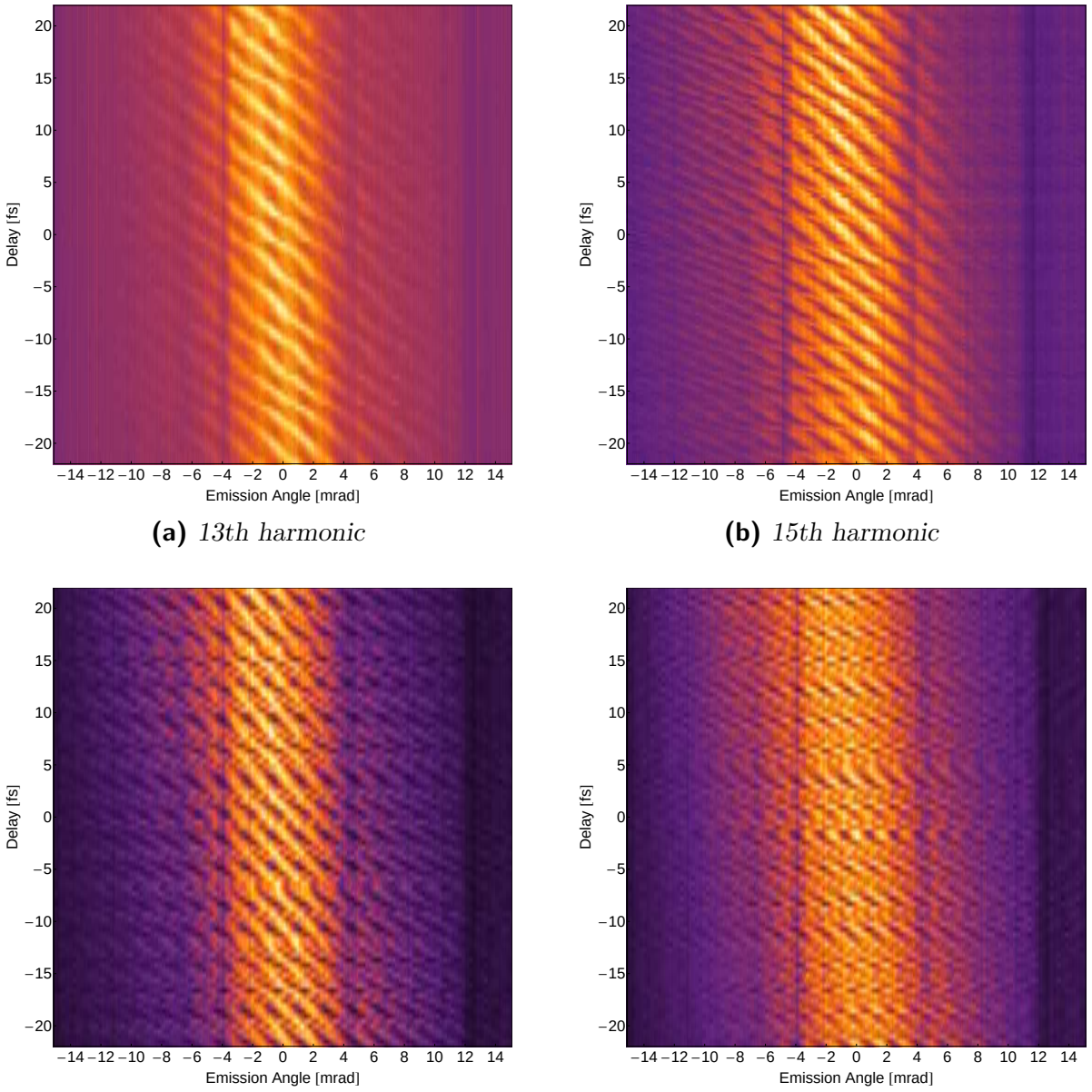

(a) *13th harmonic*

(b) *15th harmonic*

(c) *17th harmonic*

(d) *19th harmonic*

Figure 4.15: *Precision delay scans (0.5 fs temporal resolution) for (a) 13th, (b) 15th, (c) 17th, and (d) 19th harmonic order around zero delay between the driving pulses. Regular fringe patterns can be observed for all four depicted orders. Exposure times were different for different harmonic orders (3s, 2s, 1s, 2s) to compensate for their varying signal strengths.*

4.6 Numerical simulations based on a simplified model

In order to gain a qualitative understanding of the observed high harmonic far field profiles, we have set up a numerical simulation of NCHHG based on a simplified model of the microscopic harmonic dipole response[4]. The simulation is a refined version of the one already described and used in [256] that has been adapted to better reproduce the latest experimental data.

4.6.1 Theoretical description

As mentioned in Chapter 3, a full numerical simulation of the macroscopic high harmonic response is a computationally involved task, especially in a not rotationally symmetric geometry like the one employed in our case. Therefore, our code neither solves the time-dependent Schrödinger equation nor resorts to the Lewenstein model to calculate the high harmonic dipole moment but just assumes a simple power law scaling. This is justified because the intensity of a harmonic order q in the plateau has been seen to follow a modified power law $I_q \propto I_1^p$ with an exponent $p < q$ in good approximation (cf. Section 3.3.3).

Since we are particularly interested in phase effects, we describe the harmonic dipole moment at frequency $\omega_q = q\omega_1$ by a power law for the fundamental field with exponent p_f according to

$$D(\boldsymbol{r},t) \propto |E_f(\boldsymbol{r},t)|^{p_f}\ e^{i\left(q\,\phi_f+\varphi_I\right)} \left(1+\frac{|E_s|^s}{|E_f(\boldsymbol{r},t)|^s}\right)^{p_f/s} \tag{4.2}$$

where $\boldsymbol{r} = (x,y,z)$ has been used and ϕ_f and φ_I denote the phase of the fundamental field and the atomic dipole phase, respectively. The latter depends on the squared modulus of the fundamental field, as discussed in Section 3.2.3. The last factor in (4.2) is a heuristic saturation term, where $|E_s|$ and s denote the saturation field strength and the saturation exponent, respectively. This saturation term was not included in the code used previously [256]. As will be detailed below, we found the inclusion of a saturation factor to be necessary to reproduce our experimental observations.

To obtain the high harmonic far field emission profiles as recorded by the CCD in the experiment, the contributions from all gas atoms in the target have to be calculated. These contributions are then propagated to a virtual screen and summed up coherently (compare Figure 4.3). In particular, radiation emitted from the target at time τ_e at a position $\boldsymbol{r}$ arrives at a position $\boldsymbol{R} = (X,Y,z)$ on the screen at time $l/c + \tau_e$ where l is the distance between $\boldsymbol{r}$ and $\boldsymbol{R}$. Since the screen is located a large distance away from the emission region, the Fraunhofer approximation can be employed. The angular distribution of the qth harmonic is then proportional to

$$U(\alpha_x,\alpha_y,\tau_e) = \iiint D(\mathbf{r}, t=\tau_e+z/c)e^{iqk(x\alpha_x+y\alpha_y)}dxdydz \tag{4.3}$$

[4]The numerical implementation and testing was done in C++ by Igor Gotlibovych.

where the angular coordinates (α_x, α_y) have been introduced. The overall harmonic emission pattern recorded by the CCD can be calculated from

$$U(\alpha_x, \alpha_y) = \int |U(\alpha_x, \alpha_y, \tau_e)|^2 d\tau_e \tag{4.4}$$

where integration is performed over a time span covering the interaction of the driving field with the gas target, which corresponds to the passage of both pulses through the gas jet in our case.

4.6.2 Simple analogy to NCHHG

Before moving on to the discussion of the simulation results, a simple analogy of NCHHG to a well-known problem shall be highlighted. If we neglect the heuristic saturation term in (4.2) for a moment, the dipole moment scales as the p_fth power of the field. The distribution of the harmonic dipole moment $|D(\boldsymbol{r}, t)|$ resulting from the non-collinear driving field discussed in Section 4.3 is shown in Figure 4.16 in the plane of the non-collinear driving beams ($x = 0$) for the two typical pulse delays $\Delta\phi = 0$ and $\Delta\phi = \pi$ and for $p_f = 8$. The latter value is the approximate number of fundamental photons that it takes to overcome the ionization potential of Xe.

Since the harmonic dipole moment $|D|$ peaks around the field maxima, we can see that the emission region is structured into a three-dimensional array of equidistant emitters of varying strength. According to Babinet's principle, we can expect the high harmonic far field pattern to resemble that of a triple slit for a delay of $\Delta\phi = 0$ (see Figure 4.16b) and that of a double slit for a delay of $\Delta\phi = \pi$ (Figure 4.16b), respectively.

When not considering the intensity-dependent dipole phase φ_I, the phases of the individual "slits" are simply given by the phases of the respective interference fringes of the fundamental field and consequently change by a factor of π between subsequent peaks because q is odd (cf. (4.2)). For $\Delta\phi = \pi$, the two dominant peaks have equal strength and their phase differs by π. Depending on the considered harmonic order q, we thus expect the far field pattern to exhibit fringes with an angular spacing of θ/q, where $\theta = 2\beta$ is the full non-collinear angle, and a minimum along the bisector of the driving beams. For $\Delta\phi = 0$, there are three distinct peaks of different intensities. From the triple slit analogy, we anticipate a set of principal maxima in the far field with the same periodicity of θ/q as the one derived for the double slit case. Since it is well known that the diffraction pattern of m slits will additionally exhibit $(m - 2)$ subsidiary maxima between principal maxima, one such subsidiary maximum between each pair of principal maxima is expected in our case. In the following discussions of experimental data, the principal maxima are called "primary fringes" while the subsidiary maxima are denoted "secondary fringes".

The fringe periodicity of a double slit diffraction pattern is given by its Fourier transform and will thus contain a strong peak at an angular frequency of q/θ. Likewise, the occurrence of subsidiary maxima (i.e. secondary fringes) in the case of a triple slit corresponds to an additional peak in the Fourier space at twice the frequency, i.e. $2q/\theta$. The spatial fringe periods that could be extracted from the experimental delay scan data

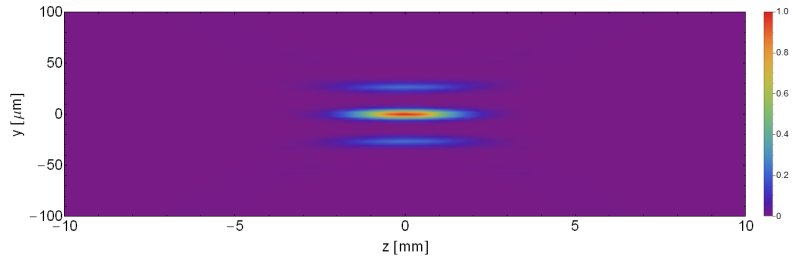

(a) *Harmonic dipole moment near the focus in the* $x = 0$ *plane for* $\Delta\phi = 0$, $\beta = 15\,\mathrm{mrad}$, *and* $w_0 = 63\,\mu\mathrm{m}$

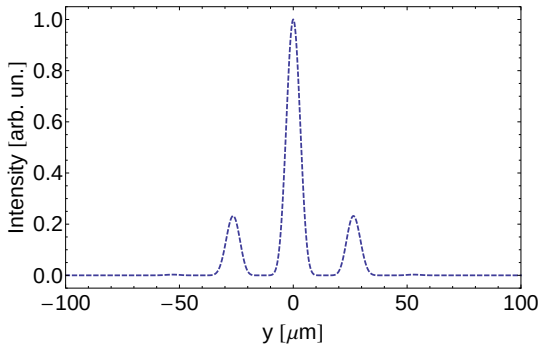

(b) *Profile of harmonic dipole moment distribution in (a) at* $x = z = 0$.

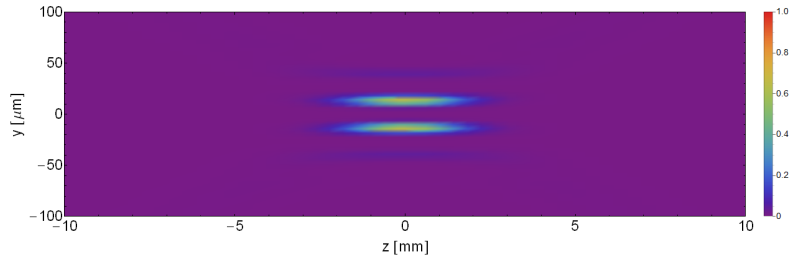

(c) *Harmonic dipole moment near the focus in the* $x = 0$ *plane for* $\Delta\phi = \pi$, $\beta = 15\,\mathrm{mrad}$, *and* $w_0 = 63\,\mu\mathrm{m}$

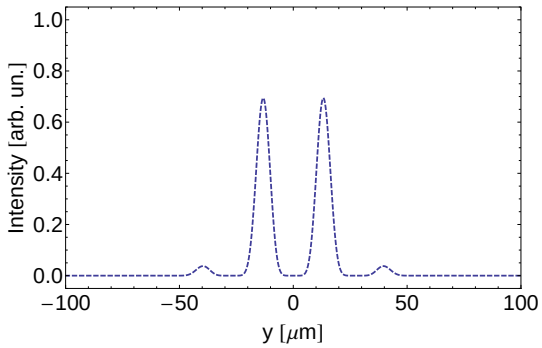

(d) *Profile of harmonic dipole moment distibution in (c) at* $x = z = 0$.

Figure 4.16: *Non-collinear dipole moment distribution near the focus.*

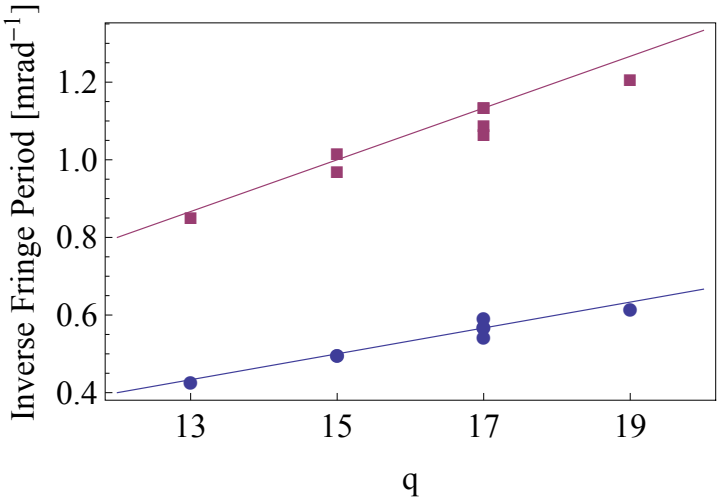

Figure 4.17: *Fringe periodicities extracted from Fourier transforms of several experimental delay scan datasets for different harmonic orders. The circles correspond to the inverse fringe periods obtained for both $\Delta\phi = \pi$ and $\Delta\phi = 0$, the squares indicate the additional Fourier frequencies for $\Delta\phi = 0$. The solid lines are the analytical predictions q/θ and $2q/\theta$ described in the text.*

with high enough resolution and fringe contrast are shown Figure 4.17 for the different harmonic orders. The average fringe periodicities extracted from several individual experimental datasets for different harmonic orders are shown as separate points. Most experimental data were taken for the 17th harmonic, hence there are more datasets available. The solid lines are the predictions resulting from the simple geometric predictions. The agreement is very good.

So far, we neglected the influence of the intensity-dependent dipole phase φ_I on the far-field patterns. For $\Delta\phi = \pi$, the two main generating peaks have the same intensity (Figure 4.16d) and will thus acquire no relative phase. The far field fringes should therefore remain unaffected but the overall emission profile is expected to broaden due to phase variations within each harmonic dipole "slit". For $\Delta\phi = 0$, however, the two weaker side peaks (Figure 4.16b) will acquire an additional phase difference $\Delta\varphi_I$ relative to the strong central "slit" which is determined by the intensity difference between the central and the neighboring fundamental fringes, i.e. $\Delta\varphi_I \propto \Delta\,|E_f|^2$. It can thus be expected that the appearance of secondary fringes in the observed high harmonic far field pattern for phase delays $\Delta\phi = 0$ is affected by the intensity-dependent phase. In particular, the secondary fringes should be sensitive to different quantum trajectories for which the magnitude of the resulting phase shift $\Delta\varphi_I$ between the central and the side "slits"differs.

As we shall see, the fringe patterns produced by our numerical simulation are very sensitive to the intensity-dependent dipole phase. A comparison between experimental data and simulation thus shows the potential to gain some qualitative insight about the intensity-dependence of the harmonic phase.

4.6.3 Simulation details and limitations

This section provides some more details about the implementation of our numerical simulation. Identical Gaussian beams with a moving temporal envelope function are inserted into (4.1) to compute the the fundamental driving field. The spatial integration in (4.3) can be performed efficiently using a fast-Fourier transform (FFT) routine. Here, the interaction region and thus the spatial integration is limited to a cylindrical region $y^2 + z^2 \leq L_{\mathrm{med}}^2$, i.e. we simply approximate the gas density distribution by a uniform target via a step function. In addition, since the gas density is not explicitly included, we neglect refraction and dispersion of both the incident and the harmonic beams in the target. This means that ionization is neglected as well which is not necessarily a good approximation for the driving pulse durations, intensities, and the gas used in the experiment (Xe). Indeed, saturation of the high harmonic emission was observed for an experiment in a collinear geometry at comparable intensities. Since we could not reproduce the results of the experimental precision delay scan data with our code numerically at the beginning, the last factor in (4.2) was included heuristically to account for saturation effects. Systematic studies of the parameter space spanned by the saturation field strength $|E_s|$ and the saturation exponent s revealed that the obtained numerical results showed only a weak dependence on the exact implementation of saturation in the code. For the data presented here, a saturation intensity $I_s = \frac{c\epsilon_0}{2} E_s^2 \approx 5 \times 10^{13}\,\mathrm{W/cm^2}$ and $s = -3$ were used.

To investigate the predicted effects of the intensity-dependent dipole phase, we employed the linearized model $\varphi_I^{(i)}(q) = \alpha_q^{(i)} \frac{c\epsilon_0}{2} |E_f|^2$ (cf. (3.30)) and used the phase coefficient $\alpha_q^{(i)}$ as a free parameter to match experimental and simulated results. Note that the current version of our code can only simulate the harmonic far field pattern as a function of one phase coefficient at a time and for one harmonic order at a time. In the experiment, the observed harmonic profiles can contain contributions from many quantum trajectories, predominantly the short and the long one, and quantum path interferences between these trajectories are possible [210]. With our current code, we can just add up the contributions of different trajectories in the far field incoherently, i.e. we can only add intensities.

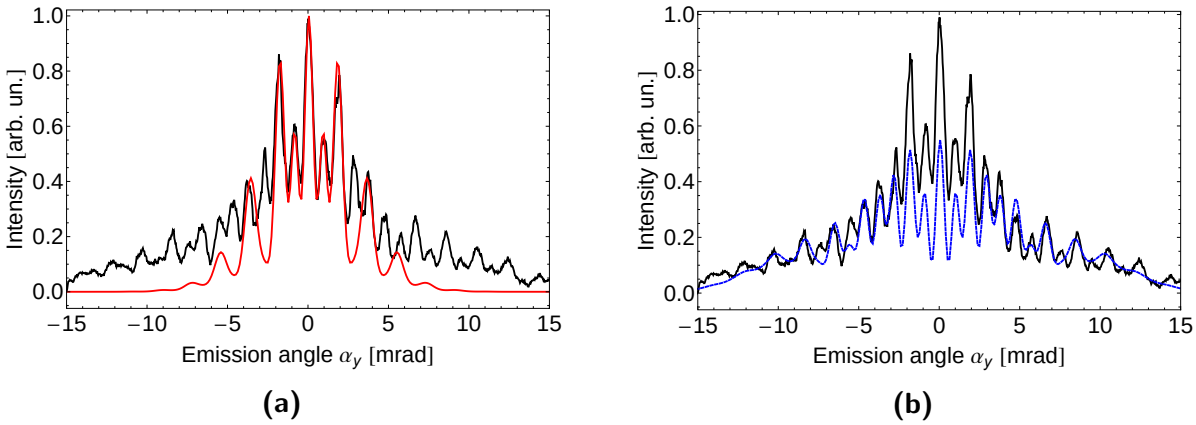

Figure 4.18: *Comparison of experimental (black) and numerically simulated (red, dashed blue) high harmonic far field profiles for the 17th harmonic at a phase delay of $\Delta\phi = 0$. (a) Best visual agreement of relative intensities of fringes at the center of the emission pattern obtained after manual adjustment of phase coefficient to $\alpha_{17}^{(1)} = 2.1$ (b) Same for larger emission angles, obtained for $\alpha_{17}^{(2)} = 5.1$. See text for details.*

4.6.4 Discussion of results

As already became obvious from the description of our numerical simulation in the previous Section 4.6.3, the simulation results can only be compared qualitatively to the experimental data. The following discussion concentrates on the 17th harmonic which is the strongest harmonic order observed experimentally.

A comparison of typical experimental and numerically simulated 17th harmonic integrated far field profiles for the two significant phase delays $\Delta\phi = 0$ and $\Delta\phi = \pi$ is shown in Figure 4.18 and Figure 4.19, respectively. Since the phase coefficients α_q are continuous free parameters in the simulation, the far field patterns of the 17th harmonic at fixed phase delays $\Delta\phi = \pi$ and $\Delta\phi = 0$ are numerically simulated for values[5] of α_{17} in the range of $\alpha_{17} = 0...60$. It turns out that the experimentally observed secondary fringes[6] for $\Delta\phi = 0$ cannot be reproduced for $\alpha_{17} = 0$. This statement also remains true when other simulation parameters such as the driving intensity, the size of the focus, and the size of the gas target are varied. When saturation is not included, the secondary fringes are not reproduced either. In fact, without taking into account saturation in the simulation, there is no phase coefficient for which the agreement between experiment and simulation is as good as with saturation.

When including saturation, we find that the secondary fringes can be reproduced for certain narrow ranges of values for α_{17}. This is exemplified by Figure 4.18. Within the value ranges of α_{17} that produce secondary fringes, visual selection is used to determine the $\alpha_{17}^{(i)}$ that lead to the best agreement between the experimental data and the simu-

[5] From here on, all discussed values of α_q are given in units of $10^{-14}\,\mathrm{cm}^2/\mathrm{W}$.

[6] In Figure 4.18a and similar plots for a phase delay of $\Delta\phi = 0$, we consider "secondary fringes" the signal observed at emission angles of about ± 1 mrad, ± 3 mrad etc. The stronger signal at 0 mrad, ± 2 mrad is denoted "primary fringes".

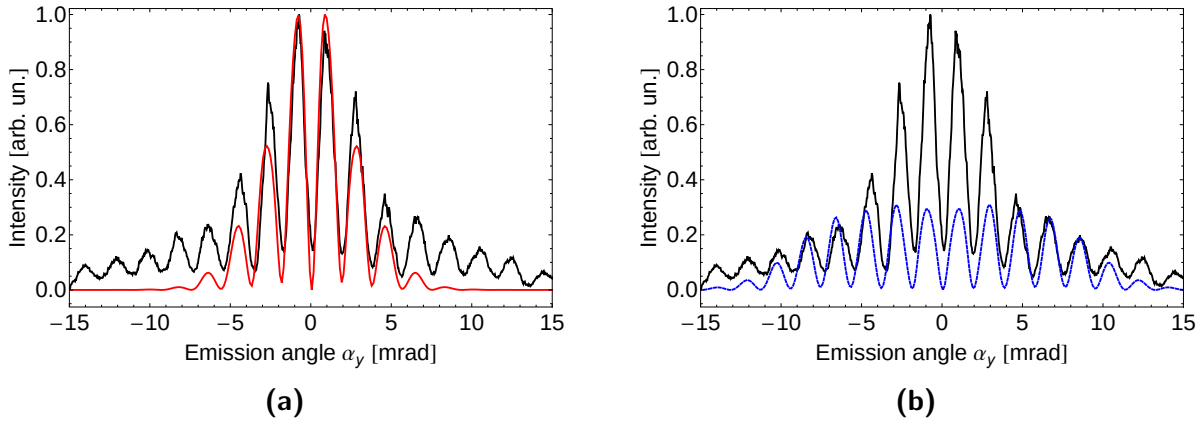

Figure 4.19: *Comparison of experimental (black) and numerically simulated (red, dashed blue) high harmonic far field profiles for the 17th harmonic at a phase delay of $\Delta\phi = \pi$. (a) Simulation for phase coefficient $\alpha_{17}^{(1)} = 2.1$ that was determined from the comparison for $\Delta\phi = \pi$ (Figure 4.18a) (b) Same for $\alpha_{17}^{(2)} = 5.1$ (Figure 4.18b). See text for details.*

lation in terms of the intensity ratio between the primary and the secondary fringes at the center of the emission pattern.

The two smallest phase coefficients extracted from that comparison are $\alpha_{17}^{(1)} = 2.1$ and $\alpha_{17}^{(2)} = 5.1$. As we can see from Figure 4.18a, the intensity ratio of the fringes is reproduced very well with $\alpha_{17}^{(1)}$ for small divergence angles, whereas the profile simulated with the larger $\alpha_{17}^{(2)}$ shows acceptable agreement for larger divergence angles (Figure 4.18b). Figure 4.19 shows a comparison of experimental and simulated data for a phase delay $\Delta\phi = 0$. The phase coefficients used in these simulation are the same as those extracted from the data for $\Delta\phi = \pi$ where the numerical reproduction of the secondary fringes was seen to be very sensitive to $\alpha_{17}^{(i)}$. We can see that the position of the fringes is very well reproduced for both $\alpha_{17}^{(i)}$ and that the relative fringe intensities are also reproduced fairly well.

In general, the profiles simulated with $\alpha_{17}^{(1)}$ are less divergent than those simulated with $\alpha_{17}^{(2)}$. It is interesting to note that both contributions seem to be necessary to approximately reproduce the full experimental emission pattern for both phase delays, that is, the more collimated central part in the angular range within about ± 5 mrad and the weaker and more divergent part for larger divergence angles. This is reminiscent of the long and the short quantum trajectories of which the long one leads to more divergent emission. Note, however, that the absolute values of the phase coefficients extracted from our visual comparison do not have any significance since their exact values depend on the simulation parameters of which some, e.g. the driving intensity, are not known precisely enough. In addition, without including our heuristic saturation model, there is no phase coefficient for which the agreement between experiment and simulation is as good as with saturation included. In the latter case, the absolute value of the α_{17} yielding the best agreement depends on the saturation parameters. Therefore, although our simulation is capable of reproducing the shape of the emission pattern remarkably

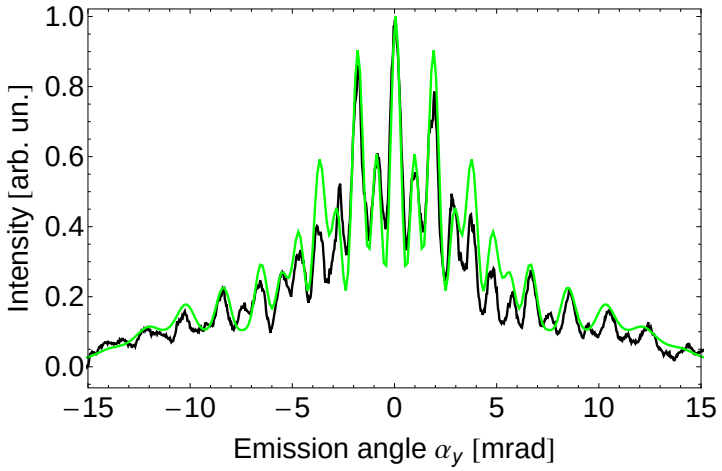

Figure 4.20: *Comparison between experimental data (black) and incoherently added simulation results (green) for a phase delay of $\Delta\phi = 0$. Simulation runs with different phase coefficients $\alpha_{17}^{(1)} = 1.94$ and $\alpha_{17}^{(2)} = 5.46$ were added according to $S(\alpha_{17}^{(1)}) + rS(\alpha_{17}^{(2)})$ where $r = 1.48$ and the obtained sum was normalized. Note that the phase coefficients in the incoherent sum are slightly different from the parameter values in Figure 4.18a.*

well, it does not allow to unequivocally identify contributions from the short and the long trajectory or to differentiate between them. Both extracted values for the phase coefficients are in good agreement with typical literature values for the short trajectory ($\alpha_s \approx 1$, cf. [161, 257]).

Although contributions from different quantum trajectories have to be added phase-coherently, which is currently not possible with our numerical simulation, it is still interesting to see the result of an incoherent sum. The result of incoherently adding two numerically simulated far field profiles (i.e. intensities) for a phase delay of $\Delta\phi = 0$ is illustrated in Figure 4.20. The green curve depicts the normalized sum $S(\alpha_{17}^{(1)}) + rS(\alpha_{17}^{(2)})$, where $S(\alpha_{17}^{(i)})$ is the result of a simulation run using $\alpha_{17}^{(i)}$ as a phase coefficient and r is a scaling factor. The phase coefficients have been slightly varied compared to those determined in Figure 4.18 for better overall agreement. It can be seen that the experimental profile is reproduced well and better than by the contribution of a single phase coefficient alone.

Using the phase coefficients $\alpha_{17}^{(1)}$ and $\alpha_{17}^{(2)}$ extracted from the comparison with typical experimental data for the characteristic delay $\Delta\phi = 0$, we numerically simulated the far field emission profiles of the 17th harmonic for a large range of delays around maximum temporal overlap. Subsequently, the profiles were combined into delay scans for comparison with experimental data. Note again that the results for $\alpha_{17}^{(1)}$ and $\alpha_{17}^{(2)}$ are obtained in independent runs of the simulation.

Figure 4.21 shows both experimental and numerical delay scans. Precision delay scans covering a delay range of ± 2 fundamental periods about maximum temporal overlap are shown in Figures 4.21a, 4.21c, and 4.21e. In contrast, the range of the delay scans shown in Figures 4.21b, 4.21d, and 4.21f is large enough to fully cover the temporal

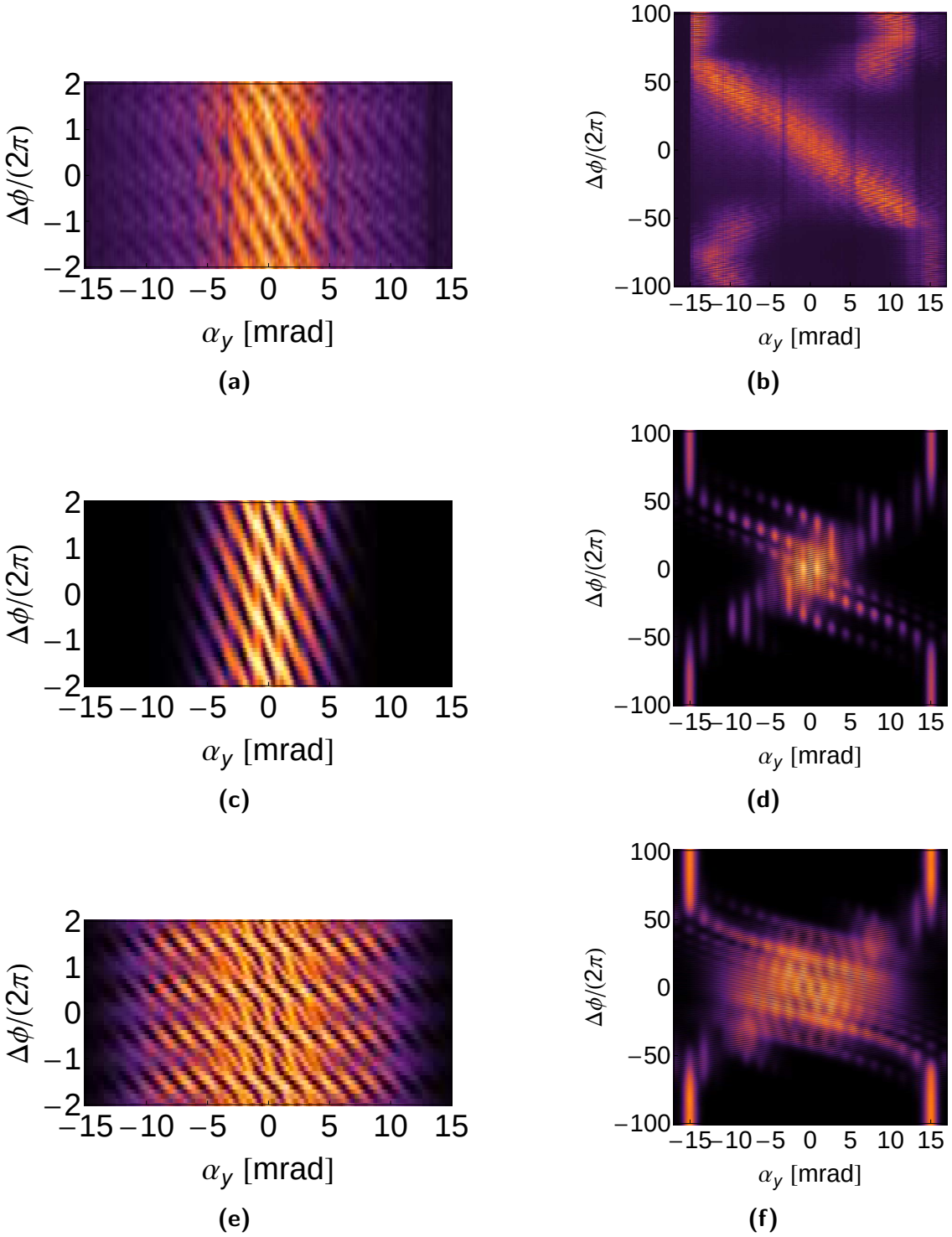

Figure 4.21: *Comparison of experimental (a, b) and simulated (c, d, e, f) delay scans for the 17th harmonic for delays around maximum temporal overlap (a, c, e) and for the full range of delays for which the pulses overlap (b, d, f). Simulations shown in (c) and (d) used* $\alpha_{17}^{(1)} = 2.1$*, those shown in (e) and (f) were simulated for* $\alpha_{17}^{(2)} = 5.1$*. See text for details.*

evolution from collinear HHG via NCHHG to collinear HHG again. In both scan ranges, experiment and simulation are in good agreement.

In particular, the spatio-temporal patterns of the simulated precision delay scans (Figures 4.21c and 4.21e) exhibit both a similar divergence and a similar regular alteration with delay compared to the experimental one (Figure 4.21a). The smaller divergence of the spatial emission pattern simulated with $\alpha_{17}^{(1)} = 2.1$ compared to that simulated with $\alpha_{17}^{(2)} = 5.1$ could be expected from the above discussions of the integrated far field profiles. In addition, however, the fringes in the underlying far field profiles simulated with $\alpha_{17}^{(1)}$ move at different angular speeds for the same phase advance $\Delta\phi$ than those simulated with $\alpha_{17}^{(2)}$, i.e. the "slopes" of the spatio-temporal patterns in Figures 4.21c and 4.21e are different. In the experimental precision delay scan shown in Figure 4.21a, the slope of the spatio-temporal pattern is similar to that of Figure 4.21c for small emission angles. With increasing angles, the slope seems to decrease continuously and becomes more similar to that of Figure 4.21e. We think that this is another indication that contributions from more than a single $\alpha_{17}^{(i)}$ are required to explain our experimental results.

In contrast to the precision delay scans, both simulated large range delay scans (Figures 4.21d and 4.21f) show obvious deviations from the experimentally observed spatio-temporal pattern (Figure 4.21b) in the region of temporal overlap. In particular, while the intensity of the generated radiation in the experiment is about equally strong and collimated in the temporal window in which the direction of emission changes continuously, the simulation with $\alpha_{17}^{(1)}$ predicts a strong and collimated signal just along the bisectrix of the driving beams. Both simulated delay patterns share the asymmetry with their experimental counterpart. Since the pulses in our code are not subject to any asymmetry, we cannot explain the origin of this agreement at this moment.

4.7 Work in progress: further numerical investigations

Based on a simplified description of the high harmonic dipole response, our numerical simulation can qualitatively reproduce several important features of the experimental data. At the same time, it is interesting to compare our experimental and simulation results to a more advanced numerical simulation, which may also allow a more quantitative understanding of NCHHG.

We thus started a collaboration with Carlos Hernández-García from the group of Luis Plaja at the University of Salamanca who adapted his numerical code to simulate non-collinear HHG in Xe. Details of the numerical approach are described in reference [258]. In brief, the single atom response is calculated using an extended version of the commonly used strong field approximation (see Section 3.2.3) that has been termed SFA+ [203]. The far field emission pattern is then obtained within the so-called discrete dipole approximation, i.e. the target volume is discretized into cells of macroscopic size that are subsequently treated as point-like dipoles for which analytical solutions of Maxwell's equations exist.

On the following pages, first results of ongoing systematic investigations of NCHHG for varying parameters are shown to exemplify general dependences. Unless stated otherwise, all results have been obtained for two Gaussian driving beams and $\sin^2$ pulse envelopes[7] with a FWHM duration of 16 fs. The beams are non-collinearly focused at an angle of $\theta = 30$ mrad to a common focus of $w_0 = 60$ nm in a Xe target with a Gaussian gas distribution ($L_{\mathrm{med}} = 140\,\mu$m). The single beam peak intensity is $2.2 \times 10^{13}\,\mathrm{W/cm^2}$, and both ionization and neutral dispersion are taken into account. Compared to the experiment, shorter pulses and lower intensities were used for our first investigations to reduce computational time and to avoid potential inaccuracies due to the implemented ionization model (ADK) near the barrier suppression regime of Xe (cf. Section 3.2.1), respectively.

[7] Using a pulse envelope of this form is computationally easier than both Gaussian and hyberbolic secant pulse envelopes since the latter only asymptotically decay to zero.

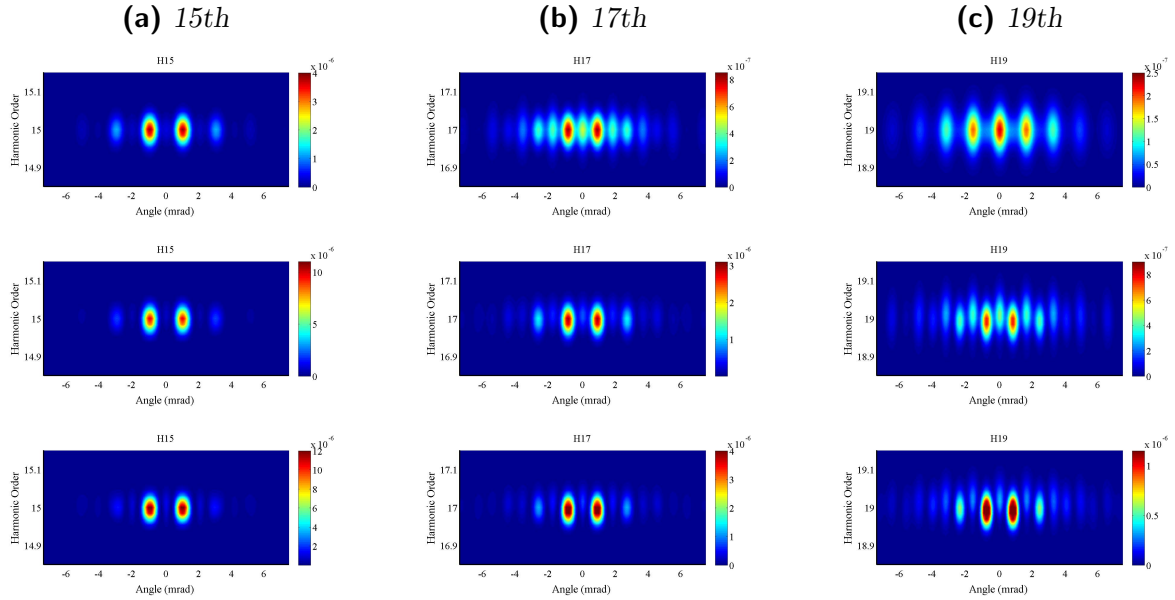

Figure 4.22: *Simulated far field profiles for the (a) 15th, (b) 17th, and (c) 19th harmonic order for different single beam driving intensities of, from top to bottom,* $2.2 \times 10^{13}\,\mathrm{W/cm^2}$, $3.2 \times 10^{13}\,\mathrm{W/cm^2}$, *and* $4.3 \times 10^{13}\,\mathrm{W/cm^2}$ *at a phase delay of* $\Delta\phi = 0$. *Note that individual color scales corresponding to the respective intensities in atomic units are used in each plot.*

4.7.1 Dependence on driving intensity

Figure 4.22 shows the simulated far field profiles of the strongest harmonic orders observed in our experiment (15th, 17th, and 19th) for a phase delay of $\Delta\phi = 0$ and three different (single beam) driving intensities, namely $2.2 \times 10^{13}\,\mathrm{W/cm^2}$, $3.2 \times 10^{13}\,\mathrm{W/cm^2}$, and $4.3 \times 10^{13}\,\mathrm{W/cm^2}$.

In agreement with our experimental results, the profiles of the 15th and 17th harmonic orders show two groups of fringes at each of the simulated intensities. However, the relative strengths of the fringes are seen to change with intensity so that it is no longer unambiguous to use the differentiation into "primary" and "secondary" fringes. This is particularly obvious for the 19th harmonic, where on-axis emission and only one group of fringes are observed at the lowest intensity. In contrast, a second group of fringes appears quite prominently at the two other intensities and only weak and spectrally shifted on-axis emission can be observed. A similar spectral offset was also visible in our experiments (cf. Figure 4.13). As a first conclusion, we note that the non-collinear emission profile is very sensitive to the intensity of the driving beams.

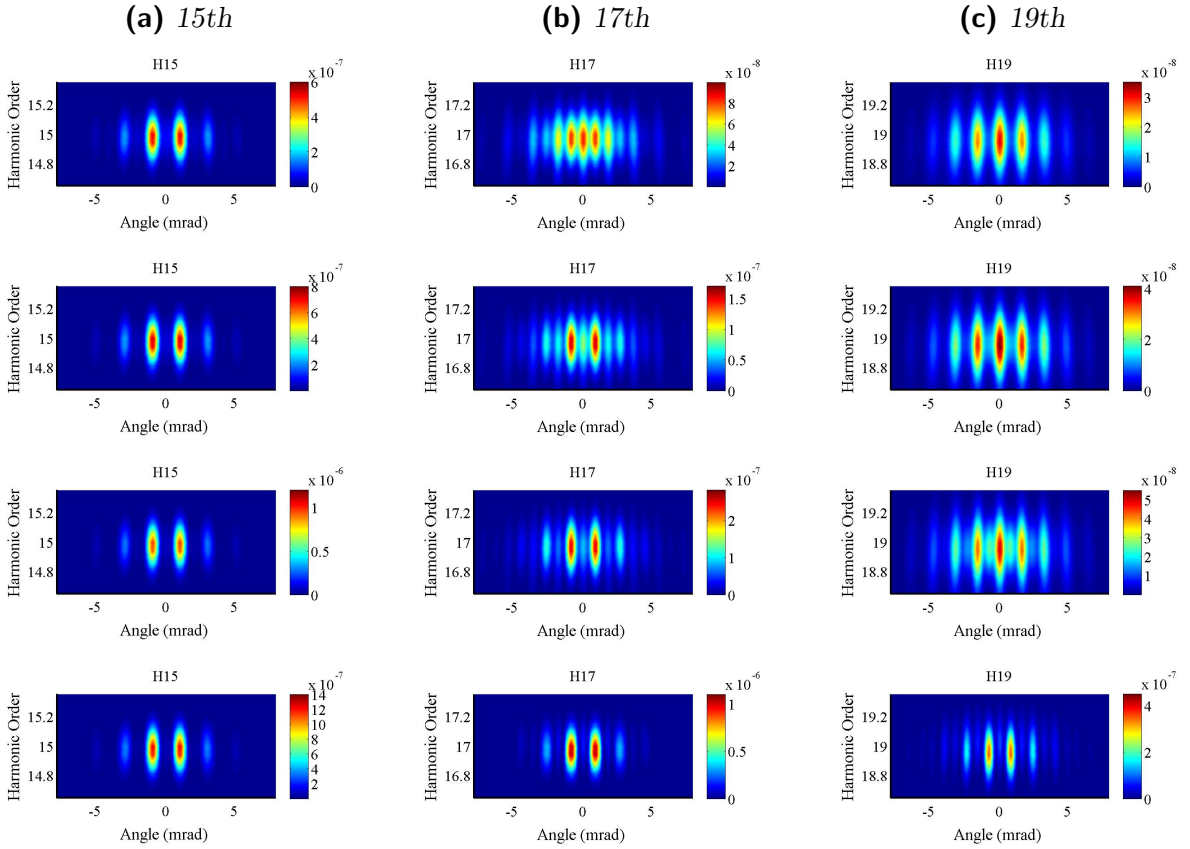

Figure 4.23: *Simulated far field profiles at a phase delay of $\Delta\phi = 0$ for (a) 15th, (b) 17th, and (c) 19th harmonic order for different waists of, from top to bottom,* 55 μm, 60 μm, 65 μm, *and* 70 μm. *Note that individual color scales corresponding to the respective intensities in atomic units are used in each plot.*

4.7.2 Dependence on waist

Figure 4.23 shows the simulated far field profiles of the 15th, 17th, and 19th harmonic for a phase delay of $\Delta\phi = 0$ and four different waists, from top to bottom, 55 μm, 60 μm, 65 μm, and 70 μm.

The simulation results indicate that the size of the waist is a crucial parameter for the observation of high harmonic emission along the bisector of the driving beams. While strong on-axis emission is present at the smallest waist for the 17th and the 19th harmonic, the on-axis contribution continuously decreases with increasing waist. The 15th harmonic profile does not vary strongly for the simulated waists and does only show very weak emission along the bisectrix.

As a conclusion, we note that the simulated profiles are extremely sensitive to comparably small variations of the driving beam waist. The latter should thus be precisely measured and controlled in an experiment.

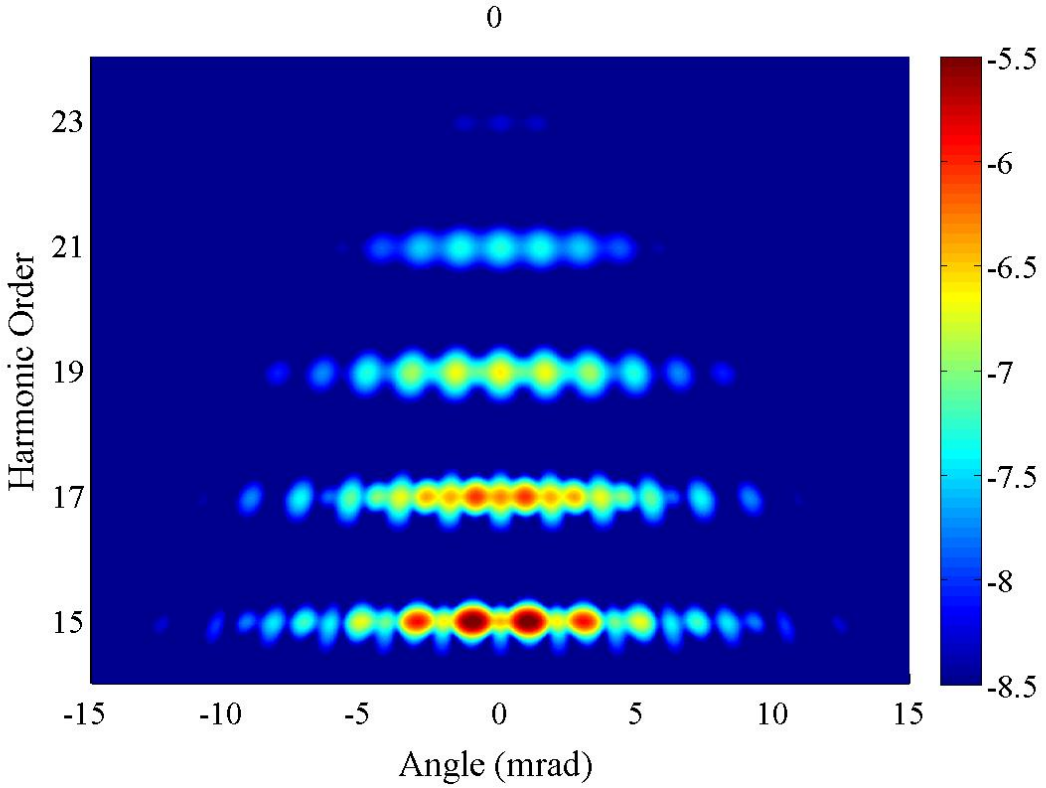

Figure 4.24: *Simulated non-collinear spectrum for a phase delay of* $\Delta\phi = 0$*. The logarithmic color scale represents the intensity in atomic units.*

4.7.3 Non-collinear spectrum

Figure 4.24 shows the simulated non-collinear spectrum for a phase delay of $\Delta\phi = 0$. In agreement with the measured spectrum shown in Figure 4.10, different harmonic orders exhibit a different fringe spacing so that the spectral content of the observed high harmonic radiation varies with the angle of emission. Since the divergence of the harmonic radiation decreases with order, the highest orders can only be detected close to the bisector of the driving beams. These aspects are further exemplified in Figure 4.25, which compares the emission angles 0 mrad and 1 mrad with regard to their spectral content, the corresponding temporal domain description (i.e. the generated attosecond pulse trains), and a time-frequency (wavelet) analysis.

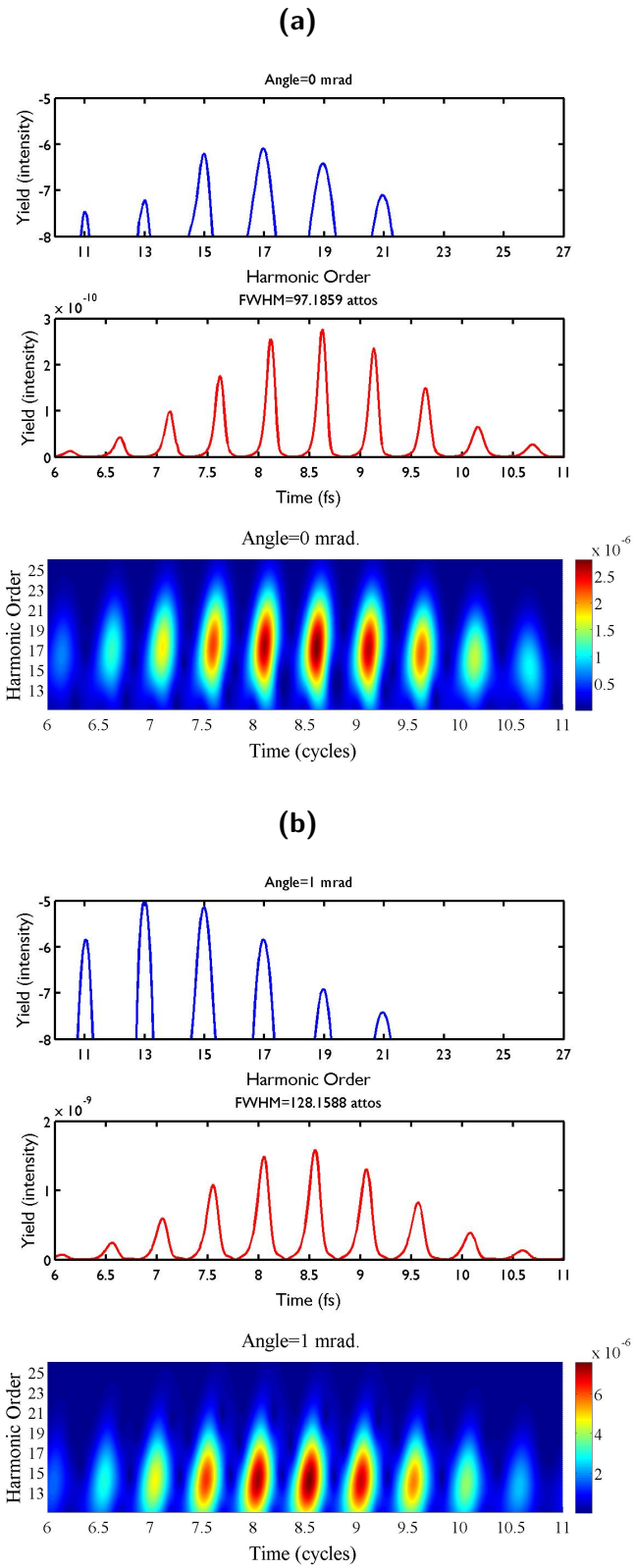

Figure 4.25: *Spectrum (top panel), corresponding temporal domain description (center panel), and time-frequency analysis (bottom panel) for emission angles of (a)* 0 mrad *and (b)* 1 mrad. *All data shown in atomic units. Compare Figure 4.24.*

4.8 Conclusion and outlook

Detailed experimental and numerical investigations of non-collinear high harmonic generation (NCHHG) were performed with amplified laser pulses. The potential of NCHHG as a combined generation and outcoupling method for cavity-assisted high harmonic generation had been verified in initial, spectrally not resolved experiments. In view of this application, the spectrally resolved far field profiles of the non-collinearly generated radiation and their dependence on the delay between the driving pulses were measured and analyzed. Strong spatial modulations of the harmonic emission patterns were observed for all detected harmonic orders. The appearance of the modulations, their spatial periods, and the delay dependence of the far field profilees could be reproduced qualitatively by a numerical simulation based on a simplified description of the high harmonic dipole response when a linearly intensity-dependent phase and saturation of the harmonic emission were considered. The agreement suggests that the far field profiles can be generally seen as the Fraunhofer diffraction pattern of the time-dependent spatially modulated interference structure created by the two non-collinear driving beams. However, first results of additional, more sophisticated numerical simulations reveal that the particular appearance of the emission pattern shows a high sensitivity to the specific experimental parameters used. Further investigations are under way.

The theoretical and experimental investigations presented in this chapter confirm that NCHHG is a wavelength-independent outcoupling method with high efficiency. However, challenges arise from its nature as an intereference phenomenon. For conceivable angles, the far-field intensity patterns are spatially modulated so that in some applications only a certain fraction of the generated light can be used. In addition, the requirements on beam quality and pointing stability are high. But we expect that a realization using e.g. two crossed bowtie cavities provides sufficient spatial filtering and enhanced stability. At the same time, since the direction of emission depends on the delay, chirped or broadband driving pulses may still cause angular chromatic dispersion within a single harmonic order. In that case, a spatially filtered beam could still suffer from spectral modulations across its profile.

An interesting option offered by NCHHG may be to experimentally determine the linear phase coefficients of the intensity-dependent atomic dipole phase. Although the latter can crucially influence the macroscopic properties of the observed high harmonic radiation, there have been only few attempts to measure it experimentally [134, 141, 149, 150]. In one of those, using a setup similar to ours, information about the phase coefficients could be extracted from the observation of shifts in high harmonic interference patterns, which were produced by two closely spaced sources, as a function of intensity [149, 150]. Such an investigation may also be possible in a refined version of the experiments presented here.

Independent control of the two driving beams allows to study a large number of interesting combinations of experimental parameters and their effects on the spatial, spectral, and temporal characteristics of the non-collinearly generated radiation. Among others, the fundamental wavelength could be different for the two beams. Bertrand and co-workers studied the wave-mixing characteristics of NCHHG by focusing a strong

fundamental beam and its weak second harmonic into a gas target at an angle [247]. Considering momentum conservation, they could clearly attribute emission observed under a certain angle to a specific number of contributing photons from each beam.

An important application of NCHHG may arise from the spatio-temporal mapping that can be achieved by scanning the delay between the driving pulses. This mapping could be used as a high order autocorrelation method to determine the pulse duration and the pulse shape of the fundamental. It was recently shown that under suitable conditions, the non-collinear geometry can also be used for an all-optical space-time characterization of attosecond pulses [259]. In fact, as pointed out by Vasily Strelkov [260], the spatio-temporal mapping may be exploited for the production of isolated attosecond pulses if two pulses with different pulse durations and intensities are used. Consider NCHHG driven by a weak short pulse and an intense long pulse. The temporal window in which non-collinear emission can be observed is defined by the duration of the shorter pulse. If the weak pulse consists of just a few optical cycles, the harmonic radiation will be emitted mainly in the direction of the beam of the intense longer pulse except for the narrow temporal window when the short pulse beam contributes to the high harmonic generation process. The prerequisite for this gate to work is that the angular separation of the non-collinearly emitted radiation from the collinear radiation is large enough to be resolved. That way, it may be feasible to realize a "digital" version of the recently demonstrated "attosecond lighthouse" [230, 231, 261], i.e. emission of an angularly separated isolated attosecond pulse in a defined direction. It may also be possible to use identical driving pulses or to combine the non-collinear generation geometry with polarization or ionization gating techniques to produce angularly resolved isolated attosecond pulses.

While an implementation of NCHHG in an enhancement cavity brings about severe technical challenges, the advent of high power solid state and fiber amplifiers may enable the realization of NCHHG and potentially a non-collinear gating scheme at unprecedented repetition rates of several MHz. The first demonstration of (collinear) single pass high harmonic generation experiments at multi-MHz repetition rates is the topic of the following chapter.

5 Single pass high harmonic generation at multi-MHz repetition rate

In this chapter, the first successful realizations of single pass high harmonic generation at repetition rates exceeding 10 MHz with a state-of-the-art high power amplifier system are reported. Technical constraints still limit the achievable performance in our experiments and the generated EUV power levels are not comparable yet to those currently achievable through cavity-assisted HHG. However, our proof-of-principle demonstrations show that multi-MHz EUV radiation can now be produced using more versatile table-top setups than before, thus paving the way for a wide range of applications.

5.1 Introduction

Currently, the only routinely available coherent EUV sources are based on laser-driven high harmonic generation (HHG). These have enabled the generation of coherent radiation with photon energies well into the soft x-ray range [80] as well as the production and usage of EUV pulses on the attosecond time scale [71].

However, although desirable for many applications, table-top sources that provide coherent EUV radiation at repetition rates in the MHz regime have remained scarce so far. The main reason for that is that the extremely nonlinear HHG process shows a threshold behavior. Since the required peak intensities exceeding $10^{13}\,\mathrm{W/cm^2}$ cannot be attained routinely with the output of a typical femtosecond oscillator, the commonly used approach is based on reducing the repetition rate of the laser system to the kHz regime in order to concentrate the achievable average power in fewer, but more intense driving pulses. Using such laser systems, which usually take advantage of the chirped pulse amplification (CPA) technique [7], high harmonic radiation can then be generated in a simple single pass geometry. For typically achieved peak powers on the order of $10^{10}\,\mathrm{W}$, weak focusing conditions are sufficient to reach the required threshold intensities so that comparably high conversion efficiencies and high harmonic yields are obtained (cf. Section 3.3.3.5).

Scaling the repetition rate of laser systems suitable for single pass HHG into the MHz regime is very challenging even when CPA is used. Increasing the repetition rate of a typical 1 kHz CPA system by a factor of $\sim 10^3$ requires a simultaneous increase of the same order in average power to keep the pulse energy constant. Aside from a lack of suitable high brightness pump sources in many cases, the resulting high average and peak powers are on the order of the surface and bulk damage thresholds of the employed gain materials and optical components. So far, progress in fiber amplifier

technology has enabled HHG at up to 500 kHz [262] and 1 MHz [263] with amplified pulses. Direct HHG with the output of a long-cavity Ti:sapphire oscillator operating at a repetition rate of 4 MHz was reported only recently [264]. At the same time, advances in thin disk laser technology [265], where output powers approaching ~ 300 W at a repetition rate of 16.3 MHz and a pulse duration of ~ 600 fs directly from the oscillator are now achievable [266], have brought oscillator-driven single pass HHG at repetition rates exceeding 5 MHz into reach.

The generation of usable coherent EUV radiation at repetition rates higher than ~ 10 MHz has so far only been possible with cavity-assisted HHG[1]. Since its first demonstration [8, 9], the cavity approach has matured significantly. Systems generating EUV power levels of $\sim 100\,\mu$W in a single harmonic order [10] and EUV radiation with photon energies exceeding 100 eV [15] have been reported, and first spectroscopic experiments employing a cavity-assisted EUV source have been performed [11, 12]. However, the attainable average intracavity driving powers are currently limited to below 10 kW because of ionization dynamics in the intracavity gas target and both damage and nonlinear responses of the cavity mirrors [10, 16–18]. As long as the level of ionization is the main factor preventing a further increase of the intracavity power, the obvious choice to improve the yield for a certain harmonic order is to resort to looser focusing conditions. This, of course, requires a modification of the resonator and is not easily possible without reducing the spot sizes on the cavity mirrors. To address the problem of mirror damage, an enhancement cavity design with larger spot sizes on the cavity mirrors has been proposed and realized [268]. Although this design has enabled the demonstration of unprecedented average power levels of almost 200 kW in an empty resonator with 200 ps pulses [269], further improvements of the cavity-concept under conditions suitable for efficient HHG become increasingly challenging.

In contrast, the realization of single pass HHG at multi-MHz repetition rates primarily relies on the (commercial) availability of a high power laser system and can take advantage of existing techniques from the kHz domain. It may depend on the application whether the omission of an actively stabilized high finesse enhancement cavity in a HHG setup at the expense of a probably equally complex high power laser system is advantageous. It is unquestionable, however, that HHG at moderate repetition rates of ~ 10 MHz can be realized more easily in a single pass geometry than with a cavity with impractically large dimensions. In addition, the single pass approach promises several general advantages both in terms of versatility and usability that shall be summarized in the following.

The single pass geometry is not as sensitive to nonlinear phase shifts as an enhancement cavity, where the phase shifts can significantly limit the achievable enhancement and thus the EUV output power. Possible sources for such phase shifts are nonlinear responses of the cavity mirrors, ionization dynamics in the gas target, and the method that is used to separate the generated EUV radiation from the fundamental, e.g. a

[1] A demonstration of multi-MHz HHG with a standard Ti:sapphire oscillator relying on plasmonic field enhancement in nanostructures [267] is not considered here since the long-term stability and the beam quality of this EUV source are still to be proven.

grating mirror [13]. This reduced sensitivity also leads to relaxed requirements on the separation of fundamental and EUV radiation in single pass HHG systems compared to cavity-assisted EUV sources. Furthermore, multi-color HHG and other well-known quasi-phase-matching techniques can be employed to improve the conversion efficiency, which is currently not conceivable in an enhancement cavity. In general, more complex HHG schemes are more difficult to realize with an enhancement cavity than in a single pass geometry. For example, polarization gating cannot readily be extended to cavity-assisted HHG. The latter does not permit a fully independent adjustment of the repetition rate and the carrier-envelope offset frequency either. In terms of flexibility, only minor adjustments to a single pass HHG setup are required for a large range of repetition rates and focusing conditions while major modifications to the enhancement cavity become necessary when the repetition rate or the focusing conditions are to be varied.

In this chapter, we report on the first experimental realization of single pass HHG at multi-MHz repetition rates. These proof-of-principle demonstrations were rendered possible by the use of a high power solid state amplifier system of the latest generation.

5.2 Laser system

A master oscillator power amplifier (MOPA) system was used for the experiments described in this chapter. In all cases, an Yb:YAG-based Innoslab power amplifier stage formed the key element of the laser system. Innoslab amplifiers are particularly well-suited for multi-MHz repetition rate experiments at high average powers such as the single pass HHG experiments described in the following sections because no CPA is involved above repetition rates of about 10 MHz, which is a rather unique feature among the available high brightness laser sources. A more exhaustive review of the Innoslab concept along with a detailed comparison to other available power amplifier technologies can be found in the literature [239,270]. The basics of the Innoslab concept are described in the following.

A conceptual schematic of the Innoslab amplifier is shown in Figure 5.1. The amplification crystal is a small slab ($1 \times 10 \times 10\,\mathrm{mm}^3$ of Yb:YAG in our case). Both large facets of the slab are soldered to a water-cooled heat sink (not shown in the figure) which allows for an efficient overall thermal management. Two commercially available high power diode stacks (Jenoptik JOLD-720-HSC-4L) produce up to $\sim 660\,\mathrm{W}$ each at a wavelength of 940 nm to longitudinally pump the Yb:YAG slab from both sides. The pump radiation is shaped by a planar waveguide and subsequently focused such that it homogeneously illuminates a $\sim 0.2 \times 10 \times 10\,\mathrm{mm}^3$ volume at the center of the slab. Taking advantage of the polarization of the pump light, the overall pump absorption can be boosted to $\sim 90\,\%$ by telecentric refolding of the pump radiation that is not absorbed during its first passage of the slab.

As illustrated in Figure 5.1, a confocal cavity arrangement of just 35 mm length consisting of two cylindrical end mirrors and two dichroic plane folding mirrors allows to guide the seed radiation (shown in red) through the slab several times to multiply the

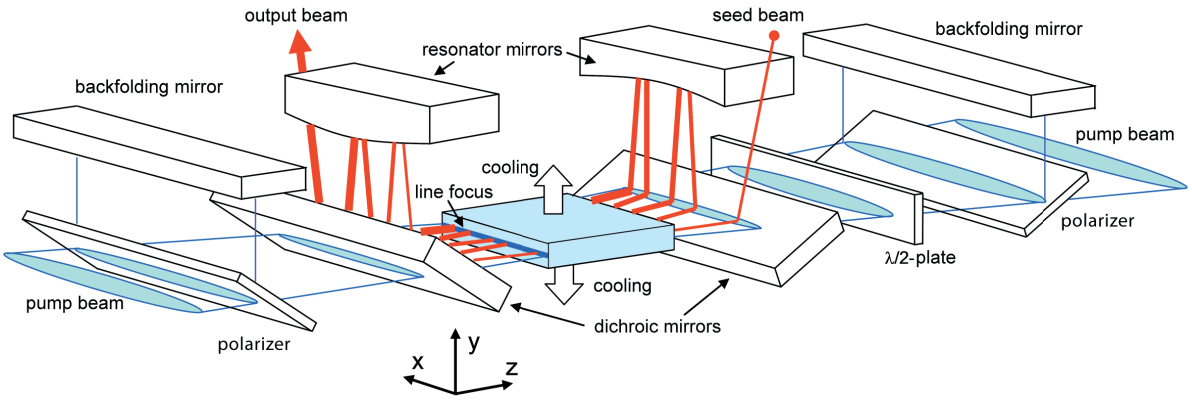

Figure 5.1: *Schematic of Innoslab amplifier concept. Figure adopted from [271] by courtesy of P. Russbueldt.*

moderate single pass gain (2–10). Apart from the compactness and ruggedness of the technical design, the key advantage of the refolding configuration is that the Innoslab amplifier effectively operates as a single pass amplifier since the seed beam traverses a different part of the gain volume during each pass. The beam parameter of the seed beam is reproduced along the fast axis of the slab (y-axis in Figure 5.1) by the resonator and the cylindrical thermal lens, which is formed due to the one-dimensional heat flow. At the same time, the cavity has a magnification of $M = 1.4$ along the slow axis (x-axis) so that the beam is continuously expanded during amplification. That way, damages due to the increase in power can be avoided and nonlinear phase shifts due to the optical Kerr effect are kept low. The latter are quantified by the so-called B-integral (cf. (2.25)) which is therefore small for an Innoslab amplifier.

For the employed slab size, an average power of more than 550 W can be achieved after amplification. A typical amplifier slope, i.e. a plot of output power vs. pump power (here parameterized by the pump diode current as the experimentally accessible parameter), is depicted in Figure 5.2 (blue circles). In practice, however, a severe technical limitation in the setup behind the Innoslab amplifier reduced the amount of usable power to around 200 W at the time when the experiments were conducted: The only then commercially available optical isolator for such high powers (Jenoptik 6-P1030-HP1) was just specified and usable for up to 200 W of polarized radiation. At higher powers, both the reduced isolation due to thermally induced double refraction in the isolator crystal and the significant deterioration of the beam quality due to strong thermal aberrations of the induced thermal lens are detrimental for the experiments[2]. Operation without an optical isolator is, of course, possible, yet not recommended if avoidable since any small amount of light that gets reflected back into the amplifier will get amplified to very high power and may damage or even destroy both optical components and the seed oscillator. We

[2]In the meantime, our collaborators from the Fraunhofer ILT in Aachen have solved this problem by developing an optical isolator design that does not suffer from these problems even at powers of up to 1 kW. A commercial product based on this design is available from the Fraunhofer spin-off company Amphos GmbH.

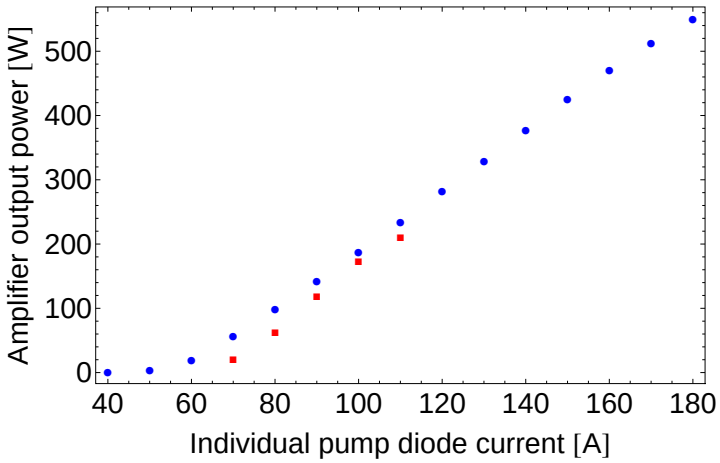

Figure 5.2: *Amplifier output power as a function of pump power, here parameterized by pump diode current. Blue dots show typical amplifier performance. Red squares indicate performance at the time of the measurement. See text for details.*

experienced such a scenario during one of our initial frequency doubling experiments with the Innoslab amplifier: Since the full output power of the amplifier was needed for efficient doubling at the high repetition rate of 584 MHz and the isolator thus had to be omitted, an optically induced defect in the doubling crystal caused enough backscattering into the amplifier to lead to the destruction of the seeding fiber oscillator used at that time.

The red squares in Figure 5.2 indicate the amplifier performance at the time of our first single pass HHG experiments with short pulses that will be described in the following Section 5.3.1. While the maximum output power of the amplifier was not used due to the optical isolator, the different threshold behavior and the offset compared to the slope formed by the blue circles originate from a minor damage of the joint between the slab crystal and the heat sink which led to different amplifier characteristics at low pump power but did not hamper our experiments.

The Fourier-limited output pulse duration of our Innoslab amplifier is $\sim 680\,\mathrm{fs}$ independent of the potentially broader spectral bandwidth of the seed source due to gain narrowing in the amplifier when a gain material with a comparably small emission bandwidth such as, in our case, Yb:YAG is used for the slab crystal. The choice of Yb:YAG over other potential gain materials with larger emission bandwidth is mainly based on its very favorable properties (e.g. high emission cross section, low saturation intensity, large heat conductivity) and the availability of crystals of high optical quality in the required size. Further development is under way in the laboratories of our collaborators with slab materials such as Yb:KGW or Yb:Lu_2O_3 that have a larger emission bandwidth and would thus allow shorter amplifier output pulses but are technically more demanding to use due to their mechanical and thermal properties.

One of the favorable features of the Innoslab concept is the almost diffraction-limited output beam quality of the amplifier. As we have seen in Section 2.1.2.2, a source of high brightness is particularly important for the tight focusing geometries that are

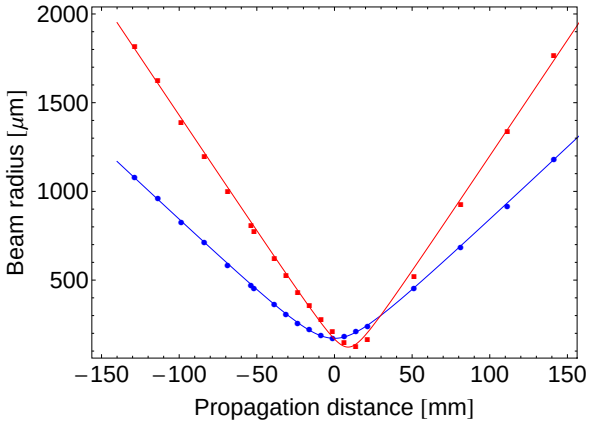

Figure 5.3: *Measured caustic for the sub-50 fs experiments.*

usually required for single pass HHG at multi-MHz repetition rates. Figure 5.3 shows a typical caustic of the amplifier output that was measured behind the optical isolator with a beam propagation analyzer (Spiricon M2-200FW) during the sub-50 fs single pass HHG experiments (see Section 5.3.1). The measured beam quality factor is $M^2 = 1.08 \times 1.22$ (fast $\times$ slow axis) with a slightly astigmatic and elliptic focus. While the slightly suboptimal ellipticity and astigmatism originate from inevitable day-to-day drifts of alignment and can easily be optimized again, further improvement of the currently achievable beam quality factors is extremely challenging. Therefore, the brightness of the Innoslab amplifier is $\sim 25\,\%$ lower than that of an enhancement cavity providing the same average power in a perfectly Gaussian cavity mode according to (2.17). In general, the Innoslab concept permits even higher amplifier output powers than used here by simply scaling the dimensions of the slab such that the efficient heat removal is not compromised. To this end, high brightness pump diodes and high quality crystals are required.

A picture of the Innoslab amplifier used for the experiments presented in the following sections is shown in Figure 5.4.

5.3 Experiments

Two different single pass HHG experiments at multi-MHz repetition rates were conducted. While most of the experimental layout and the experimental parameters just varied insignificantly, the main and most crucial difference between those experiments was the duration of the IR pulses used for HHG. In the following, we will first describe the initial proof-of-principle experiment with externally compressed sub-50 fs pulses at strongly reduced amplifier output power and then present the results of an experiment with the uncompressed sub-ps amplifier pulses at about 50% of the overall available power.

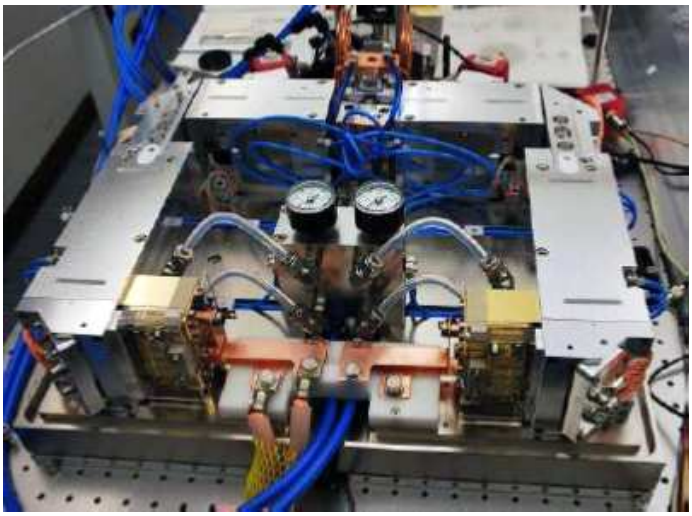

Figure 5.4: *Picture of the Innoslab amplifier used in the single pass HHG experiments described in this chapter.*

5.3.1 Sub-50fs pulses

Figure 5.5 shows a schematic of the experimental setup. A commercial passively mode-locked Yb:KGW seed oscillator (HighQ femtoTrain) delivers 300 fs pulses with an average power of 2.2 W at a center wavelength of 1030 nm to the Yb:YAG Innoslab power amplifier that has been described in detail in the previous section. At the oscillator repetition rate of 20.8 MHz, nine passes through the slab crystal are used for optimum amplification of the seed radiation. When operating the pump diodes at 2×110 A, the amplified output ($P \approx 175$ W) has almost diffraction limited beam quality ($M^2 = 1.08 \times 1.22$, measured with Spiricon M-200FW) while the output pulse duration is limited to ~ 680 fs by the gain bandwidth of the Yb:YAG crystal. The amplified pulses are thus unfavorably long for efficient HHG in a rare gas, particularly the most efficient Xe, due to ionization of the medium as has been discussed in Section 3.4.2. Therefore, an additional nonlinear pulse compression stage was implemented in which the pulses are first spectrally broadened and then temporally compressed.

5.3.1.1 Spectral broadening and pulse compression

As discussed in Section 2.1.4.2, many of the commonly used spectral broadening schemes are not feasible or at least very challenging to realize technically for the relatively long $\sim 10\,\mu$J-pulses that our amplifier provides. We chose self-phase modulation (SPM) in a large mode area (LMA) photonic crystal fiber (PCF) as the nonlinear spectral broadening scheme based on the results of detailed studies that were carried out by our collaborators [43]. In these investigations, one of the employed fibers (NKT Photonics LMA-35) had been identified as the most promising in terms of spectral broadening and mode quality. Unfortunately, however, this fiber was reproducably damaged at pulse energies above $\sim 2\,\mu$J. Consequently, the input power to the nonlinear pulse compression

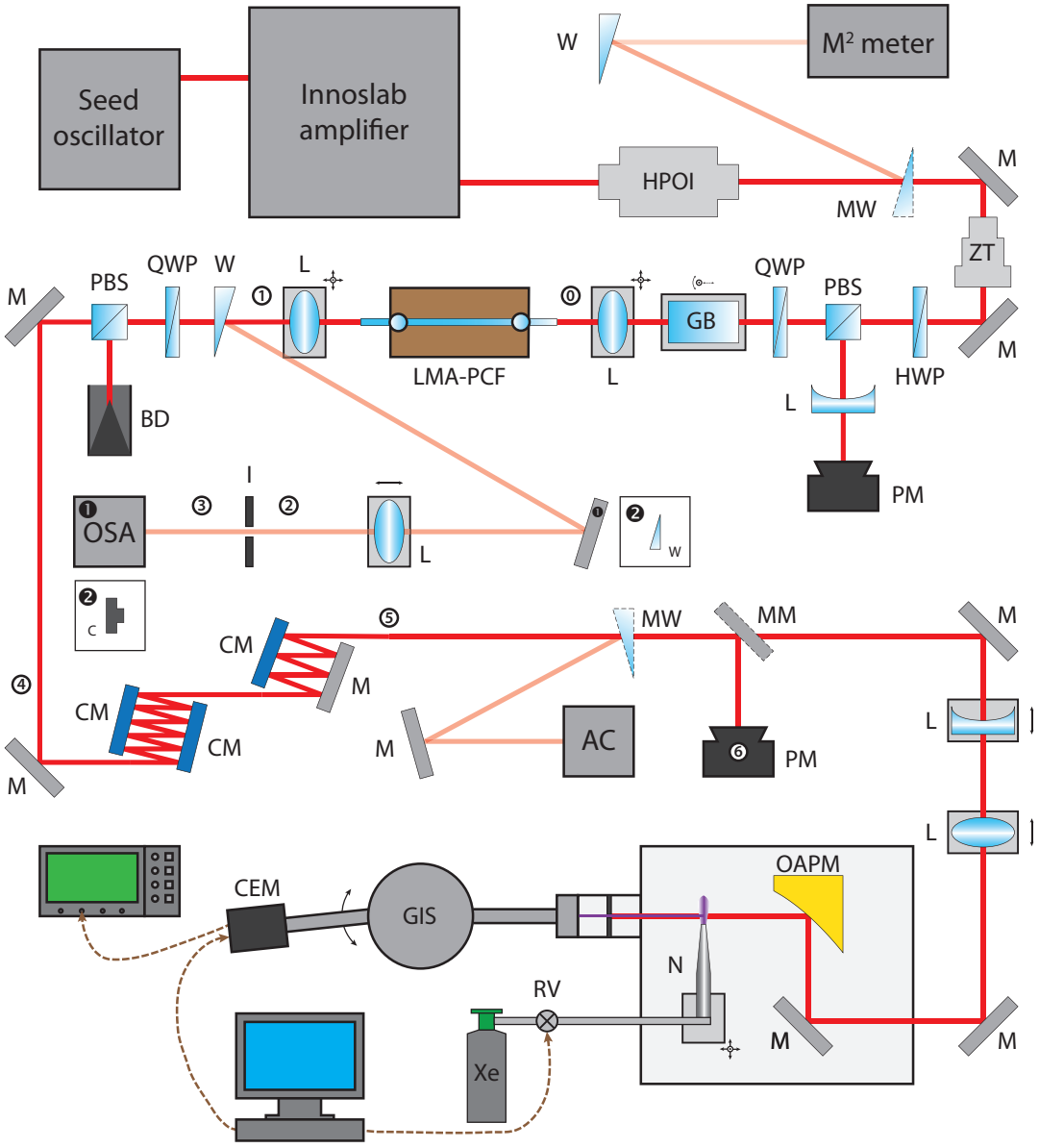

Figure 5.5: *Schematic of experimental setup. HPOI: high power optical isolator, (M)W: (movable) wedge, (M)M: (movable) mirror, ZT: zoom telescope, HWP: half-wave plate, PBS: polarizing beam splitter, L: lens, PM: power meter, QWP: quarter-wave plate, GB: glass block, LMA-PCF: large mode area photonic crystal fiber, I: iris, OSA: optical spectrum analyzer, C: camera, BD: beam dump, CM: chirped mirror, AC: auto-correlator, OAPM: off-axis parabolic mirror, N: nozzle, RV: regulating valve, GIS: grazing incidence spectrometer, CEM: channel electron multiplier. See text for further details.*

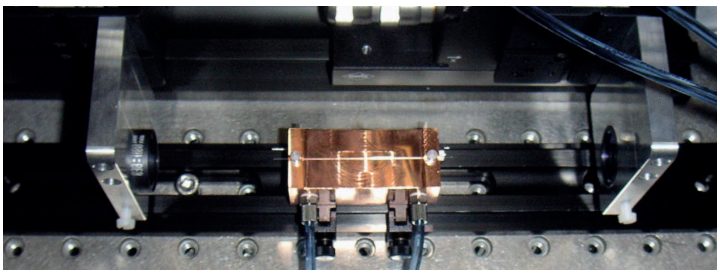

Figure 5.6: *Picture of the assembly used to hold the PCF. The fiber is held by the two glass cylinders located at the ends of the copper block and is not in direct contact with the latter.*

stage had to be limited to about 40 W (of the available $\sim$ 200 W) in all our experiments which turned out to be the main limitation of this setup.

As depicted in Figure 5.5, the power sent to the PCF can be adjusted using a polarization-based attenuator consisting of a half-wave plate and a polarizing beam splitter cube. The PCF is held above a V-shaped groove in a copper block by two notched glass cylinders located at both ends of the groove. A picture of the assembly is shown in Figure 5.6. In order to minimize potential heating effects of the power not coupled into the fiber, the copper block is actively water-cooled. An anti-reflection (AR) coated focusing lens ($f = 60\,\mathrm{mm}$) mounted to a 3d precision positioning stage (Thorlabs NanoMax) is used to couple the light into the PCF. When angled with respect to the direction of propagation by a goniometer, a 20 mm thick AR coated fused silica window in front of the focusing lens causes a parallel shift of the beam and thus allows to adjust the coupling angle in combination with the lens. That way, it is possible to compensate for fiber cleave angles of up to 5 °. Coupling to the PCF can be further optimized through matching the input beam diameter to the fiber by means of a zoom telescope (1–3x, Sill Optics S6ASS5310/328). The spectrally broadened beam is recollimated behind the fiber by an achromatic focusing lens ($f = 60\,\mathrm{mm}$) held by an identical 3d precision positioning stage and then sent to a chirped mirror compressor. Two $\lambda/4$-plates are installed to convert the linearly polarized amplifier output into circularly polarized light for the nonlinear spectral broadening setup and to recover the linear polarization afterwards. This procedure is advantageous because the electric field amplitude of circularly polarized light is a factor of $\sqrt{2}$ smaller than that of linearly polarized light of the same average power so that the same spectral broadening can be achieved at higher average power without damaging the fiber.

Diagnostics is implemented at different points of the nonlinear pulse compression stage. A permanently installed wedge sampling the spectrally broadened main beam allows to image the near field of the fiber exit onto an actively water-cooled iris whose diameter is chosen such that the cladding modes of the fiber are clipped. Behind the iris, the power coupled into the core of the PCF can thus be determined reliably with a temporarily installed power meter. Without the latter, the light goes to an optical spectrum analyzer (OSA) which monitors the broadened spectrum. Alternatively, the spatial mode of the fiber-coupled light can be assessed by imaging the end facet of the fiber to a CMOS camera using an additional wedge in the beampath (insets ❷ in

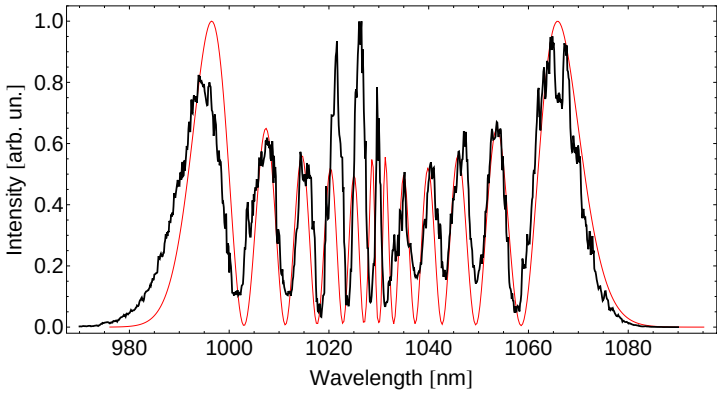

Figure 5.7: *Measured infrared spectrum after broadening due to self-phase modulation in a 7.1 cm long piece of LMA-35 PCF. The width of the broadened spectrum is* $\Delta\lambda \simeq 80\,\mathrm{nm}$. *For comparison, the spectrally broadened spectrum calculated using the experimental parameters according to* (2.29) *in Section 2.1.4.2 is shown as a thin red line.*

Figure 5.5). Behind the chirped mirror compressor, a wedge and a broadband high reflector on flip mounts allow us to measure the autocorrelation and the average power of the compressed pulses, respectively. In combination with additional (not permanently installed) power measurements at specific points along the beam path (indicated as ① – ⑥ in Figure 5.5), the overall performance of the nonlinear pulse compression stage can be monitored and controlled.

For the experiment, we launched about 40 W of the available amplifier output into a PCF of 7.1 cm length. At that input power, the amplifier output spectrum broadens to a FWHM of $\Delta\lambda \simeq 80\,\mathrm{nm}$. A broadened spectrum is shown in black in Figure 5.7. The additional thin red line in the figure corresponds to the SPM-broadened spectrum calculated via (2.29) using the experimental parameters (cf. Section 2.1.4.2) and shows very good agreement with the measured spectrum in terms of both modulation and spectral width. The coupling efficiency to the fiber was found to be above 80 %. The amount of the input power that is coupled into the core of the fiber and thus determines the amount of self-phase modulation can be obtained from measuring the power both in front of and behind the iris in the diagnostics beam (i.e. at the positions ② and ③ in Figure 5.5). We found that it reproducably amounts to $> 80\,\%$ with minor differences depending on both alignment and the individual fiber pieces used.

After spectral broadening, the pulses are compressed in the chirped mirror compressor. We found a multi-pass configuration with one high reflector and three custom-made chirped mirrors introducing 13 bounces with a nominal group delay dispersion of approximately $-450\,\mathrm{fs}^2$ per bounce to best compress the pulses. Both the measured autocorrelation trace (red) and the autocorrelation trace calculated from the spectrum assuming a flat spectral phase (blue, dashed) are shown in Figure 5.8. Since the exact pulse shape corresponding to the broadened spectrum is not known, we retrieved the FWHM pulse duration from the measured autocorrelation using the following method: In a first step, the FWHM of the pulse calculated from the spectrum under the assumption of a flat spectral phase is determined. This calculated pulse is then mathematically

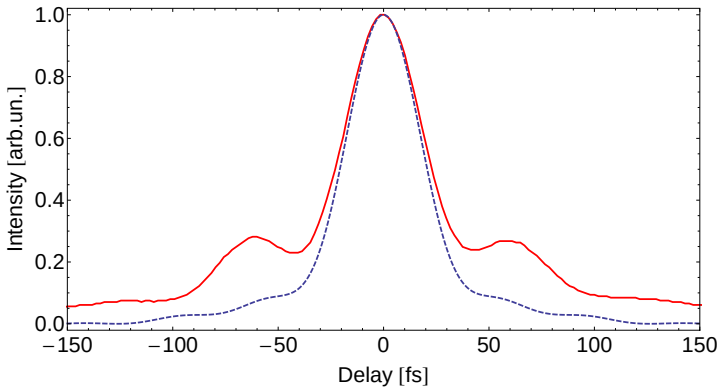

Figure 5.8: *Measured (red, solid) and calculated (blue, dashed) autocorrelation trace. The retrieved FWHM pulse duration is* $\tau_p = 35\,\mathrm{fs}$.

autocorrelated to obtain the FWHM of the autocorrelation trace. Comparison of these two FWHM's then yields a retrieval factor that enables us to estimate the pulse duration from the experimental autocorrelation data. Using this method, we obtained $\tau_p = 35\,\mathrm{fs}$ from the measured autocorrelation trace. The more prominent side lobes in the measured autocorrelation trace compared to the calculated one probably indicate that higher order dispersion is not efficiently compensated for by the mirrors used. At a compression factor of ∼20, the overall transmission of the whole nonlinear pulse compression stage is about 60%, resulting in an average power of up to 23 W available for HHG after compression (⑥ in Figure 5.5). However, taking the shape of the measured autocorrelation into account, we can estimate that just about 60% of this power is concentrated around the temporal center of the underlying pulse while the wings contain the remaining 40%. Thus, the achieveable peak intensity is about a factor of 2 lower than it could be with ideally compressed pulses.

5.3.1.2 Vacuum system and HHG setup

Since the pulse energy after compression was limited to $\sim 1\,\mu\mathrm{J}$ in our setup, tight focusing was required to reach a peak intensity sufficient for HHG. Therefore, we magnified the IR beam with a 1:2-telescope consisting of two fused silica lenses with a broadband AR coating that are mounted on translation stages for fine adjustment of the telescope. The spot size ($1/e^2$ intensity radius) of the magnified beam is $w = 2.4\,\mathrm{mm}$. After magnification, the beam is guided into the main experimental chamber which can be evacuated to a pressure of $\sim 6 \times 10^{-6}\,\mathrm{mbar}$ without additional gas load.

Inside the vacuum chamber, a gold-coated 90° off-axis parabolic mirror (OAPM) with an effective focal length of 20 mm focuses the pulses to a waist radius of $w_0 = 4.6\,\mu\mathrm{m}$ (see Figure 5.9a). Since the quality of the focus and thus the achievable peak intensity critically depend on the incidence angle of the beam on the OAPM, we replaced two high reflectors in front of the OAPM by wedges to be able to analyze and optimize the beam profile at the focus before evacuation. However, since the pixel size of the CCD-based beam profiler (DataRay WinCamD) was too large to adequately determine

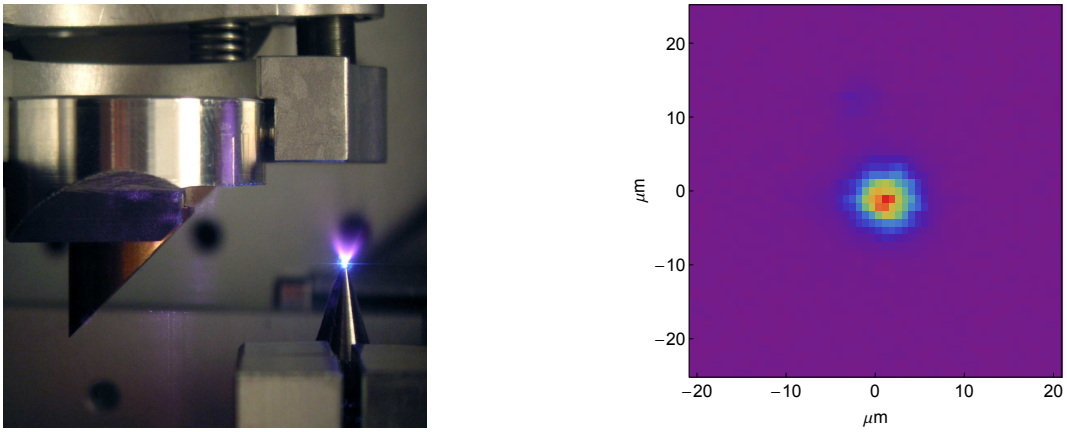

(a) (b)

Figure 5.9: *(a) Picture of gold-coated off-axis parabolic mirror and Laval gas nozzle with bright violet plasma created from Xe gas. (b) Measured beam profile at the focus from which* $w_0 = 4.6\,\mu$m *is determined.*

the spot size, we had to image the focus by means of a magnifying microscope objective. The required pre-calibration of the whole assembly was done by imaging the lines of a transmission grating with 200 lines per mm. Figure 5.9b shows the recorded beam profile at the focus after first optimization. It can be seen that the beam is still slightly elliptic as a consequence of astigmatism introduced by the OAPM. However, pre-alignment turned out to be good enough to observe plasma generation in air after switching back to the high reflectors. The brightness of the generated plasma proved to be a sensitive indicator of the focus quality and can thus be exploited for further optimization of the alignment. For the measured spot size and the achieved laser parameters, a peak intensity of $4 \times 10^{13}\,\mathrm{W/cm^2}$ at the focus can be estimated.

Once the experimental chamber is evacuated, high harmonic radiation is generated in a continuous Xe gas jet that is produced in the vicinity of the focus by a Laval nozzle (orifice $L_{\mathrm{med}} \simeq 150\,\mu$m). The position of the nozzle is pre-aligned using the plasma spot generated in air before evacuation and can be precisely adjusted with motorized translation stages to optimize the harmonic yield under vacuum conditions. When the nozzle is operated at a Xe backing pressure of 2 bar and a flow rate of $\sim 3 \times 10^{-1}\,\mathrm{mbar \cdot l/s}$ set by a manual gas dosing valve (Pfeiffer EVN 116), the pressure in the experimental chamber stabilizes at around $1 \times 10^{-3}\,$mbar. Absoption of the generated harmonic radiation on the way to the detection system is thus negligible.

5.3.1.3 Detection system and data analysis

The harmonic radiation generated in the noble gas target propagates into a differentially pumped grazing incidence EUV monochromator (McPherson Model 248/310), which is separated from the interaction chamber by a 2 mm diameter pinhole located 244 mm downstream of the gas jet. The pinhole also serves as a partial beam block for the fundamental beam which diverges more strongly than the generated harmonic radiation

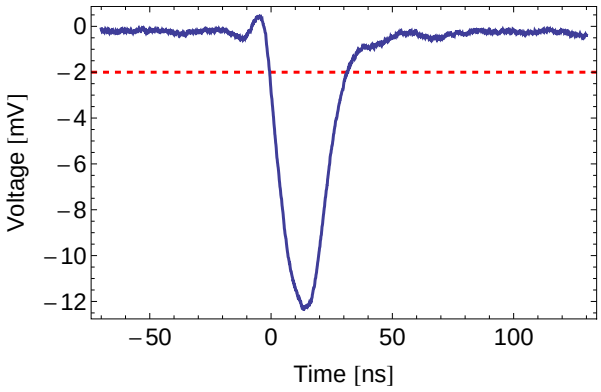

Figure 5.10: *Typical event signature obtained with the CEM detector. The trigger level of* $-2\,\mathrm{mV}$ *used for post-processing of the acquired data is indicated by a dashed red line. At that trigger level, the pulse duration is about* 30 ns.

(cf. Section 3.3.3.3). The monochromator is equipped with a 133.6 grooves/mm grating and a solar blind channel electron multiplier (CEM) in pulse counting mode so that computer-controlled movement of the CEM along the Rowland circle enables the detection of the spectrally resolved harmonic radiation with virtually no background from residual (scattered) fundamental radiation. Since differential pumping ensures that the pressure at the CEM remains at a level of $\sim 1 \times 10^{-5}\,\mathrm{mbar}$ with the gas load in the experimental chamber, the detector can be operated at a voltage of 2.9 kV without risk of breakthrough. During the wavelength scan, the signal from the CEM is acquired with a fast oscilloscope (LeCroy WavePro 7300A) as a trace of pulse counts versus time. The typical signature of a single detection event, i.e. the voltage signal resulting from the electron avalanche created by a single harmonic photon incident on the CEM, is shown in Figure 5.10.

For the evaluation of the recorded time trace, background noise and unavoidable ringing of the detector itself after a previous event have to be discriminated from real events by setting an appropriate threshold level. We found a threshold value of $-2\,\mathrm{mV}$ to yield reliable results when post-selecting the data. The typical event duration at this threshold level is about 30 ns. From the dataset of the post-selected signal events, we calculate a photon count rate as a function of time. Using the scanning parameters of the monochromator, this data can be synchronized with the counter values of the monochromator. Those correspond to the mechanical movement of the detector along the Rowland circle during data acquisition and are thus directly related to the wavelength of the observed photons. To obtain a smooth spectrum, a moving Gaussian window function is applied to the data before the final conversion into a spectrally resolved photon count rate. Note that the spectral resolution is limited to about 3 nm by this data acquisition and evaluation technique.

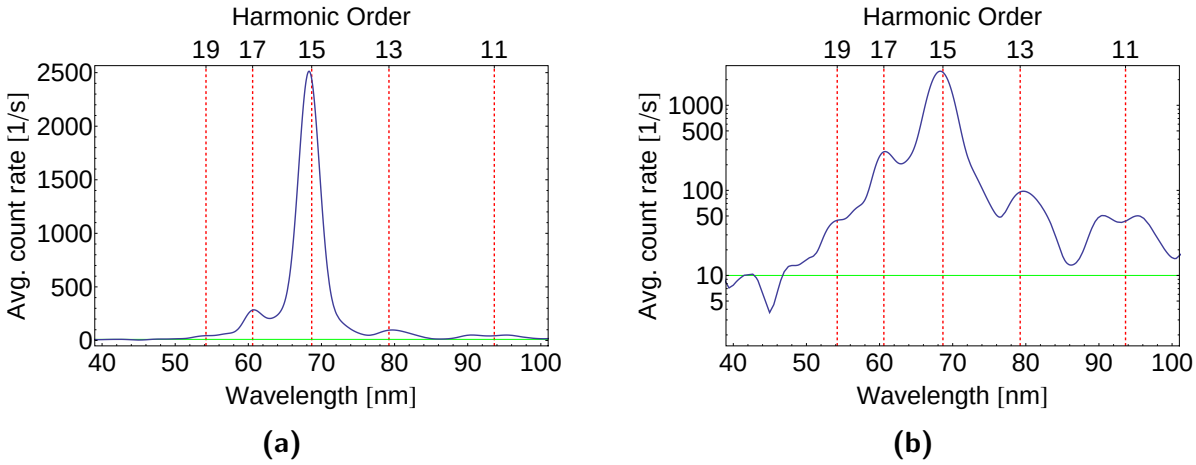

Figure 5.11: *Measured high harmonic spectrum in (a) linear and (b) logarithmic scale. The red dashed lines indicate odd harmonics of the fundamental. The green line marks the background. The strong peak near* 70 nm *corresponds to the 15th harmonic.*

5.3.1.4 Results and discussion

The resulting spectrum is shown in Figs. 5.11a and 5.11b in linear and logarithmic scale, respectively. The red dashed lines indicate the 11th to 19th harmonic order of the fundamental. High harmonic radiation ranging from the 11th (93.6 nm) up to the 17th order (60.6 nm) can be identified in Figure 5.11b and there are strong indications that the 19th order (54.2 nm) was generated as well. Those are supported by the fact that the single atom cutoff lies between the 19th and the 21st harmonic order for the estimated experimental peak intensity of $\sim 4 \times 10^{13}\,\mathrm{W/cm^2}$. The strongest observed peak with an about one order of magnitude higher count rate than the other harmonics corresponds to the 15th harmonic (68.7 nm).

Since systematic investigations in this setup were hampered by the unexpected temporary unavailability of a seed laser, the huge difference in yield between the observed harmonic orders cannot be explained in a conclusive way. While we can hence not generally exclude beam pointing instabilities and fluctuations in the overall performance of the laser system during the acquisition of the spectrum, we did not observe such fluctuations while setting up the experiment. We also consider it unlikely that the spectral diffraction efficiency of the monochromator grating, which is only theoretically known, strongly affected the detectable intensities of neighboring harmonic orders in the experiment. However, since the conditions for phase matching can differ significantly for different harmonic orders in tight focusing geometries (cf. Section 3.3.1), the observed relative intensities can at least partly be attributed to phase matching effects. For the experimental parameters, the level of ionization caused by a single pulse is below 3 % (see Figure 3.8a) and thus negligible. Since the gas jet is located very close to the focus, where the contribution of the intensity-dependent phase can be neglected as well, the neutral dispersion of the target gas has to compensate for the geometric phase mismatch. This can typically not be realized equally well for all harmonics at the same time or may

not be possible at all at experimentally feasible pressures [102].

The absolute high harmonic output power that can be obtained with our system is limited in both a general and a technical way by the extremely tight focusing geometry that is necessary because of the limited peak power of the system when including the spectral broadening unit:

The obvious general limitation originates from the small interaction volume and phase matching. For the realized focusing conditions, the threshold length defined by (3.33) is $L_{th}(15) \simeq 150\,\mu$m for the 15th harmonic. However, according to (3.29), the geometrical phase lag induced by focusing accumulates to π for a harmonic order q after a distance

$$L_q^{\text{geo}} \simeq \frac{\pi b}{2(q-1)} \tag{5.1}$$

so that the high harmonic yield in a gas target of length L_{med} is limited by the reduced effective source volume due to phase matching when $L_q^{\text{geo}} \lesssim L_{\text{med}}$ [272]. For our experimental conditions, this applies for all observed harmonic orders. In particular, $L_{15}^{\text{geo}} \simeq 15\,\mu\text{m} \ll L_{th}(15) \simeq L_{\text{med}}$.

The technical limitation of the achievable EUV output power due to tight focusing is the reduced geometric transmission of the generated light through the experimental apparatus. The divergence of the generated harmonic radiation, while always lower than that of the fundamental, increases for tighter focusing of the latter. In our setup, if we consider the divergence model $\theta_q = \sqrt{p}\,\theta_1/q$ discussed in Section 3.3.3.3 with $p = 6$, $\sim 90\,\%$ of the EUV is geometrically clipped by the $425\,\mu$m wide entrance slit of the monochromator, which is located about 670 mm downstream of the noble gas target. Therefore, if the harmonic radiation produced in a tight focusing geometry is to be delivered to an experiment, great care has to be taken in the design of the setup to minimize geometrical losses.

To evaluate the system performance independent of the specific setup behind the gas target (e.g. apertures and diagnostic elements), it is common practice to calculate the amount of EUV generated in the target from the detected power by correcting it for all power-reducing factors along the way from the target to the detector.

In our case, the generated power in the 15th harmonic is estimated according to the following equation

$$P_{\text{EUV}}(q) = q\,\frac{hc}{\lambda_1} \cdot N_\nu\ \chi_s\ \chi_c\ \chi_m\ \chi_g \tag{5.2}$$

where N_ν is the total number of detected photons per second in harmonic order q and the factors χ_g, χ_m, χ_c, and χ_s account for the geometric transmission through the experimental apparatus, the efficiency of the monochromator grating, the quantum efficiency of the CEM, and the undersampling of the oscilloscope, respectively. The latter is the result of recording a time trace of 64 s with average sampling intervals of $4\,\mu$s with the oscilloscope during the wavelength scan of the monochromator. Since the typical event duration at the employed trigger level of -2 mV was ~ 30 ns as shown in Figure 5.10, $\chi_s \approx 133$. Assuming $\chi_m^{-1} \lesssim 30\,\%$ and $\chi_c^{-1} \lesssim 40\,\%$ based on the (calculated) values provided by the manufacturers and taking into account $\chi_g^{-1} \approx 10\,\%$, we can thus give a

conservative estimate of $\sim 1\,\mathrm{nW}$ for the total generated power in the 15th harmonic order.

This power is about three to five orders of magnitude lower than the EUV powers now routinely provided by cavity-assisted HHG [10–12, 15], which emphasizes the impressive level of maturity that these systems have reached since the first proof-of-principle demonstrations. It is therefore quite interesting to compare our results with those achieved with the first and second generation enhancement cavity systems.

In the first demonstration of cavity-assisted HHG by Gohle et al. [8, 273], a generated power of $\sim 0.82\,\mathrm{nW}$ in the 11th harmonic of a Ti:sapphire system with an intracavity peak power of $P_p = 2.1 \times 10^7\,\mathrm{W}$ was reported. Both the peak power and the generated power of this system are comparable to the respective parameters of the single pass experiments presented in this section. In a second generation enhancement cavity system [249, 256], the generated EUV power could be increased by about three orders of magnitude. This achievement was mainly enabled by the 10 times higher available peak power which allowed looser focusing.

With our amplifier system, at least an order of magnitude more peak power should be available for HHG when using a more robust spectral broadening scheme, e.g. the one introduced in reference [26] or a method similar to the one realized by Nurhuda et. al [34, 35][3]. Therefore, power levels on the order of several μW and beyond seem quite feasible for the next generation multi-MHz single pass EUV sources.

5.3.2 Sub-ps pulses

The single pass HHG experiment with externally compressed pulses described in the previous section was mainly limited by the nonlinear pulse compression stage, which capped the usable driving power. Therefore, ignoring the unfavorable effects of ionization for a moment, it seems a somewhat logical choice to entirely omit that bottleneck in the setup.

However, according to (2.31), if the 680 fs pulses provided by the Innoslab amplifier shall be used for HHG without compression, the pulse energy will have to be scaled up by a factor of ~ 20 to keep the peak power constant. Fortunately, our amplifier allows scaling the driving power by a factor of up to 10 compared with the short pulse experiments before the aforementioned disadvantageous effects of the high power optical isolator set in. The remaining factor of 2 required for peak power equivalence can be realized by using a seed oscillator with a reduced repetition rate of 10 MHz.

The effects of ionization can be addressed in the following way: According to Figure 3.8a, a fraction of ionization exceeding 30 % is expected in Xe for a single 680 fs pulse with the same peak intensity as in the short pulse case. While ionization may thus limit the overall yield in Xe, Figure 3.8a predicts a strongly reduced level of ionization at the same peak intensity in Kr. This trend continues for Ar (cf. Figure 3.6a) so that

[3] In fact, a scheme to which the author contributed the first and still very vague idea has recently been demonstrated by our collaborators. Details cannot be disclosed here due to a pending patent application.

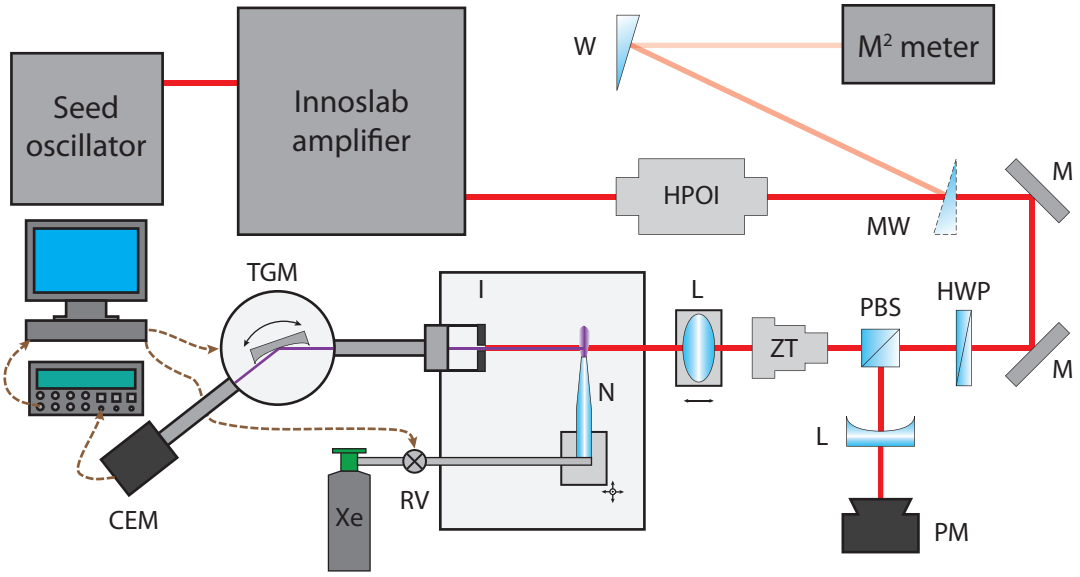

Figure 5.12: *Schematic of experimental setup for single pass HHG with long pulses. HPOI: high power optical isolator, (M)W: (movable) wedge, M: mirror, HWP: half-wave plate, PBS: polarizing beam splitter, L: lens, PM: power meter, ZT: zoom telescope, N: nozzle, RV: regulating valve, I: iris, TGM: toroidal grating monochromator, CEM: channel electron multiplier. See text for further details.*

we devised a set of experiments exploiting the versatility of the single pass geometry to investigate the achievable yield in different target gases for different focusing conditions. However, before we could obtain conclusive data, the main amplifier was scheduled to be used in a joint experiment with our collaborators (see Section 5.4). Therefore, just the results of our very first experiments in Xe can be reported in the following.

Figure 5.12 shows a schematic of the experimental setup. Apart from the omission of the nonlinear pulse compression stage, the schematic reveals three important alterations compared to the sub-50 fs experiment: (i) the exchange of the seed oscillator, (ii) the use of different focusing optics, and (iii) the implementation of a fully computer-controlled data acquisition in conjunction with a different EUV monochromator. The 20.8 MHz solid state seed oscillator was replaced by a customized commercial Yb-doped fiber laser system (MenloSystems Orange A) which provides 600 fs pulses with an average power of up to 3 W at a center wavelength of 1030 nm. The fundamental repetition rate of 100 MHz can be reduced by integer divisors with an intracavity electro-optic modulator (EOM). For the experiments detailed here, the repetition rate of the oscillator was set to 10 MHz. After amplification of the seed radiation in seven passes through the slab crystal of the Innoslab amplifier, 680 fs pulses with pulse energies exceeding 21 μJ at an M^2 factor of about 1.35 $\times$ 1.65 are available. The considerably reduced beam quality compared to our first single pass experiments at multi-MHz repetition rate (cf. Section 5.3.1) can partially be attributed to the onset of thermal aberrations caused by the high power optical isolator above $\sim$ 200 W. However, it is also a consequence of degraded amplifier performance due to suboptimal alignment that could not be fixed at

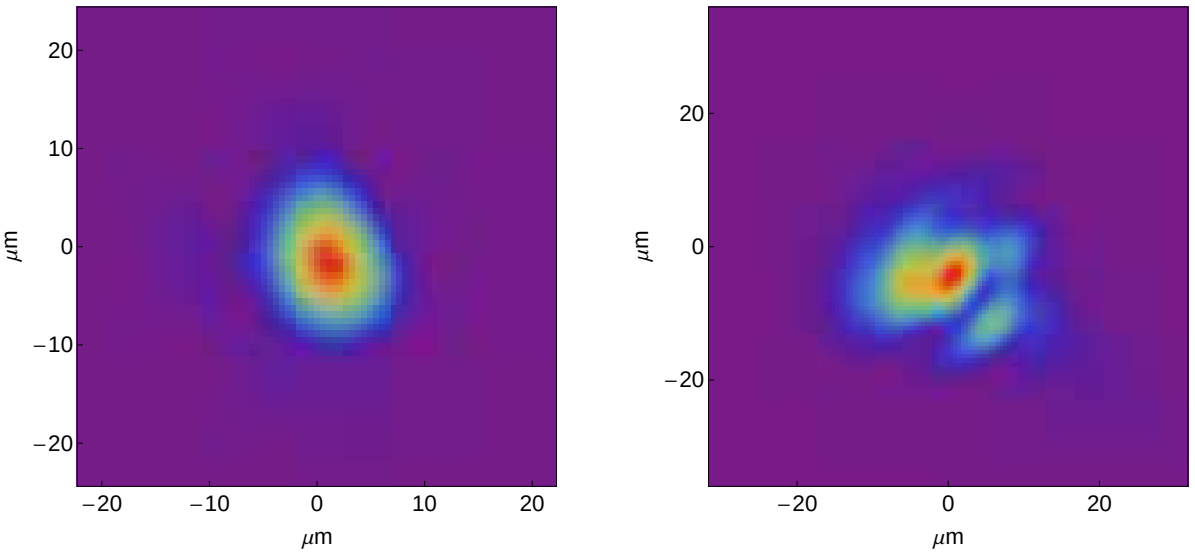

(a) *Magnification 2.0* **(b)** *Magnification 2.5*

Figure 5.13: *Measured beam profiles at focus with estimated waist radii of (a)* $w_0 \approx 7.1\,\mu$m *and (b)* $w_0 \approx 11\,\mu$m*. Note that the scale of the plots is different.*

the time of the experiment.

5.3.2.1 Vacuum system and HHG setup

A polarization-based attenuation unit behind the high power optical isolator allows to send pulses of variable energy into the vacuum chamber. In general, the requirements on the focusing optics are less demanding due to the long pulse duration and the corresponding narrow spectral bandwidth. However, to reach peak intensities above $10^{13}\,\mathrm{W/cm^2}$, tight focusing is still mandatory. Therefore, the beam is magnified with a fused silica zoom beam expander (1–3x, Sill Optics S6ASS5310/328) before being focused by a single AR-coated fused silica lens ($f = 50\,$mm) whose position can be varied with a translation stage. In contrast to our experiments with sub-50 fs pulses, all optics are located outside the vacuum chamber, thus facilitating alignment or exchange. The gas target is the only remaining element inside the chamber and consists of a motorized 3d translation stage that can be equipped with custom-made end-fire glas nozzles of various orifice diameters between $10\,\mu$m and $200\,\mu$m (Hilgenberg GmbH).

Before attempting single pass HHG, a pre-calibrated assembly consisting of a microscope objective and a beam profiler (DataRay WinCamD) was positioned in the open vacuum chamber to analyze the focus for different magnification settings of the beam expander and for different powers. For that purpose, a 45 ° high reflector placed in the beam path behind the zoom telescope temporarily directed most of the IR into a beam dump while the small fraction of transmitted light could be used for the measurement.

Figure 5.13 shows two beam profiles at the focus that were measured at different times for slightly altered experimental parameters. While the profile depicted in Figure 5.13a

was recorded at $\sim 215\,\mathrm{W}$, $M^2 = 1.11 \times 1.36$, and a magnification of 2.0, Figure 5.13b shows the profile for $\sim 215\,\mathrm{W}$, $M^2 = 1.32 \times 1.66$, and a magnification of 2.5 at the time the HHG experiments were conducted. The former profile is that of a slightly elliptic Gaussian beam with a waist of $w_0 \approx 7.1\,\mu\mathrm{m}$. The waist radius of the distorted profile of the latter can be estimated to be about $11\,\mu\mathrm{m}$ despite the stronger magnification of the IR beam before focusing that should theoretically compensate the effect of the higher M^2 value. From the measured waist radius, a peak intensity of up to $4 \times 10^{13}\,\mathrm{W/cm^2}$ at the focus can be inferred.

While it was rather straightforward to identify the deteriorating output beam quality of the amplifier as an obviously detrimental factor for the beam quality at the focus, measurements at different times during an experimental day clearly revealed that thermal effects occuring on a slow time scale were also involved. The latter, primarily suspected to originate from thermal lensing in the beam expander, not only led to an increased spot size at the (additionally shifted) focus, but also further deteriorated the beam quality. Unexpected at the time of the experiments, these observations illustrate that both an amplifier with high brilliance and careful selection and thermal management of all optical elements along the beam path are mandatory requirements for efficient and stable operation of such a single pass EUV source.

Before evacuation of the chamber for the main experiment, plasma generation in air is exploited to pre-align and optimize the position of the nozzle with respect to the focused IR beam. Under vacuum conditions, the latter generates high harmonic radiation in the continuous gas jet that is produced by supplying xenon to the nozzle at a backing pressure of 2.5 bar and alternable flow rates controlled by a motorized gas regulating valve (Pfeiffer EVR 116). With the additional gas load from the target, the pressure in the interaction chamber rises from around $9 \times 10^{-6}\,\mathrm{mbar}$ to stable values ranging from about $1.5 \times 10^{-2}\,\mathrm{mbar}$ to $\sim 6 \times 10^{-2}\,\mathrm{mbar}$ depending on the respective flow rates. At these pressure levels, the reabsorption of the harmonic radiation by the Xe background becomes relevant as will be discussed later.

5.3.2.2 Detection system and data analysis

A water-cooled pinhole with a diameter of 1 mm, which is located about 20 cm downstream of the gas jet, separates the interaction chamber from a differentially pumped EUV monochromator (Jobin Yvon LHT-30) with fixed entrance and exit slits (1 mm width). The incident EUV radiation is spectrally resolved by computer-controlled rotation of the toroidal monochromator grating (550 grooves/mm) and subsequently detected with a solar-blind channel-electron multiplier (Photonis CEM4839), which is operated in current mode at a voltage of 2.3 kV. As a consequence of differential pumping, the pressure at the detector remains at a level of $\sim 4 \times 10^{-5}\,\mathrm{mbar}$ throughout the experiments. The current from the detector is measured with a multimeter (Keithley 2001) as the voltage over a properly dimensioned resistor (100 MΩ for all data presented here) and recorded with a computer using the GPIB interface of the multimeter. A software interface based on the LabVIEW environment unites the control of both the regulating valve and the monochromator grating rotation and the data acquisition from the CEM

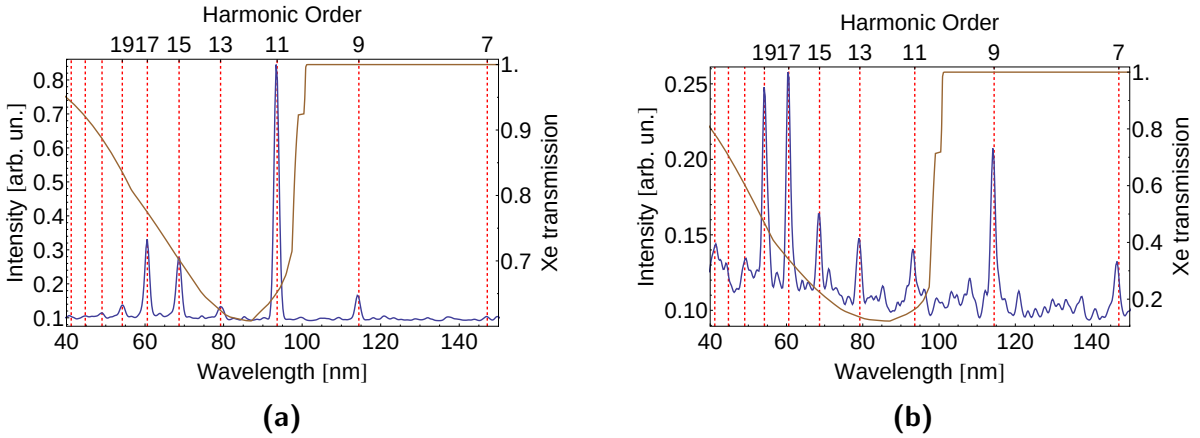

Figure 5.14: *Measured high harmonic spectra obtained for (a)* $\sim 24\,\mu$J *pulses, a Xe gas flow of* 6×10^{-1} mbar $\cdot$ l/s, *and a chamber pressure of* 1.5×10^{-2} mbar *and (b)* $\sim 26\,\mu$J *pulses, a Xe gas flow of* 8×10^{-1} mbar $\cdot$ l/s, *and a chamber pressure of* 6.3×10^{-2} mbar. *Odd harmonics of the fundamental are indicated by red dashed lines. The transmission spectra of Xe at the respective pressure levels for a* 21 cm *path are shown as a brown line.*

via the multimeter.

Since the employed EUV monochromator is not absolutely calibrated, the acquired data is shifted in wavelength such that the observed harmonic spectrum coincides best with the expected spectral positions of the high harmonics of the fundamental radiation. The shifted data is then averaged with a 1 nm wide moving Gaussian window function.

5.3.2.3 Results and discussion

Two experimental high harmonic spectra recorded at slightly altered experimental parameters are shown in Figure 5.14. The spectral positions of the odd harmonics of the fundamental are shown as red dashed lines. After the correctional wavelength shift of the data mentioned in the previous section, high harmonics ranging from the 19th (54.2 nm) to the 7th (147.1 nm) order can be identified unequivocally in both cases[4]. Lower harmonics cannot be detected because the CEM is not sensitive above ~ 150 nm.

The spectrum depicted in Figure 5.14a was obtained during our first experimental single pass HHG attempt with long pulses for a pulse energy of about $24\,\mu$J at a Xe gas flow of 6×10^{-1} mbar $\cdot$ l/s. With the additional gas load from the target, the pressure in the interaction chamber stabilized at 1.5×10^{-2} mbar. At that pressure level, reabsorption of the generated EUV radiation in Xe begins to matter and influences the observed spectrum. The brown line in Figure 5.14a illustrates the spectrally resolved transmission of EUV radiation for approximately the experimental conditions, i.e. a 21 cm path through Xe gas at a pressure of 1.5×10^{-2} mbar[5]. As one can see, less than

[4]The signal detected below 50 nm in Figure 5.14b may partially be caused by high harmonic radiation but could not be clearly identified as such.

[5]Note that a constant and pure Xe background is assumed here, ignoring the gas distribution in the vicinity of the target. Since neither the pressure nor the absorptive beam path are known precisely,

90 % are transmitted between 50 nm and 100 nm with a minimum reaching below 65 % around 85 nm. This absorption window coincides with the observed harmonic orders 11 to 21, of which the 11–17th are affected the strongest.

Despite more than 30 % absorption losses on the way from the gas jet to the monochromator, the detected signal strength of the 11th order (93.6 nm) is more than a factor of 2 higher than that of the other observed orders. Since the intensity ratios between different harmonics remain largely the same even after taking into account the Xe transmission for all orders in the spectrum and the decreasing detection efficiency of the CEM for wavelengths above ~ 100 nm, the pronounced signal strength of the 11th order is likely to be caused by favorable phase matching conditions for that specific order. Further support for that explanation arises from the fact that during the first experiments, the optimization of the nozzle position and the gas flow was not performed for a single order, but for the overall harmonic signal by maximizing the yield in zeroth diffraction order of the grating. Although this approach is favorable because of the up to two orders of magnitude stronger signal-to-noise ratio in zeroth order, it excludes the deliberate maximization of the signal of a specific harmonic order before a spectrum has been recorded. Therefore, phase matching will determine the strongest observed harmonic for certain experimental conditions.

The spectrum shown in Figure 5.14b was recorded with minimally higher pulse energy ($\sim 26\,\mu$J) and at a slightly higher setpoint of Xe gas flow (8×10^{-1} mbar $\cdot$ l/s) whereas the other experimental parameters remained unchanged compared to Figure 5.14a. Despite the intended moderate change in gas flow, the plasma generated in the gas jet seemed disproportionately brighter than before upon visual inspection, indicating an even higher gas flow. This suspicion was partially corroborated by a concurrent increase of the background pressure in the interaction chamber to up to 6.3×10^{-2} mbar. Although the latter may also be caused by the limited pumping speed of the employed turbomolecular pump, it can be suspected that the regulating valve was not working properly at the time[6].

Figure 5.14b exemplifies the particular sensitivity of HHG in a tight focusing geometry to the experimental conditions. While causing stronger reabsorption between 50 nm and 100 nm on the one hand, the higher pressure in the gas jet leads to a much larger 19th harmonic signal on the other hand. The calculated single atom cutoff is almost identical with that of Figure 5.14a so that the increased conversion efficiency of the 19th harmonic can be attributed to better phase matching because of the higher gas pressure [102]. Notably, the 17th and 19th harmonic appear to be much stronger than the 11th harmonic judging from the detected spectrum. However, looking at the spectrally resolved transmission of a 21 cm path in Xe at a pressure of 6.3×10^{-2} mbar which is shown as a brown line in Figure 5.14b reveals that about 80 % of the 11th and 13th harmonic radiation is absorbed before detection. Transmission is higher for higher orders so that a correction of the measured spectrum for the estimated absorption in the Xe

the pressure indicated by the employed pressure gauge has not been corrected for Xe.

[6] This was a recurring issue for this device. In most cases, a simple restart of the valve controller restored reasonable operation.

background results in a high harmonic spectrum with a plateau of almost equally intense harmonics between the 11th and the 19th order (not shown).

The system performance is evaluated in the same way as for the sub-50 fs experiments, i.e. the power of the EUV radiation generated in the target is estimated from the detected signal. For that purpose, the latter has to be corrected for the efficiency and the transmission of all elements between the gas target and the detector. Since the CEM is operated in the current mode, we first have to convert the voltage measured with the multimeter into the corresponding number of detected photons. To this end, the average charge $\bar{Q}$ created in the CEM at the operating voltage by a single incident harmonic photon, i.e. the average area of the pulses caused by a detected EUV photon (see Figure 5.10) has to be estimated. Here, we use $\bar{Q} = 3.7\,\mathrm{pAs}$ from a previous characterization of the same CEM [274]. The number of detected photons can then be calculated with the known load resistance ($R = 100\,\mathrm{M\Omega}$ in our case). For the conversion into the number of generated photons, the quantum efficiceny of the CEM ($\sim 10\,\%$), the specified spectral reflectivity of the monochromator grating in the relevant spectral region (only $\sim 4\,\%$ because the available monochromator grating was designed for lower wavelengths), the absorption by the Xe background, and the geometric transmission have to be considered. The last two factors strongly depend on the harmonic order. With the estimated Xe transmission shown in Figure 5.14b and assuming a minimal divergence $\propto 1/q$ (corresponding to a geometric transmission of $\sim 62\,\%$), we very conservatively estimate a generated power of about 3 pW for the 17th harmonic at a wavelength of 60.6 nm. This power level is about two orders of magnitude lower than that estimated for the 15th harmonic in the short pulse experiment. Among other factors, the higher level of ionization caused in Xe by the long driving pulses can be assumed to contribute strongly to this reduction of the generated power.

Although the planned systematic investigations of ionization effects were not possible, important experiences for the design and the operation of a single pass HHG setup could be gained. In particular, the employed gas flow rates, about a factor of 2 higher than in the short pulse experiment, were found to result in a limited transmission of the generated EUV radiation because of a higher background pressure. The use of a gas catch assembly (see Section 3.4.3) may thus be considered for future experiments.

5.4 Conclusions and outlook

Using an Innoslab solid state amplifier system, single pass HHG in xenon with amplified laser pulses was demonstrated in two proof-of-principle experiments at multi-MHz repetition rates. These demonstrations constitute the highest repetition rate single pass HHG experiments reported with an infrared amplifier system so far. In the first experiment at a repetition rate of 20.8 MHz, pulses with an energy of $\sim 1\,\mu$J and a duration of ~ 35 fs after external compression were employed to generate harmonics of up to the 17th order (60.6 nm) with an estimated power of ~ 1 nW in the 15th harmonic (68.7 nm). In the second experiment, high harmonic radiation at wavelengths down to 54.2 nm (19th harmonic) could be generated at a reduced repetition rate of 10 MHz using the uncom-

pressed amplifier pulses of 680 fs duration directly.

Technical constraints limited the usable amplifier and hence the achievable EUV power in both experiments. The limiting factors that we identified were the low damage threshold of the employed spectral broadening scheme and the thermal aberrations caused by the only commercially available high power optical isolator. Both of these limitations have been addressed and partially overcome in the meantime: Our collaborators at the Fraunhofer Institute of Laser Technology developed an isolator that did not deteriorate the measured beam quality at power levels of up to 1 kW[7]. Joint experimental efforts to realize single pass HHG with two successive Innoslab amplifiers at the full usable average power of ~ 1 kW and a repetition rate of 10 MHz did not reach the stage of generating EUV radiation before this thesis was compiled. Addressing the second limitation, a scheme to realize spectral broadening at the full amplifier output power is currently also investigated in detail by our collaborators.

In the course of the experiments presented here, the single pass approach could not yet be exploited to its full extent. Our results are thus by far not competitive with cavity-assisted HHG in terms of generated power. Nevertheless, based on the experiences gained during the experiments and extrapolating from the rapid progress in amplifier development, we believe that single pass HHG will quickly mature into a versatile and easy to operate table-top high repetition rate EUV source. In particular, Innoslab amplifiers with the same parameters as the still provisional one employed in our experiments have become available as a commercial product so that HHG at multi-MHz repetition rates is now, at least in principle, accessible to all people in the community.

A possible next step apart from repeating the first experiments at improved laser parameters is the implementation of quasi-phase matching techniques, e.g. specially designed gas targets, to improve the conversion efficieny. In addition, experiments at different repetition rates, under varying focusing conditions, and for different target gases could be performed to investigate the influence of ionization on the high harmonic yield. These studies may contribute to the current understanding of the effects of residual ionization that arise at repetition rates in the MHz-regime because the target gas is not exchanged completely before the next driving pulse is incident.

A favorable property of the single pass approach compared to cavity-assisted HHG is its reduced sensitivity to nonlinear responses or changes in reflectivity of the employed mirrors. In a cavity-assisted HHG system with a visible driving laser that has been set up in our group to exploit the favorable wavelength scaling of the high harmonic yield (cf. Section 3.3.3.5), detrimental mirror degradations are observed under vacuum conditions and currently limit the performance of the cavity [209, 274]. Performing a similar experiment in a single pass geometry promises to be affected less by similar effects. Hence, the author of this thesis was among the initiators of single pass HHG experiments with the frequency-doubled output of an Innoslab amplifier that were then performed in the research group of Matthias Kling. At an average driving power of 250 W and a repetition rate of 50 MHz, the generation of the 5th (103.0 nm) and the 7th harmonic (73.6 nm) in Xe was demonstrated at estimated power levels of 5 nW and

[7] A commerical product based on this isolator design is now available from Amphos GmbH.

20 pW, respectively [275]. The observed 5th harmonic power is about two orders of magnitude lower than that estimated for the cavity-generated light. This cannot be explained in a fully conclusive way so that further investigations may be scheduled.

Last, but not least, once single pass HHG at multi-MHz repetition rates generates sufficiently strong high harmonic radiation, all applications that can leverage high repetition rate EUV sources come into reach.

Bibliography

[1] T. H. Maiman, "*Stimulated Optical Radiation in Ruby*," Nature **187**, 493 (1960).

[2] T. Udem, R. Holzwarth, and T. W. Hänsch, "*Femtosecond optical frequency combs*," Eur. Phys. J. Spec. Top. **172**, 69 (2009).

[3] S. A. Diddams, "*The evolving optical frequency comb*," J. Opt. Soc. Am. B **27**, B51 (2010).

[4] O. Schmidt, M. Bauer, C. Wiemann, R. Porath, M. Scharte, O. Andreyev, G. Schönhense, and M. Aeschlimann, "*Time-resolved two photon photoemission electron microscopy*," Appl. Phys. B **74**, 223 (2002).

[5] M. I. Stockman, M. F. Kling, U. Kleineberg, and F. Krausz, "*Attosecond nanoplasmonic-field microscope*," Nature Photon. **1**, 539 (2007).

[6] J. Ullrich, R. Moshammer, A. Dorn, R. Dörner, L. P. H. Schmidt, and H. Schmidt-Böcking, "*Recoil-ion and electron momentum spectroscopy: reaction-microscopes*," Rep. Prog. Phys. **66**, 1463 (2003).

[7] D. Strickland and G. Mourou, "*Compression of amplified chirped optical pulses*," Opt. Commun. **56**, 219 (1985).

[8] C. Gohle, T. Udem, M. Herrmann, J. Rauschenberger, R. Holzwarth, H. A. Schuessler, F. Krausz, and T. W. Hänsch, "*A frequency comb in the extreme ultraviolet*," Nature **436**, 234 (2005).

[9] R. J. Jones, K. D. Moll, M. J. Thorpe, and J. Ye, "*Phase-Coherent Frequency Combs in the Vacuum Ultraviolet via High-Harmonic Generation inside a Femtosecond Enhancement Cavity*," Phys. Rev. Lett. **94**, 193201 (2005).

[10] J. Jones, "*Intracavity high harmonic generation with fs frequency combs*," in *High Intensity Lasers and High Field Phenomena*, HFB5, Optical Society of America (2011).

[11] A. Cingoz, D. C. Yost, T. K. Allison, A. Ruehl, M. E. Fermann, I. Hartl, and J. Ye, "*Direct frequency comb spectroscopy in the extreme ultraviolet*," Nature **482**, 68 (2012).

[12] A. Ozawa and Y. Kobayashi, "*vuv frequency-comb spectroscopy of atomic xenon*," Phys. Rev. A **87**, 022507 (2013).

[13] D. C. Yost, T. R. Schibli, and J. Ye, "*Efficient output coupling of intracavity high-harmonic generation*," Opt. Lett. **33**, 1099 (2008).

[14] K. D. Moll, R. J. Jones, and J. Ye, "*Output coupling methods for cavity-based high-harmonic generation*," Opt. Express **14**, 8189 (2006).

[15] I. Pupeza, S. Holzberger, T. Eidam, H. Carstens, D. Esser, J. Weitenberg, P. Russbueldt, J. Rauschenberger, J. Limpert, T. Udem, A. Tünnermann, T. W. Hänsch, A. Apolonski, F. Krausz, and E. Fill, "*Compact high-repetition-rate source of coherent 100 eV radiation*," Nature Photon. **7**, 608 (2013).

[16] I. Pupeza, T. Eidam, J. Rauschenberger, B. Bernhardt, A. Ozawa, E. Fill, A. Apolonski, T. Udem, J. Limpert, Z. A. Alahmed, A. M. Azzeer, A. Tünnermann, T. W. Hänsch, and F. Krausz, "*Power scaling of a high-repetition-rate enhancement cavity*," Opt. Lett. **35**, 2052 (2010).

[17] T. K. Allison, A. Cingöz, D. C. Yost, and J. Ye, "*Extreme Nonlinear Optics in a Femtosecond Enhancement Cavity*," Phys. Rev. Lett. **107**, 183903 (2011).

[18] D. R. Carlson, J. Lee, J. Mongelli, E. M. Wright, and R. J. Jones, "*Intracavity ionization and pulse formation in femtosecond enhancement cavities*," Opt. Lett. **36**, 2991 (2011).

[19] J. Diels and W. Rudolph, *Ultrashort Laser Pulse Phenomena*, Optics and photonics, Elsevier Science (2006).

[20] W. Koechner, *Solid-State Laser Engineering*, Springer Series in Optical Sciences, Springer (2006).

[21] A. Weiner, *Ultrafast Optics*, Wiley Series in Pure and Applied Optics, Wiley (2009).

[22] A. E. Siegman, "*How to (Maybe) Measure Laser Beam Quality*," in *DPSS (Diode Pumped Solid State) Lasers: Applications and Issues*, MQ1, Optical Society of America (1998).

[23] I. Walmsley, L. Waxer, and C. Dorrer, "*The role of dispersion in ultrafast optics*," Rev. Sci. Instrum. **72**, 1 (2001).

[24] D. Georgiev, J. Herrmann, and U. Stamm, "*Cavity design for optimum nonlinear absorption in Kerr-lens mode-locked solid-state lasers*," Opt. Commun. **92**, 368 (1992).

[25] J. P. Gordon, R. C. C. Leite, R. S. Moore, S. P. S. Porto, and J. R. Whinnery, "*Long-Transient Effects in Lasers with Inserted Liquid Samples*," J. Appl. Phys. **36**, 3 (1965).

[26] M. Nisoli, S. D. Silvestri, and O. Svelto, "*Generation of high energy 10 fs pulses by a new pulse compression technique*," Appl. Phys. Lett. **68**, 2793 (1996).

[27] M. Nisoli, S. Stagira, S. De Silvestri, O. Svelto, S. Sartania, Z. Cheng, M. Lenzner, C. Spielmann, and F. Krausz, "*A novel-high energy pulse compression system: Generation of multigigawatt sub-5-fs pulses*," Appl. Phys. B **65**, 189 (1997).

[28] M. Nisoli, S. D. Silvestri, O. Svelto, R. Szipöcs, K. Ferencz, C. Spielmann, S. Sartania, and F. Krausz, "*Compression of high-energy laser pulses below 5 fs*," Opt. Lett. **22**, 522 (1997).

[29] M. Nisoli, G. Sansone, S. Stagira, C. Vozzi, S. De Silvestri, and O. Svelto, "*Ultrabroadband continuum generation by hollow-fiber cascading*," Appl. Phys. B **75**, 601 (2002).

[30] B. Schenkel, J. Biegert, U. Keller, C. Vozzi, M. Nisoli, G. Sansone, S. Stagira, S. D. Silvestri, and O. Svelto, "*Generation of 3.8-fs pulses from adaptive compression of a cascaded hollow fiber supercontinuum*," Opt. Lett. **28**, 1987 (2003).

[31] C. Vozzi, M. Nisoli, G. Sansone, S. Stagira, and S. De Silvestri, "*Optimal spectral broadening in hollow-fiber compressor systems*," Appl. Phys. B **80**, 285 (2005).

[32] C. Hauri, W. Kornelis, F. Helbing, A. Heinrich, A. Couairon, A. Mysyrowicz, J. Biegert, and U. Keller, "*Generation of intense, carrier-envelope phase-locked few-cycle laser pulses through filamentation*," Appl. Phys. B **79**, 673 (2004).

[33] A. Couairon, M. Franco, A. Mysyrowicz, J. Biegert, and U. Keller, "*Pulse self-compression to the single-cycle limit by filamentation in a gas with a pressure gradient*," Opt. Lett. **30**, 2657 (2005).

[34] M. Nurhuda, A. Suda, and K. Midorikawa, "*Spectral broadening of 50 milli joule laser pulses in a neon-filled Herriot multiple-pass cell (MPC)*," in *Ultrafast Phenomena XIV* (T. Kobayashi, T. Okada, T. Kobayashi, K. Nelson, and S. Silvestri, eds.), vol. 79 of Springer Series in Chemical Physics, pp. 58–60, Springer Berlin Heidelberg (2005).

[35] M. Nurhuda, A. Suda, and K. Midorikawa, "*Plasma-induced spectral broadening of high-energy ultrashort laser pulses in a helium-filled multiple-pass cell*," J. Opt. Soc. Am. B **23**, 1946 (2006).

[36] T. Südmeyer, F. Brunner, E. Innerhofer, R. Paschotta, K. Furusawa, J. C. Baggett, T. M. Monro, D. J. Richardson, and U. Keller, "*Nonlinear femtosecond pulse compression at high average power levels by use of a large-mode-area holey fiber*," Opt. Lett. **28**, 1951 (2003).

[37] A. Vernaleken, J. Weitenberg, T. Sartorius, P. Russbueldt, W. Schneider, S. L. Stebbings, M. F. Kling, P. Hommelhoff, H.-D. Hoffmann, R. Poprawe, F. Krausz,

T. W. Hänsch, and T. Udem, "*Single-pass high-harmonic generation at 20.8 MHz repetition rate*," Opt. Lett. **36**, 3428 (2011).

[38] O. H. Heckl, C. J. Saraceno, C. R. E. Baer, T. Südmeyer, Y. Y. Wang, Y. Cheng, F. Benabid, and U. Keller, "*Temporal pulse compression in a xenon-filled Kagome-type hollow-core photonic crystal fiber at high average power*," Opt. Express **19**, 19142 (2011).

[39] J. Rothhardt, S. Demmler, S. Hädrich, J. Limpert, and A. Tünnermann, "*Octave-spanning OPCPA system delivering CEP-stable few-cycle pulses and 22 W of average power at 1 MHz repetition rate*," Opt. Express **20**, 10870 (2012).

[40] C. Jocher, T. Eidam, S. Hädrich, J. Limpert, and A. Tünnermann, "*Sub 250fs pulses from solid-core nonlinear compression stage at 250W of average power*," Opt. Lett. **37**, 4407 (2012).

[41] F. Emaury, C. F. Dutin, C. J. Saraceno, M. Trant, O. H. Heckl, Y. Y. Wang, C. Schriber, F. Gerome, T. Südmeyer, F. Benabid, and U. Keller, "*Beam delivery and pulse compression to sub-50 fs of a modelocked thin-disk laser in a gas-filled Kagome-type HC-PCF fiber*," Opt. Express **21**, 4986 (2013).

[42] R. Szipöcs, K. Ferencz, C. Spielmann, and F. Krausz, "*Chirped multilayer coatings for broadband dispersion control in femtosecond lasers*," Opt. Lett. **19**, 201 (1994).

[43] T. Sartorius, "*Spektrale Verbreiterung ultrakurzer Laserpulse hoher mittlerer Leistung in Glasfasern*," Diplomarbeit, Rheinisch-Westfälische Technische Hochschule Aachen (2010).

[44] S. T. Cundiff and J. Ye, "*Colloquium: Femtosecond optical frequency combs*," Rev. Mod. Phys. **75**, 325 (2003).

[45] T. Hänsch and N. Picqué, "*Frequency Combs*," in *Springer Handbook of Lasers and Optics* (F. Träger, ed.), pp. 1285–1304, Springer Berlin Heidelberg (2012).

[46] J. Reichert, R. Holzwarth, T. Udem, and T. W. Hänsch, "*Measuring the frequency of light with mode-locked lasers*," Opt. Commun. **172**, 59 (1999).

[47] S. A. Diddams, D. J. Jones, J. Ye, S. T. Cundiff, J. L. Hall, J. K. Ranka, R. S. Windeler, R. Holzwarth, T. Udem, and T. W. Hänsch, "*Direct Link between Microwave and Optical Frequencies with a 300 THz Femtosecond Laser Comb*," Phys. Rev. Lett. **84**, 5102 (2000).

[48] D. J. Jones, S. A. Diddams, J. K. Ranka, A. Stentz, R. S. Windeler, J. L. Hall, and S. T. Cundiff, "*Carrier-Envelope Phase Control of Femtosecond Mode-Locked Lasers and Direct Optical Frequency Synthesis*," Science **288**, 635 (2000).

[49] S. Koke, C. Grebing, H. Frei, A. Anderson, A. Assion, and G. Steinmeyer, "*Direct frequency comb synthesis with arbitrary offset and shot-noise-limited phase noise*," Nature Photon. **4**, 462 (2010).

[50] S. Koke, A. Anderson, H. Frei, A. Assion, and G. Steinmeyer, "*Noise performance of a feed-forward scheme for carrier-envelope phase stabilization*," Appl. Phys. B **104**, 799 (2011).

[51] T. Udem, R. Holzwarth, and T. W. Hänsch, "*Optical Frequency Metrology*," Nature **416**, 233 (2002).

[52] T. Steinmetz, T. Wilken, C. Araujo-Hauck, R. Holzwarth, T. W. Hänsch, L. Pasquini, A. Manescau, S. D'Odorico, M. T. Murphy, T. Kentischer, W. Schmidt, and T. Udem, "*Laser Frequency Combs for Astronomical Observations*," Science **321**, 1335 (2008).

[53] S. A. Diddams, T. Udem, J. C. Bergquist, E. A. Curtis, R. E. Drullinger, L. Hollberg, W. M. Itano, W. D. Lee, C. W. Oates, K. R. Vogel, and D. J. Wineland, "*An Optical Clock Based on a Single Trapped $^{199}Hg^{+}$ Ion*," Science **293**, 825 (2001).

[54] B. J. Bloom, T. L. Nicholson, J. R. Williams, S. L. Campbell, M. Bishof, X. Zhang, W. Zhang, S. L. Bromley, and J. Ye, "*A New Generation of Atomic Clocks: Accuracy and Stability at the 10^{-18} Level*," ArXiv e-prints arXiv:1309.1137v1 (2013).

[55] G. A. Kazakov, A. N. Litvinov, V. I. Romanenko, L. P. Yatsenko, A. V. Romanenko, M. Schreitl, G. Winkler, and T. Schumm, "*Performance of a ^{229}Thorium solid-state nuclear clock*," New J. Phys. **14**, 083019 (2012).

[56] M. P. Hehlen, R. R. Greco, W. G. Rellergert, S. T. Sullivan, D. DeMille, R. A. Jackson, E. R. Hudson, and J. R. Torgerson, "*Optical spectroscopy of an atomic nucleus: Progress toward direct observation of the ^{229}Th isomer transition*," J. Lumin. **133**, 91 (2013).

[57] M. C. Stowe, M. J. Thorpe, A. Pe'er, J. Ye, J. E. Stalnaker, V. Gerginov, and S. A. Diddams, "*Direct frequency comb spectroscopy*," Adv. At., Mol., Opt. Phys. **55**, 1 (2008).

[58] J. Mandon, G. Guelachvili, and N. Picqué, "*Fourier transform spectroscopy with a laser frequency comb*," Nature Photon. **3**, 99 (2009).

[59] S. Schiller, "*Spectrometry with frequency combs*," Opt. Lett. **27**, 766 (2002).

[60] A. McPherson, G. Gibson, H. Jara, U. Johann, T. S. Luk, I. A. McIntyre, K. Boyer, and C. K. Rhodes, "*Studies of multiphoton production of vacuum-ultraviolet radiation in the rare gases*," J. Opt. Soc. Am. B **4**, 595 (1987).

[61] M. Ferray, A. L'Huillier, X. F. Li, L. A. Lompré, G. Mainfray, and C. Manus, "*Multiple-harmonic conversion of 1064 nm radiation in rare gases*," J. Phys. B **21**, L31 (1988).

[62] B. W. Shore and P. L. Knight, "*Enhancement of high optical harmonics by excess-photon ionisation*," J. Phys. B **20**, 413 (1987).

[63] K. C. Kulander and B. W. Shore, "*Calculations of Multiple-Harmonic Conversion of 1064-nm Radiation in Xe*," Phys. Rev. Lett. **62**, 524 (1989).

[64] J. L. Krause, K. J. Schafer, and K. C. Kulander, "*High-order harmonic generation from atoms and ions in the high intensity regime*," Phys. Rev. Lett. **68**, 3535 (1992).

[65] K. C. Kulander, K. J. Schafer, and J. L. Krause, "*Dynamics of Short-Pulse Excitation, Ionization and Harmonic Conversion*," in *Super-Intense Laser-Atom Physics* (B. Piraux, A. L'Huillier, and K. Rzazewski, eds.), vol. 316 of NATO Advanced Study Institutes, Series B: Physics, 95, New York: Plenum (1993).

[66] P. B. Corkum, "*Plasma Perspective on Strong-Field Multiphoton Ionization*," Phys. Rev. Lett. **71**, 1994 (1993).

[67] M. Lewenstein, P. Balcou, M. Y. Ivanov, A. L'Huillier, and P. B. Corkum, "*Theory of high-harmonic generation by low-frequency laser fields*," Phys. Rev. A **49**, 2117 (1994).

[68] M. Protopapas, C. H. Keitel, and P. L. Knight, "*Atomic physics with super-high intensity lasers*," Rep. Prog. Phys. **60**, 389 (1997).

[69] T. Brabec and F. Krausz, "*Intense few-cycle laser fields: Frontiers of nonlinear optics*," Rev. Mod. Phys. **72**, 545 (2000).

[70] A. Scrinzi, M. Y. Ivanov, R. Kienberger, and D. M. Villeneuve, "*Attosecond physics*," J. Phys. B **39**, R1 (2006).

[71] F. Krausz and M. Ivanov, "*Attosecond physics*," Rev. Mod. Phys. **81**, 163 (2009).

[72] Z. Chang, *Fundamentals of attosecond optics*, vol. 1, CRC Press Boca Raton (2011).

[73] C. J. Joachain, N. Kylstra, and R. Potvliege, *Atoms in intense laser fields*, Cambridge University Press (2012).

[74] O. Smirnova and M. Ivanov, "*Multielectron High Harmonic Generation: Simple Man on a Complex Plane*," in *Attosecond and XUV Physics*, pp. 201–256, Wiley-VCH (2013).

[75] L. V. Keldysh, "*Ionization in the field of a strong electromagnetic wave*," Sov. Phys. JETP **20**, 1307 (1965).

[76] G. L. Yudin and M. Y. Ivanov, "*Nonadiabatic tunnel ionization: Looking inside a laser cycle*," Phys. Rev. A **64**, 013409 (2001).

[77] A. M. Perelomov, V. S. Popov, and M. V. Terentev, "*Ionization of atoms in an alternating electric field*," Sov. Phys. JETP **23**, 924 (1966).

[78] M. Ammosov, N. Delone, and V. Krainov, "*Tunnel ionization of complex atoms and of atomic ions in an alternating electromagnetic field*," Sov. Phys. JETP **64**, 1191 (1986).

[79] C. Spielmann, N. H. Burnett, S. Sartania, R. Koppitsch, M. Schnürer, C. Kan, M. Lenzner, P. Wobrauschek, and F. Krausz, "*Generation of Coherent X-rays in the Water Window Using 5-Femtosecond Laser Pulses*," Science **278**, 661 (1997).

[80] T. Popmintchev, M.-C. Chen, D. Popmintchev, P. Arpin, S. Brown, S. Ališauskas, G. Andriukaitis, T. Balčiunas, O. D. Mücke, A. Pugzlys, A. Baltuška, B. Shim, S. E. Schrauth, A. Gaeta, C. Hernández-García, L. Plaja, A. Becker, A. Jaron-Becker, M. M. Murnane, and H. C. Kapteyn, "*Bright Coherent Ultrahigh Harmonics in the keV X-ray Regime from Mid-Infrared Femtosecond Lasers*," Science **336**, 1287 (2012).

[81] Z. Chang, A. Rundquist, H. Wang, M. M. Murnane, and H. C. Kapteyn, "*Generation of Coherent Soft X Rays at 2.7 nm Using High Harmonics*," Phys. Rev. Lett. **79**, 2967 (1997).

[82] W. Gordon, "*Der Comptoneffekt nach der Schrödingerschen Theorie*," Zeitschrift für Physik **40**, 117 (1926).

[83] D. Volkov, "*Über eine Klasse von Lösungen der Diracschen Gleichung*," Zeitschrift für Physik **94**, 250 (1935).

[84] H. R. Reiss, "*Limits on Tunneling Theories of Strong-Field Ionization*," Phys. Rev. Lett. **101**, 159901 (2008).

[85] H. Reiss, "*Foundations of Strong-Field Physics*," in *Lectures on Ultrafast Intense Laser Science 1* (K. Yamanouchi, ed.), vol. 94 of Springer Series in Chemical Physics, pp. 41–84, Springer Berlin Heidelberg (2011).

[86] M. Y. Ivanov and O. Smirnova, "*Ionization in strong low-frequency fields: from quantum S-matrix to classical pictures*," Lecture Notes, CORINF Network (2012).

[87] P. Salières, B. Carre, L. Le Deroff, F. Grasbon, G. G. Paulus, H. Walther, R. Kopold, W. Becker, D. B. Milosevic, A. Sanpera, and M. Lewenstein, "*Feynman's Path-Integral Approach for Intense-Laser-Atom Interactions*," Science **292**, 902 (2001).

[88] M. Y. Ivanov, M. Spanner, and O. Smirnova, "*Anatomy of strong field ionization*," J. Mod. Opt. **52**, 165 (2005).

[89] M. Y. Ivanov, T. Brabec, and N. Burnett, "*Coulomb corrections and polarization effects in high-intensity high-harmonic emission*," Phys. Rev. A **54**, 742 (1996).

[90] M. Lewenstein, P. Salières, and A. L'Huillier, "*Phase of the atomic polarization in high-order harmonic generation*," Phys. Rev. A **52**, 4747 (1995).

[91] Z. Chen, A.-T. Le, T. Morishita, and C. D. Lin, "*Quantitative rescattering theory for laser-induced high-energy plateau photoelectron spectra*," Phys. Rev. A **79**, 033409 (2009).

[92] A.-T. Le, R. R. Lucchese, S. Tonzani, T. Morishita, and C. D. Lin, "*Quantitative rescattering theory for high-order harmonic generation from molecules*," Phys. Rev. A **80**, 013401 (2009).

[93] C. D. Lin, A.-T. Le, Z. Chen, T. Morishita, and R. Lucchese, "*Strong-field rescattering physics—self-imaging of a molecule by its own electrons*," J. Phys. B **43**, 122001 (2010).

[94] P. Salières and I. Christov, "*Macroscopic Effects in High-Order Harmonic Generation*," in *Strong Field Laser Physics* (T. Brabec, ed.), vol. 134 of Springer Series in Optical Sciences, pp. 261–280, Springer Berlin/Heidelberg (2008).

[95] P. Salières, A. L'Huillier, P. Antoine, and M. Lewenstein, "*Study of the Spatial and Temporal Coherence of High-Order Harmonics*," vol. 41 of Advances In Atomic, Molecular, and Optical Physics, pp. 83–142, Academic Press (1999).

[96] S. Kazamias, D. Douillet, F. Weihe, C. Valentin, A. Rousse, S. Sebban, G. G. F. Augé, D. Hulin, and P. Balcou, "*Global Optimization of High Harmonic Generation*," Phys. Rev. Lett. **90**, 193901 (2003).

[97] S. Kazamias, S. Daboussi, O. Guilbaud, K. Cassou, D. Ros, B. Cros, and G. Maynard, "*Pressure-induced phase matching in high-order harmonic generation*," Phys. Rev. A **83**, 063405 (2011).

[98] P. D. Maker, R. W. Terhune, M. Nisenoff, and C. M. Savage, "*Effects of Dispersion and Focusing on the Production of Optical Harmonics*," Phys. Rev. Lett. **8**, 21 (1962).

[99] S. Kazamias, D. Douillet, C. Valentin, F. Weihe, F. Augé, T. Lefrou, G. Grillon, S. Sebban, and P. Balcou, "*Observation of high-contrast coherence fringes in high-order harmonic generation*," Phys. Rev. A **68**, 033819 (2003).

[100] C. M. Heyl, J. Güdde, U. Höfer, and A. L'Huillier, "*Spectrally Resolved Maker Fringes in High-Order Harmonic Generation*," Phys. Rev. Lett. **107**, 033903 (2011).

[101] A. Kramida, Yu. Ralchenko, and J. R. and NIST ASD Team, NIST Atomic Spectra Database (ver. 5.1) [Online: `http://physics.nist.gov/asd`], National Institute of Standards and Technology, Gaithersburg, MD (2013).

[102] C. M. Heyl, J. Güdde, A. L'Huillier, and U. Höfer, "*High-order harmonic generation with μJ laser pulses at high repetition rates*," J. Phys. B **45**, 074020 (2012).

[103] E. Constant, D. Garzella, P. Breger, E. Mével, C. Dorrer, C. Le Blanc, F. Salin, and P. Agostini, "*Optimizing High Harmonic Generation in Absorbing Gases: Model and Experiment*," Phys. Rev. Lett. **82**, 1668 (1999).

[104] C. G. Durfee, A. R. Rundquist, S. Backus, C. Herne, M. M. Murnane, and H. C. Kapteyn, "*Phase Matching of High-Order Harmonics in Hollow Waveguides*," Phys. Rev. Lett. **83**, 2187 (1999).

[105] S. Kazamias, F. Weihe, D. Douillet, C. Valentin, T. Planchon, S. Sebban, G. Grillon, F. Augé, D. Hulin, and P. Balcou, "*High order harmonic generation optimization with an apertured laser beam*," Eur. Phys. J. D **21**, 353 (2002).

[106] H. Dachraoui, T. Auguste, A. Helmstedt, P. Bartz, M. Michelswirth, N. Mueller, W. Pfeiffer, P. Salières, and U. Heinzmann, "*Interplay between absorption, dispersion and refraction in high-order harmonic generation*," J. Phys. B **42**, 175402 (2009).

[107] C.-J. Lai and F. X. Kärtner, "*The influence of plasma defocusing in high harmonic generation*," Opt. Express **19**, 22377 (2011).

[108] A. Rundquist, C. G. Durfee III, Z. Chang, C. Herne, S. Backus, M. M. Murnane, and H. C. Kapteyn, "*Phase-Matched Generation of Coherent Soft X-rays*," Science **280**, 1412 (1998).

[109] P. L. Shkolnikov, A. Lago, and A. E. Kaplan, "*Optimal quasi-phase-matching for high-order harmonic generation in gases and plasma*," Phys. Rev. A **50**, R4461 (1994).

[110] I. Christov, H. Kapteyn, and M. Murnane, "*Quasi-phase matching of high-harmonics and attosecond pulses in modulated waveguides*," Opt. Express **7**, 362 (2000).

[111] A. Paul, R. A. Bartels, R. Tobey, H. Green, S. Weiman, I. P. Christov, M. M. Murnane, H. C. Kapteyn, and S. Backus, "*Quasi-phase-matched generation of coherent extreme-ultraviolet light*," Nature **421**, 51 (2003).

[112] A. V. Birulin, V. T. Platonenko, and V. V. Strelkov, "*High-harmonic generation in interfering waves*," J. Exp. Theor. Phys. **83**, 33 (1996).

[113] J. Peatross, S. Voronov, and I. Prokopovich, "*Selective zoning of high harmonic emission using counter-propagating light*," Opt. Express **1**, 114 (1997).

[114] X. Zhang, A. L. Lytle, T. Popmintchev, X. Zhou, H. C. Kapteyn, M. M. Murnane, and O. Cohen, "*Quasi-phase-matching and quantum-path control of high-harmonic generation using counterpropagating light*," Nat. Phys. **3**, 270 (2007).

[115] O. Cohen, A. L. Lytle, X. Zhang, M. M. Murnane, and H. C. Kapteyn, "*Optimizing quasi-phase matching of high harmonic generation using counterpropagating pulse trains*," Opt. Lett. **32**, 2975 (2007).

[116] K. O'Keeffe, T. Robinson, and S. M. Hooker, "*Quasi-phase-matching high harmonic generation using trains of pulses produced using an array of birefringent plates*," Opt. Express **20**, 6236 (2012).

[117] M. Landreman, K. O'Keeffe, T. Robinson, M. Zepf, B. Dromey, and S. M. Hooker, "*Comparison of parallel and perpendicular polarized counterpropagating light for suppressing high harmonic generation*," J. Opt. Soc. Am. B **24**, 2421 (2007).

[118] M. Zepf, B. Dromey, M. Landreman, P. Foster, and S. M. Hooker, "*Bright Quasi-Phase-Matched Soft-X-Ray Harmonic Radiation from Argon Ions*," Phys. Rev. Lett. **99**, 143901 (2007).

[119] J. Seres, V. S. Yakovlev, E. Seres, C. Streli, P. Wobrauschek, C. Spielmann, and F. Krausz, "*Coherent superposition of laser-driven soft-X-ray harmonics from successive sources*," Nat. Phys. **3**, 878 (2007).

[120] A. Willner, F. Tavella, M. Yeung, T. Dzelzainis, C. Kamperidis, M. Bakarezos, D. Adams, M. Schulz, R. Riedel, M. C. Hoffmann, W. Hu, J. Rossbach, M. Drescher, N. A. Papadogiannis, M. Tatarakis, B. Dromey, and M. Zepf, "*Coherent Control of High Harmonic Generation via Dual-Gas Multijet Arrays*," Phys. Rev. Lett. **107**, 175002 (2011).

[121] X. Wang, M. Chini, Q. Zhang, K. Zhao, Y. Wu, D. A. Telnov, S.-I. Chu, and Z. Chang, "*Mechanism of quasi-phase-matching in a dual-gas multijet array*," Phys. Rev. A **86**, 021802 (2012).

[122] C. Serrat and J. Biegert, "*All-Regions Tunable High Harmonic Enhancement by a Periodic Static Electric Field*," Phys. Rev. Lett. **104**, 073901 (2010).

[123] C. Serrat, "*Control of high-order harmonics for attoscience using a static-electric-field pattern*," Phys. Rev. A **84**, 061803 (2011).

[124] A. L'Huillier, P. Balcou, S. Candel, K. J. Schafer, and K. C. Kulander, "*Calculations of high-order harmonic-generation processes in xenon at 1064 nm*," Phys. Rev. A **46**, 2778 (1992).

[125] S. C. Rae and K. Burnett, "*Detailed simulations of plasma-induced spectral blueshifting*," Phys. Rev. A **46**, 1084 (1992).

[126] C.-G. Wahlström, J. Larsson, A. Persson, T. Starczewski, S. Svanberg, P. Salières, P. Balcou, and A. L'Huillier, "*High-order harmonic generation in rare gases with an intense short-pulse laser*," Phys. Rev. A **48**, 4709 (1993).

[127] S. Rae, "*Spectral blueshifting and spatial defocusing of intense laser pulses in dense gases*," Opt. Commun. **104**, 330 (1994).

[128] S. C. Rae, K. Burnett, and J. Cooper, "*Generation and propagation of high-order harmonics in a rapidly ionizing medium*," Phys. Rev. A **50**, 3438 (1994).

[129] C. Kan, C. E. Capjack, R. Rankin, and N. H. Burnett, "*Spectral and temporal structure in high harmonic emission from ionizing atomic gases*," Phys. Rev. A **52**, R4336 (1995).

[130] P. Salières, A. L'Huillier, and M. Lewenstein, "*Coherence Control of High-Order Harmonics*," Phys. Rev. Lett. **74**, 3776 (1995).

[131] J. M. Schins, P. Breger, P. Agostini, R. C. Constantinescu, H. G. Muller, G. Grillon, A. Antonetti, and A. Mysyrowicz, "*Observation of Laser-Assisted Auger Decay in Argon*," Phys. Rev. Lett. **73**, 2180 (1994).

[132] T. E. Glover, R. W. Schoenlein, A. H. Chin, and C. V. Shank, "*Observation of Laser Assisted Photoelectric Effect and Femtosecond High Order Harmonic Radiation*," Phys. Rev. Lett. **76**, 2468 (1996).

[133] E. Constant, V. D. Taranukhin, A. Stolow, and P. B. Corkum, "*Methods for the measurement of the duration of high-harmonic pulses*," Phys. Rev. A **56**, 3870 (1997).

[134] T. Sekikawa, T. Kanai, and S. Watanabe, "*Frequency-Resolved Optical Gating of Femtosecond Pulses in the Extreme Ultraviolet*," Phys. Rev. Lett. **91**, 103902 (2003).

[135] Y. Mairesse, O. Gobert, P. Breger, H. Merdji, P. Meynadier, P. Monchicourt, M. Perdrix, P. Salières, and B. Carré, "*High Harmonic XUV Spectral Phase Interferometry for Direct Electric-Field Reconstruction*," Phys. Rev. Lett. **94**, 173903 (2005).

[136] A. Bouhal, P. Salières, P. Breger, P. Agostini, G. Hamoniaux, A. Mysyrowicz, A. Antonetti, R. Constantinescu, and H. G. Muller, "*Temporal dependence of high-order harmonics in the presence of strong ionization*," Phys. Rev. A **58**, 389 (1998).

[137] T. E. Glover, A. H. Chin, and R. W. Schoenlein, "*High-order harmonic pulse broadening in an ionizing medium*," Phys. Rev. A **63**, 023403 (2001).

[138] D. H. Reitze, S. Kazamias, F. Weihe, G. Mullot, D. Douillet, F. Aug, O. Albert, V. Ramanathan, J. P. Chambaret, D. Hulin, and P. Balcou, "*Enhancement of high-order harmonic generation at tuned wavelengths through adaptive control*," Opt. Lett. **29**, 86 (2004).

[139] E. S. Toma, H. G. Muller, P. M. Paul, P. Breger, M. Cheret, P. Agostini, C. Le Blanc, G. Mullot, and G. Cheriaux, "*Ponderomotive streaking of the ionization potential as a method for measuring pulse durations in the XUV domain with fs resolution*," Phys. Rev. A **62**, 061801 (2000).

[140] J. Norin, J. Mauritsson, A. Johansson, M. K. Raarup, S. Buil, A. Persson, O. Dühr, M. B. Gaarde, K. J. Schafer, U. Keller, C.-G. Wahlström, and A. L'Huillier, "*Time-Frequency Characterization of Femtosecond Extreme Ultraviolet Pulses*," Phys. Rev. Lett. **88**, 193901 (2002).

[141] J. Mauritsson, P. Johnsson, R. López-Martens, K. Varjú, W. Kornelis, J. Biegert, U. Keller, M. B. Gaarde, K. J. Schafer, and A. L'Huillier, "*Measurement and control of the frequency chirp rate of high-order harmonic pulses*," Phys. Rev. A **70**, 021801 (2004).

[142] K. Varjú, Y. Mairesse, B. Carré, M. B. Gaarde, P. Johnsson, S. Kazamias, R. Lopez-Martens, J. Mauritsson, K. J. Schafer, P. Balcou, A. L'Huillier, and P. Salières, "*Frequency chirp of harmonic and attosecond pulses*," J. Mod. Opt. **52**, 379 (2005).

[143] P. Salières, T. Ditmire, K. S. Budil, M. D. Perry, and A. L'Huillier, "*Spatial profiles of high-order harmonics generated by a femtosecond Cr:LiSAF laser*," J. Phys. B **27**, L217 (1994).

[144] J. W. G. Tisch, R. A. Smith, J. E. Muffett, M. Ciarrocca, J. P. Marangos, and M. H. R. Hutchinson, "*Angularly resolved high-order harmonic generation in helium*," Phys. Rev. A **49**, R28 (1994).

[145] L. Le Déroff, P. Salières, and B. Carré, "*Beam-quality measurement of a focused high-order harmonic beam*," Opt. Lett. **23**, 1544 (1998).

[146] J. Lohbreier, S. Eyring, R. Spitzenpfeil, C. Kern, M. Weger, and C. Spielmann, "*Maximizing the brilliance of high-order harmonics in a gas jet*," New J. Phys. **11**, 023016 (2009).

[147] J. Peatross and D. D. Meyerhofer, "*Intensity-dependent atomic-phase effects in high-order harmonic generation*," Phys. Rev. A **52**, 3976 (1995).

[148] J. Peatross and D. D. Meyerhofer, "*Angular distribution of high-order harmonics emitted from rare gases at low density*," Phys. Rev. A **51**, R906 (1995).

[149] C. Corsi, A. Pirri, E. Sali, A. Tortora, and M. Bellini, "*Direct Interferometric Measurement of the Atomic Dipole Phase in High-Order Harmonic Generation*," Phys. Rev. Lett. **97**, 023901 (2006).

[150] A. Pirri, C. Corsi, E. Sali, A. Tortora, and M. Bellini, "*First Interferometric Measurement of the Atomic Dipole Phase in High-Order Harmonic Generation*," Acta Phys. Hung. B **26**, 343 (2006).

[151] A. Pirri, C. Corsi, E. Sali, A. Tortora, and M. Bellini, "*Interferometric measurement of the atomic dipole phase for the two electronic quantum paths generating high-order harmonics*," Laser Phys. **17**, 138 (2007).

[152] T. Sekikawa, T. Katsura, S. Miura, and S. Watanabe, "*Measurement of the Intensity-Dependent Atomic Dipole Phase of a High Harmonic by Frequency-Resolved Optical Gating*," Phys. Rev. Lett. **88**, 193902 (2002).

[153] M. Herrmann, M. Haas, U. D. Jentschura, F. Kottmann, D. Leibfried, G. Saathoff, C. Gohle, A. Ozawa, V. Batteiger, S. Knünz, N. Kolachevsky, H. A. Schüssler, T. W. Hänsch, and T. Udem, "*Feasibility of coherent xuv spectroscopy on the 1S-2S transition in singly ionized helium*," Phys. Rev. A **79**, 052505 (2009).

[154] T. Ditmire, E. T. Gumbrell, R. A. Smith, J. W. G. Tisch, D. D. Meyerhofer, and M. H. R. Hutchinson, "*Spatial Coherence Measurement of Soft X-Ray Radiation Produced by High Order Harmonic Generation*," Phys. Rev. Lett. **77**, 4756 (1996).

[155] T. Ditmire, J. Tisch, E. Gumbrell, R. Smith, D. Meyerhofer, and M. Hutchinson, "*Spatial coherence of short wavelength high-order harmonics*," Appl. Phys. B **65**, 313 (1997).

[156] R. A. Bartels, A. Paul, H. Green, H. C. Kapteyn, M. M. Murnane, S. Backus, I. P. Christov, Y. Liu, D. Attwood, and C. Jacobsen, "*Generation of Spatially Coherent Light at Extreme Ultraviolet Wavelengths*," Science **297**, 376 (2002).

[157] L. Le Déroff, P. Salières, B. Carré, D. Joyeux, and D. Phalippou, "*Measurement of the degree of spatial coherence of high-order harmonics using a Fresnel-mirror interferometer*," Phys. Rev. A **61**, 043802 (2000).

[158] R. Zerne, C. Altucci, M. Bellini, M. B. Gaarde, T. W. Hänsch, A. L'Huillier, C. Lyngå, and C.-G. Wahlström, "*Phase-Locked High-Order Harmonic Sources*," Phys. Rev. Lett. **79**, 1006 (1997).

[159] M. Bellini, C. Lyngå, A. Tozzi, M. B. Gaarde, T. W. Hänsch, A. L'Huillier, and C.-G. Wahlström, "*Temporal Coherence of Ultrashort High-Order Harmonic Pulses*," Phys. Rev. Lett. **81**, 297 (1998).

[160] C. Lyngå, M. B. Gaarde, C. Delfin, M. Bellini, T. W. Hänsch, A. L'Huillier, and C.-G. Wahlström, "*Temporal coherence of high-order harmonics*," Phys. Rev. A **60**, 4823 (1999).

[161] M. B. Gaarde, F. Salin, E. Constant, P. Balcou, K. J. Schafer, K. C. Kulander, and A. L'Huillier, "*Spatiotemporal separation of high harmonic radiation into two quantum path components*," Phys. Rev. A **59**, 1367 (1999).

[162] P. Balcou, A. S. Dederichs, M. B. Gaarde, and A. L'Huillier, "*Quantum-path analysis and phase matching of high-order harmonic generation and high-order frequency mixing processes in strong laser fields*," J. Phys. B **32**, 2973 (1999).

[163] M. B. Gaarde, "*Time-frequency representations of high order harmonics*," Opt. Express **8**, 529 (2001).

[164] D. C. Yost, T. R. Schibli, J. Ye, J. L. Tate, J. Hostetter, M. B. Gaarde, and K. J. Schafer, "*Vacuum-ultraviolet frequency combs from below-threshold harmonics*," Nat. Phys. **5**, 815 (2009).

[165] C. Benko, T. K. Allison, A. Cingöz, D. C. Yost, and J. Ye, "*Direct Measurement of the XUV Frequency Comb Coherence*," BAPS.2013.DAMOP.U3.2, APS Division of Atomic, Molecular & Optical Physics (2013).

[166] D. Carlson, T.-H. Wu, and R. J. Jones, "*A phase coherent dual-comb source in the VUV based on intracavity high harmonic generation*," BAPS.2013.DAMOP.U3.1, APS Division of Atomic, Molecular & Optical Physics (2013).

[167] L. A. Lompré, A. L'Huillier, M. Ferray, P. Monot, G. Mainfray, and C. Manus, "*High-order harmonic generation in xenon: intensity and propagation effects*," J. Opt. Soc. Am. B **7**, 754 (1990).

[168] P. Balcou, C. Cornaggia, A. S. L. Gomes, L. A. Lompré, and A. L'Huillier, "*Optimizing high-order harmonic generation in strong fields*," J. Phys. B **25**, 4467 (1992).

[169] A. L'Huillier, K. J. Schafer, and K. C. Kulander, "*Theoretical aspects of intense field harmonic generation*," J. Phys. B **24**, 3315 (1991).

[170] J. Peatross and D. D. Meyerhofer, "*Novel gas target for use in laser harmonic generation*," Rev. Sci. Instrum. **64**, 3066 (1993).

[171] T. Ditmire, J. K. Crane, H. Nguyen, L. B. DaSilva, and M. D. Perry, "*Energy-yield and conversion-efficiency measurements of high-order harmonic radiation*," Phys. Rev. A **51**, R902 (1995).

[172] C. Altucci, T. Starczewski, E. Mevel, C.-G. Wahlström, B. Carré, and A. L'Huillier, "*Influence of atomic density in high-order harmonic generation*," J. Opt. Soc. Am. B **13**, 148 (1996).

[173] C. Delfin, C. Altucci, F. D. Filippo, C. de Lisio, M. B. Gaarde, A. L'Huillier, L. Roos, and C.-G. Wahlström, "*Influence of the medium length on high-order harmonic generation*," J. Phys. B **32**, 5397 (1999).

[174] G. Tempea and T. Brabec, "*Optimization of high-harmonic generation*," Appl. Phys. B **70**, S197 (2000).

[175] Y. Tamaki, J. Itatani, M. Obara, and K. Midorikawa, "*Optimization of conversion efficiency and spatial quality of high-order harmonic generation*," Phys. Rev. A **62**, 063802 (2000).

[176] V. T. Platonenko and V. V. Strelkov, "*Phase matching and the spectrum of high-order harmonics generated in an extended medium*," Quantum Electron. **30**, 236 (2000).

[177] J. Sutherland, E. Christensen, N. Powers, S. Rhynard, J. Painter, and J. Peatross, "*High harmonic generation in a semi-infinite gas cell*," Opt. Express **12**, 4430 (2004).

[178] J. Tate, T. Auguste, H. G. Muller, P. Salières, P. Agostini, and L. F. DiMauro, "*Scaling of Wave-Packet Dynamics in an Intense Midinfrared Field*," Phys. Rev. Lett. **98**, 013901 (2007).

[179] P. Colosimo, G. Doumy, C. I. Blaga, J. Wheeler, C. Hauri, F. Catoire, J. Tate, R. Chirla, A. M. March, G. G. Paulus, H. G. Muller, P. Agostini, and L. F. DiMauro, "*Scaling strong-field interactions towards the classical limit*," Nat. Phys. **4**, 386 (2008).

[180] J.-P. Brichta, M. C. H. Wong, J. B. Bertrand, H.-C. Bandulet, D. M. Rayner, and V. R. Bhardwaj, "*Comparison and real-time monitoring of high-order harmonic generation in different sources*," Phys. Rev. A **79**, 033404 (2009).

[181] G. Wang, C. Jin, A.-T. Le, and C. D. Lin, "*Influence of gas pressure on high-order-harmonic generation of Ar and Ne*," Phys. Rev. A **84**, 053404 (2011).

[182] W. Boutu, T. Auguste, J. P. Caumes, H. Merdji, and B. Carré, "*Scaling of the generation of high-order harmonics in large gas media with focal length*," Phys. Rev. A **84**, 053819 (2011).

[183] D. C. Yost, A. Cingöz, T. K. Allison, A. Ruehl, M. E. Fermann, I. Hartl, and J. Ye, "*Power optimization of XUV frequency combs for spectroscopy applications*," Opt. Express **19**, 23483 (2011).

[184] C. Jin and C. D. Lin, "*Comparison of high-order harmonic generation of Ar using truncated Bessel and Gaussian beams*," Phys. Rev. A **85**, 033423 (2012).

[185] A. Cabasse, G. Machinet, A. Dubrouil, E. Cormier, and E. Constant, "*Optimization and phase matching of fiber-laser-driven high-order harmonic generation at high repetition rate*," Opt. Lett. **37**, 4618 (2012).

[186] C.-J. Lai, G. Cirmi, K.-H. Hong, J. Moses, S.-W. Huang, E. Granados, P. Keathley, S. Bhardwaj, and F. X. Kärtner, "*Wavelength Scaling of High Harmonic Generation Close to the Multiphoton Ionization Regime*," Phys. Rev. Lett. **111**, 073901 (2013).

[187] E. Takahashi, Y. Nabekawa, and K. Midorikawa, "*Generation of 10- μJ coherent extreme-ultraviolet light by use of high-order harmonics*," Opt. Lett. **27**, 1920 (2002).

[188] J.-F. Hergott, M. Kovacev, H. Merdji, C. Hubert, Y. Mairesse, E. Jean, P. Breger, P. Agostini, B. Carré, and P. Salières, "*Extreme-ultraviolet high-order harmonic pulses in the microjoule range*," Phys. Rev. A **66**, 021801 (2002).

[189] E. Takahashi, Y. Nabekawa, T. Otsuka, M. Obara, and K. Midorikawa, "*Generation of highly coherent submicrojoule soft x rays by high-order harmonics*," Phys. Rev. A **66**, 021802 (2002).

[190] E. Takahashi, Y. Nabekawa, H. Mashiko, H. Hasegawa, A. Suda, and K. Midorikawa, "*Generation of strong optical field in soft X-ray region by using high-order harmonics*," IEEE J. Select. Topics Quantum Electron. **10**, 1315 (2004).

[191] E. J. Takahashi, Y. Nabekawa, and K. Midorikawa, "*Low-divergence coherent soft x-ray source at 13 nm by high-order harmonics*," Appl. Phys. Lett. **84**, 4 (2004).

[192] J. Lee, D. R. Carlson, and R. J. Jones, "*Optimizing intracavity high harmonic generation for XUV fs frequency combs*," Opt. Express **19**, 23315 (2011).

[193] T. J. Hammond, A. K. Mills, and D. J. Jones, "*Near-threshold harmonics from a femtosecond enhancement cavity-based EUV source: effects of multiple quantum pathways on spatial profile and yield*," Opt. Express **19**, 24871 (2011).

[194] M. D. Perry and J. K. Crane, "*High-order harmonic emission from mixed fields*," Phys. Rev. A **48**, R4051 (1993).

[195] A. Gordon and F. Kärtner, "*Scaling of keV HHG photon yield with drive wavelength*," Opt. Express **13**, 2941 (2005).

[196] K. Schiessl, K. L. Ishikawa, E. Persson, and J. Burgdörfer, "*Quantum Path Interference in the Wavelength Dependence of High-Harmonic Generation*," Phys. Rev. Lett. **99**, 253903 (2007).

[197] V. S. Yakovlev, M. Ivanov, and F. Krausz, "*Enhanced phase-matching for generation of soft X-ray harmonics andattosecond pulses in atomic gases*," Opt. Express **15**, 15351 (2007).

[198] M. V. Frolov, N. L. Manakov, and A. F. Starace, "*Wavelength Scaling of High-Harmonic Yield: Threshold Phenomena and Bound State Symmetry Dependence*," Phys. Rev. Lett. **100**, 173001 (2008).

[199] A. D. Shiner, C. Trallero-Herrero, N. Kajumba, H.-C. Bandulet, D. Comtois, F. Légaré, M. Giguère, J.-C. Kieffer, P. B. Corkum, and D. M. Villeneuve, "*Wavelength Scaling of High Harmonic Generation Efficiency*," Phys. Rev. Lett. **103**, 073902 (2009).

[200] M. V. Frolov, N. L. Manakov, T. S. Sarantseva, M. Y. Emelin, M. Y. Ryabikin, and A. F. Starace, "*Analytic Description of the High-Energy Plateau in Harmonic Generation by Atoms: Can the Harmonic Power Increase with Increasing Laser Wavelengths?*," Phys. Rev. Lett. **102**, 243901 (2009).

[201] E. L. Falcão-Filho, V. M. Gkortsas, A. Gordon, and F. X. Kärtner, "*Analytic scaling analysis of high harmonic generation conversion efficiency*," Opt. Express **17**, 11217 (2009).

[202] K. L. Ishikawa, E. J. Takahashi, and K. Midorikawa, "*Wavelength dependence of high-order harmonic generation with independently controlled ionization and ponderomotive energy*," Phys. Rev. A **80**, 011807 (2009).

[203] J. A. Pérez-Hernández, L. Roso, and L. Plaja, "*Harmonic generation beyond the Strong-Field Approximation: the physics behind the short-wave-infrared scaling laws*," Opt. Express **17**, 9891 (2009).

[204] E. L. Falcão-Filho, C.-J. Lai, K.-H. Hong, V.-M. Gkortsas, S.-W. Huang, L.-J. Chen, and F. X. Kärtner, "*Scaling of high-order harmonic efficiencies with visible wavelength drivers: A route to efficient extreme ultraviolet sources*," Appl. Phys. Lett. **97**, 061107 (2010).

[205] P. Lan, E. J. Takahashi, and K. Midorikawa, "*Wavelength scaling of efficient high-order harmonic generation by two-color infrared laser fields*," Phys. Rev. A **81**, 061802 (2010).

[206] V.-M. Gkortsas, S. Bhardwaj, C.-J. Lai, K.-H. Hong, E. L. Falcão Filho, and F. X. Kärtner, "*Interplay of mulitphoton and tunneling ionization in short-wavelength-driven high-order harmonic generation*," Phys. Rev. A **84**, 013427 (2011).

[207] T. Auguste, F. Catoire, P. Agostini, L. F. DiMauro, C. C. Chirila, V. S. Yakovlev, and P. Salières, "*Driving-frequency scaling of high-harmonic quantum paths*," New J. Phys. **14**, 103014 (2012).

[208] D. R. Austin and J. Biegert, "*Strong-field approximation for the wavelength scaling of high-harmonic generation*," Phys. Rev. A **86**, 023813 (2012).

[209] B. Bernhardt, A. Ozawa, A. Vernaleken, I. Pupeza, J. Kaster, Y. Kobayashi, R. Holzwarth, E. Fill, F. Krausz, T. W. Hänsch, and T. Udem, "*Vacuum ultraviolet frequency combs generated by a femtosecond enhancement cavity in the visible*," Opt. Lett. **37**, 503 (2012).

[210] A. Zaïr, M. Holler, A. Guandalini, F. Schapper, J. Biegert, L. Gallmann, U. Keller, A. S. Wyatt, A. Monmayrant, I. A. Walmsley, E. Cormier, T. Auguste, J. P. Caumes, and P. Salières, "*Quantum Path Interferences in High-Order Harmonic Generation*," Phys. Rev. Lett. **100**, 143902 (2008).

[211] T. Auguste, P. Salières, A. S. Wyatt, A. Monmayrant, I. A. Walmsley, E. Cormier, A. Zaïr, M. Holler, A. Guandalini, F. Schapper, J. Biegert, L. Gallmann, and U. Keller, "*Theoretical and experimental analysis of quantum path interferences in high-order harmonic generation*," Phys. Rev. A **80**, 033817 (2009).

[212] K. S. Budil, P. Salières, A. L'Huillier, T. Ditmire, and M. D. Perry, "*Influence of ellipticity on harmonic generation*," Phys. Rev. A **48**, R3437 (1993).

[213] P. B. Corkum, N. H. Burnett, and M. Y. Ivanov, "*Subfemtosecond pulses*," Opt. Lett. **19**, 1870 (1994).

[214] P. Dietrich, N. H. Burnett, M. Ivanov, and P. B. Corkum, "*High-harmonic generation and correlated two-electron multiphoton ionization with elliptically polarized light*," Phys. Rev. A **50**, R3585 (1994).

[215] A. Fleischer, P. Sidorenko, and O. Cohen, "*Generation of high-order harmonics with controllable elliptical polarization*," Opt. Lett. **38**, 223 (2013).

[216] T. W. Hänsch, "*A proposed sub-femtosecond pulse synthesizer using separate phase-locked laser oscillators*," Opt. Commun. **80**, 71 (1990).

[217] G. Farkas and C. Tóth, "*Proposal for attosecond light pulse generation using laser induced multiple-harmonic conversion processes in rare gases*," Phys. Lett. A **168**, 447 (1992).

[218] S. E. Harris, J. J. Macklin, and T. W. Hänsch, "*Atomic scale temporal structure inherent to high-order harmonic generation*," Opt. Commun. **100**, 487 (1993).

[219] P. Antoine, A. L'Huillier, and M. Lewenstein, "*Attosecond Pulse Trains Using High–Order Harmonics*," Phys. Rev. Lett. **77**, 1234 (1996).

[220] M. B. Gaarde and K. J. Schafer, "*Quantum path distributions for high-order harmonics in rare gas atoms*," Phys. Rev. A **65**, 031406 (2002).

[221] P. M. Paul, E. S. Toma, P. Breger, G. Mullot, F. Augé, P. Balcou, H. G. Muller, and P. Agostini, "*Observation of a Train of Attosecond Pulses from High Harmonic Generation*," Science **292**, 1689 (2001).

[222] Y. Mairesse, A. de Bohan, L. J. Frasinski, H. Merdji, L. C. Dinu, P. Monchicourt, P. Breger, M. Kovačev, R. Taïeb, B. Carré, H. G. Muller, P. Agostini, and P. Salières, "*Attosecond Synchronization of High-Harmonic Soft X-rays*," Science **302**, 1540 (2003).

[223] K. J. Schafer and K. C. Kulander, "*High Harmonic Generation from Ultrafast Pump Lasers*," Phys. Rev. Lett. **78**, 638 (1997).

[224] I. P. Christov, M. M. Murnane, and H. C. Kapteyn, "*High-Harmonic Generation of Attosecond Pulses in the "Single-Cycle" Regime*," Phys. Rev. Lett. **78**, 1251 (1997).

[225] P. Antoine, D. B. Milošević, A. L'Huillier, M. B. Gaarde, P. Salières, and M. Lewenstein, "*Generation of attosecond pulses in macroscopic media*," Phys. Rev. A **56**, 4960 (1997).

[226] M. Hentschel, R. Kienberger, C. Spielmann, G. A. Reider, N. Milosevic, T. Brabec, P. Corkum, U. Heinzmann, M. Drescher, and F. Krausz, "*Attosecond metrology*," Nature **414**, 509 (2001).

[227] E. Goulielmakis, M. Schultze, M. Hofstetter, V. S. Yakovlev, J. Gagnon, M. Uiberacker, A. L. Aquila, E. M. Gullikson, D. T. Attwood, R. Kienberger, F. Krausz, and U. Kleineberg, "*Single-Cycle Nonlinear Optics*," Science **320**, 1614 (2008).

[228] K. Zhao, Q. Zhang, M. Chini, Y. Wu, X. Wang, and Z. Chang, "*Tailoring a 67 attosecond pulse through advantageous phase-mismatch*," Opt. Lett. **37**, 3891 (2012).

[229] C. Altucci, J. Tisch, and R. Velotta, "*Single attosecond light pulses from multi-cycle laser sources*," J. Mod. Opt. **58**, 1585 (2011).

[230] H. Vincenti and F. Quéré, "*Attosecond Lighthouses: How To Use Spatiotemporally Coupled Light Fields To Generate Isolated Attosecond Pulses*," Phys. Rev. Lett. **108**, 113904 (2012).

[231] J. A. Wheeler, A. Borot, S. Monchoce, H. Vincenti, A. Ricci, A. Malvache, R. Lopez-Martens, and F. Quere, "*Attosecond lighthouses from plasma mirrors*," Nature Photon. **6**, 829 (2012).

[232] P. Agostini and L. F. DiMauro, "*The physics of attosecond light pulses*," Rep. Prog. Phys. **67**, 813 (2004).

[233] P. B. Corkum and F. Krausz, "*Attosecond science*," Nat. Phys. **3**, 381 (2007).

[234] S. Watanabe, K. Kondo, Y. Nabekawa, A. Sagisaka, and Y. Kobayashi, "*Two-Color Phase Control in Tunneling Ionization and Harmonic Generation by a Strong Laser Field and Its Third Harmonic*," Phys. Rev. Lett. **73**, 2692 (1994).

[235] H. Eichmann, A. Egbert, S. Nolte, C. Momma, B. Wellegehausen, W. Becker, S. Long, and J. K. McIver, "*Polarization-dependent high-order two-color mixing*," Phys. Rev. A **51**, R3414 (1995).

[236] E. Cormier and M. Lewenstein, "*Optimizing the efficiency in high order harmonic generation optimization by two-color fields*," The European Physical Journal D-Atomic, Molecular, Optical and Plasma Physics **12**, 227 (2000).

[237] I. J. Kim, C. M. Kim, H. T. Kim, G. H. Lee, Y. S. Lee, J. Y. Park, D. J. Cho, and C. H. Nam, "*Highly Efficient High-Harmonic Generation in an Orthogonally Polarized Two-Color Laser Field*," Phys. Rev. Lett. **94**, 243901 (2005).

[238] T. Siegel, R. Torres, D. J. Hoffmann, L. Brugnera, I. Procino, A. Zaïr, J. G. Underwood, E. Springate, I. C. E. Turcu, L. E. Chipperfield, and J. P. Marangos, "*High harmonic emission from a superposition of multiple unrelated frequency fields*," Opt. Express **18**, 6853 (2010).

[239] P. Russbueldt, T. Mans, J. Weitenberg, H. D. Hoffmann, and R. Poprawe, "*Compact diode-pumped 1.1 kW Yb:YAG Innoslab femtosecond amplifier*," Opt. Lett. **35**, 4169 (2010).

[240] T. Eidam, S. Hanf, E. Seise, T. V. Andersen, T. Gabler, C. Wirth, T. Schreiber, J. Limpert, and A. Tünnermann, "*Femtosecond fiber CPA system emitting 830 W average output power*," Opt. Lett. **35**, 94 (2010).

[241] T. J. Hammond, "*Intracavity Generation of High Order Harmonics*," PhD thesis, University of British Columbia, Vancouver (2011).

[242] G. Scoles, ed., *Atomic and Molecular Beam Methods*, vol. 1, Oxford University Press (1988).

[243] D. C. Yost, "*Development of an Extreme Ultraviolet Frequency Comb for Precision Spectroscopy*," PhD thesis, University of Colorado (2011).

[244] J. Peatross, J. L. Chaloupka, and D. D. Meyerhofer, "*High-order harmonic generation with an annular laser beam*," Opt. Lett. **19**, 942 (1994).

[245] A. V. Birulin, V. T. Platonenko, and V. V. Strelkov, "*High-order harmonic generation in colliding beams*," Quantum Electron. **26**, 377 (1996).

[246] S. Fomichev, P. Breger, B. Carré, P. Agostini, and D. Zaretsky, "*Non-Collinear High-Harmonic Generation*," Laser Phys. **12**, 383 (2002).

[247] J. B. Bertrand, H. J. Wörner, H.-C. Bandulet, E. Bisson, M. Spanner, J.-C. Kieffer, D. M. Villeneuve, and P. B. Corkum, "*Ultrahigh-Order Wave Mixing in Noncollinear High Harmonic Generation*," Phys. Rev. Lett. **106**, 023001 (2011).

[248] J. Wu and H. Zeng, "*Cavity-enhanced noncollinear high-harmonic generation for extreme ultraviolet frequency combs*," Opt. Lett. **32**, 3315 (2007).

[249] A. Ozawa, J. Rauschenberger, C. Gohle, M. Herrmann, D. R. Walker, V. Pervak, A. Fernandez, R. Graf, A. Apolonski, R. Holzwarth, F. Krausz, T. W. Hänsch, and T. Udem, "*High Harmonic Frequency Combs for High Resolution Spectroscopy*," Phys. Rev. Lett. **100**, 253901 (2008).

[250] K. Moll, R. Jones, and J. Ye, "*Nonlinear dynamics inside femtosecond enhancement cavities*," Opt. Express **13**, 1672 (2005).

[251] O. Pronin, V. Pervak, E. Fill, J. Rauschenberger, F. Krausz, and A. Apolonski, "*Ultrabroadband efficient intracavity XUV output coupler*," Opt. Express **19**, 10232 (2011).

[252] J. Weitenberg, P. Rußbüldt, T. Eidam, and I. Pupeza, "*Transverse mode tailoring in a quasi-imaging high-finesse femtosecond enhancement cavity*," Opt. Express **19**, 9551 (2011).

[253] I. Pupeza, E. E. Fill, and F. Krausz, "*Low-loss VIS/IR-XUV beam splitter for high-power applications*," Opt. Express **19**, 12108 (2011).

[254] W. P. Putnam, D. N. Schimpf, G. Abram, and F. X. Kärtner, "*Bessel-Gauss beam enhancement cavities for high-intensity applications*," Opt. Express **20**, 24429 (2012).

[255] A. Ozawa, A. Vernaleken, W. Schneider, I. Gotlibovych, T. Udem, and T. W. Hänsch, "*Non-collinear high harmonic generation: a promising outcoupling method for cavity-assisted XUV generation*," Opt. Express **16**, 6233 (2008).

[256] A. Ozawa, "*Frequency combs in the extreme ultraviolet*," PhD thesis, Ludwig-Maximilians-Universität München (2009).

[257] M. B. Gaarde, J. L. Tate, and K. J. Schafer, "*Macroscopic aspects of attosecond pulse generation*," J. Phys. B **41**, 132001 (2008).

[258] C. Hernández-García, J. A. Pérez-Hernández, J. Ramos, E. C. Jarque, L. Roso, and L. Plaja, "*High-order harmonic propagation in gases within the discrete dipole approximation*," Phys. Rev. A **82**, 033432 (2010).

[259] K. T. Kim, C. Zhang, A. D. Shiner, S. E. Kirkwood, E. Frumker, G. Gariepy, A. Naumov, D. M. Villeneuve, and P. B. Corkum, "*Manipulation of quantum paths for space-time characterization of attosecond pulses*," Nat. Phys. **9**, 159 (2013).

[260] V. V. Strelkov, private communication (2013).

[261] C. Zhang, K. T. Kim, T. Ruchon, J.-F. Hergott, D. Villeneuve, P. Corkum, and F. Quéré, "*The Attosecond Lighthouse in Gas: Spatial Gating Technique for Isolated Attosecond Pulses generation*," in *Frontiers in Optics 2012/Laser Science XXVIII*, LW1H.5, Optical Society of America (2012).

[262] S. Hädrich, J. Rothhardt, M. Krebs, F. Tavella, A. Willner, J. Limpert, and A. Tünnermann, "*High harmonic generation by novel fiber amplifier based sources*," Opt. Express **18**, 20242 (2010).

[263] J. Boullet, Y. Zaouter, J. Limpert, S. Petit, Y. Mairesse, B. Fabre, J. Higuet, E. Mével, E. Constant, and E. Cormier, "*High-order harmonic generation at a megahertz-level repetition rate directly driven by an ytterbium-doped-fiber chirped-pulse amplification system*," Opt. Lett. **34**, 1489 (2009).

[264] C.-T. Chiang, A. Blattermann, M. Huth, J. Kirschner, and W. Widdra, "*High-order harmonic generation at 4 MHz as a light source for time-of-flight photoemission spectroscopy*," Appl. Phys. Lett. **101**, 071116 (2012).

[265] C. J. Saraceno, C. Schriber, F. Emaury, O. H. Heckl, C. R. E. Baer, M. Hoffmann, K. Beil, C. Kränkel, M. Golling, T. Südmeyer, and U. Keller, "*Cutting-Edge High-Power Ultrafast Thin Disk Oscillators*," Appl. Sci. **3**, 355 (2013).

[266] C. J. Saraceno, F. Emaury, O. H. Heckl, C. R. E. Baer, M. Hoffmann, C. Schriber, M. Golling, T. Südmeyer, and U. Keller, "*275 W average output power from a femtosecond thin disk oscillator operated in a vacuum environment*," Opt. Express **20**, 23535 (2012).

[267] S. Kim, J. Jin, Y.-J. Kim, I.-Y. Park, Y. Kim, and S.-W. Kim, "*High-harmonic generation by resonant plasmon field enhancement*," Nature **453**, 757 (2008).

[268] H. Carstens, S. Holzberger, J. Kaster, J. Weitenberg, V. Pervak, A. Apolonski, E. Fill, F. Krausz, and I. Pupeza, "*Large-mode enhancement cavities*," Opt. Express **21**, 11606 (2013).

[269] H. Carstens, N. Lilienfein, S. Holzberger, C. Jocher, T. Eidam, J. Limpert, A. Tünnermann, A. Apolonski, E. Fill, I. Pupeza, and F. Krausz, "*Cavity-Enhanced 196 kW Average-Power Infrared Pulses*," in *Advanced Solid-State Lasers Congress*, JTh5A.3, Optical Society of America (2013).

[270] P. Russbueldt, T. Mans, G. Rotarius, J. Weitenberg, H. D. Hoffmann, and R. Poprawe, "*400W Yb:YAG Innoslab fs-Amplifier*," Opt. Express **17**, 12230 (2009).

[271] T. Mans, P. Rußbüldt, J. Weitenberg, G. Rotarius, D. Hoffmann, and R. Poprawe, "*Ultrafast Ytterbium Doped INNOSLAB Amplifier with High Average Power*," in *Conference on Lasers and Electro-Optics/International Quantum Electronics Conference*, CThJ2, Optical Society of America (2009).

[272] A. L'Huillier, M. Lewenstein, P. Salières, P. Balcou, M. Y. Ivanov, J. Larsson, and C. G. Wahlström, "*High-order harmonic-generation cutoff*," Phys. Rev. A **48**, R3433 (1993).

[273] C. Gohle, "*A Coherent Frequency Comb in the Extreme Ultraviolet*," PhD thesis, Ludwig-Maximilians-Universität München (2006).

[274] B. Bernhardt, "*Dual Comb Spectroscopy*," PhD thesis, Ludwig-Maximilians-Universität München (2011).

[275] W. Schneider, L. Lötscher, S. Stebbings, A. Vernaleken, T. Udem, T. Hänsch, P. Rußbüldt, D. Hoffmann, A. Apolonsky, M. Kling, and F. Krausz, "*Single pass high harmonic generation with 515 nm pulses at 50 MHz repetition rate*," in *DPG Frühjahrstagung, Stuttgart*, Q 66.3, Deutsche Physikalische Gesellschaft (2012).

List of publications

- **Carrier-envelope frequency stabilization of a Ti:sapphire oscillator using different pump lasers**
  A. Vernaleken, B. Schmidt, M. Wolferstetter, T. W. Hänsch, R. Holzwarth, and P. Hommelhoff
  Optics Express **20**, 18387 (2012)

- **Vacuum ultraviolet frequency combs generated by a femtosecond enhancement cavity in the visible** [209]
  B. Bernhardt, A. Ozawa, A. Vernaleken, I. Pupeza, J. Kaster, Y. Kobayashi, R. Holzwarth, E. Fill, F. Krausz, T. W. Hänsch, and Th. Udem
  Optics Letters **37**, 503 (2012)

- **Single-pass high-harmonic generation at 20.8 MHz repetition rate** [37]
  A. Vernaleken, J. Weitenberg, T. Sartorius, P. Russbueldt, W. Schneider, S. L. Stebbings, M. F. Kling, P. Hommelhoff, H.-D. Hoffmann, R. Poprawe, F. Krausz, T. W. Hänsch, and Th. Udem
  Optics Letters **36**, 3428 (2011)

- **Non-collinear high harmonic generation: a promising outcoupling method for cavity-assisted XUV generation** [255]
  A. Ozawa, A. Vernaleken, W. Schneider, I. Gotlibovych, Th. Udem, T. W. Hänsch
  Optics Express **16**, 6233 (2008)

Danksagung

Eine Promotion ist zu einem großen Teil eine Mannschaftsleistung, und so möchte ich abschließend die Gelegenheit nutzen, mich bei all jenen zu bedanken, die mich während meiner Zeit am MPQ direkt oder indirekt unterstützt haben.

Mein erster Dank gebührt meinem Doktorvater Prof. Theodor Hänsch, der mir in seiner Gruppe das wissenschaftliche Arbeiten unter bestmöglichen Rahmenbedingungen und mit großen individuellen Freiheiten ermöglicht hat und auch in eher zähen Phasen keine Zweifel an seinem Vertrauen aufkommen ließ.

Thomas Udem war als "Co-Trainer" der MPQ-Mannschaft mein direkter Betreuer und immer bereit, mich von seinem enormen Fachwissen, seiner Begeisterung für Physik und seiner Fähigkeit, schwierige Zusammenhänge anschaulich zu erklären, profitieren zu lassen. Dafür danke ich ihm ganz herzlich - und natürlich auch dafür, dass er mich aufs Glatteis des Großen Löfflers geführt hat und bei unseren Radtouren nach Ringberg an jedem Hügel für unkontrollierte Tempoverschärfungen zu haben war.

Zu größtem Dank verpflichtet bin ich Akira Ozawa, mit dem ich die meiste Zeit im Labor verbracht habe. Er war nicht nur mein geduldiger Lehrmeister für Kurzpulslaser und HHG, sondern auch später noch mein erster Ansprechpartner bei allen Fragen zu und Problemen mit meinen Experimenten und meiner Doktorarbeit - dank Skype selbst nach seiner Rückkehr nach Tokio, wo ich ihn zu meiner großen Freude einige Wochen vor meiner Prüfung besuchen konnte.

Mit Birgitta Bernhardt durfte ich zum bestmöglichen Zeitpunkt an ihrer "grünen Cavity" arbeiten: als es die ersten Ergebnisse gab. Ich danke ihr herzlich für die stets angenehme und gute Zusammenarbeit am EUV-Frequenzkamm-Projekt und für die Regie zahlreicher schöner Weihnachtsfilme. Ein großes Dankeschön geht auch an Igor Gotlibovych, der mich tatkräftig bei der Simulation und Auswertung der NCHHG-Experimente unterstützt hat.

Mit Peter Rußbüldt, Johannes Weitenberg, Thomas Sartorius, Torsten Mans und Dieter Hoffmann vom Fraunhofer ILT in Aachen habe ich im Rahmen des "Korona"-Projekts nicht nur Stunden am Telefon, sondern auch einige Tage und Nächte in Labors (und vereinzelt auch in Kneipen) in Garching und Aachen verbracht. Dabei habe ich nicht nur von ihrer Erfahrung mit Innoslab-Verstärkern, Lasern und Kühlern aller Art und dem Arbeiten unter Reinraumbedingungen profitiert, sondern konnte auf ihre Initiative hin auch einen schönen Preis mit nach Hause nehmen. Dafür sowie für die trotz aller Verzögerungen immer freundschaftlich-angenehme und humorvolle Kollaboration bedanke ich mich herzlich.

Für die erfolgreiche Zusammenarbeit bei den Experimenten zur single pass HHG gilt mein Dank Waldemar Schneider, Sarah Stebbings, Matthias Kling und Prof. Ferenc Krausz, dem zusätzlich noch besonderer Dank für die Übernahme des Zweitgutachtens

gebührt (und dafür, dass er beim Firmenlauf wenigstens einmal langsamer war als ich).

Danke sage ich auch Bernhard Schmidt, Martin Wolferstetter, Ronald Holzwarth und Peter Hommelhoff für die fruchtbare Zusammenarbeit beim Vermessen der kommerziellen Pumplaser.

Bei meinen Kollegen Simon Holzberger, Henning Carstens, Jan Kaster und Ernst Fill aus der Krausz-Gruppe bedanke ich mich für die hilfreichen Diskussionen über Überhöhungsresonatoren und HHG. Gleiches gilt für Ioachim Pupeza, dem ich darüber hinaus für die Einladung nach Spanien zu seiner Hochzeit danke.

Ohne die maßgefertigten Teile aus den Händen und Maschinen von Charly Linner und Wolfgang Simon sowie die Elektronik von Helmut Brückner wären viele Ideen nicht in die Praxis umzusetzen gewesen. Ihnen gilt meine Bewunderung und mein Dank dafür, dass es trotz schlampiger Skizzen und komplizierter Wünsche meistens doch eine glänzende Lösung gab.

Ingrid Hermann und Gabriele Gschwendtner haben für einen unkomplizierten und reibungslosen Ablauf aller administrativen Dinge gesorgt, wofür ich ihnen zu großem Dank verpflichtet bin.

Meine Zimmergenossen aus D0.27 waren sowohl kompetente Ansprechpartner bei allen Arten von (fachlichen) Fragen als auch eine stete Quelle willkommener Abwechslung, und so gab es wahrscheinlich keinen Tag, an dem nicht mindestens einmal schallend gelacht wurde. Für seinen Anteil daran danke ich Dylan Yost, der als dienstjüngster D0.27er stets gut gelaunt, immer hilfsbereit und mit einem schier unerschöpflichen Vorrat an angeblich sehenswerten Youtube-Videos ausgestattet war.

Ebenso bedanke ich mich bei Stefan Droste, der sowohl ein harter Gegner beim Würfeln und allen erdenklichen Varianten des Bürosports mit Kaffeekapseln als auch ein geschätzter Begleiter bei unseren Ausflügen in Laufschuhen, auf dem Rad und auf die Wiesn sowie der bestmögliche Reisepartner für gemeinsame Erkundungen und Abenteuer in Dubai und Tokio war.

Mit Maximilian Herrmann und Guido Saathoff verbinden mich seit dem Tag, an dem sie mich in D0.27 unter ihre Fittiche genommen haben, eine Vielzahl gemeinsamer Interessen und Aktivitäten auch neben der Arbeit. Daher danke ich ihnen nicht nur herzlich für ihre Unterstützung mit Rat und Tat im Labor und bei der sorgfältigen Korrektur meiner Doktorarbeit, sondern auch für ihre qualifizierte Gesellschaft beim Radfahren, Fußballschauen, Bierbrauen, Diskutieren und beim Pubquiz.

Allen übrigen Mitgliedern und Alumni der Hänsch-Gruppe samt allen Untergruppen danke ich für den großartigen kollegialen Zusammenhalt und die zahlreichen fröhlichen Stunden innerhalb und außerhalb des Instituts.

Zuletzt möchte ich mich aus tiefstem Herzen bei meinen Eltern bedanken, die mich zeit meines Lebens uneingeschränkt gefördert und mir gemeinsam mit meinen Geschwistern sowie meiner Freundin immer den nötigen Rückhalt gegeben haben.